SEARCH FOR NEUTRON ANTI-NEUTRON OSCILLATION AT THE SUDBURY NEUTRINO OBSERVATORY

A Thesis

Presented to

The Faculty of Graduate Studies

of

The University of Guelph

by

MARC BERGEVIN

In partial fulfilment of requirements

for the degree of

Doctor of Philosophy

December, 2010

ABSTRACT

SEARCH FOR NEUTRON ANTI-NEUTRON OSCILLATION AT THE SUDBURY NEUTRINO OBSERVATORY

Marc Bergevin
University of Guelph, 2010

Advisors:
Professor Jimmy Law
Dr. Alan W. P. Poon

Baryon violating processes are expected in order to explain the baryon asymmetry of the universe. In this thesis, a limit on the neutron anti-neutron (nnbar) baryon violating process ($\Delta(B-L)=2$) is given for part of the data of the SNO experiment; data is sampled from the three phases of the SNO experiment to construct a three-phase blind analysis. The profile likelihood method is used to evaluate a lower limit on the three-phase open data set of SNO giving a oscillation lifetime for a neutron bound in deuteron of $T_{nucl} > 1.09 \times 10^{31}$ sec (bounded) and $T_{nucl} > 3.01 \times 10^{31}$ sec (unbounded) at 90% CL for 326.4 days of detector live time. This translates into a free oscillation lifetime of $\tau_{nnbar} > 1.18 \times 10^{8}$ sec (bounded) and $\tau_{nnbar} > 1.96 \times 10^{8}$ sec (unbounded) at 90% CL for 326.4 days of detector live time; this free oscillation lifetime include nuclear information using Dover and Gal model (a suppression rate of $T_R = 0.248 \times 10^{23}$ sec^{-1}) in order to compare to experiment that use other nuclear targets. It also includes the systematic errors on both the atmospheric neutrino backgrounds and the detection efficiency of the nnbar signal. This result is comparable to the Soudan-II result of $\tau_{nnbar} > 1.3 \times 10^{8}$ sec at 90% CL; it is expected that the full analyses will improve the SNO result by approximatively a factor of 2 which will give a lower limit comparable to the Super-Kamiokande result of $\tau_{nnbar} > 2.36 \times 10^{8}$ sec (bounded) at 90% CL.

Preface

The Sudbury Neutrino Observatory (SNO) was constructed to detect solar neutrinos. However, more exotic searches such as proton decay were also considered due to the the depth at which the laboratory is located which greatly reduces the flux of cosmic rays. The size of SNO (1 kiloton of D_2O) is smaller than Super-Kamiokande (50 kiloton of H_2O) and offers less sensitivity to proton decay, but reduces also the amount of atmospheric neutrino events which constitute the background of the proton decay search. Newer limits from Super-Kamiokande for the search of proton decay now far outreach the sensitivity of SNO.

The D_2O media used within the SNO detector opens new possibility for parallel search of symmetry breaking process. The neutron anti-neutron (nnbar) oscillation within the deuteron is predicted to be less suppressed than within oxygen. The deuteron advantage combined with the reduced rate of atmospheric neutrino events puts the SNO sensitivity on par with the Super-Kamiokande experiment. While the concept of neutron oscillating into an anti-neutron seems counterintuitive, oscillation of neutral particles such as neutrinos and $K^o \leftrightarrow \bar{K}^o$ have been observed in nature.

This thesis addresses the various challenges of the search of this exotic signal: the SNO sensitivity to the nnbar signal and the simulation of the signal; the propagation behavior of the various particles emitted from this signal; the isolation of the signal from the large amount of data and the creation of various tools that are needed for a proper signal extraction.

Acknowledgments

It is hard to thank all the people who have had an impact on this project since I have started working on this in 2003 since many things evolve in six years. If I forget anyone important, I am sorry.

First and foremost I would like to thank Jimmy Law for his constant support and making it possible for me to work on this exotic project. I also thank Alan Poon for allowing me to come to the Lawrence Berkeley Laboratory to work with him and his group, I have enjoyed my time here more than I can express.

I should not forget Bernie Nickel whose approach to physic is an inspiration for me, thank you for all the illuminating and lively conversations.

I want to say a special thanks to Gersende Prior who has helped me greatly with the project and for convincing me to stick with this a little while longer. I thank also Joao Pequenao for dragging me to the gym and making me lose all that weight; and also for the memorable lunches (which I do not think contributed to the weight..).

It takes more time to finish a PhD than a post-doc and I have seen many fly by. I would like to thank James Loach, Jason Detwiller, Charles Currat, Ian Lawson and Reyco Henning for kindly answering my many many questions, most often by asking me more complex questions.

I would like the thank Christiane Tremblay, Annie Bergevin and Isabelle Tremblay for their support and encouragement throughout the many years it took me to finish this

project. I would like to thank Jonathan Leboeuf and Jean-François Lacroix for their friendship (and also for coming to see me in California).

I would also like to give a nod to *l'équipe d'initiation 1998 #3*, "Pôpa" Sylvie Brunet, "Môman" David Côté, "Môman" Vincent Bouchard and Hendrick Labranche "la dinde" who have been friends and survivors of the University of Montreal undergrad program.

I would like to thank Michael Arthurs, Lin Chen, Andrew Tersigni, Ian MacKay, Simon Comeau, Julia Parkman and Dan Glickman for making my stay in Guelph as lively as it was.

Finally I would like to thank Jana Johnson for her love and support. I would also like to thank her for asking me "Are you done yet?" for those five months where I thought I had only one more week left to go, which gave me the drive to actually get through that eternal week.

Contents

List of Tables

List of Figures

Chapter 1

Neutrino Physics and the SNO Detector

Liebe Radioacktive Damen und Herren,

Wolfgang Pauli

1.1 Particle Physics Status

The scientific methods introduced by Sir Francis Bacon in *Novum Organum* (1620) has allowed scientific fields to systematically evolve with each discoveries with the ultimate goal of gaining a complete understanding of the fundamental laws of nature. The science of particle physics has had throughout its development important indications that missing or contradictory elements were present in the theories of the times.

At many stages, theories regarding the nature of particles were thought complete, but had to be revisited due to unexplained phenomena. The original road block involved two opposing theories, the corpuscular, Newton's concept that light was constituted of small clump of matter, and the wave theory, Hooke's and Huygens concept that light was akin to a wave, were in conflict for nearly three centuries. Ironically, these two theories were

then both proven to be correct and incomplete at the same time by the advent of quantum dynamics.

At the beginning of the twentieth century, the theory of quantum dynamic was developed to understand phenomena that could not otherwise be explained by classical mechanics[1]. These phenomena are:

- Blackbody Radiation
- The Photoelectric Effect
- The Compton Effect
- The Bohr Atom
- Wave-Particle Diffraction

which are all well explained today with quantum physics.

Within the same time period, the study of radioactive decays led to the observation of the beta decay anomaly. The resolution of this anomaly led to the proposal of the neutrino. Today, the field of neutrino physics[2] is one in its own right involving large scale international experiments that study the behavior of this small nearly undetectable particle.

The standard model is the theoretical model that describes interactions between elementary particles. This model was established to understand the interactions between particles such as lepton, quarks and mediator bosons (photons, W, Z, Higgs). The Large hadron Collider (LHC) is starting operation in the search for the Higgs particle; this particle is at the base of the theory that explain why some particles gain mass.

Some enigma are however still present within the theoretical frame of particle physics. These can be summarized as,

[1] Concept taken from [1] in which a detailed treatment of the creation of quantum theory is given. While the treatment is not historically accurate, these phenomena showed the need of a new theory or explanation of nature.

[2] A very comprehensive overview of neutrino physics is *Fundamentals of Neutrino Physics and Astrophysics* by C. Guinti and C.W. Kim [2]. Some of the historical facts and concepts are taken from that textbook.

- CP Violation
- Neutrino Properties
- Proton Stability
- Dark Matter and Energy

The observed CP violation in meson decay is a predicted condition to explain the baryon asymmetry that is present in our universe [3], but the observed violation is too small to explain the baryon asymmetry. Certain theoretical models that try to address the proton stability, which will be detailed in the next chapter, may also explain baryon asymmetry. Ultimately, the validation of these models may address why there is more matter than antimatter in our universe.

This thesis tries to address some of these topics indirectly by looking for an exotic signal that offers alternatives to proton decays for the search of baryon asymmetry. The search for neutron-antineutron (nnbar) oscillation is made with the SNO detector, a large heavy water Čerenkov detector situated in Sudbury, Canada.

1.2 Neutrino Physics

There are three types of nuclear decays. These are known as the beta, alpha and gamma decays so called because of the type of emerging radioactive particles. Beta decay was first observed in 1892 by Becquerel on Uranium and two problems were observed: the beta energy spectrum was continuous which was not the case for the spectrum of radiative decays involving α and γ; the spin was not conserved. The neutrino was first predicted in 1930 by Pauli to try to solve the beta decay problem.

While many elements were known, only a handful of particles were known at the time; the neutron being experimentally discovered only 2 years later by Chadwick, the neutrino was originally named neutron by Pauli, but was renamed “neutrino” (small neutron) by

Fermi.

The beta decay is governed by the following equation,

$$ {}^{A}_{Z}X \rightarrow {}^{A}_{Z\pm1}Y + \beta^{\mp} + (\bar{\nu}_e)\nu_e \tag{1.1} $$

where the β particle is the electron. While the neutrino was required for both spin and energy conservation, the idea of an undetectable particle was not liked[3], that is until the neutrino was detected from a nuclear reactor experiment done by Reines and Cowan in 1956.

Pauli proposed that the mass of the neutrino would be on the same scale as that of the electron, which did not turn out to be the case. Fermi and Perrin showed that the mass of the neutrino could be null in 1933. The mass of the neutrino was assumed null until the observation of atmospheric neutrino oscillation by Super-Kamiokande a decade ago[4].

The tools available for neutrino detection use in one way or another the following interactions,

$$ \begin{aligned} \nu_e n &\rightarrow pe^- \text{ (IBD)} \\ \bar{\nu}_e p &\rightarrow ne^+ \text{ (IBD)} \\ \nu_e e^- &\rightarrow \nu_e e^- \text{ (ES)} \end{aligned} \tag{1.2} $$

which are known as the inverse beta decay (IBD) and electron scattering (ES). While the cross section for these neutrino interactions is very small, it is not zero!

Neutrino Sources

The search of the neutrino properties are done from three type of neutrino sources,

- Terrestrial neutrinos production from nuclear reactors
- Solar neutrino production from the *pp* and CNO cycle [5]. These neutrinos will have low to moderate energies up to ≈20 MeV.

[3] *I have done a terrible thing, I have postulated a particle that cannot be detected*, Pauli.

- Atmospheric neutrino production originating from by-products of cosmic rays interacting with the earth's atmosphere. These neutrinos may have energies of up to 1 TeV.

The sources that are relevant to the SNO experiment are the solar and atmospheric ones. Reactor neutrinos have a threshold energy of 1.806 MeV which fall below the energy sensitivity of SNO of 5.5 MeV's, this threshold was lowered to 3.5 MeV for the Low energy Threshold Analysis (LETA) [6]. Early measurements of the solar neutrino flux showed another anomaly: the flux of electron-type neutrinos was much less, about a factor of three, than the expected flux from the solar model.

Solar Neutrino Experiments

There are three type of solar neutrino experiments,

- **Radiochemical Detectors**: Detector for low energy solar neutrinos (down to 0.233 MeV for Galium experiment). The Chlorine experiment at Homestake was the first solar neutrino experiment. The reaction,

$$\nu_e + {}^{37}\mathrm{Cl} \rightarrow {}^{37}\mathrm{Ar} + e^- \tag{1.3}$$

  has an energy threshold $E_{threshold} = 0.814$ MeV. The ^{37}Ar atoms were collected afterward for counting using proportional counters. Gallium has a lower neutrino detection energy threshold in :

$$\nu_e + {}^{71}\mathrm{Ga} \rightarrow {}^{71}\mathrm{Ge} + e^- \tag{1.4}$$

  with $E_{threshold} = 0.233$ MeV. Results from these experiment indicated a lower neutrino flux than was expected; the Chlorine experiment saw 3.3 time fewer neutrinos than was predicted and the Gallium experiment saw 1.9 times less neutrinos than expected.

- **Water Čerenkov Imaging Detectors**: Detectors (IMB, Super-Kamiokande) that detect Čerenkov radiation resulting from charged particles emerging after solar neutrino interactions in their water target. SNO used a heavy water (D_2O) target. These

experiments have a detection threshold of ∼5 MeV of energy and are well suited for solar and atmospheric neutrino detection.

- **Scintillator Detectors**: Detectors that use liquid scintillator to detect solar neutrino and are sensitive to geoneutrinos (KamLAND, Borexino).

1.3 SNO Solar Neutrino Results

The SNO experiment began data taking on November 2nd, 1999 and finished taking data on November 28th, 2006. During that time span, the solar neutrino flux was measured in three different operational phases.

The first phase of data taking used 1 kT of heavy water (D_2O), contained in a 12-m diameter spherical acrylic vessel, as the neutrino target. In the salt phase, two tonnes of NaCl were added to the D_2O in order to increase the neutron capture efficiency. In the last phase of SNO, ^{3}He proportional counters were added in order to make an independent measurement of neutrons, the signature for neutrino-deuteron neutral-current interaction.

Pure D_2O Phase

Solar neutrinos interact with the heavy water in the following ways:

$$\begin{aligned} \nu_e + d &\rightarrow p + p + e^- \text{ (CC)} \\ \nu_x + d &\rightarrow p + n + \nu_x \text{ (NC)} \\ \nu_x + e^- &\rightarrow \nu_x + e^- \text{ (ES)} \end{aligned} \tag{1.5}$$

while the electron from both the CC (Charge Current) and ES (Elastic Scattering) can be measured directly from the Čerenkov light it produces, the neutron from the NC (Neutral Current) interaction needs first be captured before it can be detected. In the D_2O phase, the only capture process is,

$$n + d \rightarrow {}^3\text{H} + \gamma \text{ (6.25 MeV)}. \tag{1.6}$$

The NC is unique to SNO and offers important information on the solar neutrino flux since the interaction is equally sensitive to all neutrino flavors.

Salt Phase

In the salt phase, another means of capturing neutrons was introduced. Two tonnes of high purity salt (NaCl) were introduced. The following interaction shows the neutron capture relation,

$$n + {}^{35}\text{Cl} \rightarrow {}^{36}\text{Cl} + n\gamma(8.6\text{ MeV}) \tag{1.7}$$

where n denotes that a cascade of γ's are produced. The total active solar neutrino flux was found to be (in units of 10^6 cm^{-2} s^{-1}) [6]

$$\Phi_{^8B} = 5.046^{+0.159}_{-0.152}(stat)^{+0.107}_{-0.123}(syst) \tag{1.8}$$

for the combination of the D_2O and salt phases.

NCD Phase

In the NCD phase, thirty six ^{3}He counters and four ^{4}He counters were introduced. The measured flux from the CC, ES and NC reactions are (in units of 10^6 cm^{-2} s^{-1}):

$$\begin{aligned}
\phi^{SNO}_{CC} &= 1.67^{+0.05}_{-0.04}(stat)^{+0.07}_{-0.08}(syst) \\
\phi^{SNO}_{ES} &= 1.77^{+0.24}_{-0.21}(stat)^{+0.09}_{-0.10}(syst) \\
\phi^{SNO}_{NC} &= 5.54^{+0.33}_{-0.31}(stat)^{+0.36}_{-0.34}(syst)
\end{aligned} \tag{1.9}$$

with $\phi_{CC}/\phi_{NC} = 0.301 \pm 0.033(total)$ [7]. This result confirms that the electron neutrinos created in the sun change flavor before reaching earth.

1.3.1 SNO's Atmospheric Neutrino Results

The SNO Collaboration published its measurement of the atmospheric neutrino flux in 2009 [8]. The conclusion of the analysis was a shift from the predicted three-dimensional Bartol flux and the neutrino cross-section which have been implemented in NUANCE [9]. SNO measured a higher flux of neutrino induced events than the prediction by a factor of $\phi_{norm} = 1.22 \pm 0.09$. More details of the atmospheric neutrino analysis will be given in Chapter 4.

1.4 SNO Analysis Tools and Detector

1.4.1 Analysis Software

The simulation tools used in the description of the detector condition to various physical and instrumental situations have been developed over a the life of SNO. The early codes were written with the Fortran architecture and later codes migrated to a C++ architecture.

The SNO simulation software called SNOMAN[4] uses a variety of software libraries common to particle physics. SNOMAN was built upon the following packages:

- **Zebra**: Data array structure for Fortran architecture [11]
- **Geant3/4**: Particle Monte Carlo propagation Software [12]. Geant3 is fortran based while Geant4 is follows a C++ architecture.
- **Cernlib**: Cern Data Architecture including Cernlib libraries [13].
- **Geant-Fluka**: High energy particle propagation simulation software [14]
- **Calor**: High energy particle propagation interacting with nuclear media Monte Carlo Simulation software [15]
- **EGS4**: Electron and photon transport simulation software [16]. Electron and Čerenkov photon transport are simulated with this simulation software.

These various packages - with the exception of Geant4 - are fully integrated into the SNOMAN simulation and are called by SNOMAN at various stages of particle propagation. In Chapter 3 corrections to the Calor routines - which are routines used in the propagation of the pion particle - will be benchmarked against a stand-alone Geant4 simulation which is not integrated within SNOMAN.

[4]Detailed description found in section Offline Analysis and Simulation Code - SNOMAN of [10]

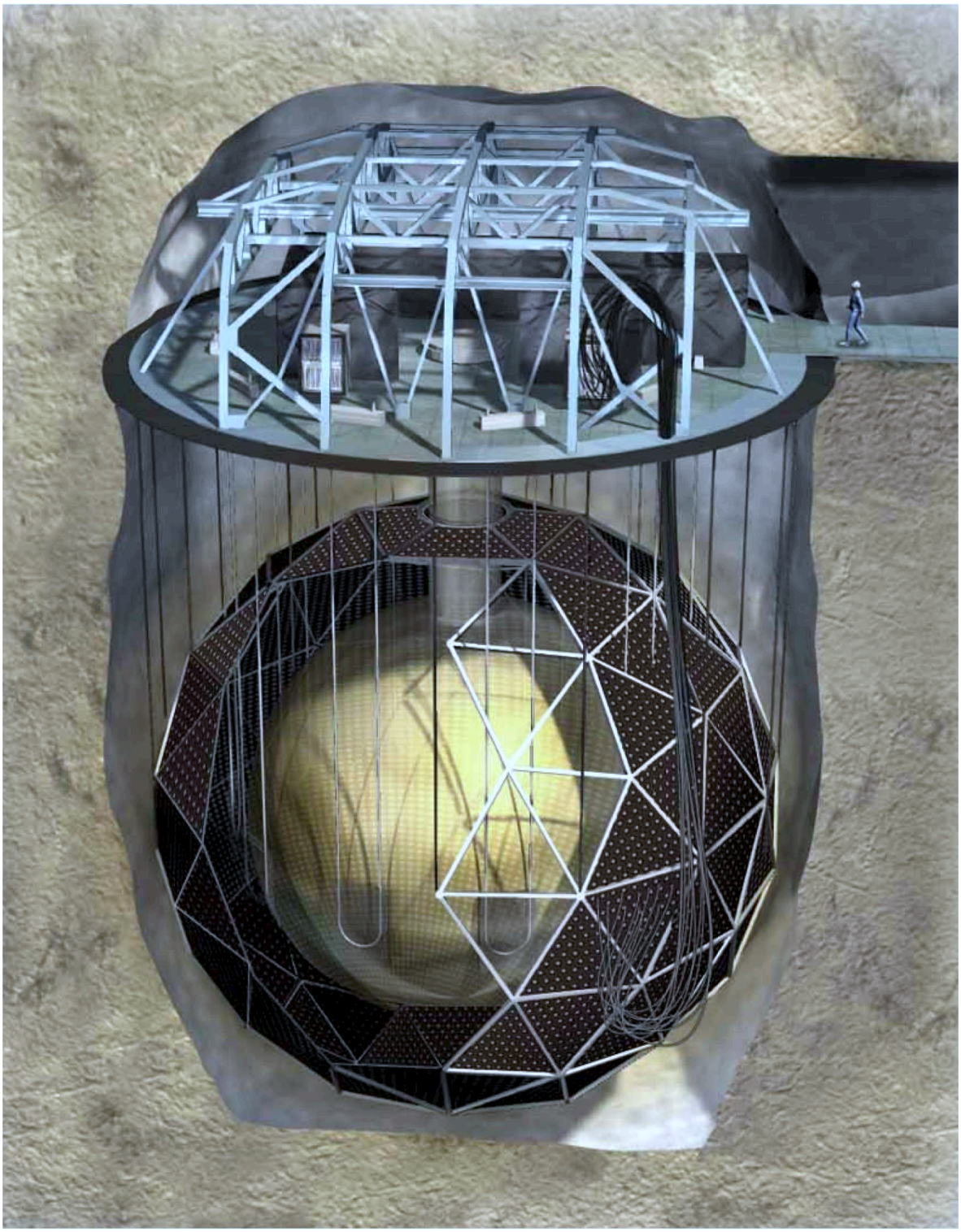

Figure 1.1: Depiction of the SNO Detector. Shown in the picture is the 12 m diameter acrylic vessel which contains 1kilotonne of D_2O. The PMT structure which contains 9438 20 cm PMTs has a diameter of 17.8 meters. Image courtesy of National Geographic.

1.4.2 Photomultiplier Tubes

SNO detects Čerenkov events with series of photomultiplier tubes (PMT) mounted on an icosahedron support structure (PSUP) as seen in Figure 1.1. The photomultiplier tubes chosen for the SNO detector are Hamamatsu R1408 with light concentrators of 27 cm diameter mounted on each PMT's which improve the photocathode coverage to 54% [10].

Along with the 9438 inward looking PMTs, three other categories of tubes are in place[17]:

- **OWL Tubes**: 91 outward looking (OWL) tubes are placed on the outer surface of the PSUP to detect light that originate from outside of the detector. These tubes will be used as a veto to reject external events.
- **BUTTS**: 22 Berkeley Underwater Test Tubes which have been deployed in the H_2O volume during the commissioning phase.These tubes are used as a veto to reject external events.
- **NECK Tubes**: 4 tubes placed in the neck of the detector that are used as a veto for certain instrumental backgrounds.

1.4.3 Calibration Techniques

The SNO experiment is optimized for events with energies of a few MeV's. The calibration was considered paramount and as such the experiment spent more than 30% of its live time in calibration runs. The principal calibrations are:

- ^{16}**N** : A source that generates 6.1 MeV gammas. It is useful in the characterization of the energy response of the detector.
- **Californium** :The ^{252}Cf isotope was used as a source for neutron production. These neutrons were used in the calibration of the neutron detection efficiency [18].

- **Laserball**: A diffuse light source for calibrating the PMT charge and timing response to single photoelectrons.

While the ^{16}N calibration and the neutron response of the detector are not relevant to the nnbar analysis, the PMT response to single photo-electrons is. However, no controllable calibration can be made at high energy to calibrated the energy response of the detector above a value of 50 MeV.

Parameters like the effective electron kinetic energy, β_{14} or θ_{ij} are unreliable at higher energies; alternative parameters such as $N_{photoelectrons}$ (or simply photoelectrons) are needed to characterize events [8]. In the context of this analysis, where events have several GeV of energy, cosmic muons offer a source of high energy events that can be used to calibrate the response of the ring fitter. Useful parameters proper to this analysis will also be discussed in Chapter 6.

1.5 Thesis Layout and Previous Work

The goal of this thesis is to present an analysis of the nnbar search. The studies presented in this thesis are mostly independent from other SNO analyses, although some of the work from various other analyses have been incorporated.

This thesis is divided in several chapters:

- Signal Properties
- Daughter Particle Propagation Properties
- Physical and Instrumental Background Properties
- Event Reconstruction Technique
- Event Reconstruction and Characterization
- Error Propagation and Signal Extraction

In Chapter 2, the nnbar theory as well as the expected signal and sensitivity from such a process are presented. In Chapter 3, the propagation of particle within the detector will be studied with a focus on the propagation of the pions, which constitute the nnbar signal, in the D_2O.

The major backgrounds to the nnbar signal, both physical and instrumental, will be studied in Chapter 4 for the D_2O phase only. A description of the detector run conditions will also be given in this chapter. Chapter 5 will address the event reconstruction and ring counting algorithms.

The analysis requirements are explained in Chapter 6. The requirements include the type of parameters and cuts needed for the extraction of the signal. Comparisons between the simulations and the actual events in the detector are made.

Chapter 7 will present the techniques used in the extraction of the signal and the results from an analysis of data from all three SNO phases.

The multiple ring fitter was developed between the year 2004 and 2005. The work has been published in Master's thesis form [19] by the author. Improvements to this work are presented in Chapter 5.

Chapter 2

Neutron-Antineutron Oscillation

In the beginning there was nothing, and it exploded.

Terry Pratchett

The first of the Sakharov conditions dictates that the baryon number (B) must be violated in order to obtain the imbalance between matter and anti-matter seen in the universe today [3]. However, it is not known if the quantum number ($B-L$) is a conserved quantity or not; if this quantum number is taking as a symmetry of Grand Unified Theory (GUT) model, then exotic process such as proton decay or nnbar oscillation are possible.

More specifically, if this quantity is conserved, proton decay is permitted and the neutrino is defined as a Dirac neutrino. On the other hand, if this quantity is violated, then neutrino-less double beta decay, neutrino oscillation and even nnbar oscillation are then possible [20].

In this chapter, a brief review of the theory leading to nnbar oscillation process will be presented. Furthermore, the study of the signature of such a process in large water Čerenkov imaging detector will be presented.

2.1 Sakharov Conditions

The necessary conditions to explain the observed matter-antimatter asymmetry within the universe were proposed by Sakharov [3]. The three conditions are:

- Baryon number violating interactions
- C and CP violation
- Departure from thermal equilibrium

in which the thermal equilibrium condition is satisfied in a hot expanding universe and the B, C, CP violations can be included in various GUT models. The search for baryon violating processes is the focus of this chapter.

Two baryon violating scenarios are of interest, the case where $(B-L)$ is conserved and the case where it is violated by 2 units. For example, the case of a proton decaying into the channel $p \to e^+\pi^0$ would have a conserved quantum $(B-L)$ number of 1 such that $\Delta(B-L) = 0$. In the case of a nnbar oscillation ($n \to \bar{n}$), the quantum number is not conserved such that $\Delta(B-L) = 2$.

Leptogenesis and Baryogenesis[1]

The U(1) group is proposed to test the baryon and lepton conservation [20]. In the left-right symmetric models the electric charge and the $\mathrm{U}(1)_{B-L}$ symmetry is analogous to the Gell-Mann-Nishijima formula $Q = I_3 + \frac{1}{2}Y$,

$$Q = I_{3L} + I_{3R} + \frac{B-L}{2} \tag{2.1}$$

where $B-L$ is equivalent to the hypercharge, I_{3L} and I_{3R} are respectively the left-handed and right-handed isospin. By allowing parity violation ($\Delta I_{3R} = 1$) and imposing charge conservation $\Delta Q = 0$ then $\Delta(B-L) = 2$ for scale shorter than the electoweak scale

[1] A process that creates an imbalance in the lepton number is called *leptogenesis* while a process creating an imbalance in baryon number is called *baryogenesis*. Lepto-Baryogenesis is a proposed process that creates a lepton imbalance (but conserves B+L), which later translates into a baryon asymmetry at the electroweak scale.

($\Delta I_{3L} = 0$)[20]; this can imply either $\Delta L = 2$ which is required for a Majorana neutrino or $\Delta B = 2$ as in the nnbar oscillation.

2.2 Proton Decay

The proton is a stable particle, the question might be asked, why is it stable? Many theories predicted the proton decay rate to be within the reach of experimental measurements at the beginning of the 1980's with predicted lifetime of $T \sim 1 \times 10^{31}$ years with a mass of the U_{B-L} gauge boson of $M_X \sim 5 \times 10^{14}$ GeV [21]. No such decay has been found to date with current experimental limits reaching beyond the original predictions; newer results from Super-Kamiokande gives 6.6×10^{33} years at 90% CL [22].

The primary model that led to the early predictions of proton decay is the symmetry group SU(5). The mediator boson responsible for the decay would need to have a mass of $M_x = 10^{14\sim15}$ GeV which is the mass scale of GUT [23].

The SU(5) model is currently ruled out by experimental results. However, in [24] it is shown that all proton decay modes can be suppressed due to the seesaw mechanism. Also, newer SO(10) models have emerged that might still make proton decay possible [25], a detailed overview of these models is beyond the scope of this thesis.

2.3 Neutron-Antineutron Oscillation Theory

The $SU(2)_L$x$SU(2)_R$x$SU(4)_C$ model with light diquarks is a concurrent model of partial unification that would inhibit proton decay but would allow nnbar oscillation and other processes such as seesaw mechanism [20]. The various fields involved in the interactions of this group are:

- ψ: **(2,1,4)** and ψ^c: **(1,2,$\bar{4}$)** (Quark and lepton fields)
- ϕ_1: **(2,2,1)** and ϕ_{15}: **(2,2,15)** (Scalar fields)

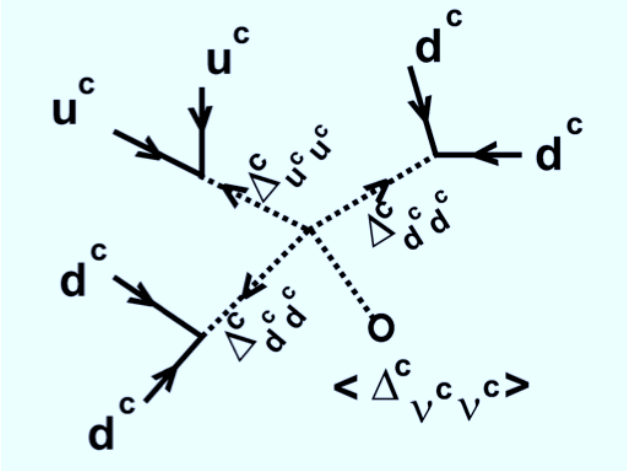

Figure 2.1: Possible Feynmann diagram of the nnbar process.

- Δ^c: **(1,3,10)** and $\bar{\Delta}^c$: **(1,3,**$\bar{10}$**)** (Fields that break $B-L$).

The interaction between these fields are given by the Yukawa potential,

$$L_Y = h_1 \bar{\Psi}_L \Phi_1 \Psi_R + h_{15} \bar{\Psi}_L \Phi_{15} \Psi_R + f \Psi_R^T C^{-1} \Delta_R \Psi_R + (R \leftrightarrow L) + H.C. \tag{2.2}$$

This form allows the Feynman diagram shown in Figure 2.1. Contrary to the mass scale of $10^{14\sim15}$ GeV needed for proton decay, the mass scale for the measurement of a nnbar transition is $10^{5\sim6}$ GeV [26].

Transition Probabilities

The time evolution of a system in which a neutron state can transform into an antineutron [20] follows,

$$i\hbar \frac{\partial}{\partial t} \begin{pmatrix} n \\ \bar{n} \end{pmatrix} = \begin{pmatrix} E_n & \delta m \\ \delta m & E_{\bar{n}} \end{pmatrix} \begin{pmatrix} n \\ \bar{n} \end{pmatrix}, \tag{2.3}$$

where δm is the nnbar mixing rate of the process that violates B which will be detailed in the next section. The energies for neutron and antineutron are arbitrary in order to account for the possibility of external fields.

The antineutron transition probability, that is obtained by solving the linear differential equation given by equation 2.3 with the boundary conditions that at time zero $P_n(0) = 1$

and $P_{\bar{n}}(0) = 0$, is given by the following equation[2],

$$P_{\bar{n}}(t) = \frac{4\delta m^2}{\Delta E^2 + 4\delta m^2} \sin^2 \left(\frac{\sqrt{\Delta E^2 + 4\delta m^2}}{2\hbar} t \right) \tag{2.4}$$

This oscillation can occur in two different settings: one when the neutron propagates while not being bound within a nucleus and the other when the neutron is bound in a nucleus. There is a suppression factor within the nucleus that affects the oscillation lifetime. In the case of $\frac{\sqrt{\Delta E^2+4\delta m^2}}{2\hbar} t << 1$, then,

$$P_{\bar{n}}(t) \approx \frac{4\delta m^2}{\Delta E^2 + 4\delta m^2} \left(\frac{\sqrt{\Delta E^2 + 4\delta m^2}}{2\hbar} t \right)^2 \approx \left(\frac{\delta m \cdot t}{\hbar} \right)^2 \equiv \left(\frac{t}{\tau_{n-\bar{n}}} \right)^2, \tag{2.5}$$

which defines the free oscillation rate of the nnbar transition, $1/\tau_{nnbar}$, in vacuum. In vacuum there is still an energy if a magnetic field acts along the propagation path of the neutron since an energy difference between the neutron and the antineutron would have the order of (ΔE_b)=μB with the magnetic moment $\mu = 6 \times 10^{-14}$ MeV/T ; the result is however very small $(\Delta E_b) \sim 10^{-18}$ MeV [27].

For the case of a neutron in a bound nucleus, the situation is more complex due to the neighboring nucleons. This topic will be covered in the next section. However interesting qualitative arguments can be made to understand the order of magnitude of the suppression.

First Argument

A simple qualitative solution is proposed by V. Kuzmin which involves the limit where a neutron in a nuclei environment can be considered free[3] [28][29]. In this limit you can consider that the neutron is free for

$$\Delta t \sim \frac{1}{\Delta E} \sim \frac{1}{10 \text{ MeV}} \sim 10^{-22} \text{ sec} \tag{2.6}$$

and that it can be free $1/\Delta t$ per seconds such that the transition probability is

$$P_{n\bar{n}cl} = \frac{1}{T_{nucl}} = \left(\frac{\Delta t}{\tau_{nnbar}} \right)^2 \cdot \left(\frac{1}{\Delta t} \right). \tag{2.7}$$

[2]This is different from [20] by a factor of 1/2 within the sine term, a detailed treatment is given in Appendix A. While equation (2.5) is equivalent to the one found in [20], equation (2.10) is different by a factor of 16 to the equation found in [20].

[3]The author would like to thank Yuri Kamyshkov for pointing out this elegant solution

The suppressed oscillation lifetime in the nuclei and the free oscillation lifetime are then related by,

$$T_{nucl} = \tau_{nnbar}^2 T_R \tag{2.8}$$

where T_R is called the suppression factor and is of the order of 10^{22} sec.

In the next section it explained that a complex potential to an energy solution of the form $E = \Delta + i\Gamma/2$; in this scenario the imaginary part represent the rate of decay of a $\bar{n}p$ state. Equation 2.6 should not be evaluated as a function of ΔE in this scenario but more as a function of Γ (since $\Gamma \gg \Delta$) which leads to $T_R \sim 10^{-23}$ sec for $\Gamma_R \sim 100$ MeV

Second Argument

The period, t, of one $n \to \bar{n}$ transition satisfies $\sqrt{\Delta E^2 + 4\delta m^2}\frac{t}{2\hbar} = 2\pi$. Solving with $\hbar = 6.58 \times 10^{-22}$ MeV·s leads to a period of 8.27×10^{-23} second for $\Delta E \approx 100$ MeV[4]. The observation time for any experiment is much greater than this such that,

$$P_{\bar{n}}(t) \approx \frac{4\delta m^2}{\Delta E^2 + 4\delta m^2}\left(\frac{1}{2}\right), \tag{2.9}$$

The mixing parameter $\delta m << \Delta E$ such that,

$$P_{\bar{n}}(t) \approx \frac{4\delta m^2}{\Delta E^2}\left(\frac{1}{2}\right) \approx \frac{1}{2}\left(\frac{2\delta m}{\Delta E}\right)^2, \tag{2.10}$$

which is the fraction of the time that a neutron spends as an anti-neutron in a nucleus. Note that equation 2.10 ignores the annihilation of the antineutron and takes into account only the energy difference between a neutron and antineutron in a nucleus. If the lifetime of a pure antineutron state in a nucleus is long compared to the nnbar oscillation period (8.27×10^{-23} s) then $P_{\bar{n}}$ given in equation 2.10 is the approximate suppression factor for the pure nnbar decay rate Γ_{nnbar} in the nucleus. That is,

$$\Gamma(observed) = P_{\bar{n}} \times \Gamma_{nnbar} \approx \frac{1}{2}\left(\frac{2\delta m}{\Delta E}\right)^2 \times \Gamma_{nnbar}. \tag{2.11}$$

The more general case in which the lifetime of the pure antineutron state is not necessarily long compared to the oscillation period in a nucleus is treated in the next section.

[4]This difference comes from the fact that the neutron and antineutron see a different potential within the nucleus [20]

2.4 Neutron-Antineutron Oscillation in bound Nuclei

The suppression factor due to the different modes within the nuclei plays an important part in the observation of this rare signal. An antineutron created within a nuclear medium will have the same orbital as the neutron that has oscillated. The suppression factor on the annihilation of the antineutron with the surrounding nuclei is studied in this section.

2.4.1 The Deuteron Case

The interaction between a nucleon and an antinucleon is described well in isospin interactions. In isospin interactions, there is no fundamental difference between an antiproton colliding with a neutron and an antineutron colliding with a proton. The evaluation of the nnbar oscillation in matter was first derived by Dover *et al* as a function of the stability of deuteron [30]; the major ideas from this paper are presented in this section. The wave function of the deuteron is given by,

$$\psi_D(r) = \frac{u_0(r)}{r} \left|{}^3S_1\right\rangle + \frac{w_0(r)}{r} \left|{}^3D_1\right\rangle . \tag{2.12}$$

where u_0 and w_0 are the spatial wave functions obtained from the Paris potential. The S orbital of the deuteron wave function has a higher cross section for an antineutron-proton annihilation than the D orbital. The nnbar oscillation can be considered by first approximation on only the S orbital wave function component, the perturbed time-independent Schrödinger equation is

$$\frac{1}{2\mu}u''(r) + \left[U_{\bar{n}p} + iW_{\bar{n}p} - E_D\right] u(r) = \delta m \; u_0(r), \tag{2.13}$$

where u is the spatial ${}^3S_1$ waveform for the $\bar{n}p$ state, u_o is the spatial ${}^3S_1$ waveform for the unperturbed np state, μ is the antineutron-proton reduced mass, the binding $E_D = 2.2267$ MeV, $\delta m = 1/\tau_{n\bar{n}}$ and $U_{\bar{n}p} + iW_{\bar{n}p}$ is the complex potential describing the $\bar{n}p$ interactions. The introduction of a complex potential, also known as the *optical model*, is helpful in treating elastic scattering absorption in nuclear interactions. The introduction of

this complex potential leads to complex eigenvalues such that the solution is of the form $e^{ik_r r}e^{-k_i r}/r$ [31]. The real exponential represents the spatial contribution to the non-elastic absorption: in the case of $k_i < 0$ this contribution will increase with r, while for $k_i > 0$ this will fall off exponentially.

Since the inclusion of a complex potential leads to solution with complex eigenvalues, the resulting matrix is non-hermitian; the solution found in the previous section does not include information on the surrounding potential. Solving the time-dependent Schroedinger equation for the pure $\bar{n}p$ state with complex energy eigenstate

$$i\frac{\partial}{\partial t}\psi_{\bar{n}p} = (\Delta - i\frac{\Gamma_R}{2})\psi_{\bar{n}p} \tag{2.14}$$

leads to $|\psi_{\bar{n}p}|^2 = e^{-\Gamma_R t}$ which represents the decay rate of the state. By including the free oscillation rate of the $n \leftrightarrow \bar{n}$ oscillation of $\delta m = 1/\tau_{nnbar}$ and by setting the ground state of the deuteron (the np state) to zero [32], a solution to the coupled quantum states is obtained by solving the equation of motion

$$i\frac{\partial}{\partial t}\begin{pmatrix} np \\ \bar{n}p \end{pmatrix} = \begin{pmatrix} 0 & \delta m \\ \delta m & \Delta - i\frac{\Gamma_R}{2} \end{pmatrix}\begin{pmatrix} np \\ \bar{n}p \end{pmatrix} \tag{2.15}$$

The eigenvalues are given by:

$$\begin{aligned} \lambda_1 &= \frac{1}{2}\left(\Delta - i\frac{\Gamma_R}{2} + \sqrt{\left(\Delta - i\frac{\Gamma_R}{2}\right)^2 + 4\delta m^2}\right), \\ \lambda_2 &= -\frac{\delta m^2}{\lambda_1}. \end{aligned} \tag{2.16}$$

The solution with $\psi_{np} = 1$ at time $t = 0$ is

$$\begin{pmatrix} np \\ \bar{n}p \end{pmatrix} = \frac{\delta m/\lambda_1}{1 + (\delta m^2/\lambda_1)^2}\begin{pmatrix} \frac{\delta m}{\lambda_1} \\ 1 \end{pmatrix} e^{-i\lambda_1 t} + \frac{1}{1 + (\delta m^2/\lambda_1)^2}\begin{pmatrix} 1 \\ -\frac{\delta m}{\lambda_1} \end{pmatrix} e^{i\frac{\delta m^2}{\lambda_1}t}. \tag{2.17}$$

An approximation may be made by requiring $\delta m^2/\lambda_1^2 \approx 0$ and by setting $\lambda_1 \approx \Delta - i\frac{\Gamma_R}{2}$. The equation becomes

$$\begin{pmatrix} np \\ \bar{n}p \end{pmatrix} \approx \begin{pmatrix} 0 \\ \frac{\delta m}{\Delta - i\Gamma_R/2} \end{pmatrix} e^{-i\lambda_1 t} + \begin{pmatrix} 1 \\ -\frac{\delta m}{\Delta - i\Gamma_R/2} \end{pmatrix} e^{i\frac{\delta m^2}{\Delta - i\Gamma_R/2}t}. \tag{2.18}$$

The disappearance rate of the np state is then

$$|\psi_{np}|^2 = \left| e^{i\frac{\delta m^2}{\Delta - i\Gamma_R/2}t} \right|^2 = \left| e^{i\delta m^2 \frac{(\Delta + i\Gamma_R/2)}{\Delta^2 + \Gamma_R^2/4}t} \right|^2 = \left| e^{i\delta m^2 \left(\frac{\Delta}{\Delta^2+\Gamma_R^2/4}\right)t} \times e^{-\delta m^2 \left(\frac{\Gamma_R/2}{\Delta^2+\Gamma_R^2/4}\right)t} \right|^2 . \tag{2.19}$$

In the limit where $\Gamma_R \gg \Delta$, then

$$|\psi_{np}|^2 \approx e^{-4\frac{\delta m^2}{\Gamma_R}t} \tag{2.20}$$

This represent the decay width of the coupled np state when the pure $\bar{n}p$ state has a decay width of Γ_R. The decay rate that is measured in the experiment is expressed as $\Gamma_{nucl} = \frac{4\delta m^2}{\Gamma_R} = \frac{4}{\tau_{nnbar}^2 \Gamma_R}$ such that $\tau_{nnbar} = 2\left(\frac{1}{\Gamma_R \Gamma_{nucl}}\right)^{1/2}$, which is equivalent to the result from Gal and Friedman [33]. The relaxation rate[5] T_R relates the nuclear lifetime to the free nnbar oscillation lifetime $T_R = T_{nucl}/\tau_{n-\bar{n}}^2$.

In Dover *et al* [30], the evaluation of the components of the optical potential can follow two models DR1 or DR2 which consists of G-parity meson-exchange terms and include fits for $\bar{p}p$ elastic reaction, charge exchange and reaction cross section [34].

Solving equation 2.13 using two different potential model leads to [30],

$$\begin{aligned} T_R &= 0.275 \text{ x } 10^{23} \text{ sec}^{-1} \text{ (model DR1)} \\ T_R &= 0.271 \text{ x } 10^{23} \text{ sec}^{-1} \text{ (model DR2)} \end{aligned} \tag{2.21}$$

By including the D orbital components the value of the suppression factor changes slightly,

$$\begin{aligned} T_R &= 0.256 \text{ x } 10^{23} \text{ sec}^{-1} \text{ (model DR1)} \\ T_R &= 0.240 \text{ x } 10^{23} \text{ sec}^{-1} \text{ (model DR2)} \end{aligned} \tag{2.22}$$

This suppresion factor T_R in deuteron is smaller by a factor of four than ^{16}O which is detailed in the next section.

[5]It is a somewhat confusing convention in the nnbar community to denote $T_R \equiv \alpha\Gamma_R$ (here α denotes the absorption of any additional terms) as a "lifetime" with sec^{-1} units since T usually represent a time and not a rate; whether it is called a rate or a "lifetime", the nuclear lifetime and free oscillation rate are related to one another in the nuclei by this single parameter T_R.

2.4.2 The Oxygen Case

In the case of ^{16}O, the P and D mode will have a significant impact on the relaxation rate T_R. The weight of each orbital component is given by the following relation:

$$\Gamma_a = (2\Gamma_{s_{1/2}} + 2\Gamma_{p_{1/2}} + 4\Gamma_{p_{3/2}})/8 \tag{2.23}$$

The Schroedinger equation is modified such that,

$$\frac{1}{2\mu}u''(r) + \left[\frac{U_{\bar{n}p} + iW_{\bar{n}p}}{1 + exp\left[(r-R)/a\right]} - E_i\right] u(r) = \delta m\ u_0(r), \tag{2.24}$$

where a Wood-Saxon potential has been added to take into account the multiple nuclei within the nuclear medium. The values of the suppression factor for ^{16}O are given by,

$$\begin{aligned} T_R &= 1.2 \text{ x } 10^{23} \text{ sec}^{-1} \text{ (model DR1)} \\ T_R &= 0.8 \text{ x } 10^{23} \text{ sec}^{-1} \text{ (model DR2).} \end{aligned} \tag{2.25}$$

In Friedman and Gal [33], the T_R factors were reevaluated for both ^{16}O and ^{56}Fe, but were not reevaluated for deuteron. The Friedman and Gal result for T_R were approximatively two times lower than the one found from Dover *et al*:

$$\begin{aligned} \frac{T_R^{dover}}{T_R^{gal}}(^{16}\text{O}^1) &= 1.9 \pm 0.4 \\ \frac{T_R^{dover}}{T_R^{gal}}(^{16}\text{O}^2) &= 1.8 \pm 0.4 \\ \frac{T_R^{dover}}{T_R^{gal}}(^{56}\text{Fe}) &= 2.1 \pm 0.4 \end{aligned} \tag{2.26}$$

where the T_R values for oxygen were evaluated with two different techniques[6]. The result in this thesis uses the values of T_R from the Dover *et al* studies which were also used in the evaluation of the Super-K limit [35].

[6]The values shown here are the average T_R value of the two models of Dover *et al*; the error show the difference between the two model found in Dover *et al*.

2.5 Antineutron Physics

A thorough treatment of the antineutron physics is given by Bressani and Filippi in a *Physics Reports* publication [36]. The discovery of the antineutron was first made in a charge exchange of antiprotons beams ($\bar{p} \rightarrow \bar{n}$). In this section the results from previous nnbar oscillation search are presented.

2.5.1 Neutron Antineutron Experiments

A few experiments have tested the oscillation lifetime in both cases: where the neutron was unbounded and when it was bounded in either oxygen or iron.

Antineutron bounded in nuclei

The most recent result came from a search for nnbar oscillation in ^{16}O from the Super-Kamiokande experiment [35]. No nnbar signal was seen at $\tau_{nnbar} > 2.36 \times 10^8$ sec evaluated at 90% CL. The evaluation of this limit included both the systematic error on the flux of background events and the systematic uncertainties on the nnbar detection efficiency. The search was on 22.5 kilotonne of fiducial volume and 1489.2 days of detector livetime.

Prior to this result, the best limit was found at the Sudan II experiment [37]. The limit was evaluated in ^{56}Fe at 1.3×10^8 sec at 90% C.L. by observing 5 candidate events against an expectation of 4.5 ± 1.2 backgrounds.

Free antineutron search

The ILL experiment evaluated the possibility of cold neutrons transforming into antineutrons in flight, the free limit was evaluated at 0.86×10^8 sec at 90% C.L. with a beam of neutron with $v \sim 600$ m/s at a beam intensity of 10^{11} n/s [27]. No candidates were found.

Final State	$\pi^- X^o$	M_x (MeV/c^2)	Γ_x (MeV/c^2)	BR (%)
$2\pi^-\pi^+$	$\pi^-\rho^o(\rightarrow \pi^+\pi^-)$	806 ± 6	140 ± 12	20 ± 1
	$\pi^- f^o(\rightarrow \pi^+\pi^-)$	1258 ± 3	262 ± 8	75 ± 2
	$\pi^- f_2'(\rightarrow \pi^+\pi^-)$	1522 ± 7	59 ± 12	5 ± 1
$2\pi^-\pi^+\pi^o$	$\pi^-\omega(\rightarrow \pi^+\pi^-\pi^o)$	784 ± 3	43 ± 9	5 ± 0.3
	$\pi^- X^o(\rightarrow \pi^+\pi^-\pi^o)$	1468 ± 6	88 ± 18	25 ± 2
	$\pi^- X'^o(\rightarrow \pi^+\pi^-\pi^o)$	1594 ± 9	81 ± 12	9 ± 1
	$\pi^- A_2^o(\rightarrow \pi^\pm\rho^\pm)$	1342 ± 4	81 ± 10	18 ± 1
	$\pi^o A_2^-(\rightarrow \pi^-\rho^o)$			9 ± 1
	$\rho^-\rho^o$			34 ± 3
$3\pi^-2\pi^+$	$\pi^- X^0(\rightarrow 2\pi^-2\pi^+)$	1477 ± 5	116 ± 9	82 ± 5

Table 2.1: Decay channels of proton antineutron annihilation at rest. Table taken from [39] in which it was found that most (>> 50%) of the $\bar{p}n$ annihilation occur via a two-body intermediate state. The branching ratios for the the $2\pi^+\pi^-$, $2\pi^+\pi^-\pi^0$ and $3\pi^+2\pi^-$ are respectively $(3.4 \pm 0.2)\%$, $(17 \pm 2)\%$ and $(4.2 \pm 0.2)\%$.

2.6 Neutron Anti-neutron signal in SNO

We assume that the nnbar annihilation occur at rest. This is not entirely true however due to the Hulthen momentum distribution; this was noticed in $\bar{p}d$ annihilation by tagging the outgoing proton or neutron [38]. The S-orbital of the deuteron will contribute more to the decay than the D-orbital; this effect is incorporated into the evaluation of T_R.

Various bubble experiments have looked at the different channels of antiproton on nucleon. A paper by D. Bridges *et al* investigated the annihilation channels of antiproton on neutron at rest [39]. The conclusion of the study was that most of the channels (>>50%) involved two body decays that would later on decay into more pions.

Shown in Table 2.1 is the decay scheme for the study of antineutron annihilation with a proton. This table was modified from that found in [39] which consists of the antiproton annihilation with a neutron target; this modification is allowed since in isospin representation there is no distinction between $\bar{n}p$ and $\bar{p}n$ interaction.

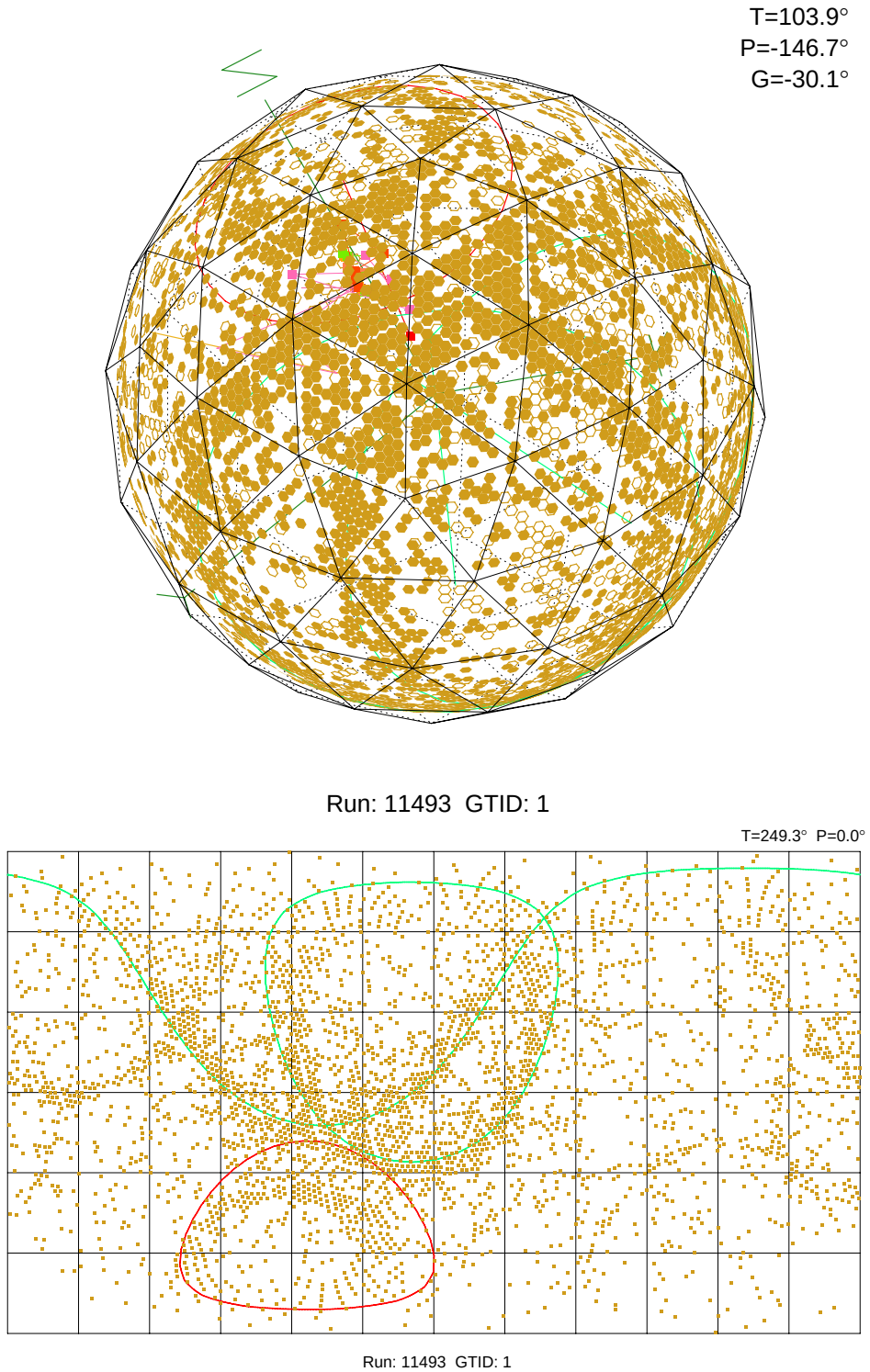

Figure 2.2: Monte Carlo simulation of a nnbar event simulated within the SNO run conditions. Results of the Multiple Ring fitter are included in the figure. The red ring shows the ring with the poorest reconstruction.

While the decay channels of Table 2.1 do not represent the total $\bar{n}p$ channels, they will serve as a basis for the behavior of nnbar within the SNO detector which will be the subject of the next chapter. The results from [39] indicate a majority (>> 50%) of the annihilation channels follow the short lived two-body state[7].

As it will be shown in the next chapter, the charged pion components of the nnbar signal inhibit a precise measurement of any decay channel because of frequent inelastic nuclear interactions, which in certain cases create more pions. The decay channels presented in Table 2.1 show a good sample of the possible decay channels expected from an annihilation of an antineutron on a proton within the deuteron. In Figure 2.2 the visual display of the simulation of a nnbar event is presented; multiple rings can be seen in the detector along with the fit results of the MRF routines which are described in Chapter 5.

2.7 SNO's Neutron-Antineutron Sensitivity

The sensitivity to the nnbar oscillation process has been evaluated in the context of the SNO experiment's D_2O phase [40][41]. This work has been extended to the three phases of the experiments in 2007 [42]. In this section the description of these sensitivities is given. At that time, the actual detection efficiency and background estimate were not fully understood. In Chapter 8, the final sensitivity of the SNO experiment after the real detection efficiency, the expected rate of background and the inclusion of systematic errors will be given.

The deuteron has a bigger contribution on the lifetime measurement than oxygen due to the suppression model described in the previous section. The calculations are made with the weighted average of the T_R for the two models in both the deuteron (T_R = 0.248 x 10^{23} sec^{-1}) and oxygen cases (T_R = 1.00 x 10^{23} sec^{-1}). The possible reach of SNO is made by assuming a detection efficiency of the nnbar signal of 100%.

[7]Four-body decay kinematics have not been implemented in SNOMAN. The implementation of further decays would require the implementation of other simulation software such as Genbot in CERNLIB [13] and the seeding of each particle kinematic information to the SNOMAN routines.

Search within only the Deuteron Case

The lifetime of an antineutron-proton annihilation from a nnbar oscillation within deuteron in the D_2O phase if no candidates (2.3 events at 90 % CL.) are found is given by:

$$\begin{aligned} T_{n\bar{n}} &> \frac{6 \text{ x } 10^{31} \text{ neutrons}}{2.3 \text{ candidates}} \frac{337.25 \text{ days}}{365.25 \text{ days/year}} \\ T_{n\bar{n}} &> 2.4 \text{ x } 10^{31} \text{ years} \end{aligned} \tag{2.27}$$

The conversion to the nnbar free oscillation lifetime is given by,

$$\begin{aligned} \tau_{n\bar{n}} &> \left(\frac{2.4 \text{ x } 10^{31} \text{ years } \cdot 3.16 \text{ x } 10^{7} \text{ sec/years}}{0.248 \text{ x } 10^{23} \text{ sec}^{-1}} \right)^{1/2} \\ \tau_{n\bar{n}} &> 1.75 \text{ x } 10^{8} \text{ seconds} \end{aligned} \tag{2.28}$$

at 90% CL. By adding the lifetime of the SALT and NCD phase and assuming that still no candidates are found (2.3 events at 90 % CL.) then $\tau_{n\bar{n}} > 3.34$ x 10^8 seconds. If only the SALT phase is added, the sensitivity of the nnbar oscillation lifetime is $\tau_{n\bar{n}} > 2.76$ x 10^8 seconds.

Search within both the Deuteron and the Oxygen Case

As described in [40], the effect of oxygen on the reach of the nnbar oscillation signal can be accounted for within the T_R parameter. The combination of all the weights leads to an effective $T_R = \frac{(2\times 0.248 + 8 \times 1.00)}{10}$ x 10^{23} sec^{-1} = 0.85 x 10^{23} sec^{-1}. On the other hand, there is an increase of available neutrons such that $(2+8) \times 3 \times 10^{31}$ possible neutrons are available for oscillation.

The impact on the reach is then

$$\frac{\tau_{n\bar{n}}(D+O)}{\tau_{n\bar{n}}(D)} = \left(\frac{0.248 \times 10^{23} \text{ sec}^{-1}}{0.85 \times 10^{23} \text{ sec}^{-1}} \cdot \frac{(2+8)}{2} \right)^{1/2} = 1.21 \tag{2.29}$$

which is a 21% improvement.

Discussion

There is one major issue with the inclusion of nnbar in oxygen that is not present for deuteron: the proximity of the surrounding nucleons that scatter and absorb the outgoing

pions, which create even more uncertainty in the pion multiplicity and propagation. A careful treatment of the kinematics of the surrounding nuclei is needed which increases the systematic error.

The deuteron offers a simpler decay channels due to Isospin arguments and no neighboring nuclei. This make the simulation of the decay simpler since no consideration of the position of the annihilation within the nuclei is required. Furthermore, the nuclear propagation uncertainty due to the surrounding nuclear media does not not affect the deuteron.

However, the propagation of charged pions within the D_2O medium is prone to inelastic nuclear interactions as will be seen in the next chapter. In these interactions, a single pion propagating in the media is very likely to create more pions; on the other hand it is also likely to be absorbed[8].

This makes any measurement of a single decay channel unrealistic since we are only able to measure the propagation of a charged pion via the light signature of the observed events: it is not possible to distinguish a pion that has hard scattered through a nuclear interaction and two pions generated in the same area.

2.8 Summary

In this chapter the theory behind the nnbar oscillation in both the bounded within a nuclear medium case and unbounded case have been briefly explored. The previous experimental limits for both the free oscillation and bounded oscillation lifetimes have been described. The signal signature of nnbar oscillation in SNO was also described. The early estimate of the expected sensitivity of this oscillation lifetime was also studied in the context where no candidate events are seen.

In the next chapter, the properties of the propagation of pions - which are the principle particles in the antineutron-proton annihilation signal - in D_2O will be studied.

[8]This will be the subject of the next chapter, see Table 3.1 for nuclear interaction probabilities.

Chapter 3

Pion Propagation in SNO

Reality is complicated. There is no justification for all of the hasty conclusions.

Hideki Yukawa

Pions are the main products from antineutron-nucleon annihilation. It is therefore important to understand the properties of pions and in particular their behavior in the medium of the detector. Due to the strong interaction, the pions interact in a different way than leptons when in the presence of other nuclei; this difference will have an impact on the nnbar analysis which will be explained in this chapter. In order to verify the implementation of the pion physics within the SNO simulation software, a study of the hadron Calor simulation software (which is used in SNOMAN) benchmarked against Geant4 simulation will also be presented.

3.1 Particle Propagation in a Medium

Charged particle propagating in that medium at a speed greater than the speed of light of the medium - c/n where n is the index of refraction of the medium - will emit light known as Čerenkov light; this is due to the polarization of the bound electrons along the path of the charge particle as it propagates in the medium. This principle is the basis on which

Čerenkov imaging detector such as SNO are built. The energy of each Čerenkov photon is in the order of a few eV's and as such this process is not the dominating energy loss process for particles of several hundreds of MeV of energy. The loss of energy from charged leptons is governed by other processes which will be detailed in this section.

Neutral massive particles can only be detected in Čerenkov imaging detectors if the particle is captured in a nucleus or decays into a Čerenkov light emitting particle.

Gammas, which are high energy photons, have the ability to produce electron-positron pairs. These charged leptons in turn produce Cherenkov photons that can be detected in a transparent medium such as heavy water.

Positrons and electrons can also create gammas through Bremsstrahlung; these gammas can then in turn create more electron-positron pair through pair production. This cascade process is known as the electron-photon shower effect [43]. This makes the gamma and electron signatures indistinguishable from one other.

Energy loss processes fall into two main categories: continuous and non-continuous. All processes described below have an energy dependence: at various energies the strength of the process may differ from each other.

Charged Lepton Interactions

For charged leptons, the continuous energy loss process include the following interactions [43],

- **Ionization Loss :** Energy loss from electrons knocked off from atoms as the particle is propagating in a medium.

- **Multiple Scattering :** Energy loss by multiple Coulomb scattering with surrounding nuclei. The cross section for the process follows the Rutherford formula which has a $1/\sin^4(\theta/2)$ dependence on the scattering, leading to small deviations from the original path.

- **Čerenkov Radiation :** Čerenkov radiation is emitted when a charged particle travels

in a medium with a speed greater than the speed of light of the medium, i.e. $v > c_{medium} \equiv c/n$.

For charged leptons, the non-continuous processes in which they lose a significant amount of energy are:

- **Bremsstrahlung :** The emission of an energetic gamma when the charged lepton is accelerated by the Coulomb field of a nearby nucleus. This effect becomes more important at higher energies.

- **Moller Scattering :** A form of ionization, the knock-off of bound electrons, due to muon-electron or electron-electron interactions.

- **Absorption :** In the case of β electrons and γ-ray particles passing through a material, they may be absorbed by surrounding nuclei, leading to their disappearance; this absorption leads to a lower intensity $I(x) = I_0 \exp(-\mu x)$ where μ is the absorption coefficient of the material.

- **Deep Inelastic Scattering :** Hard scatter of the particles by the quark constituents in the nuclei; a minimal energy is required by the particle in order for this process to occur. In SNO, the cross section for this process is modeled by $\sigma_\mu(E_\mu) = 0.3\mu\text{b}(E_\mu/30\text{ GeV})^{\frac{1}{4}}$ [44].

In the case of the muon or the tau particles,

- **Lepton decay :** The muon or tau leptons can also decay. For the muon case, the most probable decay channel is given by $\mu^- \to e^- \bar{\nu}_e \nu_\mu$.

For charged particles, the *critical* energy is defined as the energy where the amount of energy loss by radiation is equal to the amount of energy loss by ionization and collisions. Above this critical energy, the loss of energy is dominated by Bremsstrahlung radiation, while below this critical energy, collisions are the dominating energy loss process.

This critical energy in H_2O is 92 MeV for electrons-positrons and 1.03 TeV for muons [45][46]. The typical energy for cosmic muons once they have reached the SNO detector will be less than 1.03 TeV. As such, there are two type of signature for Čerenkov events, showering and non-showering.

Photon Interactions

In the case of photons, energy loss is made through the following processes [43]:

- **Photoelectric Effect :** Absorption of a photon by electron bound in an atom, which results in the expulsion of the electron from the atom.
- **Compton Scattering :** Scattering of the photon off of free electrons; at energies higher than the binding energy of the electrons, bound electron are considered free.
- **Pair Production :** Transformation of a photon to a electron-positron pair; the presence of a nucleon is required to conserve momentum.
- **Photonuclear interactions :** Virtual photons from high energy muons passing through matter create neutrons; neutrons created by this process are known as muon spalation neutrons.

The Compton effect and pair production are the major processes for the energy scale of interest [47].

3.2 Showering and Non-Showering Signatures

As stated previously, only particles that emit Čerenkov light may be detected by the PMT's in SNO. Two different signatures are identified: the e-like and μ-like signature.

The difference between the two signatures is due to the different critical energy of the particles: in the case of the electrons, the critical energy is much lower than the typical energies for nnbar events, which leads to the showering signature.

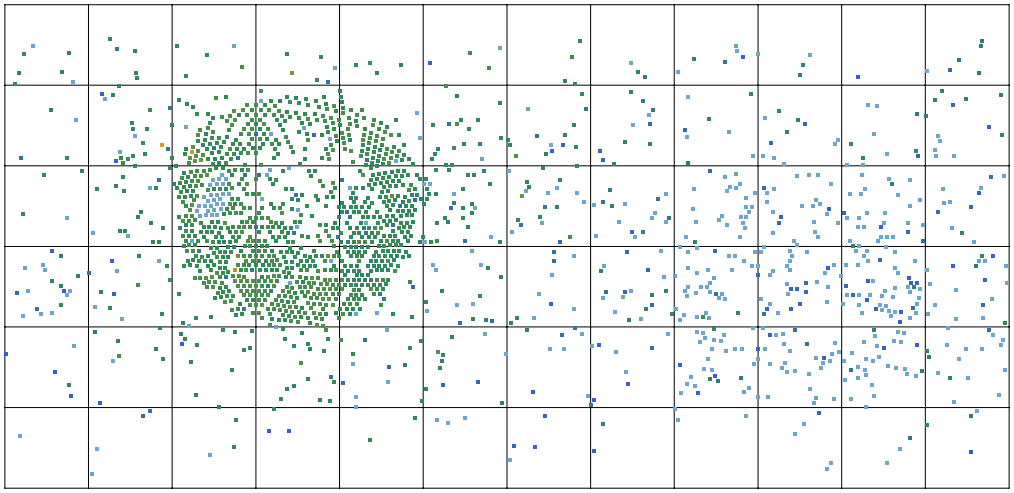

Run: 1 GTID: 5

(a)

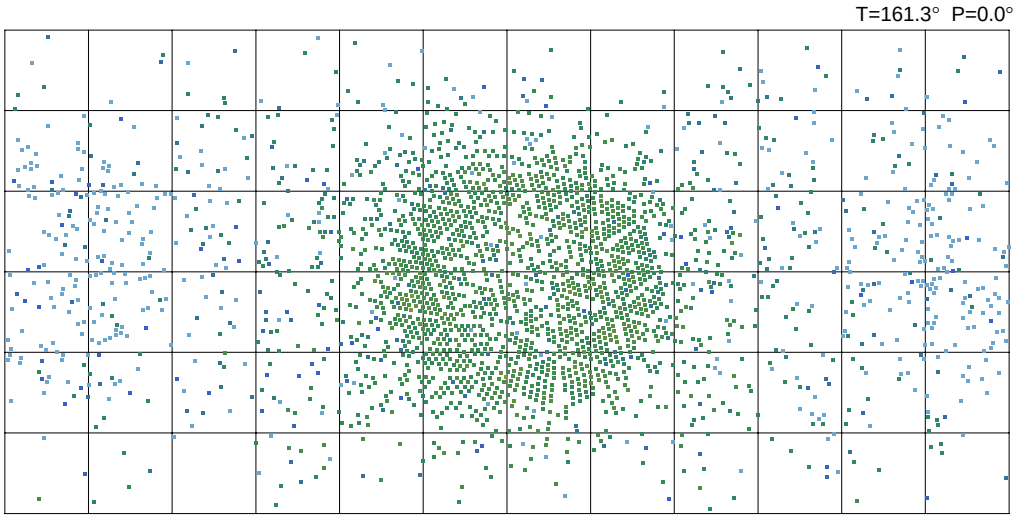

Run: 1 GTID: 4

(b)

Figure 3.1: Monte Carlo Simulation of a muon (a) and electron (b) event of 600 MeV kinetic energy created at the origin of the detector. The different colors represent the charge seen in the PMTs.

In the case of the muons, the critical energy is much higher than the typical energies of nnbar events, which leads to a non-showering signature.

Shown in Figure 3.1 are two simulated events with kinetic energy of 600 MeV. Their difference is the outer border of the rings: in the case of the muon there is a clearer edge compared to the electron events that have a fuzzier edge[1].

This distinction is important for particle identification (PID). It will be shown in Section 5.5.4 that the Multiple Ring Fitter is more efficient in finding μ-like rings using an e-like expectation[2] than using a μ-like expectation. The tradeoff is the lost of PID and an accurate invariant mass measurement. Other tools will be defined in Chapter 6 in order to evaluate the isotropy of multiple ring events.

The presence of the acrylic vessel adds another dimension to particle identification compared to other water Čerenkov experiments due to reflected light. This additional scattered light tends to blur the μ-like signature; this is particulary noticeable when more than one μ-like particles are present in the D_2O volume[3].

3.3 Pion Properties

The pion was first predicted as a mediator in the strong interaction between the protons and neutrons in a nuclei. This particle was later confirmed in cosmic ray showers. Contrary to other interaction mediators that have a spin 1, the pion has spin 0. It is a pseudo-scalar particle: there are three possible isospin configurations leading to two charged states (π^+ and π^-) and one neutral state (π^o).

[1] There is isotropic scattered light in both events due to the reflection of Čerenkov light by the acrylic vessel.

[2] The μ-like and e-like expectations are shown in Figure 5.5; the expectation is the angular distribution of hit PMTs with respect to the vertex of the particle.

[3] And this may explain the detection performance of the μ-like reconstruction observed in Section 5.5.4

3.3.1 Neutral Pions

The propagation of neutral pions in the SNO detector is fairly simple due to its short lifetime and the properties of their daughters. The most probable decay channels consist only of electrons and gammas which have the same propagation properties in the detector medium.

$$\begin{aligned} \pi^o &\rightarrow \gamma\gamma \qquad (98.798 \pm 0.032)\% \\ \pi^o &\rightarrow e^+e^-\gamma \ (\ 1.198 \pm 0.032)\% \end{aligned} \tag{3.1}$$

The light signature of a neutral pion is therefore that of an electron signature. Since the mass difference between a neutral pion and a electron (or gamma) is large, the gammas from the neutral pion decay will generate more light than a charged pion of the same energy.

3.3.2 Charged Pions

The theory that the pion is the mediator of the strong interaction is not quite correct since gluons are the actual mediator. However, due to the quark constituent of the pions, nuclear interactions are much stronger than for muons or electrons. In a medium, pions propagate differently whether they are inside or outside the nuclei.

Outside Nuclei

The propagation outside of the nuclei follows the same law as a lepton such that its energy loss follows the Bethe-Bloch equation, which will be described in the next section.

Inside Nuclei

The propagation within the nuclei is a bit more complex as it involves showering of particle with the nuclei. This showering is due to the de Broglie wavelength being shorter than the intra-nucleon distance. The process starts with a rapid cascade followed by a slow evaporation of particles (n, p, γ) [48]. Nuclear inelastic scattering process such as the charge exchange particular to charged pions will occur in the nuclear environment.

3.4 Stopping Power of Pions

The range of a particle is defined as the distance that it can propagate in a medium before losing all of its energy. This range is a function of the stopping power of a particle which defines the amount of energy loss as a function of length. The amount of energy loss is given by the Bethe-Bloch equation,

$$-\frac{dE}{dx} = Kz^2\frac{Z}{A}\frac{1}{\beta^2}\left[\frac{1}{2}\ln\frac{2m_ec^2\beta^2\gamma^2T_{max}}{I^2} - \beta^2 - \frac{\delta(\beta\gamma)}{2}\right] \tag{3.2}$$

where T_{max} is the maximum kinetic energy which can be imparted to a free electron in a collision, $K \equiv 4\pi N_A r_e^2 m_e c^2$, Z and A are respectively the atomic number and mass of the target, z is the charge of the incoming particle, I is the mean excitation energy, $\delta(\beta\gamma)$ is the density effect correction due to ionization loss [47].

In the case of the pion, this is not the complete story. Due to the quark constituents of the pion, energy loss is also affected by the nuclear interactions which often absorb or scatter the pion before it has lost all of it's energy through ionization. Because of these nuclear interactions, the pion will rarely propagate in a straight path as it loses its energy.

The range defined in this section is defined as the length a pion would travel if it had not encountered any nuclear interactions. The range for a muon of 400 MeV of energy was evaluated with SNOMAN at 198.25 cm in D_2O[4] [46]. In this study, continuous-slowing-down-approximation (CDSA) was used to evaluate the range of the muon. It was also argued in the study that the density difference between D_2O and H_2O of 10% cancels out the atomic number A difference which is also 10%. This allows range estimated in H_2O media useful for SNO estimations.

[4]The range distribution evaluated in [46] is not Gaussian, a tail exists at higher range; the value presented here is the most probable range of the particle evaluated with SNOMAN.

3.4.1 Mean Free Path of Pion Nuclear Interactions

The minimal mean free path of a particle can be simply calculate in the following way,

$$\frac{1}{\lambda_{min}} = \left(\frac{N_A \rho}{M}\right) \sigma_{max} \tag{3.3}$$

with

$$\begin{aligned}
\mathrm{M}_{D_2O} &= 20.04 \quad \mathrm{g/mol} \\
\rho_{D_2O} &= 1.11 \quad \mathrm{g/cm^3} \\
\mathrm{N}_A &= 6.02\mathrm{x}10^{23}\ \mathrm{mol}^{-1} \\
\sigma_{max} &= 0.20\mathrm{x}10^{-24}\mathrm{cm}^2 \quad \text{(Deuteron)} \\
\sigma_{max} &= 0.80\mathrm{x}10^{-24}\mathrm{cm}^2 \quad \text{(Oxygen)}
\end{aligned}$$

the minimal value for the range is then 75 cm for ^{16}O and 37.5 cm for D. The maximal inverse mean free path in D_2O is then simply,

$$\frac{1}{\lambda_{D_2O}} = \frac{1}{\lambda_D} + \frac{1}{\lambda_O} < 0.04\ \mathrm{cm}^{-1} \tag{3.4}$$

leading to a minimal mean free path of > 25 cm for a pion in the D_2O medium at the delta resonance. Since pions of 600 MeV energy have a range of $\sim$300 cm, this would lead to frequent inelastic nuclear interactions. The situation is more complex since the inelastic cross section is energy dependent; this dependency is incorporated in the SNOMAN routines.

3.5 Scattering Effects and SNOMAN Code Modifications

In this section, the effect due to the scattering of pions on deuteron and oxygen in their direction of travel is studied. Some issues with the handling of multi-prong events were noticed in the CALOR routines that have been integrated within SNOMAN. A comparison of the reconstruction of events generated by CALOR and Geant4 was made to understand these issues.

Two issues were found in the implementation of the hadron CALOR code[5]. The first issue is a normalization from momentum vector to direction cosine being omitted and the second is due to mixing energy units within the quantity that conserves the momentum of the incoming particle.

3.5.1 First Correction: Momentum Normalization

The energy and the mass of the projectile are passed to a function that handles the different processes that can happen in the collision (inelastic or elastic scattering, absorption, pion creation,...). The direction of the incoming particle is assumed to be in the positive z direction to facilitate calculations. Once the interaction process is chosen and processed the resulting outgoing particles are sent to a function CB2LAB.

The function takes as input the direction of the projectile and rotates the direction of the resulting particles to be in the correct lab orientation. This function is the only function that takes the original input direction of the incoming particle. This rotation is made with the unitary rotation matrix:

$$\begin{pmatrix} u_{LAB} \\ v_{LAB} \\ w_{LAB} \end{pmatrix} = \begin{pmatrix} \cos\phi & -\sin\phi & 0 \\ \sin\phi & \cos\phi & 0 \\ 0 & 0 & 1 \end{pmatrix} \begin{pmatrix} \cos\theta & 0 & \sin\theta \\ 0 & 1 & 0 \\ -\sin\theta & 0 & \cos\theta \end{pmatrix} \begin{pmatrix} \alpha \\ \beta \\ \gamma \end{pmatrix} \tag{3.5}$$

such that,

$$\begin{aligned} u_{LAB} &= \cos\phi * T_1 - \sin\phi * \beta \\ v_{LAB} &= \sin\phi * T_1 + \cos\phi * \beta \\ w_{LAB} &= \cos\theta * \gamma - \sin\theta * \alpha \\ T_1 &= \cos\theta * \alpha + \sin\theta * \gamma \end{aligned} \tag{3.6}$$

[5]This was first noticed in the non-conservation of momentum and energy of the nuclear interactions within the CALOR routines.

with,

$$\begin{aligned} \sin\theta &= R_T = \sqrt{u^2+v^2}. \\ \cos\theta &= w \\ \cos\phi &= u/R_T \\ \sin\phi &= v/R_T \end{aligned} \tag{3.7}$$

Here (u, v, w) is the direction cosine of the incoming projectile and (α, β, γ) are the direction cosines of the outgoing particles that have been calculated with the energy and mass of the incoming projectile; $(u_{LAB}, v_{LAB}, w_{LAB})$ is the direction cosine that takes into account the original direction of the particle.

The issue with the code is that the direction cosines of the incoming projectile are not normalized. In the main routine of hadron CALOR the direction cosine of the projectile is defined as $(u,\ v,\ w) = (p_x,\ p_y,\ p_z)$ where $\vec{p}$ is the momentum of the incoming particle. Most calculations are made with the energy and the mass[6] of the particle and as such, this error should not have an impact elsewhere. This error skews the final rotation:

$$\begin{aligned} \sin\theta &= R_T >> 1(\text{MeV/c}) \\ \cos\theta &= w >> 1(\text{MeV/c}) \\ \cos\phi &= u/R_T < 1(\text{Unitless}) \\ \sin\phi &= v/R_T < 1\ (\text{Unitless}) \end{aligned} \tag{3.8}$$

and with

$$T_1 = \cos\theta * \alpha + \sin\theta * \gamma >> 1(\text{MeV/c}) \tag{3.9}$$

the u_{LAB} and v_{LAB} components, in most case, have the following issue:

$$\begin{aligned} (\cos\phi * T_1)(\text{MeV}) &> (\sin\phi * \beta)(\text{Unitless}) \\ (\sin\phi * T_1)(\text{MeV}) &> (\cos\phi * \beta)(\text{Unitless}) \end{aligned} \tag{3.10}$$

[6] When mass and energy are available, initial momentum is a redundant quantity

having the effect of suppressing the β contribution. The direction cosine in the laboratory from equation 3.6 is finally multiplied by momentum giving it an amplitude and unit of the square of the momentum. Since this outgoing momentum is renormalized to a direction cosine after the hadron CALOR routine has been called, this error only affects the direction of outgoing particles.

This input error affects only the direction and not energy or mass.

3.5.2 Second Correction: Energy Conservation In Nucleus Recoil

A second error has been found in the Hadron-Calor routines. This error can be found in the subroutine call RECOIL. This routine calculates the amount of recoil energy from a projectile collision by enforcing momentum conservation. The initial total momentum as a function of kinetic energy and mass for a projectile moving in the positive z direction is given by:

$$\begin{aligned} p_{xi} &= 0 \\ p_{yi} &= 0 \\ p_{zi} &= E_k\sqrt{1+2m_\pi/E_k} \equiv p_\pi, \end{aligned} \tag{3.11}$$

where the p_z expression is derived with $E_{tot} = E_p + E_k$ and $E_p = m_\pi$. Enforcing momentum conservation, the momentum of a recoiling nucleus is then,

$$\begin{aligned} p_{xN} &= -\sum_{j=1}^{n} p_{xj} \\ p_{yN} &= -\sum_{j=1}^{n} p_{yj} \\ p_{zN} &= p_\pi - \sum_{j=1}^{n} p_{zj} \end{aligned} \tag{3.12}$$

where p_j is the momentum of outgoing particles other than the nucleus.

The error is a problem with unit conversion: the mass of the incoming and outgoing particle in this routine are in units of GeV while the kinetic energy and rest mass of the

nucleus are in units of MeV. For the pion energy involve in the collision (E_k >100 MeV), this has the following consequence,

$$p_\pi = E_k\sqrt{1 + 2m_\pi/E_k} = E_k\sqrt{1 + 2(0.137)/E_k} \simeq E_k. \tag{3.13}$$

which underestimates the momentum of the incoming particle[7]. The Geant4 code [12] was used to simulate 600 MeV pions in a water volume with the module BERT (Bertini cascade) enabled. This energy is typical of pions emerging from a nucleon-antineutron annihilation. The pion inelastic flag was used to better understand the pion scattering distribution and to verify any discrepancy with the CALOR code that has been inputed into SNOMAN.

This correction and the one found in the previous sub-section may have an effect on the number of rings seen in the detector. Since the correction of these effects are consistent with the Geant4 results as will be seen in the next section, the code is simply corrected and no error has been evaluated.

3.6 Inelastic Interaction with Geant4 and Hadron-calor

In inelastic interactions within Geant4, the incoming particle track is killed and new tracks are created. For example, a neutron colliding with a nucleus in an inelastic collision will have a different track *id* before and after the collision. The same is true in the track *id* for Hadron-Calor and SNOMAN.

Since there are more than one outgoing particle in an inelastic collision, one has to choose which of the outgoing particles to take in calculating the scattering distribution[8]. In the case of multiple particles of the same type as the incoming particle, it is common to choose the outgoing particle with the highest energy in order to calculate the scattering distribution.

[7] This does not seem to be an issue with the implementation with the SNOMAN routines and is more likely to be an issue with the Hadron-Calor routines.

[8] All particles are propagated in the full simulation, a single outgoing particle is chosen here to compare the behavior of each type of interaction after a scatter.

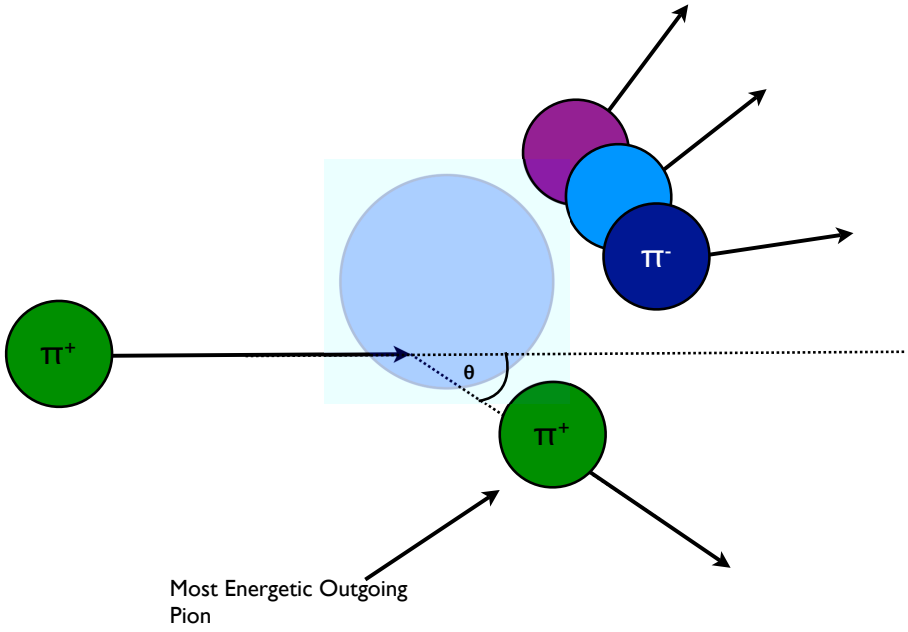

Figure 3.2: Single pion creation via inelastic scattering leading to the creation of secondary particles. All outgoing particles - including the scattered pion - are assigned new track IDs.

In certain cases, the outgoing particle with the highest energy may not be the same as the incoming particle, such as a particle that has been knocked back by hard scattering. Since in the SNO detector only particles that emit Cherenkov light can be detected, some particles that are not absorbed will become invisible to the detector: a hard scattered neutron or proton will go unnoticed, apart from a subsequent capture. This chapter will concentrate on the outgoing pion from inelastic interaction.

There are three scenarios after a nuclear inelastic interaction:

- no outgoing pion (absorption)
- single outgoing pion (scattering)
- multiple outgoing pions (delta resonance)

The case of a single outgoing pion can be divided further into three subcategories:

- no charge exchange (NCX): inelastic scattering of the pion
- single charge exchange (SCX): inelastic scattering with a different pion isospin state $(\pi^+ \rightarrow \pi^0)$ or $(\pi^- \rightarrow \pi^0\ )$

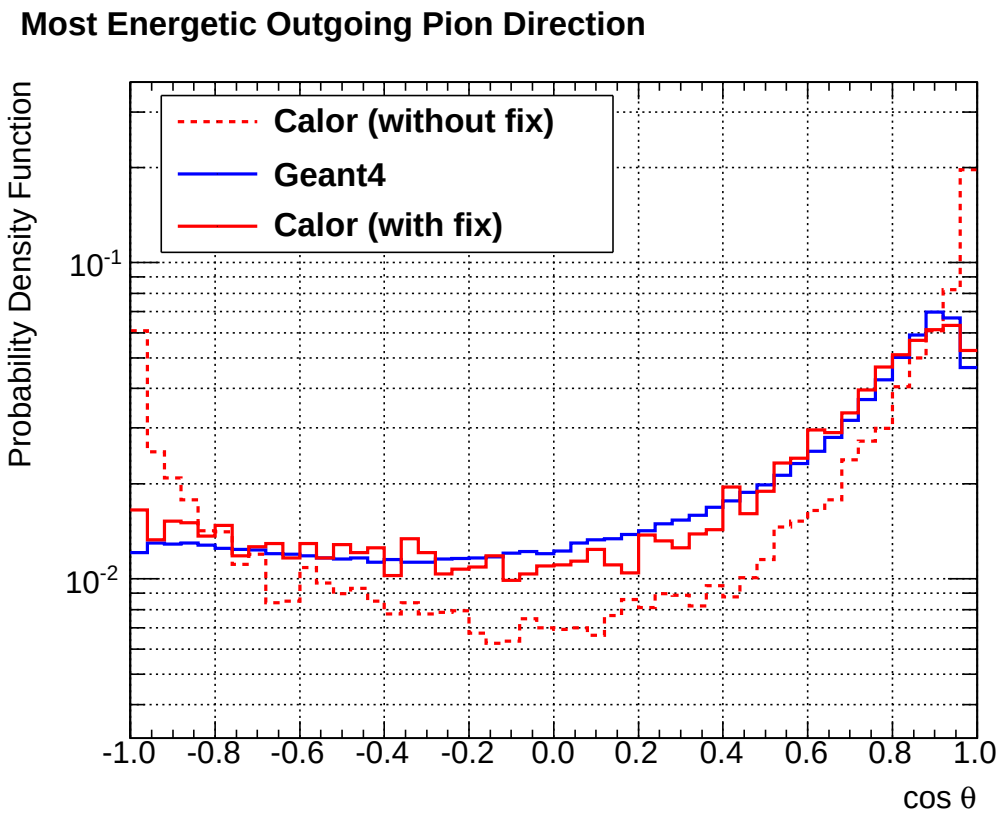

Figure 3.3: Comparing the corrected hadron-CALOR and Geant4-generated angular distribution of outgoing pions. Theta is the angle made between the incoming pion and the outgoing pion that has the highest kinetic energy. The two correction presented in Sections 3.5.1 and 3.5.2 are implemented.

- double charge exchange (DCX): inelastic scattering with a different pion isospin state ($\pi^{\pm} \rightarrow \pi^{\mp}$)

The direction of the outgoing particle is investigated in order to gain a better understanding of the scattering behavior within the SNO detector. Here isotropy is defined as the cosine of the angle between the incoming vertex direction and the outgoing one,

$$\cos\theta = \vec{u_i} \cdot \vec{u_o}. \tag{3.14}$$

In the case of hadronic scattering one would expect in most cases that the resulting particle be forward scattered ($\cos\theta = 1$). By also looking at the kinetic energy of the outgoing particle one can map the behavior of pion propagation in the detector.

Since there are slight differences between the interactions of the positive and negative

pion interactions, two studies were made. In each study, 500,000 pion events were generated in a water volume to test the inelastic interactions on ^{16}O with Geant4.

Negatively Charged Pions

A scatter plot of the isotropy and the kinetic energy of the outgoing particle with Geant4 is shown in Figure 3.4. A total of 756,682 pion induced inelastic interactions were tagged. 8.42% of these were absorbed, 77.77% had one outgoing pion and 13.81% of the interactions induced more pions. The different channels for the inelastic interactions are listed in Table 3.1.

There are two regions of interest for the outgoing pions in Figures 3.5, one in the upper right part of the map showing forward scattered pions and one in the lower left part. The section in the upper right part shows the pions that are forward scattered, while the lower left part shows the pions that are ejected in a backward direction, either from hard scattering or the absorption and reemission of the incoming pion.

In Figure 3.2 one can see isotropy distribution of the case when at least one pion comes out of the interaction. The distribution is roughly isotropic from -1.0 to about 0.2 and this section include 35.37% of outgoing pions (not including second and third pion distributions).

In Figure 3.5 the scattering behavior of a single outgoing pion is mapped. Both the NCX and SCX show the same scattering behavior. It is interesting to note that the DCX interaction is isotropic below a kinetic energy of 100 MeV. Shown in Figure 3.6 are the two-pion and three-pion distributions, these show the same overall isotropic scattering behavior.

There is a 2.46% contamination of π^+-induced inelastic interactions, and from double charge exchange interactions that have survived long enough to induce another inelastic interaction.

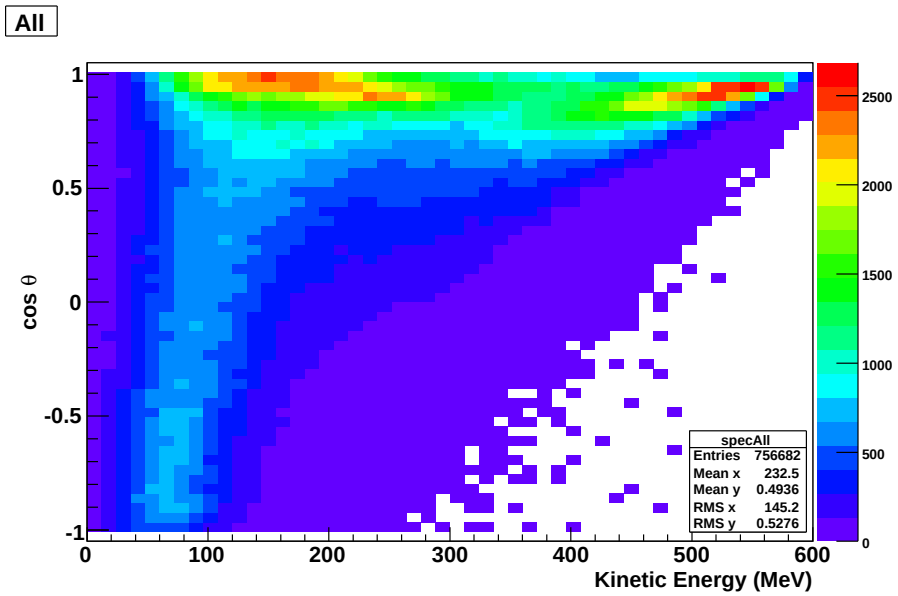

(a)

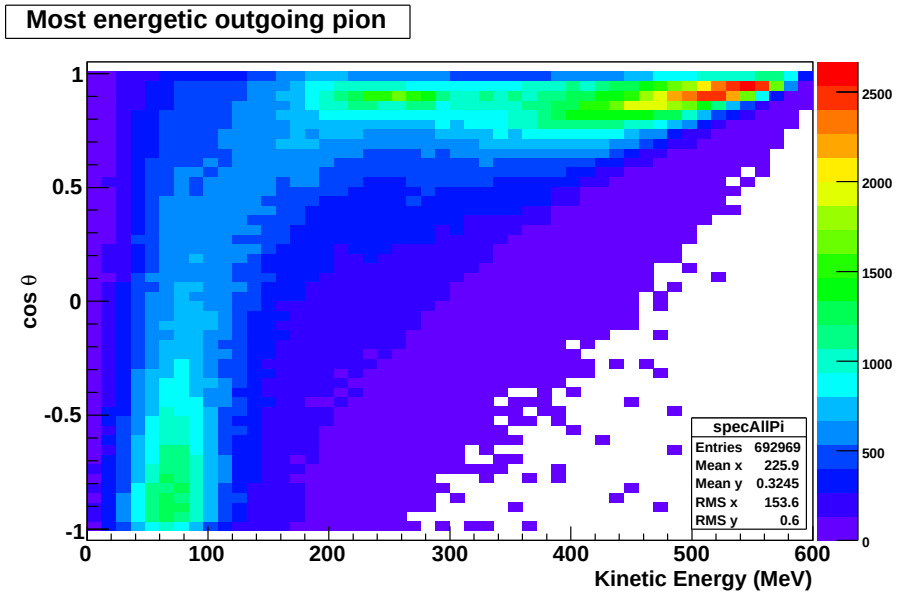

(b)

Figure 3.4: Isotropy-kinetic energy map of outgoing particle after an inelastic collision. The events were simulated with Geant4. Plot (a) shows the map of the highest energy particle while plot (b) represents the map of the highest energy pion coming out of the interaction.

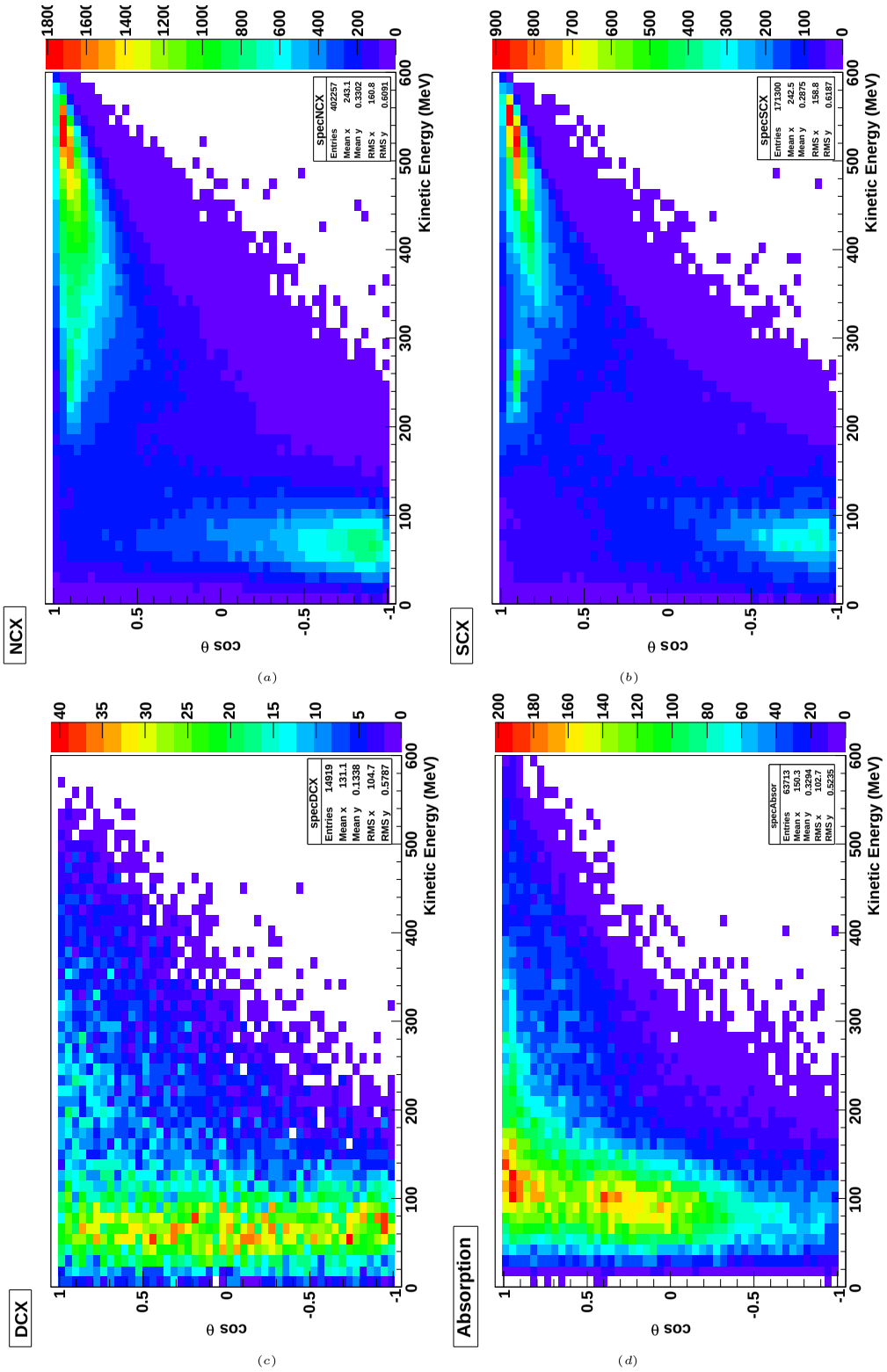

Figure 3.5: Isotropy-Energy map showing the direction and kinetic energy. The events were generated with Geant4. Plot (a), (b) and (c) are respectively the distributions for NCX, SCX and DCX process with the outgoing pion kinetic energy in the X axis. Plot (d) shows the outgoing particle with the highest energy in the case of absorption (no outgoing pion)

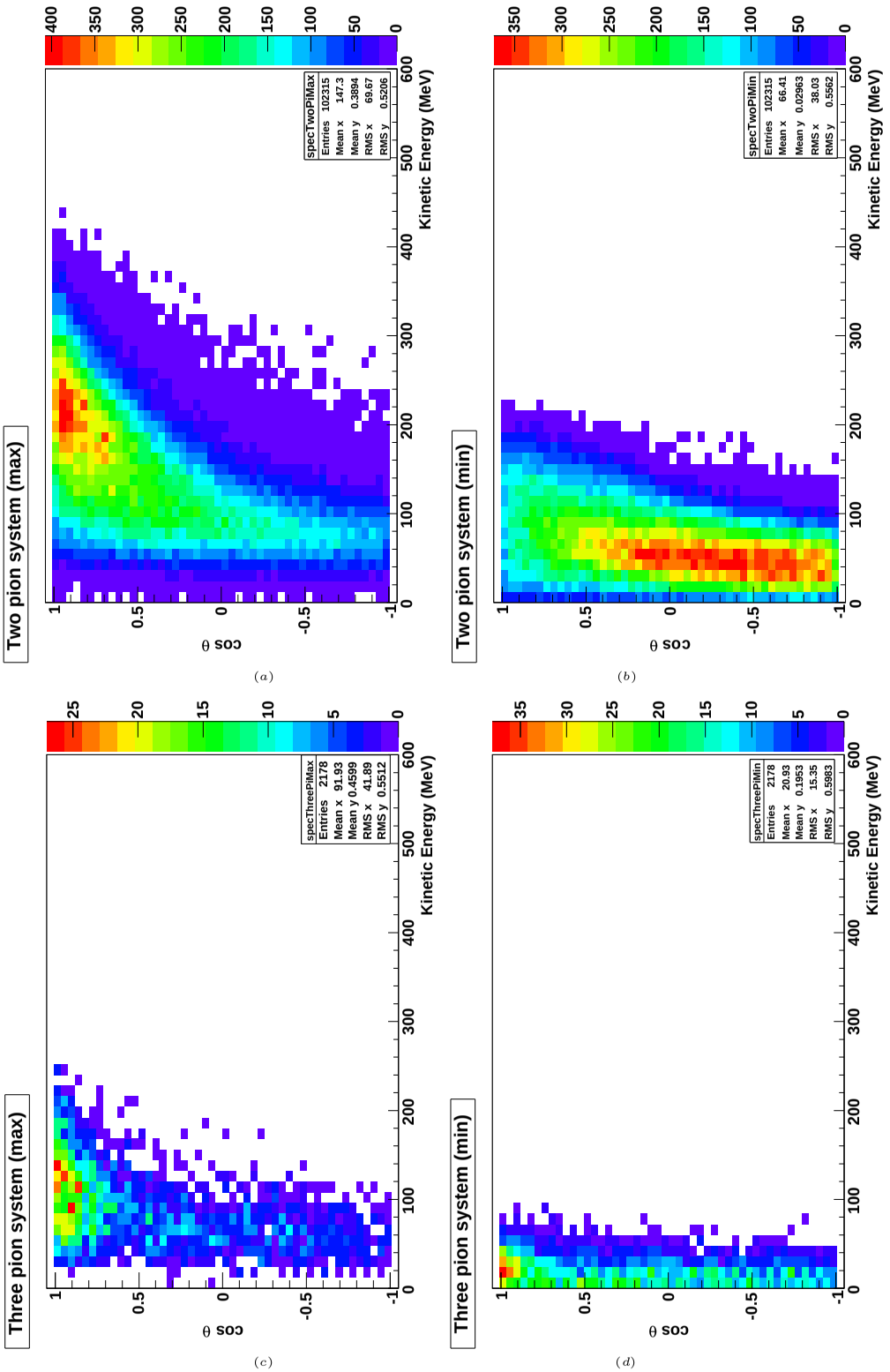

Figure 3.6: Pion Isotropy-Energy map showing the direction and kinetic energy. These events were simulated with Geant4. Plots (a) and (b) show the outgoing pion with both the highest energy and lowest energy in a pion creation process. Plots (c) and (d) also show the outgoing pion with both the highest energy and lowest energy, but in a two pion creation process.

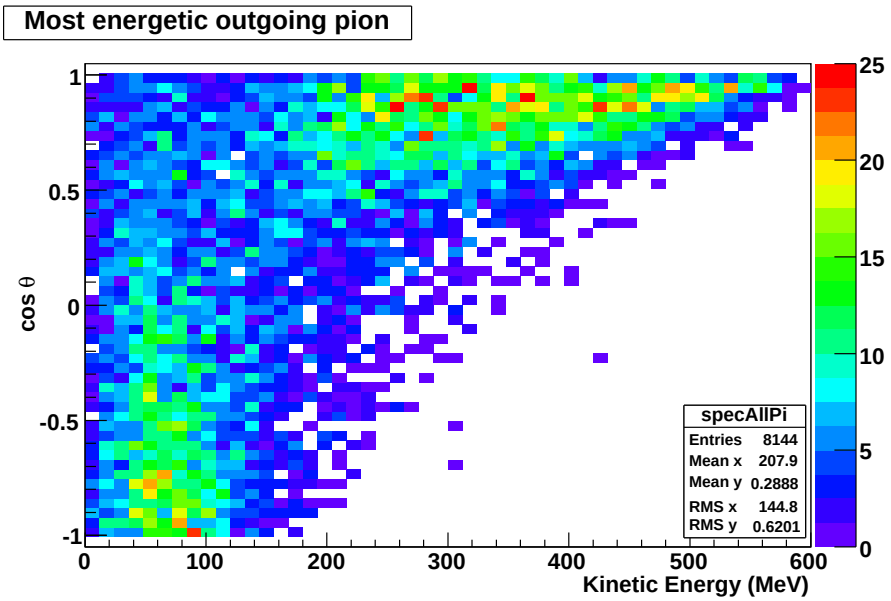

Figure 3.7: CALOR inelastic collision isotropy-kinetic energy map of the outgoing pion with the highest energy after an inelastic interaction with hadron CALOR.

Positively Charged Pion

There are different branching ratios for the different processes in nuclear inelastic interactions in oxygen between positive and negatively charged pions due to the coulomb effect. These branching ratios are summarized in Table 3.1.

The absorption rate is slightly higher for a positively charged pion, leading to a lower pion survivability. Apart from the branching ratios being slightly different, the overall behavior of the pion is the same. A contamination of 2.51% of negative pions have induced inelastic interactions. Between the cosine values of -1.0 and 0.2 are 36.53% of outgoing pions.

Hadron Calor

The corrected CALOR code (see previous section) that handles the pion nuclear inelastic interactions was integrated into SNOMAN. Its simulated properties of nuclear interactions were compared[9]. This simulation was made with the two corrections explain in the previous

[9] The lower statistics are due to the requirement to fully propagate the particles within SNOMAN.

section to those simulated with Geant4.

Shown in Table 3.1 are the different pion interaction channels for both the Geant4 and Calor simulation software. However, within Calor the target is not restricted only to ^{16}O, deuteron is also enabled. In the case of a negatively charged pion, the absorption rate is higher in the Calor code at 15.49%, than the Geant4 one at 8.42%, leading to a pion survival probability that is lower in Calor. The pion scattering behavior is similar as can be seen in Figure 3.3. The contamination rate of positive pion is 0.61%.

The nnbar analysis is statistically limited and not sensitive to an exact measurement of the different reaction channels. While the numbers do not agree perfectly between the two codes, the inelastic scattering behavior are consistent. This disagreement may be due to the presence of the deuterons in the case of the Hadron-calor routines.

3.7 Geant4 Calor Comparison Conclusions

Both the hadron Calor code and the Geant4 show similar scattering behavior for pions. While the branching ratios are different, this difference is not enough to warrant the implementation of the Geant4 routine (C++) within SNOMAN (Fortran architecture).

Since many pions are created in a pnbar collision, it follows that many nuclear interactions are probable for a nnbar event; each of these pions may experience different processes which will create the complex light signature seen in the nnbar events. It is difficult to quantify this effect on the nnbar analysis without the implementation of the Geant4 routines in SNOMAN.

However, the relaxed conditions for the detection of a nnbar event (at least two rings are required for the event to be considered a candidate) are created such that the detection sensitivity is not affected by these small variations. Also, the Multiple Ring Fitter is created to detect rings and is less sensitive to small variation in energy; it is then more important that the inelastic scattering distribution of pions is consistent so that the behavior of pions

Interaction Type	Count	Probability
Geant4 π^-		
NCX	402257	0.5316±0.0011
SCX	171300	0.2264±0.0021
DCX	14919	0.0197±0.0081
Absorption	63713	0.0842±0.0038
π creation	102315	0.1352±0.0029
2π creation	2178	0.0029±0.0214
Geant4 π^+		
NCX	455825	0.6157±0.0009
SCX	106256	0.1435±0.0028
DCX	16132	0.0218±0.0078
Absorption	67539	0.0912±0.0037
π creation	92392	0.1248±0.0031
2π creation	2200	0.0030±0.0213
Calor π^-		
NCX	16331	0.6375 ± 0.0047
SCX	3208	0.1252 ± 0.0165
DCX	400	0.0156 ± 0.0496
Absorption	3969	0.1549 ± 0.0146
π creation	1713	0.0669 ± 0.0233
2π creation	0	0.0000±1.0000
Calor π^+		
NCX	13553	0.5756 ± 0.0056
SCX	4144	0.1760 ± 0.0141
DCX	470	0.01996 ± 0.0457
Absorption	3500	0.1487 ± 0.0156
π creation	1878	0.0798 ± 0.0221
2π creation	4	0.0002 ± 0.5000

Table 3.1: Inelastic channels induced by incoming charged pion using the Geant and the Calor routine. Error calculated assuming binomial statistics for each process.

that have scattered may be studied and understood.

In this scenario, the total number of rings and the total collected light for an event may change slightly, but the ring separation distribution ($\cos\theta_{ring}$) will remain the same.

The effect of the pion scattering on event reconstruction will be described in Chapter 5. The statistical error is evaluated using binomial technique from [49]:

$$\sigma_\epsilon = \left(\frac{(k+1)(k+2)}{(n+2)(n+3)} - \frac{(k+1)^2}{(n+2)^2} \right)^{1/2} \tag{3.15}$$

where k is the sample measured and n is the size of the total sample.This technique in evaluation of statistical error is more accurate in the extreme cases where $\epsilon \approx 1$ or $\epsilon \approx 0$.

3.8 Pion Sources within the detector

Pions can appear within the detector through neutrino delta resonance interaction with the surrounding nuclei media. The delta resonance in neutron or proton can be excited by different incoming particles such as muon, neutrinos, high energy γs or even other pions.

Another source of pions originates from the interaction with the whole nuclei instead of individual nucleons. This is known as the coherent or diffractive process, such a process includes a high energy γs exchange from a high energy muon.

As will be seen in section 5.5.4, a single charged pion can mimic the nnbar signal. As such, all the different sources of pion need to be understood.

In the next chapter, the neutrino interactions modeled in SNOMAN with the NUANCE software will be explained. However, a summary of the different pion source are presented in Table 3.2. Also in the next chapter an energy cut is made in order to isolate the nnbar events from a vast majority of backgrounds.

The result in Table 3.2 are all atmospheric neutrino events seen in the detector without this energy cut[10].

[10]The ratios of events after all cuts are presented in Table D.4 and D.5.

Interaction Type	Channels	Γ_i/Γ (%) $(\nu_l/\bar{\nu}_l)$ (79009/28617)	Total (%) $(\nu_l/\bar{\nu}_l)$ (79009/28617)
Charged Current			**57.78/56.73**
CC quasi-elastic interaction	$\nu_l N \to Nl$	42.28/43.01	
CC deep inelastic interaction	$\nu_l N \to Nl$	15.50/11.55	
CC Cabibbo-suppressed scattering	$\nu_l N \to Nl$	0.00/2.17	57.78/56.73
Neutral Current			**4.87/4.36**
NC quasi-elastic interaction	$\nu_l N \to N^* l \to Nl$	0.25/0.12	
NC deep inelastic interaction	$\nu_l N \to N^* l \to Nl\pi$	4.62/4.24	4.87/4.36
Single Pion Creation			**30.32/31.50**
CC single pion creation	$\nu_l N \to N^* l \to Nl\pi$	22.72/18.94	
NC single pion creation	$\nu_l N \to N^* \nu_l \to N\nu_l\pi$	4.39/4.79	27.11/23.73
CC diffractive/coherent π production		2.46/5.73	
NC diffractive/coherent π production		0.75/2.04	3.21/7.77
Multiple Pion Creation			**6.93/7.35**
CC η creation	$N^* \to N\eta$	0.53/0.65	
NC η creation	$N^* \to N\eta$	0.18/0.21	0.71/0.86
CC ρ creation	$N^* \to N\rho$	1.14/1.17	
NC ρ creation	$N^* \to N\rho$	0.36/0.56	1.50/1.73
CC $\Delta + \pi$ creation	$N^* \to N\Delta(1232)\pi$	2.87/2.56	
NC $\Delta + \pi$ creation	$N^* \to N\Delta(1232)\pi$	0.76/1.02	3.63/3.58
CC Σ + K creation	$N^* \to N\Sigma$K	0.04/0.03	
NC Σ + K creation	$N^* \to N\Sigma$K	0.01/0.06	0.05/0.09
CC Λ + K creation	$N^* \to N\Lambda$K	0.18/0.13	
NC Λ + K creation	$N^* \to N\Lambda$K	0.07/0.10	0.25/0.23
CC Multiple Pion creation	$\nu_l N \to N^* l \to Nl\pi\pi$	0.00/0.00	
NC Multiple Pion creation	$\nu_l N \to N^* \nu_l \to N\nu_l\pi\pi$	0.79/0.86	0.79/0.86
Other process			**0.08/0.08**
Photonuclear production	$\nu_l N \to Nl\gamma$	0.06/0.06	0.06/0.06
Elastic scattering (electron)	$\nu_e e \to \nu_e e$	0.02/0.02	0.02/0.02
Inverse muon decay		0.00/0.00	0.00/0.00

Table 3.2: The various atmospheric neutrino interactions used in the creation of the atmospheric data set. None of the cuts described in section 4.8 have been applied with the exception of the Nhits>250 cut, an updated table which include the data selection cuts will be given further in the thesis (Table D.4). This table shows the various possible background pion sources due to neutrino interactions in the SNO detector. Here N stands for a nucleon, i.e. a proton or a neutron and l stands for lepton. There are a total of (79009/28617) $\nu/\bar{\nu}$ events that are detected after the SNOMAN propagation; this difference is explained in more details in Appendix E.

Particle	Channels†	Γ_i/Γ (%)
ρ	$\rho \to \pi\pi$	∼100%
K	$K^+ \to \mu^+\nu_\mu$	(63.54±0.14)%
	$K^+ \to \pi^+\pi^0$	(20.68±0.13)%
	$K^+ \to \pi^+\pi^+\pi^-$	(5.59±0.04)%
	$K^+ \to \pi^0 e^+\nu_e$	(5.08±0.05)%
	$K^+ \to \pi^0\mu^+\nu_\mu$	(3.35±0.04)%
	$K^+ \to \pi^+\pi^0\pi^0$	(1.1761±0.022)%
K^0_S	$K^0_S \to \pi^+\pi^-$	(69.20±0.05)%
	$K^0_S \to \pi^0\pi^0$	(30.69±0.05)%
K^0_L	$K^0_L \to \pi^\pm e^\mp\nu_e$	(40.55±0.12)%
	$K^0_L \to \pi^\pm\mu^\mp\nu_\mu$	(27.04±0.07)%
	$K^0_L \to \pi^0\pi^0\pi^0$	(19.52±0.12)%
	$K^0_L \to \pi^+\pi^-\pi^0$	(12.54±0.05)%
$\Delta^{\dagger\dagger}$	$\Delta(1232) \to N\pi$	∼100%
η	$\eta \to 2\gamma$	$(39.30 \pm 0.20)\%$
	$\eta \to 3\pi^0$	$(32.56 \pm 0.23)\%$
	$\eta \to \pi^+\pi^-\pi^0$	$(22.73 \pm 0.28)\%$
	$\eta \to \pi^+\pi^-\gamma$	$(\ 4.60 \pm 0.16)\%$
	$\eta \to e^+e^-\gamma$	$(\ 7.0 \pm 0.7)\text{x}10^{-3}$
Σ^0	$\Sigma^0 \to \Lambda\gamma$	100%
Σ^+	$\Sigma^+ \to p\pi^0$	$(51.57 \pm 0.30)\%$
	$\Sigma^+ \to n\pi^+$	$(48.31 \pm 0.30)\%$
	$\Sigma^+ \to p\gamma$	$(\ 1.23 \pm 0.05)\text{x}10^{-3}$
Σ^-	$\Sigma^- \to n\pi^-$	$(99.848 \pm 0.005)\%$
	$\Sigma^- \to ne^-\nu_e$	$(\ 1.017 \pm 0.034)\text{x}10^{-3}$
Λ	$p\pi^-$	$(63.9 \pm 0.5)\%$
	$n\pi^0$	$(35.8 \pm 0.5)\%$
	$n\gamma$	$(1.75 \pm 0.15)\text{x}10^{-3}$

Table 3.3: Branching ratios of particles created via the neutrino interactions in Table 3.2. The branching ratios are taken from [47]. †Not all possible decays of these particles are transcribed here, for a complete list please refer to [47]. ††This Δ resonance refers only to the channel containing the resonance peak at 1232 MeV; in Table 3.4 are shown the branching ratio for the other resonance peaks.

Mass	Width	Breit	1π	$\pi\Delta$	ρ	ΣK	η	ΛK	$> 1\pi$	γ
1232.	124.	0.928	0.9944	0.00	0.00	0.00	0.00	0.00	0.00	0.0056
1535.	150.	1.130	0.475	0.00	0.02	0.00	0.425	0.00	0.075	0.005
1520.	120.	0.939	0.55	0.20	0.20	0.00	0.00	0.00	0.045	0.005
1650.	150.	1.033	0.70	0.05	0.09	0.029	0.03	0.07	0.05	0.001
1700.	100.	1.113	0.10	0.45	0.05	0.00	0.05	0.05	0.30	0.00
1675.	150.	0.956	0.45	0.55	0.00	0.00	0.00	0.00	0.00	0.00
1620.	140.	1.026	0.25	0.45	0.16	0.00	0.00	0.00	0.14	0.00
1700.	300.	0.769	0.15	0.45	0.40	0.00	0.00	0.00	0.00	0.00
1440.	350.	0.987	0.65	0.25	0.025	0.00	0.00	0.00	0.075	0.00
1600.	350.	0.811	0.175	0.55	0.05	0.00	0.00	0.00	0.225	0.00
1720.	150.	1.169	0.15	0.00	0.77	0.00	0.00	0.08	0.00	0.00
1680.	130.	0.902	0.65	0.10	0.09	0.00	0.00	0.00	0.16	0.00
1910.	300.	1.219	0.225	0.05	0.05	0.00	0.00	0.00	0.675	0.00
1920.	250.	1.172	0.20	0.20	0.00	0.05	0.00	0.00	0.55	0.00
1905.	350.	0.618	0.10	0.20	0.70	0.00	0.00	0.00	0.00	0.00
1950.	240.	0.770	0.40	0.30	0.05	0.00	0.00	0.00	0.25	0.00
1710.	100.	1.294	0.15	0.275	0.15	0.025	0.00	0.15	0.25	0.00
1970.	325.	0.600	0.05	0.00	0.05	0.10	0.00	0.10	0.70	0.00

Table 3.4: Decay channels of the various Δ-resonance peaks used by Nuance [9]. Here it is implied that the $\pi\Delta$ channel is $\pi\Delta(1232)$. The numbers in this table are simply the branching ratios of Δ resonance decay at a specific resonance.

3.9 Summary

The propagation of pions in D_2O was the focus of this chapter. The various nuclear scattering effects that affect pion propagation create a complex Čerenkov light signature; in certain scenarios a single charged pion can mimic the nnbar signature which consists of multiple pions. The behavior of the CALOR routine that has been implemented within SNOMAN was also shown to be consistent with the Geant4 routine. After two corrections to the hadron CALOR routine, a good agreement is found between the scattering behavior of the Geant4 and the hadron CALOR routines. By assuming the same number of positive and negative charged pions[11] the inelastic scattering interactions are: ∼61% of NCX inelastic scattering; ∼15% of SCX inelastic scattering; ∼2% of DCX inelastic scattering; ∼15% of pion are absorbed; ∼7% where another pion is created.

Finally, a breakdown of the various sources of pions that appear naturally within the detector was given. For neutrino interactions it was found that 57.58% of atmospheric events were from charged current interactions; 4.87% of events were from neutral current interactions; 30.32% of events had a single outgoing pion, while 6.93% had multiple outgoing pions. For antineutrino interactions, it was found that 56.73% of atmospheric events were from charged current interactions; 4.36% of events were from neutral current interactions; 31.50% of events had a single outgoing pion while 7.35% had multiple outgoing pions. These values represent the channel probabilities of the atmospheric neutrino interactions detected at SNO with the number of fired PMTs greater than 250. In the next section a cut on the number of PMTs is made in order to select nnbar events; this cut and the various other cuts will change the ratio of pion events[12].

In the next chapter, an overview of the atmospheric neutrinos, cosmic muons and instrumental backgrounds will be given; a series of cuts to reduce these backgrounds will also be detailed.

[11] In a nnbar signal in deuteron there will always be an extra positively charged pion, the numbers presented are given as a rough estimate of the pion inelastic interactions.

[12] Table containing the corrected ratio of interaction events are shown in Tables D.4 and D.5

Chapter 4

Event Selection and Background Characterization

One Man's Music is Another Man's Noise

In this chapter, a study is presented on the properties of the various backgrounds found in detector. There are two sources of backgrounds: instrumental backgrounds and backgrounds that originate from atmospheric particles. A short description will also be given on the run selection criteria, the blindness scheme and the detector livetime for the nnbar study across all phases.

The various Monte Carlo simulations developed for the atmospheric analysis [8] to understand the behavior of atmospheric and cosmic muons are used to further separate the data into two subcategories: the internal (also known as contained events) and external (events that enter and/or leave the detector) data sets.

Finally, the study on the series of cuts designed both to remove instrumental noise and to isolate the signal region from the external events will be given; once separated, a comparison between data and simulation is made to verify the success of the separation cuts.

4.1 Run List Selection

The choice of which runs to keep and which runs to remove depends on the energy of the events of interest: lower energy events will suffer certain instrumental backgrounds that will not be present at higher energies and vice-versa.

The run selection chosen for the nnbar analysis is the one used in the muon flux analysis [8]. This run selection[1] is different than the run selection of the solar neutrino analysis, also known as the golden run selection, allowing a longer available livetime but introducing low energy backgrounds.

While the detector conditions for the neutrino run selection are optimized for energy of a few MeV's and the Hep analysis of up to 50 MeV, the muon analysis concentrated on particles with energies from a few hundred of MeV's (>500 photomultiplier calibrated tubes firing) to several hundred of GeV's. The various technical criteria for the run selection are described below.

Solar Neutrino Run Selection Criteria

The run selection for the neutrino analysis is constructed with a set of criteria [17]:

- neutrino run flag is set
- All 19 crates should be online
- No more than 512 channels offline
- Non-standard channels are online (Neck, Owl and BUTT)
- No more than 6 blind Flashers channels (tubes that emit a large amount of light within the run)
- Run should be greater than 30 minutes
- Run deadtime acceptable (no more than 25% of events cut within a burst)

[1] The run selection is found in [44]

- Shift report verification

The last point required the verification of all runs shift report filed by the detector operator[2]. This run selection is standard for many of the SNO analysis.

Muon Run Selection Criteria

Runs that would have instrumental noise that would hinder the hep or solar neutrino analysis but not the muon analysis were added to the neutrino run selection. The modified criteria for the muon run selection are [44]:

- Keep runs if the only problem is the analysis online tube (ANxx) banks pass the Second Pass Selection (SPS[3]) crate trigger checks. The SPS consists of a series of checks written to verify the tubes condition of a run.
- Keep runs if the only problem with run is trigger cables unplugged in a few crates. A crate is responsible for 512 PMTs.
- Keep runs if the only problem with run is bubblers off but not flooded. Bubbler tubes in the acrylic vessel were used to monitor the level of the H_2O and D_2O; these tubes would create water bubble that generate neutrino-like events.
- Keep runs if the only problem with run is 1 or 2 of the 14 compensational coil for Earth's magnetic field offline (or low).
- Keep runs if the only problem is confined to single "screaming tubes": a screaming tube is a single tube with extremely high firing rate.

As stated previously, the increase of livetime introduces some instrumental backgrounds which will need to be removed by additional instrumental background cuts. A treatment of these backgrounds will be given later in this chapter.

[2]For more details, the reader is encouraged to consult [17]
[3]Algorithm written for run selection by C. Kyba, M. Dunford, W. Tseung and J. Wilson [50]

Category	Time Length (Open data set)	Time Length (Full data set)
D_2O Phase:		
Number of runs:	299	603
Raw length :	171.99 days	337.35 days
Raw length(50MHz):	171.98 days	337.33 days
Muon Burst Cut :	0.06463 days	0.08571 days
Retrigger Cut :	9.320e-05 days	0.0002978 days
After dt length :	**171.92 days**	**337.26 days**
After dt length(50MHz) :	**171.91 days**	**337.24 days**
Salt Phase:		
Number of runs:	209	1628
Raw length :	76.01 days	499.47 days
Raw length(50MHz):	76.01 days	499.45 days
Muon Burst Cut :	0.005049 days	0.04039 days
Retrigger Cut :	8.815e-05 days	0.0007151 days
After dt length :	**76.01 days**	**499.43 days**
After dt length(50MHz) :	**76.00 days**	**499.41 days**
NCD Phase:		
Number of runs (NCD):	1955 (20% data splitter)	1955
Raw length :	78.58 days	392.88 days
Raw length(50MHz):	78.58 days	392.88 days
Muon Burst Cut :	1.140e-02 days	0.05670 days
Retrigger Cut :	1.302e-04 days	0.0006511 days
Run Boundary* :	0.0133 days	0.2666 days
After dt length :	**78.51 days**	**392.56 days**
After dt length(50MHz) :	**78.51 days**	**392.56 days**
D_2O 2 Phase:		
Number of runs :	N/A	69
Raw length :	N/A	13.18 days
Raw length(50MHz):	N/A	13.18 days
Muon Burst Cut :	N/A	0 days
Retrigger Cut :	N/A	1.2369e-05 days
After dt length :	N/A	**13.18 days**
After dt length(50MHz) :	N/A	**13.18 days**

Table 4.1: Detector livetime across all phases for the open and full data sets. Here dt is the amount of time loss in the phase due to the muon burst and rettriger cuts.

4.2 Blindness Scheme and Phase Livetimes

It is hard to find a conventional blindness scheme for the nnbar search, where one would look at a portion of the data that include both signal and background in order to extract their respective properties, due to the rarity of the signal.

For a proper characterization of the physical and instrumental background the blindness scheme of the atmospheric muon analysis is more appropriate [8] than the blindness scheme used in other SNO analysis; this is in part due to simplicity sake since the run list are

different and the signal for the muon analysis is the background for the nnbar oscillation search.

However, while the atmospheric muon analysis used a double blinded scheme in order to hide the true flux of events, the nnbar analysis only concentrate on a single blind analysis in order to properly understand the behavior of the atmospheric and cosmic backgrounds.

This single blind analysis consists of looking only first at one portion of the data for the D_2O phase to establish and finalize instrumental background and event selection cuts; these cuts will then be tested on the open data sets in both the Salt phase and the NCD phase of the SNO experiment in Chapter 7[4].

Runs in each phase are chosen from the open run list[5] used in the atmospheric muon analysis [8].

Treatment within this chapter

The treatment shown in this chapter concentrates only on the D_2O part of the data for clarity purposes. As will be described in Chapter 6 and 7, the number of systematic effects to take into account within this analysis is limited. A treatment of the difference between the various phases will be given in Chapter 7.

Some of the differences for the parameter distributions between the different phases have been studied within the muon analysis in [44] and in particular in [51]. The change in the parameter space of the Multiple Ring Fitter, which will be the subject of Chapter 5, throughout the phases will also be evaluated in Chapter 7.

While some differences are expected between phases, the instrumental background cuts (which will be the subject of Section 4.8) will remain fixed through all the phases; the type of instrumental and physical backgrounds will remain the same through the phase and the stability of cuts designed in this section will be tested through the phases in Chapter 7.

[4]This two-step analysis of data between phase is made in order to further reduce possible bias in the choice of cuts in the separation of internal and external events

[5]At the time of this decision, it was thought that the run list covered about 1/3 of the D_2O detector livetime. However, since the muon run list is different than the neutrino run list, the run duration is closer to 50% for the D_2O phase as can be seen in Table 4.1.

4.3 Particle Creation within the Atmosphere

One of the physical backgrounds for the nnbar oscillation search originates from neutrinos. There are three known sources of neutrinos[6]: solar, nuclear reactors and cosmic particles bombarding the atmosphere. The only physical events within the detector to have the energy range of a signal of nnbar oscillation are atmospheric neutrino events. The sun does not produce neutrino with enough energy; nuclear reactor neutrinos of energies of a few MeV's are not relevant to the nnbar signal search.

SNO, in part due its depth and size, detects a lower flux of cosmic muon events compared to other experiments. The SNO detector is sensitive to two separate source of muons: direct muons from cosmic interactions and muons induced from CC atmospheric muon neutrino interactions. SNO is also sensitive to energetic electrons from both neutrino interactions and Michel electrons originating from the decay of the muons within the detector volume.

The cosmic rays hitting the atmosphere create pions which further decay following the following scheme,

$$\begin{aligned} \pi^+(\pi^-) \rightarrow \quad & \mu^+(\mu^-) \quad + \quad \nu_\mu(\bar{\nu}_\mu) \\ & \mu^+(\mu^-) \quad \rightarrow \; e^+(e^-) + \nu_e(\bar{\nu}_e) + \bar{\nu}_\mu(\nu_\mu). \end{aligned} \tag{4.1}$$

These two decays are known as π-decay and μ-decay atmospheric neutrinos [52].

Direct muons are more abundant than the neutrino induced muons due to the low cross section of neutrino interactions. Since the cross section for muon neutrino interactions is weak, a single neutrino is more likely to propagate throughout the earth without interacting than it is to have interacted; there are on the other hand a vast number of atmospheric neutrino created. The cosmic flux is not bombarding the earth from a fixed position like the sun, the flux of atmospheric neutrinos at SNO is isotropic.

The detection of direct muons is not isotropic; muons, unlike neutrinos, interact heavily

[6]While supernovae are also known to create a vast number of neutrinos, no supernova occurred in SNO's livetime

with the surrounding matter and suffer a continuous energy loss. Only muons that are coming from above the detector, $\cos\theta_{zenith} > 0.4$, have a chance to survive and reach the detector. To reach the detector, direct muons must have an initial energy of at least 1.03 TeV [8].

While both muon sources are from atmospheric origin, it has become a convention to characterize them as "cosmic" and "atmospheric" muon events, where "atmospheric" muons denotes more precisely atmospheric neutrino induced muons and "cosmic" muons denotes more precisely direct muons. Solar neutrinos do not have the required energy to create muons from charged current interactions.

Atmospheric neutrino events are further characterized into two categories, atmospheric and upward going events. The distinction between the two categories above are related to the position of the interaction vertex leading to the muon creation with respect to the detector: if the interaction occurs outside of the detector volume, events are defined as upward going; if the interaction occurs within the detector volume, events are defined as atmospheric events.

The "upward going" muon nomenclature is used to distinguish from the more abundant direct muons which can only be seen in the downward direction ("downward going muons"); in the case of the SNO experiment, above a zenith angle of 66^o all through-going muons are atmospheric neutrino induced muons (upward muons) since no direct muon are detectable. While neutrino induced muons may be going downward, they are still defined as upward going muons[7].

4.4 Atmospheric Contained Events

Events induced from atmospheric neutrino interactions within the detector are the physics background to the nnbar analysis. The understanding of their behavior is paramount to

[7]This nomenclature comes from experiments like Super-Kamiokande which can only measure atmospheric neutrino induced through-going muons below the horizon.

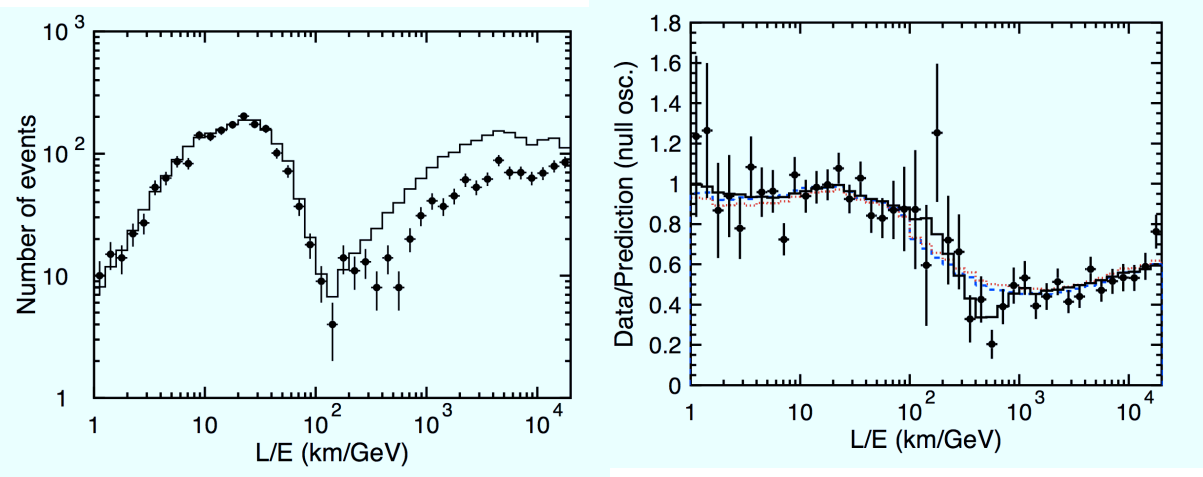

Figure 4.1: Super Kamiokande ν_μ oscillation results of muons generated within the detector volume. In the first plot the histogram shows the no-oscillation expectation and the data points show the observed events. On the second plot the ratio of the data to the MC expectation is shown as a function of L/E. Plot taken from [53].

the nnbar study.

Atmospheric neutrino interactions fall into three different types: neutral current, charged current and pion creation interactions; similarly to the lower energy neutrino analysis, the neutrino can interact through the charged current and neutral current channels; however at higher energies, the neutrino can also interact through delta resonance. The general channel for single pion creation is given by:

$$\begin{aligned} \nu N &\rightarrow l\Delta \rightarrow lN'\pi \text{ (CC)} \\ \nu N &\rightarrow \nu\Delta \rightarrow \nu N'\pi \text{ (NC)} \end{aligned} \tag{4.2}$$

Multiple-pion creation is also possible, but is suppressed as was seen in Table 3.2.

The charged current interactions will create both muons and electrons, however SNO is not sensitive to tau creation due to it's cross section. However, the oscillation of atmospheric neutrinos needs to be accounted for since the no oscillation hypothesis is rejected by the various atmospheric analyses [8][53]. The presence of neutrino oscillation leads to a lower flux of atmospheric muons; neutrino oscillation will not modify the expected amount of atmospheric induced electrons.

By assuming the oscillation parameters $\sin^2 2\theta = 1.00$ and $\Delta m^2 = 2.6 \times 10^{-3}$ eV^2, the

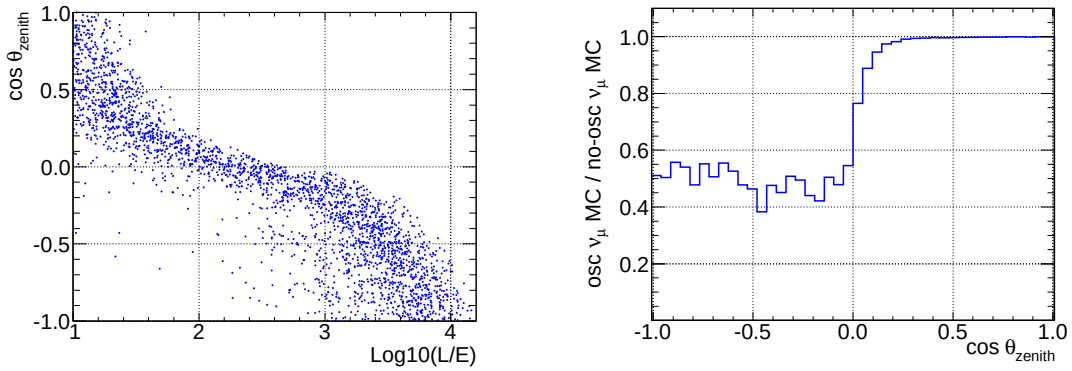

Figure 4.2: Implementation of the muon neutrino oscillation within the Monte Carlo simulation. The first plot shows the scatter plot of contained events of $\cos\theta_{zenith}$ and L/E_ν. The second plot shows the disappearance of muons within the contained event Monte Carlo as a function of the zenith angle.

survival probability of $\nu_\mu \to \nu_\mu$ is,

$$\phi(L/E_\nu, \theta, \Delta m^2)_{\mu\mu} = \phi_0 \cdot \left[1 - \sin^2 2\theta \sin^2\left(\frac{1.27\Delta m^2 L}{E_\nu}\right)\right] \tag{4.3}$$

where ϕ_0 is the neutrino flux normalization, E_ν is the neutrino energy in GeV and L is the distance between the creation of the neutrino and the detector in km. As stated previously, SNO is not sensitive to τ neutrinos and as such the above formalism leads to the disappearance of muon neutrinos.

The distance L of a neutrino produced at height $h \approx 15$ km (for π decay or $h \approx 13$ km for μ decay [2][54]) at a detector a depth $d = 2.092 \pm 0.006$ km [8] is,

$$L = \sqrt{(R_\oplus + h)^2 - (R_\oplus - d)^2 \sin^2\theta_z} - (R_\oplus - d)\cos\theta_z \tag{4.4}$$

where $R_\oplus = 6.378 \times 10^3$ km [47] is the equilateral radius of the earth and θ_z is the detector zenith angle with $\theta_z = 0$ being the detector's vertical axis. Both θ_z and E_ν are parameters in the generation of the atmospheric Monte Carlo data sets. Equation 4.3 is used with the above parameters to evaluate the number of surviving muons in the detector.

In the case of the atmospheric neutrino SNO analysis [8], the analysis concentrated on neutrino induced muons that were generated outside the detector and passing completely through the detector. Lower energy events are rejected by the muon selection cuts which

lead to a bias in a higher neutrino energy and consequently to a higher survival probability. In the case of contained events, the behavior of the neutrino flux as a function of the zenith angle will exhibit different behavior from the through-going events (as shown in Figure 4.3).

Super-Kamiokande have studied neutrino induced muon contained events [53]. The studies showed a pronounced muon neutrino disappearance for $L/E_\nu > 10^2$ km/GeV as seen in Figure 4.1. SNO showed similar behavior. Figure 4.2 shows the L/E_ν of atmospheric neutrinos as a function of the zenith angle and the disappearance of muon neutrinos within SNO. Most of the events with $L/E_\nu > 10^2$ km/GeV have a value of $\cos\theta_{zenith} < 0$, which led to a disappearance rate that is consistent to the Super-Kamiokande results.

4.4.1 Atmospheric Multiple Ring Events

Multiple rings can occur in two setting: Michel electron from atmospheric neutrino induced muon that have decayed and pion creation through delta resonance. As was seen in Chapter 3, the pion particle is hard to track within the detector due to nuclear interactions; multiple scatterings and secondary pion creation create a complex light pattern within the detector. Since a single pion may either disappear, create a single ring or even create multiple rings, a single charged pion can become the background to the nnbar oscillation search.

4.5 Cosmic Muons

The highest rate of physical events with the same visible energy as a nnbar signal are downward going cosmic muon[8] events. The rate of these cosmic events seen in SNO is $(3.31\pm0.01\ (\text{stat.})\pm0.09\ (\text{sys.}))\times10^{-10}\mu/s/cm^2$ which corresponds to 62.9 ± 0.2 muons/day [8].

The energy window for the nnbar oscillation (which will be the subject of section 4.8) reduces this rate to 14.8 ± 0.3 muons/day. The events that are within this energy window

[8] A treatment of cosmic ray physics is given in [52]

will be used to calibrate the behavior of the Multiple Ring Fitter[9], which will be defined in the next chapter.

Justification of the use of cosmic muons as a calibration source

Cosmic events are not a background to the nnbar oscillation since they can be easily vetoed with a cut on the Owl tubes (section 4.8). Also, these events will not exhibit the behavior of nnbar oscillation signal, however they offer unique opportunities to understand the behavior of the Multiple Ring Fitter on actual events.

There are two types of events within this region: the first are clipping muons (muon entering and exiting at the edge of the detector as shown in Figure G.1) and the second are known as stopping muons (muon either decaying or absorbed within the detector as shown in Figure G.2).

Michel electrons from stopped muon are one of the source of energetic electrons within the detector. The study of the fitter in these type of events is important to test consistency between data and simulation.

The second type of events are also useful for calibration purposes. Because of the presence of the acrylic vessel, clipping muons can mimic the signature of high energy electrons[10]. Due to the construct of the fitter, which will be explained in section 5.3, the Multiple Ring Fitter will mistakenly identify clipping muons as electron rings.

The behavior of clipping muons between actual data and simulated cosmic events will also be used as a calibration source. The fitter will not try distinguish between stopping and clipping muons.

4.5.1 Cosmic Multiple Ring Events

In most cases, cosmic events will not create multiple rings. However, certain cosmic events will reconstruct as multiple rings. As will be explained in the next chapter, false multiple

[9] This calibration will be explained in section 6.1

[10] Electron signature is defined in section 3.2

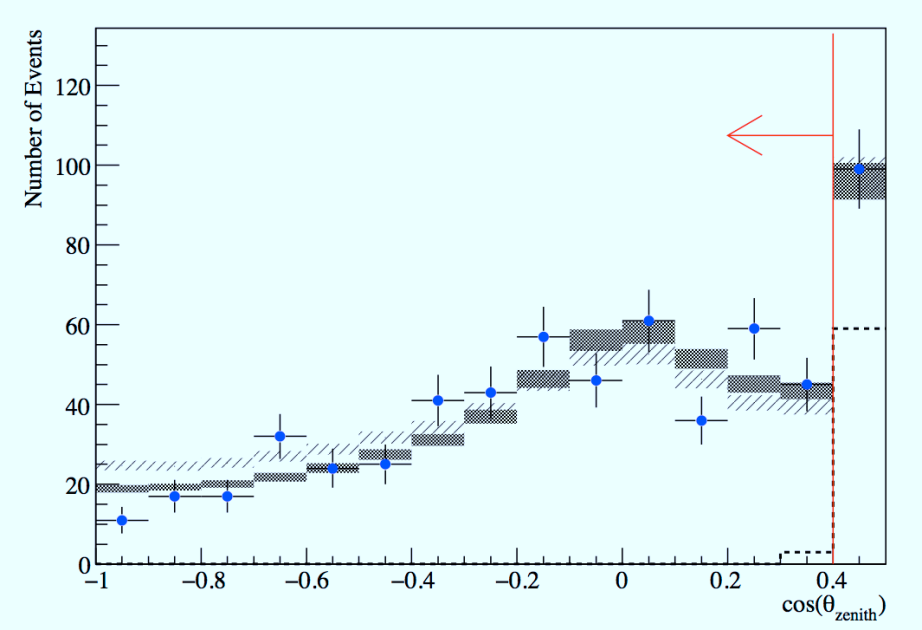

Figure 4.3: Result from the SNO atmospheric analysis. Two scenarios are presented: the dashed box shows the no-oscillation hypothesis and the solid box shows the best fit $[(\phi_0, \sin^2 2\theta, \Delta m^2) = (1.22 \pm 0.10, 1.00, 2.6 \times 10^{-3}\ \mathrm{eV}^2)]$ [8]. Here ϕ_0 is relative to the Bartol 3-D flux.

rings may be wrongly identified because of the "edge of the ring" effect.

The main source of secondary rings events are Michel electrons from stopping muons. Another source are pion created by the exchange of a high energy gamma. Both of these phenomena are included in the cosmic Monte Carlo simulations.

4.6 Upward Going Muons (UPMU)

Muons are also created through neutrino interactions. These fall into the same two categories of cosmic events: through-going events which enters and leave the detector volume and stopping muons events which decay within the detector volume.

These muons have been studied extensively in the context of the atmospheric muon analysis [8]. Certain requirements needed to be met for event selection. For example only through-going muons were selected via a series of instrumental background cuts; the muon must have a minimum energy to pass through the detector. Because of this requirement, the sample of neutrinos which results in through going muons will have a disappearance rate

which is different than contained events since the survival probability is energy dependent. This can be confirmed by comparing the disappearance behavior Figures 4.2 and 4.3.

In the context of the nnbar analysis, these events, as well as the cosmic events of the previous section, are easily rejected by a OWL cut which will be discussed in section 4.8. The rate of upward going muons that pass all analysis cuts is 0.24 ± 0.02 event per day, and is much lower than the cosmic one.

4.6.1 Upward Going Muons Multiple Ring Events

The type of the multiple ring that originates from upmu events are the same as cosmic events. The main distinctions between cosmic and upmu events are the direction of the incoming track and the rate. However, the signature of the two types of events is the same.

4.7 Instrumental Backgrounds

The instrumental backgrounds present within the SNO data have been studied in details for both the solar neutrino analysis [17] and in the atmospheric muon analysis [50]. While the energy range of nnbar is related to the muon analysis rather than solar neutrinos, many backgrounds in the solar neutrino analysis that were not present in the muon analysis will be present in the nnbar analysis. This is because the atmospheric muon cuts are optimized for events that originate from *outside* and remove various classes of instrumental backgrounds, while the focus of this study is in the detection of events that originate and are contained *within* the detector.

The signal window unfortunately lies in a region that contains more instrumental backgrounds than in the atmospheric muon analysis [8]. It is therefore important to understand the various backgrounds that may be present within the signal window[11].

Instrumental backgrounds that are relevant to this study are similar to those for the

[11]The selection of the cuts from both the neutrino and atmospheric muon analysis used in the nnbar analysis are presented in section 4.8.

muon atmospheric analysis and can be summarized as follows:

- **Electronic Pickup Events**: Events that can occur from various sources: external influence on the electronic equipment; when there's activity on deck; when the operating temperature or humidity is too high [17]. A visual example of a pickup event is shown in Figure G.4.

- **Wet End Breakdown**: Break down of the connector of a PMT. These breakdowns can be severe and appear as a successive bursts of events; the high voltage of the tube in question must be manually shut down or such breakdowns would occur at a later time.

- **Bubbler Events**: Events that originate when the bubbler system is active. These events can mimic contained atmospheric neutrino events. They can be removed by only analyzing runs with the bubbler system disabled.

- **Neck Events**: Light generated above the detector that have the same characteristics as the bubbler events. Theses events arise from mechanical pressure in the neck region of the detector (activity on deck, earth tremor, blasting, ...) and may are removed by the Neck cut.

- **Flashers**: Events that originate when a PMT emits a large amount of light; flashers may produce enough light to fire over 1000 tubes, but are more common at lower energies. An example is shown in Figure G.3.

Bubblers and neck events have similar behavior as atmospheric neutrino events and can create a large amount of light (more than 1000 tubes hit) within an event. However, the bubblers are not turned on for all runs and a separation between runs that have the bubblers enabled and those that have not is possible. Bubbler runs are not part of the muon run list selection. Neck events can be removed efficiently with the neck cut which will be described in the next section.

4.8 Instrumental Background Cuts

Several cuts were constructed during the atmospheric muon analysis [8] to reduce instrumental backgrounds in the data. However, not all of these cuts are relevant to the nnbar oscillation search; some of the atmospheric cuts will outright reject a nnbar oscillation signal.

These high energy cuts have been studied extensively by the muon working group and are well understood. The introduction of a new cut or the modification of an existing one requires a careful study of the behavior between data and simulation in all three phases.

In this section a review of the cuts included in the nnbar search are presented. Some modifications are necessary to some of the cuts and these changes will be explained.

Two categories of cuts are considered, the first set of cuts are applied only to the data (instrumental cuts) while the second set of cuts are applied to both the data and the Monte Carlo simulated data sets (physical cuts). These cuts are defined as follows: the low level cuts which remove instrumental backgrounds and the high level cuts which isolate the signal from as many physical backgrounds as possible.

The different cuts can be further divided into three sub-categories: the atmospheric muon analysis cuts that are relevant to the nnbar analysis (Atmospheric Muon Cuts), the cuts that are relevant in instrumental background removal in the solar neutrino analysis (Neutrino Cuts) and cuts that are specific to the nnbar analysis (nnbar Cuts).

Both the atmospheric and neutrino cuts are low level cuts while the nnbar cuts are high level cuts and can be applied to Monte Carlo.

4.8.1 Atmospheric Muon Cuts

The atmospheric muon analysis series of cuts have been optimized for the detection of through-going muons instead of the contained events; however, since the energies of interest overlap with the nnbar oscillation signal window, many cuts that remove instrumental

Cut Categories	Atmospheric data set Cuts	Cosmic and Upward going Muons data set Cuts
Atmospheric Muon Cuts	Neck Retrigger Muon Burst Pmt_hit > 500	Neck Retrigger Muon Burst Pmt_hit > 500
Neutrino Cuts	Q/NHIT **Owl ≤ 4**	Q/NHIT **Owl > 4**
nnbar Cuts	2000 < NHIT < 7000 Pmt_hit/NHIT > 0.7 2000 < p.e. < 18000	2000 < NHIT < 7000 Pmt_hit/NHIT > 0.7 2000 < p.e. <18000

Table 4.2: Data cleaning cuts used in the nnbar analysis. The cuts presented are a mixed of cuts developed for the solar and atmospheric neutrino analysis and some developed specifically for the nnbar oscillation signal search.

backgrounds are pertinent to this analysis.

Neck Cut

The neck flag is constructed to eliminate neck events. These events have a high energy and may be mistaken for atmospheric contained events. The cut requires that the event must have NNeck < 4 in order not to be rejected. NNeck is the number of fired PMTs in the neck region.

Retrigger Cut

Scattered light from the acrylic vessel can hit a PMT after the end of the trigger window of the event. The retrigger cut is used to remove events that are triggered from spill over light from a previous event. With some energetic events many of these retriggers can occur. A retrigger event is defined as any event that have occurred within 5 μs of a previous event. Most high energy events, be it cosmic, atmospheric or nnbar will have retrigger events after the prompt event.

Muon Burst Cut

The Muon Burst flag was constructed to tag PMT wet-end breakdown events which appear as a successive burst of high energy events. This flag tags any four events that occur

within 2 seconds of each other; if four or more events are tagged within this time period *all* tagged events are removed. This muon burst cut purpose is to remove breakdowns that occur with high intensity within the detector. A treatment of the Muon Burst and Retrigger flag within the Monte Carlo events is made in Appendix C.

PMT Calibration (Pmt_hit[12])

The tubes are compared to the ANxx bank to verify their calibration for each run. Certain instrumental backgrounds were associated to the firing of tubes with bad calibration; a requirement that at least Pmt_hit > 500 within the event has good calibration eliminates many of this instrumental events. This cut will become obsolete for reason explained later on, it is kept to explain the motivation of the implementation of the Pmt_hit/NHIT cut where NHIT is the number of PMTs that have fired in the event.

4.8.2 Neutrino Cuts

Two cuts are described in this section, a cut that removes cosmic and other externally triggered events (NOwl), and a cut to eliminate instrumental background events (Q/NHIT).

Q/NHIT

The Q/NHIT cut was constructed for the removal of various electronical pickup events [55]. These events have the property that the charge integrated over the trigger window is near pedestal.

Owl

The OWL (Outward Looking Tubes) are not simulated within the SNOMAN MC simulation which makes it a difficult cut to study. Furthermore, these tubes are not calibrated like the inward looking ones. However, the benefit of the ability to separate internal and external events outweighs the associated uncertainties. These tubes are connected to the same crates as the inward looking tubes (PMTs). In the case of noise that affects the whole

[12]The number of tubes with good calibration within the event was recorded in the Pmt_hit (for the ntuple files) and MuonFits.fHitTubes (for the root files)

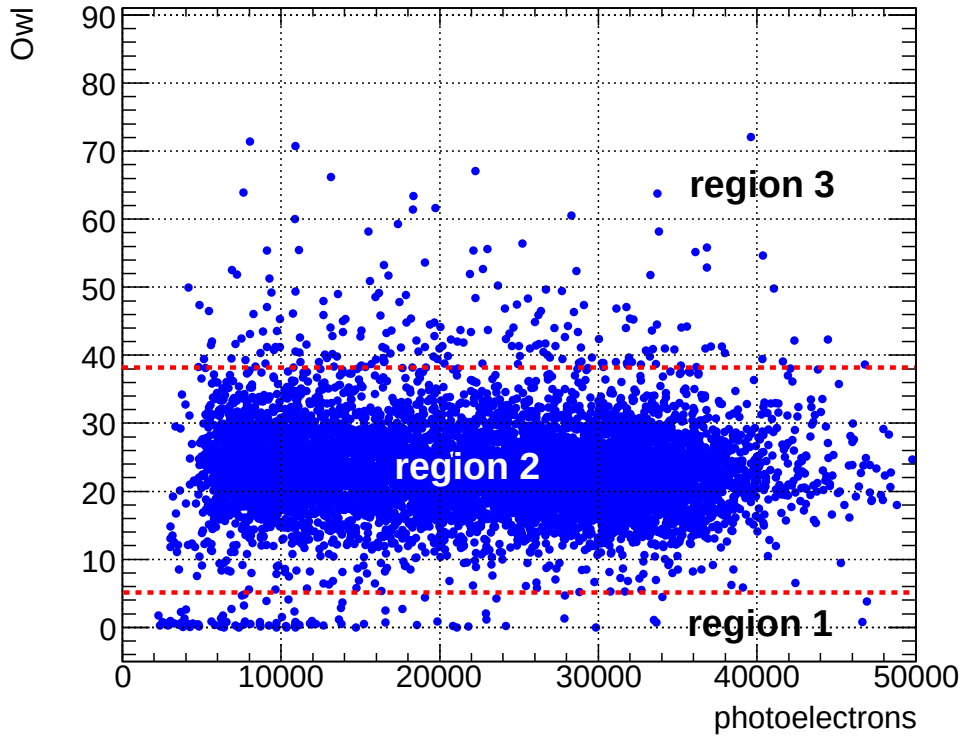

Figure 4.4: Use of the owl cut to separate a atmospheric and cosmic-upmu events in the open D2O data set. All data cleaning cuts, with the exception of the owl cut, have been applied.

crate, these will fire along with the rest of the PMTs connected to the same crate.

Shown in Figure 4.5 is the distribution of OWL tubes that fire as a function of the number of photoelectrons within the events. Three sections are defined:

- **Region 1:** Region where contained events are expected.
- **Region 2:** Region where external (through-going and stopping) events are expected.
- **Region 3:** Abnormal region where many OWL tubes fire with low amount of photoelectrons: on one side, the abundance of owl tubes would indicate a very energetic event; on the other the low amount of photoelectrons indicate a low energy event.

The events in Region 3 are some unusual instrumental background events (a visual example is shown in Figure G.5). Information on events that fail the Muon Burst cut

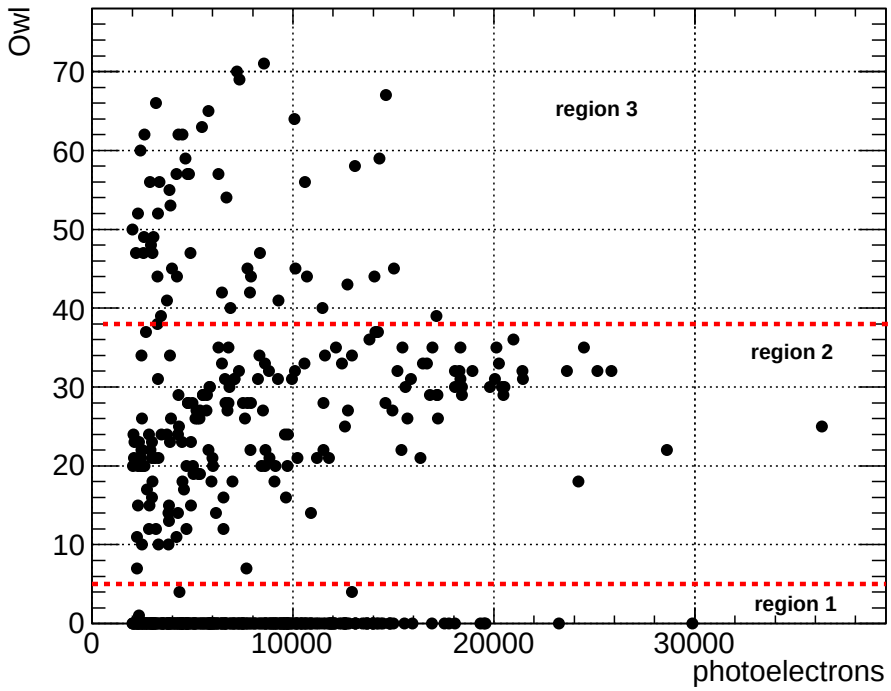

Figure 4.5: Behavior of instrumental noise within the Muon Burst events. The Pmt_hit/NHIT cut has not been applied.

events provide useful indication of possible instrumental background that may be present in the rest of the data as seen in Figure 4.5.

4.8.3 Neutron Anti-Neutron (nnbar) Cuts

The three cuts that are specific to the nnbar analysis are all modified cuts from the Muon Atmospheric analysis. The first cut is a new cut to remove possible backgrounds. The second is a cut on NHIT of the event, while the third is a cut on the amount of photoelectrons deposited within the event. These two cuts create an energy window in which the nnbar signal is isolated from many, but not all, of the major backgrounds of the analysis.

Pmt_hit/NHIT Cut

A nnbar cut is implemented because of events passing all cuts that populate region 3. While the events are fully contained within Region 3, this may be a question of chance; only part of the data is chosen for analysis at this time and the behavior of these instrumental

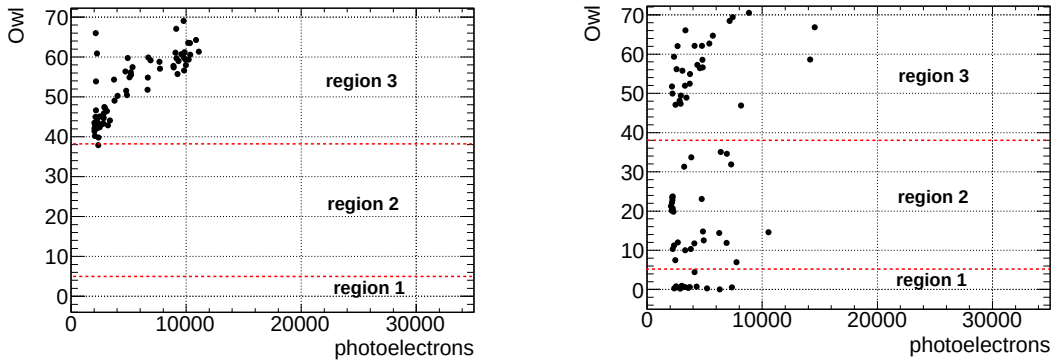

Figure 4.6: Behavior of instrumental noise within the data passing all previous cuts and the Muon Burst events with values of Pmt_hit/NHIT < 0.7. An example of the type of events that fails all cuts but the Pmt_hit/NHIT < 0.7 one is shown in Figure G.5; these events seem localized in region 3 for data, but not localized to any one section within the burst events.

events may be different in the rest of the data.

In Figure 4.6 are shown the events that are contained within Pmt_hit/Nhits < 0.7 for two types of events: events that have passed all previous cuts and events that have passed all cuts with the exception of the Muon Burst cut. The first plot shows that a cut of 0.7 cuts many events within Region 3 while not cutting any events in either Region 1 or 2.

In the second plot, burst events within all region have events with Pmt_hit/Nhits < 0.7. Events like the one shown in Figure G.5 were close in time to one another; this may be indicative of the remnant of a single wet end breakdown which may explain why all the events are localized in Region 3.

Nhits Window

The energy signature of the nnbar signal lies in a narrower energy window than the atmospheric and cosmic background. Figure 4.7 shows the event distribution normalized to unity on the different event classes. The retrigger events, which consist of spill over light from previous events, have not been removed[13].

[13]The flag to tag retrigger events was not filled in the latest version of the Monte Carlo simulation for the different event classes presented here. The manual isolation of retrigger events for the case of the nnbar is shown in Figure C.2

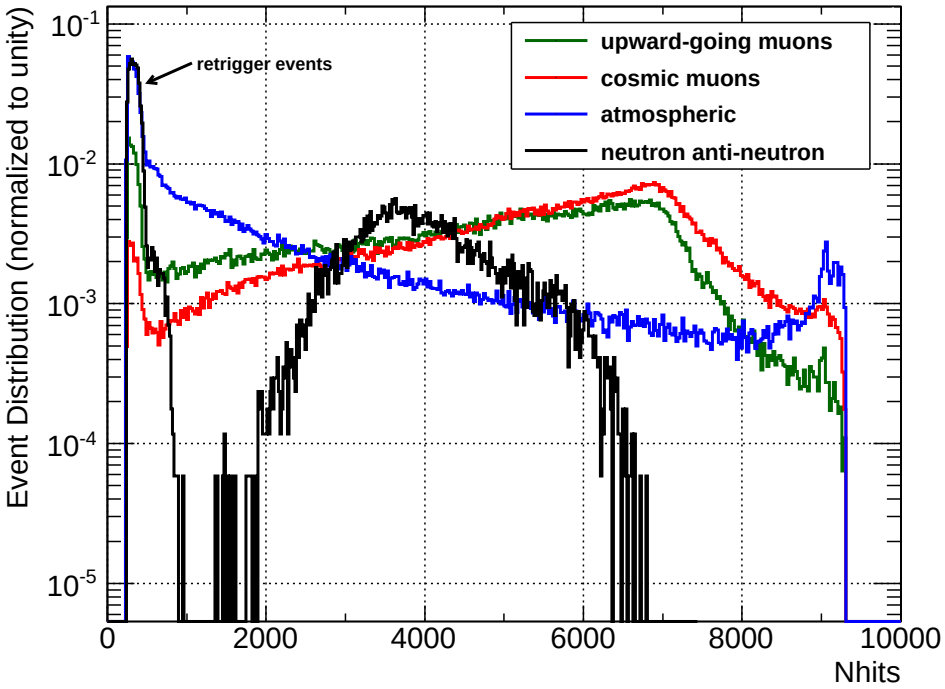

Figure 4.7: Nhits distribution for various classes of events. Retrigger events have not been removed. A window $2000 < \text{Nhits} < 7000$ leads to a signal sacrifice of 0.36%.

A cut window is made in order to isolate the nnbar signal from the majority of backgrounds.

Photoelectrons

Extensive work has been made to calibrate the charge and photoelectron distributions of the PMTs [50]. Photoelectrons are more indicative of the energy of the event then simply using the NHIT distributions since multiple photons can hit the same tube.

Shown in Figure 4.8 are the energy distribution of different Monte Carlo event classes (a cut on the NHIT distribution detailed above is applied). The nnbar signal is contained within the window $2000 < p.e. < 18000$. The lower bound of this window is implemented to further reject instrumental events that would have survived all the cuts.

The upper bound of this window eliminates 25.8% of atmospheric events, 58.0% of upward-going muons and 68.0% of cosmic events with no sacrifice of nnbar events.

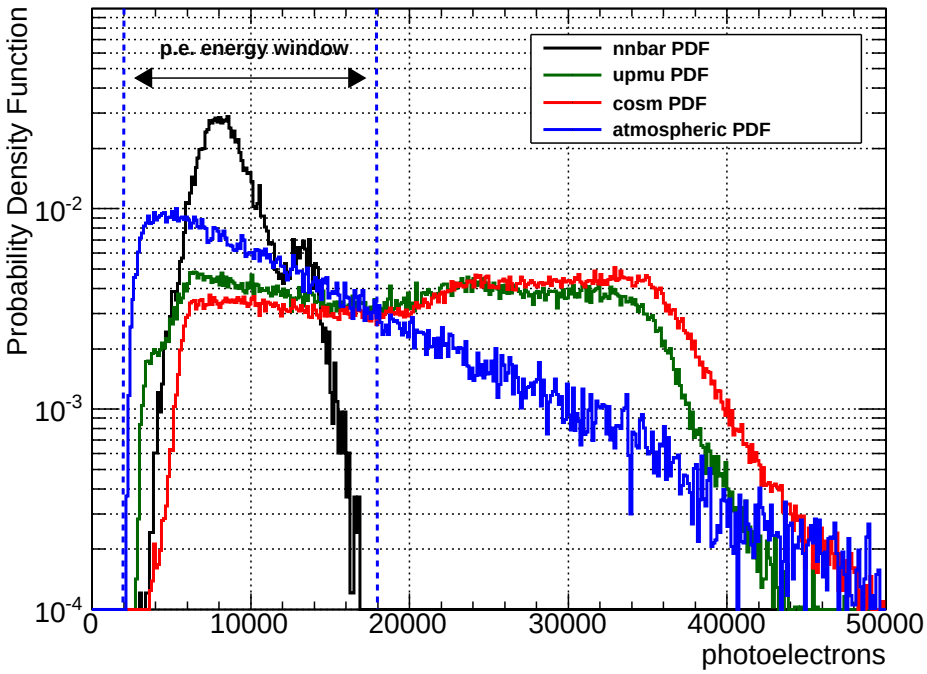

Figure 4.8: Photoelectron distribution for various classes of events. The nnbar signal is fully contained within $2000 < p.e. < 18000$.

4.8.4 Comparison between Data and Monte Carlo

Once all data cleaning cuts have been applied, two data sets are isolated: the contained events data set and the through-going events data set. The external events are a combination of through-going and stopping events.

The final rates of contained and external events are shown in Table 4.3; in the case of data, both low and high level cuts are applied; in the case of Monte Carlo, only the high level cuts are applied. The events are converted to a rate of events by adjusting for the open D_2O phase lifetime of $T_{detector} = 171.92$ days from Table 4.1. As stated previously, the salt and NCD phase will be studied in Chapter 7.

In the case of Monte Carlo, the statistic and the neutrino flux normalization to the

Bartol 3D flux $\phi_0 = 1.22 \pm 0.09$ [8] needs to be accounted for,

$$\begin{aligned} \tau_{data} &= \frac{\text{events}}{T_{detector}} \\ \tau_{MC}^{cosmic} &= \frac{\text{events}}{T_{detector} \cdot \Omega_{stats}} \\ \tau_{MC}^{neutrino} &= \frac{\text{events} \cdot \phi_0}{T_{detector} \cdot \Omega_{stats}} \end{aligned} \tag{4.5}$$

where Ω_{stats} are the increase rate of statistics of the different Monte Carlo class: 1x for the cosmic Monte Carlo, 500x for the upmu Monte Carlo and $66.\bar{6}$x for the atmospheric Monte Carlo[14]. For neutrino detection, the uncertainty on the flux normalization imposes a systematic uncertainty of $\sigma_\tau^{syst} = \tau\sigma_{\phi_0}/\phi_0$ with $\sigma_{\phi_0}/\phi_0 = 7.38\%$.

The rate of contained events seen in data of (0.46 ± 0.05) events/day is consistent with the expected rate from the atmospheric Monte Carlo of $(0.457 \pm 0.007(\text{stat}) \pm 0.034(\text{syst}))$ events/day.

The rate of external events in the data of (15.33 ± 0.30) events/day is also consistent to the total expected external events rate of (15.13±0.29) (which is the combination of cosmic rate of (14.89 ± 0.29) events/day and the upmu rate of $(0.24 \pm 0.02(\text{total}))$ events/day.)

As can be seen in Figures 4.9 and 4.10, the contained and through going events seem to be consistent with their respective Monte Carlo simulation. While some issues are seen in Figure 4.10, these issues will be explored in more details in Section 6.1.

[14]Due to the large amount of information in these high energy events, it was decided that only 1/3 of the events would have PMT information in the case of atmospheric Monte Carlo and 1/20 of events would contain PMT information in the newer cosmic Monte Carlo; the PMT information is required for the Multiple Ring Fitter. A early generation of cosmic Monte Carlo generated at 1x statistics (files ending in p0) is used in this thesis, the atmospheric Monte Carlo is simply corrected for the lower statistics. While only 1/3 of the original atmospheric Monte Carlo is processed with the MRF, the statistical error is lower than the systematic uncertainty on the Bartol flux and is more than adequate for this study.

Cuts	Contained events/Rate per day	External events/Rate per day
D_2O blind data:		
2000 < NHIT < 7000	753/4.38	13972/81.27
Retrigger	432/2.51	10607/61.70
Neck	431/2.51	8780/51.07
Pmt_hit > 500	405/2.36	8144/47.37
Pmt_hit/NHIT > 0.7	380/2.21	7857/45.70
Muon Burst	103/0.60	7686/44.71
Q/NHIT	103/0.60	7685/44.70
2000 < p.e. < 18000	79/0.46	2635/15.33
Cosmic MC:		
2000 < NHIT < 7000	—/—	7947/46.22
2000 < p.e. < 18000	—/—	2560/14.89
Pmt_hit/NHIT > 0.7	—/—	2560/14.89
Upmu MC:		
2000 < NHIT < 7000	—/—	38800/0.5507
2000 < p.e. < 18000	—/—	16752/0.2378
Pmt_hit/NHIT > 0.7	—/—	16752/0.2378
Atmospheric ν_e MC:		
2000 < NHIT < 7000	2440/0.2598	—/—
2000 < p.e. < 18000	2043/0.2175	—/—
Pmt_hit/NHIT > 0.7	2043/0.2175	—/—
Atmospheric ν_μ MC:		
2000 < NHIT < 7000	4164/0.4433	—/—
2000 < p.e. < 18000	3109/0.3310	—/—
Pmt_hit/NHIT > 0.7	3109/0.3310	—/—
Atmospheric ν_μ MC (oscillated):		
2000 < NHIT < 7000	3066.90/0.3265	—/—
2000 < p.e. < 18000	2249.45/0.2394	—/—
Pmt_hit/NHIT > 0.7	2249.45/0.2394	—/—
nnbar MC (acceptance is shown instead of event rate):		
2000 < NHIT < 7000	8265/0.9964	—/—
2000 < p.e. < 18000	8265/0.9964	—/—
Pmt_hit/NHIT > 0.7	8265/0.9964	—/—

Table 4.3: Data and Monte Carlo cut comparison.

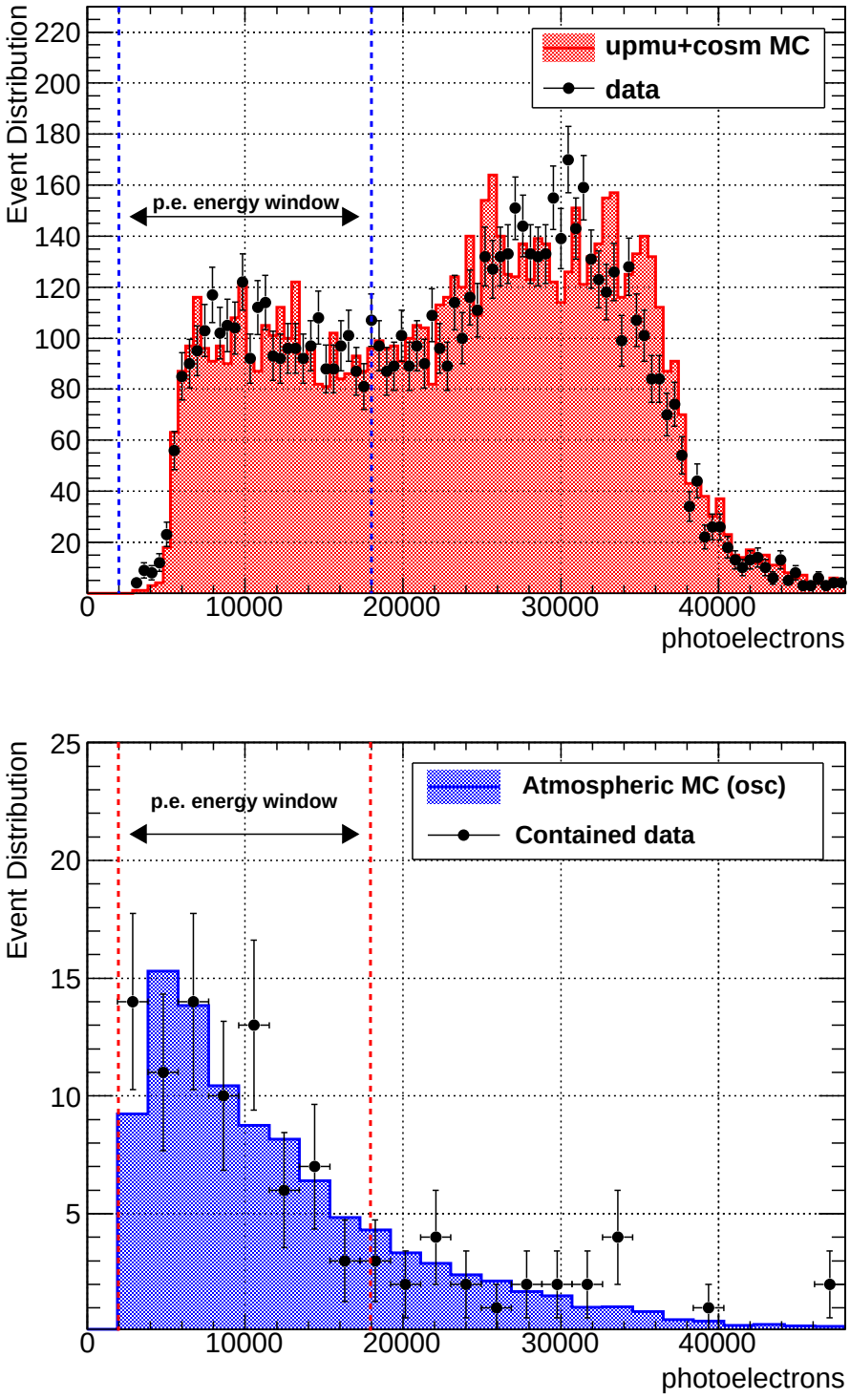

Figure 4.9: Photoelectron distribution of the contained and the external data set.

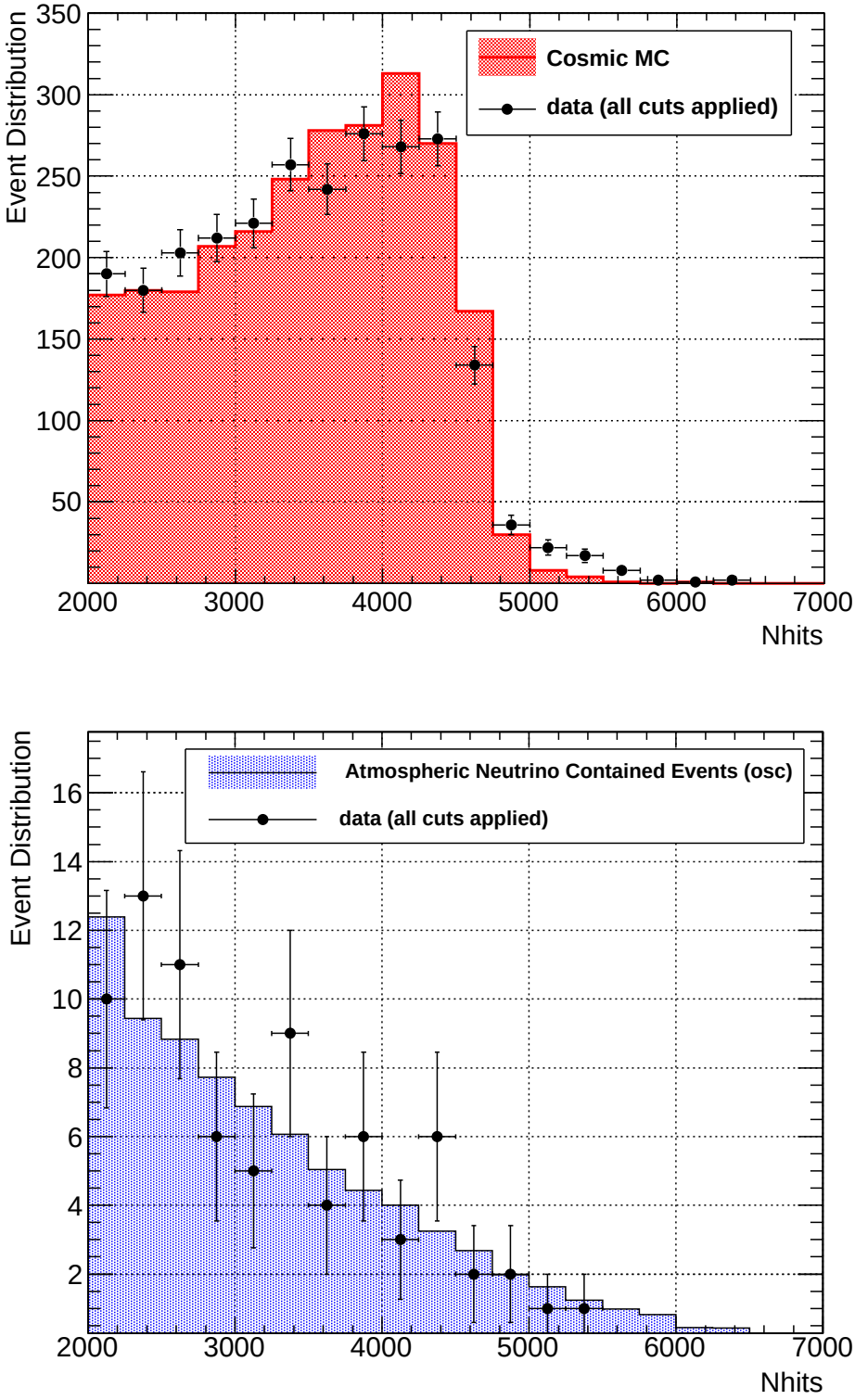

Figure 4.10: Separation of the contained and external data set with all data cleaning cuts applied. The external data set is a combination of through-going and stopping events.

4.9 Summary

In this chapter, the descriptions of the various physical and instrumental backgrounds were given. The low and high cuts used to isolate the signal region from both the physical backgrounds and the instrumental backgrounds in the open D_2O phase were also described. The separation of the physical backgrounds into two data sets was also studied: the contained atmospheric events and the external data sets. The run selection and the detector livetime for all phases were also given.

The search for the nnbar oscillation signal is statistically limited; only so much detector lifetime is available in which to perform the nnbar oscillation signal search. The systematic error of the Bartol flux of atmospheric neutrinos sets irreducible constraints on the characterization of the contained atmospheric neutrino events. Further systematics (including systematic uncertainties on the fitting technique) and a study on the background contamination will be detailed in Chapter 7.

After all cuts have been applied for the open D_2O phase, a rate of $(0.457 \pm 0.034(\text{syst}))$ events/day of contained events is expected throughout the phases and a rate of (15.13 ± 0.29) events/day of external events. A study on the other phases will be presented in Chapter 7.

However, higher level tools are available to further separate the signal from the physical backgrounds within the contained event data set. These tools are the subject of the following chapters. The next chapter focus will be on the ring counting algorithm which further characterize the nnbar oscillation signal.

Chapter 5

Multiple Ring Fitter and Reconstruction Efficiencies

Quand rien ne se passe, tout peut arriver

In this chapter the basic techniques used in the Multiple Ring Fitter (MRF), which was developed as a part of this author's master's work [19], are summarized and studied in more depth. These include the Mid-Point Pair Transform (MPPT), which generates a parameter space of candidate Čerenkov rings for each event, and the Angular Fitter (AF), which confirms the validity of these candidate rings. Furthermore, explanation of the fitter performance of single Monte Carlo simulated particles within the acrylic vessel will be given.

5.1 Circular Hough Transform

While a computer may be able to do very complex numerical calculations, algorithms for recognizing shape and form are much less developed. The breaking down of information into concepts is still handled much more efficiently by the human brain.

In a simple example, if a person is given a picture of a room, this person can classify the constituents of the room in simple categories (or concepts). How many chairs are

there? How many tables? How many windows? For the computer, routines defining these categories need first be programmed by the user. The routines must include all variations of the concepts they describe. For example, the concept of chair must include the four-legged chair, the stool, the computer chair, etc.

Given the proper tools, computers can reliably identify basic shapes such as straight lines or curves, but struggle to identify more complex objects without the use of large amounts of CPU time. The tools available for training of the recognition of simple patterns are effective but are computationally expensive.

Computers are useful in cases where one would like to recognize basic shapes in a large number of events. In the previous example, if a person is given a hundred thousand pictures, the task of shape identification becomes unmanageable for that individual; after a certain number of pictures, the person is more likely to start making mistakes and introduce bias in the extraction of information.

Generalized Hough Transform

The Hough Transform, traditionally used for the detection of straight lines rather than curves, is one of the tools available for pattern recognition [56]. A Circular Hough Transform, the simplest case of the general Hough Transform, can be used to find circle-like patterns in the SNO data, which can then be used to reconstruct the Čerenkov particle vertices. This has been attempted in the past in SNO analyses [57], in the context of low energy NC and CC events, and in [58], in the case of elliptical patterns for high energy events.

The example of the search for a circle of a fixed radius R will help illustrate the fundamental concept behind the Circular Hough Transform. The Circular Hough Transform can locate the origin of a circle of radius R which includes all three point i, j and k (the circle is shown as dashed black circle of Figure 5.1). This is done by forming new circles of radius R centered around each of the points i, j and k and looking for intersections between the new formed circles (new formed circles are shown as the blue, green and brown circles of

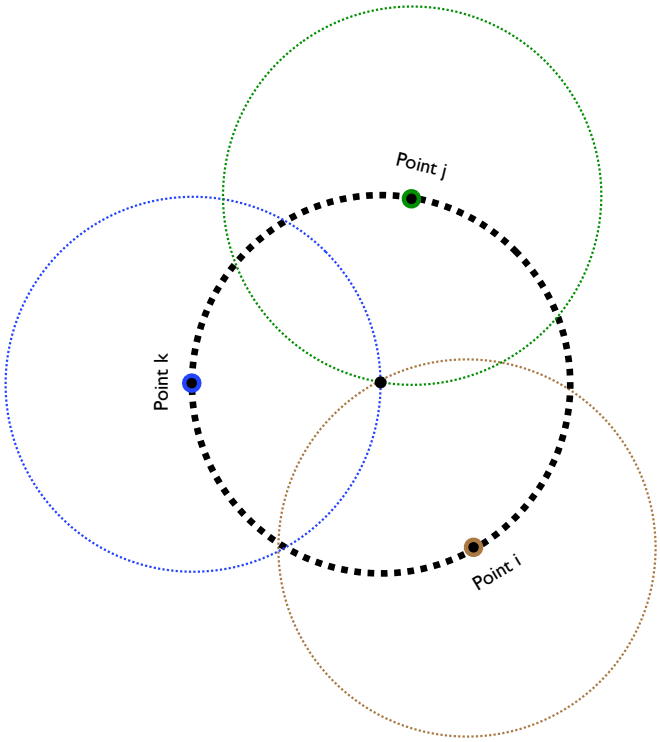

Figure 5.1: Generalized Circular Hough Transform for three points (point i, j and k) which lie on a circle of radius R described by the dashed black circle. The origin of the black dashed circle can be found at the intersection of the blue, green and brown circle if each are drawn with radius R. The point containing the most intersections, in the above case the point with three intersections, is considered the most likely center of a circle of radius R that contains the three points i, j and k.

Figure 5.1). The space into which the new circles are drawn is known as the Hough space.

The techniques relies on the fact that if a point lies on a circle of radius R, than a new formed circle of radius R drawn around that point will intersect the origin of the circle no matter what point of the circle is chosen. This technique is also useful in searching for imperfect structures such as a broken circle due to missing data.

Instead of the term drawing, the term mapping is more accurate and will be used for the rest of the section. The case of mapping from one space to another is well described by what are known as manifold spaces. A plane or the surface of a sphere are examples of two-dimensional manifolds.

For a set of N points in a planar space $\mathfrak{M}$, a circle of radius ρ is mapped around the origin of *each point* into the transform space defined as the Circular Hough Space. In the

case of a fixed search radius ρ, the Hough parameter space is described as a planar space $\mathfrak{M}'$ which is a replica of of the planar space $\mathfrak{M}$. Once all points in the space $\mathfrak{M}$ have been mapped into circles in $\mathfrak{M}'$, intersections are searched for in the Hough space $\mathfrak{M}'$.

The point in $\mathfrak{M}'$ with the highest density (the point that contains the most intersections) is considered the most likely the position of the origin of a circle of radius ρ (Figure 5.1). For the case of a known search radii ρ, the mapping for each point $(x_i,\, y_i)$ into a circle can be expressed as,

$$\mathfrak{M}(x_i, y_i) \mapsto \mathfrak{M}'(\rho\cos\lambda - x_i, \rho\sin\lambda - y_i) : \rho = R, \lambda \in [0, 2\pi] \tag{5.1}$$

where λ is the angle parameter of the circle. In the case of a search radius ρ that is not constant, the transform instead takes the following form,

$$\mathfrak{M}(x_i, y_i) \mapsto \mathfrak{M}''(\rho\cos\lambda - x_i, \rho\sin\lambda - y_i, \rho) : \rho \in [0, \rho_{max}], \lambda \in [0, 2\pi] \tag{5.2}$$

which corresponds to a mapping of a point to a paraboloid centered at $(x_i, y_i,\, 0)$ where $\mathfrak{M}''$ is a Hough Space made by the combination of $\mathfrak{M}'$ and the parameter space ρ [i.e. $\mathfrak{M}'' \equiv (\mathfrak{M}', \rho)$].

In practical applications, a binning for both λ and ρ needs to be established prior to the mappings of equation 5.1 and 5.2. Since for most cases the radius of the circle is not known, the transform requires the mapping to follow 5.2 instead of 5.1.

This need to map $\mathfrak{M} \to \mathfrak{M}'$ over all possible radii, $\rho \in \mathbb{R}^+$, within $\mathfrak{M}''$ leads to longer calculation time for the transform. The choice of binning of the Hough space then becomes paramount. The smaller the width of the search radius (higher precision) the more calculation time. On the other hand, a larger search radius width increases the number of intersections and the pattern detection loses precision.

The drawbacks of the Circular Hough Transform are the long computational time to do the transform for events with large amount of points and the arbitrary definition of binning for the Hough Space which will be defined in this section. This technique is ideal when the

number of points and the noise are low, as for CC and NC events [57]. For higher energy events, where the number of points and the noise is high, such as the nnbar signal window, this technique becomes involved due to the long calculation time.

5.2 Mid-Point Pair Transform (MPPT)

The Mid-Point Pair Transform (MPPT), developed as part of the author's Master work [19], is a modification of the Generalized Hough Transform. It is evaluated by recording over all pair of points both the position of their mid-point and half the distance between them. These two pieces of information are stored within a Hough Space. This transform is built with the assumption that each pair of points already form a circle of radius half the distance separating them. This assumption is not correct for most of the points, however the additional recording of the distance separating the two points makes this transform powerful.

As seen in the previous section, a three dimensional Hough Space can be defined with axes (x, y, ρ), where (x, y) are the "circle center" coordinates and ρ is the radius coordinate. Here a count in the bin (x', y', ρ') is filled for each pair of points, where (x', y') is the center coordinate between two points and ρ' is half the distance separating the same two points. Once filled, this space defines a Circular Hough Space and peaks within this space are considered candidate circles.

If one applies the Mid-Point Pair Transform technique to a perfect continuous circle of radius R, it is possible to show that the transform leads to two solutions: a unphysical solution and the correct solution within the Hough Space $\mathfrak{M}''$.

For this demonstration, the location of the origin of the circle can simply be described by the polar coordinate r where the origin of the circle is located at $r = 0$. The density $\sigma(r)$ of reconstructed mid-points evaluated at r for a reference point (shown in Figure 5.2) and all its neighboring points can be calculated analytically.

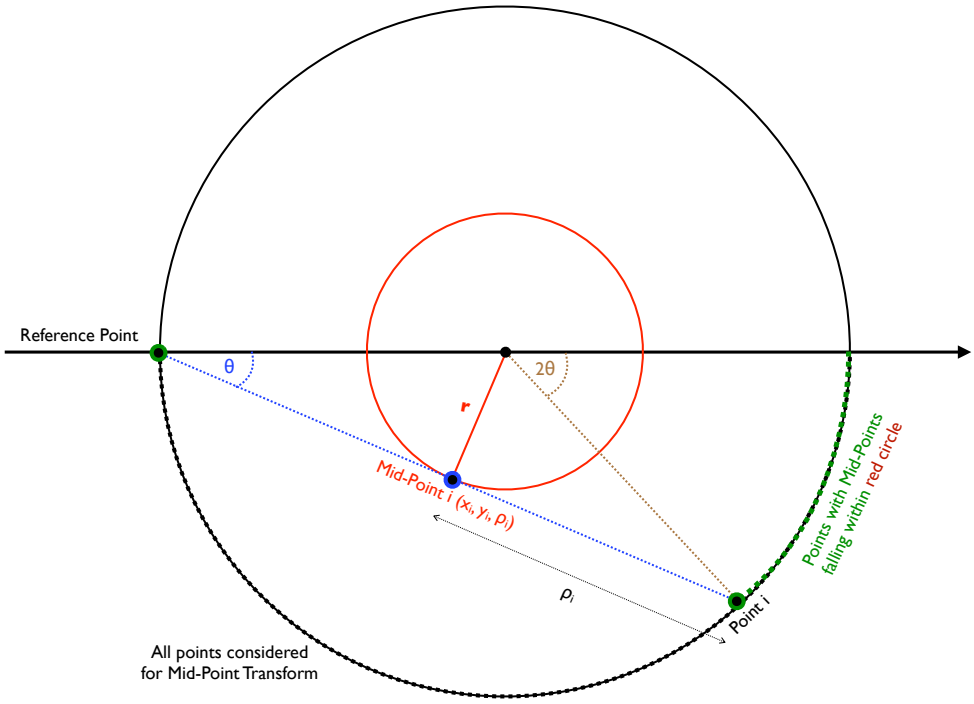

Figure 5.2: Geometrical construct of density of mid-points reconstructed at r. Here R is the radius of the black circle.

To obtain $\sigma(r)$, the Mid-Point Pair Transform is first applied to the point i. The angle between the reference point and point i with respect to the x-axis of Figure 5.2 defines the angle θ. The fraction of the reconstructed middle points that fall within r (within the red circle of Figure 5.2) is simply $2\theta/\pi$. For simplicity, the transform is applied to the semi-circle defined by the lower semi-circle. This can be expressed in the following form,

$$\int_0^r 2\pi r'\sigma(r')dr' = \frac{2\theta}{\pi}. \tag{5.3}$$

Since $\sin\theta = r/R$, we can express as a function of r,

$$\int_0^r 2\pi r'\sigma(r')dr' = \frac{2}{\pi}\sin^{-1}\left(\frac{r}{R}\right). \tag{5.4}$$

By differentiating both sides of the previous equation, the density of reconstructed points is simply,

$$\sigma(r) = \frac{1}{\pi^2 r\sqrt{R^2 - r^2}}. \tag{5.5}$$

If one changes the r variable into ρ by noting that $r = \sqrt{R^2 - \rho^2}$,

$$\sigma = \frac{1}{\pi^2 \rho \sqrt{R^2 - \rho^2}}, \tag{5.6}$$

then the density exhibits the same type of behavior for r and ρ. The equation above can be also rewritten in the following form,

$$\sigma = \frac{1}{\pi^2 \rho r}. \tag{5.7}$$

The conclusion is that the density within $\mathfrak{M}''$ diverges in two cases: at the origin of the continuous circle ($r = 0$, $\rho = R$) and at the circle periphery ($r = R$, $\rho = 0$). The case of ring of null radius is not physical and will not be considered in our situation.

Discussion Points

The formalism above was developed with two assumptions: the circle is continuous and the MPPT applied only to one reference point. By symmetry, any other reference point will also have a divergence at $\rho = R$; the impact of the choice of reference point in Hough Space does not affect the ρ parameter, only the "center" position ($\mathfrak{M}'$) in the Hough Space.

Figure 5.3 shows the example of the filling of the Hough Space from the Mid-Point Pair Transform on three reference points *i, j* and *k*. The green, brown and blue circles of Figure 5.3 shows the Hough Space filled with mid-points for the three chosen reference points. By investigating the transformed mid-point of all considered points, the mid-points of reference point k form a circle centered at $(-R/2, 0)$ of radius $R/2$. This origin of the circle made of mid-points depends on the choice of the reference point, but a simple rotation can be made from any other reference point to the one presented in Figure 5.2.

It is not hard to conclude that the position of the mid-point circle on which the center coordinate of any reference point is located at a distance $R/2$ from the reference point lies in the direction of the origin of the continuous circle. If one maps over all reference points, the center position of these mid-point circles will themselves form a circle of radius $R/2$ as can be seen by the red dashed circle of Figure 5.3.

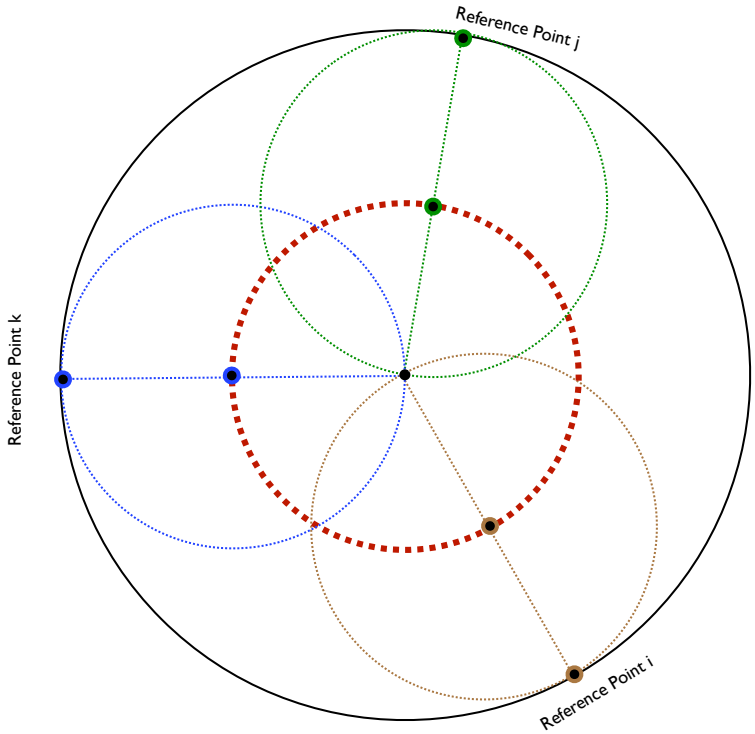

Figure 5.3: Circles of mid-points of the three reference points (i, j, k) in the projected $\mathfrak{M}'$. The red dashed circle represents the center distribution of the circles of mid-points for any reference point.

The proof that the mid-point form a circle located at $R/2$ is straightforward. The mid-point coordinate between a point (x, y) on the circle and the reference point (-R, 0) is simply $((x - R)/2, y/2)$. By defining the mid-point as simply $(a, b) \equiv (x/2, y/2)$, the mid-points $(a - R/2, b)$ are simply the points of a circle of radii $R/2$ centered at -$R/2$ within $\mathfrak{M}'$.

It is important to note that what is shown in Figures 5.2 and 5.3 are the 2-D projections of the 3-D manifold to the 2-D manifold, $\mathfrak{M}'' \rightarrow \mathfrak{M}'$. In the case of the 1-D projection for the search radius the projection is equivalent to $\mathfrak{M}'' \rightarrow \sigma(\rho)$ for all reference points.

If one assumes the mid-point circles drawn from the Mid-Point Transform in Hough Space $\mathfrak{M}'$ (blue, green and brown circles of Figure 5.3) are equivalent to a proper Generalized Hough Transform circles applied to a circle of radius $R/2$, all intersections between mid-point circles (brown, green and blue) are candidate circles.

For the reference point i associated mid-point circle there are two intersections from each other reference mid-point circles: one intersection both at $((\vec{x}_i - \vec{x}_j)/2, \rho_{ij})$ and $((\vec{x}_i -$

$\vec{x}_k)/2, \rho_{ik})$ and 2 intersections at the center of the ring from the mid-point circles j and k ($r = 0$, $\rho = R$).

If we require that for a circle to be considered a candidate at least one intersection must be present, the infinite number of solutions for the three references point reduces to only four solutions. If we require instead that at least two intersections must be present, only the correct solution is available ($r = 0$, $\rho = R$). The number of intersections will be referred as $\zeta_{threshold}$.

The same principle is applied in the practical implementation of this technique. Instead of setting a threshold on the number of intersections, a threshold is set on the minimal number of counts populating a bin within a binned Hough Space.

Relationship between the MPPT and the Hough Transform

From Figures 5.1 and 5.3 the two techniques are equivalent to one another by noticing that the the Mid-Point Pair Transform applied on a continuous circle of radius R is equivalent to applying the Generalized Hough Transform on a circle of radius $R/2$. This is true only in the cases of a large amount of reference points with no noise around the circle.

With enough statistics, the Mid-Point Pair Transform automatically draws circles of the correct radius without input from the user. Instead of a mapping of a point (x_i, y_i) to a paraboloid centered at $(x_i, y_i, 0)$, the mapping of two points to one greatly reduces the complexity of the transform.

However, the MPPT technique breaks down for low statistics. In the case of Figure 5.3, the MPPT applied to only the three reference point would lead to only three candidates (three single intersections) and the correct solution (r=0, $\rho = R$) would not be included.

Practical implementation

In the case of the SNO detector the circles created from fired PMTs are far from being continuous, but the concepts developed are still valid if the number of sampling points is high enough.

For the purpose of this analysis, an event must have at least 250 fired tubes to be

considered for fit. For fewer hit tubes, a proper Hough Transform would be preferable. In the context of this analysis however, no signal events with less than 2000 fired tubes are expected as seen in section 4.8.

In the Hough Space, all transformed mid-points (x_i, y_i, ρ_i) represent possible rings. The Hough space is calculated for each event with binning explained in the next section. The Mid-Point Pair Transform fills the Hough Space with pairs of fired tubes. In order not to double count pairs of tubes, the mapping into the event's Hough space is done by mapping each element of the sum over all possible pairs in the following way,

$$\sum_{i=0}^{N}\sum_{j=i+1}^{N}\left[\text{MPPT}(\vec{x}^{i}_{pmt},\vec{x}^{j}_{pmt})\rightarrow\text{Event's Hough space}(\vec{x}^{ij}_{mid},\rho^{ij}_{mid})\right] \tag{5.8}$$

where N is the total number of fired tubes in the event.

Up until now, only a circle on a plane has been considered. However, the SNO detection geometry is shell-like in nature (following the shape of the PSUP) and the MPPT needs to be correctly parametrized on the shell.

5.2.1 MPPT Parametrization

Like a plane, the surface of a sphere is also a 2-D manifold. The MPPT can therefore be parametrized with a spherical geometry. Instead of applying the transform on a plane, the transform is applied to the space defined by the surface of the sphere $\mathfrak{M}'$. The position coordinate become (θ, ϕ) instead of (x, y) and and the "radius coordinate" ρ is half the distance separating two points on the surface of the sphere (constrained on the space $\mathfrak{M}'$).

The Hough Space is then parametrized by ($\cos\theta$, ϕ, ρ) and peaks in this space are assumed to be candidate circles. These candidates circles ($\cos\theta_c$, ϕ_c, ρ_c) are assumed to be rings created by the projection of Čerenkov particles.

For the purpose of the ring fitter, this light projection is assumed to originate from a cone of light whose vertex direction cosine is aligned from the origin of the detector toward the center of the candidate ring (Figure 5.4). For a vertex ($\vec{x}$, $\vec{u}$), where $\vec{x}$ is the coordinate

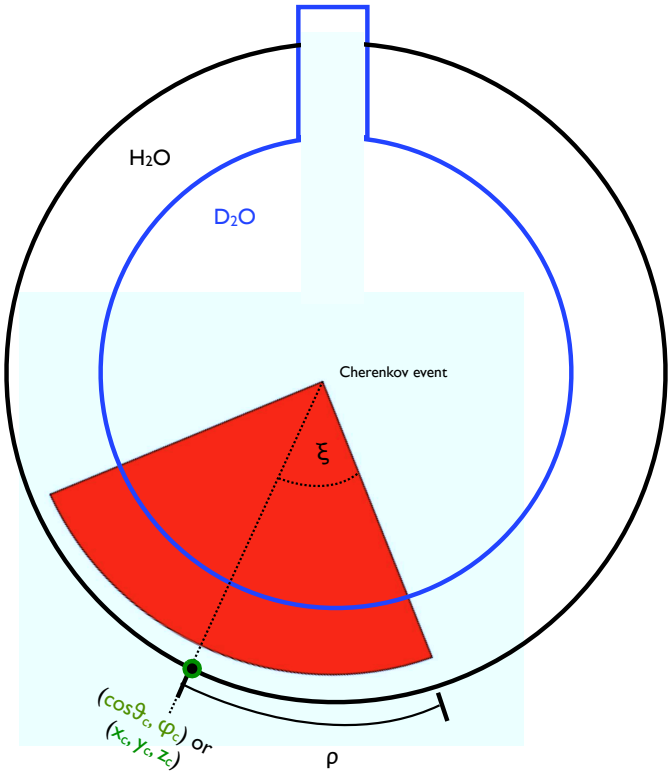

Figure 5.4: Parametrization of Čerenkov Rings with opening angle ξ. The ring center projected on the surface of the PSUP is parametrized by $(\cos\theta_c, \phi_c)$. The radius of the ring (ρ) is defined as the arc length between the parametrized ring center and the tube firing at the edge of the Čerenkov light front. All mid-points pairs of firing tubes are calculated using the arc length separating the two, constrained on the surface of the PSUP.

position of the vertex and $\vec{u}$ is the direction cosine, the previous statement is equivalent to,

$$\frac{\vec{x}_c^{ring}}{R_{PSUP}} = \vec{u} = \pm\frac{\vec{x}}{|\vec{x}|}, \tag{5.9}$$

where $\vec{x}_c^{ring}$ is the "projected point of exit" of the particle; this "projected point of exit" is constrained on the PSUP and is assumed to be at the center of the ring[1]. The position of the vertex in the detector volume can be reconstructed from the center of the ring $\vec{x}_c^{ring}$ and the radius of the ring ρ_c:

$$\vec{x}'_{rec} = \mathrm{R}_{PSUP}\left(\cos(\rho_c/\mathrm{R}_{PSUP}) - \frac{\sin(\rho_c/\mathrm{R}_{PSUP})}{\tan\theta_{\check{c}}}\right)\vec{u} \tag{5.10}$$

with $\theta_{\check{c}} = 41.4^o$ and $R_{PSUP} = 840.7$ cm. The motivation for this type of formalism comes because the fitter does not use timing information of the hit tubes. In high energy events

[1]While this is only an approximation, it will be shown later on that it reconstruct ring adequately

multiple light scattering by the acrylic vessel increase the chance of delay of hit tubes which complicates the use of timing information. A rejection of these tubes is possible but would lead to a lower statistics of hit tubes per event which in turn would make the fitter less efficient.

The lack of timing information leads to a "swirling" effect that will be described in more details in the next section.

The Hough Space binning is chosen in the following way. 132 bins are chosen for the radius ρ which translate into a search radius width of 10 cm on the periphery of the sphere. To ensure that the vertex reconstruct within the acrylic vessel, the search radius is further constrained to (1.7 m $< \rho <$ 11.0 m); this range converted to vertex position with equation 5.10 have values contained in $R < 600$ cm fiducial volume. The spherical coordinate ϕ is divide into 264 bins leading to $\Delta\phi = 1.4^o$ with respect to the origin. The $\cos\theta$ parameter is divided in to 132 bins which translate into $\Delta\cos\theta = 0.015$ with respect to the origin which has been shown to be a good enough separation [19].

The work presented in [19] used a (θ, ϕ) Hough parameter space instead of a ($\cos\theta$, ϕ) one. This creates an issue with the bin spacing within the parameter space which leads to a detection bias for the MPPT. It was more probable to find rings at the middle of the detector compared to the top or bottom ($\theta = \pi/2$). This is solved changing the Hough parameter space to ($\cos\theta$, ϕ) which ensures a uniform spacing for each bin division,

$$\int_0^{2\pi}\int_0^{\pi} \sin\theta d\theta d\phi = \int_0^{2\pi}\int_{-1}^{1} d(\cos\theta)d\phi. \tag{5.11}$$

5.3 Angular Ring Vertex Fitter

The most likely ring vertex for a particular Čerenkov event is identified by the largest peak within the Hough Space ($\mathfrak{M}''$). While a peak in the Hough Space is likely to be the position of a ring, some false positive are present between rings and so further verification of the candidates vertices is necessary. These false positive occur in two scenarios: events with

multiple rings will have a series of midpoints between each rings and for the case of small rings (where ρ is small) since equation 5.7 also diverges at $\rho = 0$.

The Angular Ring Vertex Fitter compares the angular distribution of the PMT hits associated with a candidate vertex, called the "observed" distribution, to an "expected" distribution using a binned maximum likelihood [47].

The distributions are filled with the angles made between the projected exit point of the particle, $\vec{x}_c^{ring}$, and the fired tubes with respect to the vertex position and are recorded in a binned histogram. For the fit, each bin i of the distributions is considered a likelihood estimator ξ_i^{exp} and ξ_i^{obs}. The angular distributions are referred to as ξ_{obs} and ξ_{exp}, it is however implied that the angular distribution are formed of a multitude of estimators ξ_i^{obs} and ξ_i^{exp} such that $\xi_{obs} \equiv [\xi_1^{obs}, \xi_2^{obs}, ..., \xi_n^{obs}]$ and $\xi_{exp} \equiv [\xi_1^{exp}, \xi_2^{exp}, ..., \xi_n^{exp}]$ where n is the number of bins within the histogram. Each bin value ξ_i^{obs} of the distribution is considered Poisson distributed.

The observed angle estimator ξ_{obs} for the candidate is evaluated at the particle vertex position described by equation 5.9 (Figure 5.4). This distribution is compared to a expected estimator ξ_{exp} of electron rings generated using Monte Carlo simulation (see section 5.5.1). Figure 5.5 shows the expected angular distributions for both showering (e-like) and non-showering (μ-like) type of events.

The likelihood of the candidate ring is then calculated with the likelihood ratio method: the ratio of the Poisson probability of the observed bin value, with the expectation bin value as mean, to the Poisson probability of the observed bin value, with the observed bin value as mean,

$$\begin{aligned} \lambda(\xi_{obs}, \xi_{exp}) &= \frac{f(\xi_{obs}; \xi_{exp})}{f(\xi_{obs}; \xi_{obs})} = \frac{(\xi_{exp})^{\xi_{obs}} e^{-\xi_{exp}}}{\xi_{obs}!} \cdot \frac{\xi_{obs}!}{(\xi_{obs})^{\xi_{obs}} e^{-\xi_{obs}}} \\ &= \left(\frac{\xi_{exp}}{\xi_{obs}}\right)^{\xi_{obs}} e^{(\xi_{obs} - \xi_{exp})}. \end{aligned} \tag{5.12}$$

The negative logarithm of likelihood ratio is more useful because of its relationship to the

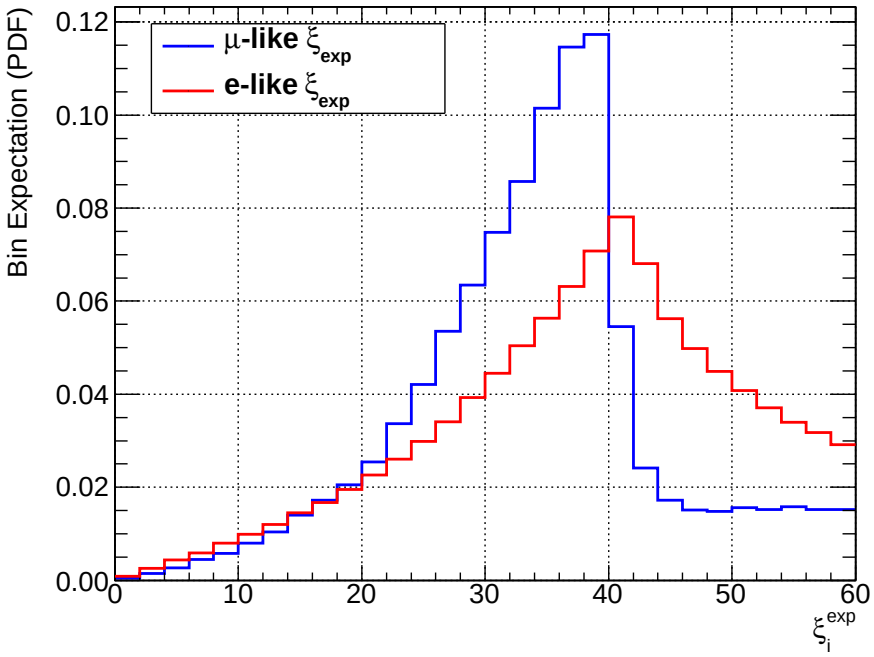

Figure 5.5: e-like and μ-like ξ_{exp} binned angular probability density function. Each bin is considered Poisson distributed. The peak at 40^o shows the edge of the Čerenkov event.

χ^2 distribution [47],

$$\begin{aligned} \chi^2_{likelihood} &= -2\ln\lambda(\xi_{obs},\xi_{exp}) \\ &= \sum_{i=1}^{n}\left[2(\xi_i^{exp}-\xi_i^{obs})+2\xi_i^{obs}\ln(\xi_i^{obs}/\xi_i^{exp})\right] \end{aligned} \tag{5.13}$$

where n is the number of bins within the angular distribution. The term $2\xi_i^{obs}\ln(\xi_i^{obs}/\xi_i^{exp}) = 0$ for $\xi_i^{obs}\to 0$ since $\xi_i^{obs}\ln(\xi_i^{obs}) = 0$ for $\xi_i^{obs}\to 0$; the ξ_i^{exp} value must be nonzero.

The ξ_{exp} angle distribution can be thought of as the combination of two different distributions. A noise distribution, giving the probability that the fired PMT belongs to a "uniform" background noise, and a signal PDF, giving the probability that the fired PMT belongs to the Čerenkov process [19].

Signal Angular Distribution

The Signal Angular Distribution is formed by the primary light-front of the Čerenkov process. The angular distribution this light creates is intrinsically the same for all vertex positions (for events of specific energies). The signal portion of the angular distribution

will have different signature for showering (electron, gammas) compared to non-showering particles (muons). In the case of showering particles the peak will be more diffuse, while in the case of non-showering particles the peak will be sharper.

Noise Angular Distribution

The noise portion includes Čerenkov light scattered by either the acrylic vessel or other scattering effects. If an event contains much scattered light it is considered to be "noisy". If the event is "noisy" the contribution of scattered Čerenkov light will affect the shape of the angular distribution, which varies as a function of the vertex position.

The uniform noise contribution to the angle distribution due to the position of the vertex within the detector will affect the values of the reconstructed $\chi^2_{likelihood}$. Studies have been made in [19] on analytical forms of this impact. Uniform noise is not expected for single showering events, however for events containing multiple particles (showering and non-showering) scattering of light by the acrylic vessel is considered uniform.

For light contained within a cone opening angle of 60^o, the noise contribution averaged over all vertex positions is equal to the noise distribution of a vertex positioned at the center of the detector. The effect on the reconstruction will be described in section 5.5.

Assumptions made by the Angular Ring Vertex Fitter

There are two underlining assumptions to the angular ring vertex fitter. They are:

(1): Ring vertices are reconstructed with only two possible directions for a given vertex position (equation 5.9)

(2): Only one ξ_{exp} estimator is used for all vertices.

For the first assumption, it is clear that for a specific vertex position that the assumption of equation 5.9 that $\vec{u} = \pm\frac{\vec{x}}{|\vec{x}|}$ is false: the direction vertex is not constrained to only two directions, this direction vertex is isotropic. For a ring candidate, the lack of timing information leads to an uncertainty in the reconstruction vertex direction. Assumption (1)

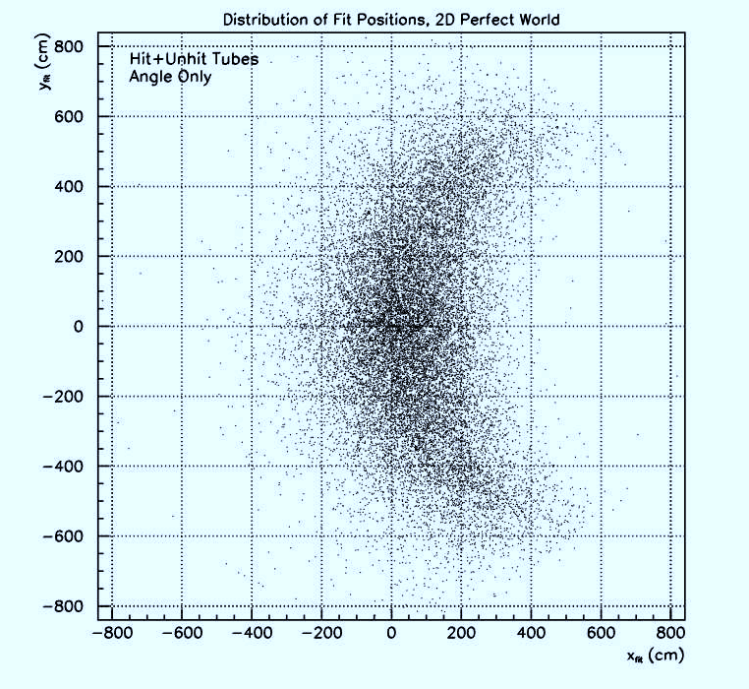

Figure 5.6: Vertex reconstruction of events generated at the origin with only path angle information used for reconstruction. The swirl effect is described in the SNO Path Fitter documentation [59].

is satisfied if one takes the average of all direction vertex. The extreme cases of two different vertex direction leading to the same ring pattern have been studied [19]. Some vertices will transform the ring from a circular shape to a elliptical shape.

It was shown in that the difference between the theoretical expectation of the elliptical shape and the result from the fitter reconstruction of electrons generated uniformly within the acrylic vessel were consistent with one another *as long as the vertex originated from within the acrylic vessel*.

In the limit case, these ellipses can have a semi-short axis up to 18% smaller than the semi-long axis. Because of the angular distribution is one dimensional, the semi-long and semi-short axis will be averaged out in the ξ_{obs} distribution, which will create a bias in detection of finding rings of smaller radii than the actual radii for those type of events which was indeed observed in the fit results.

The scatter plot in Figure 5.6 shows the reconstruction using an alternative vertex fitter called the path fitter on low energy events (5 MeV) that have been generated at the origin

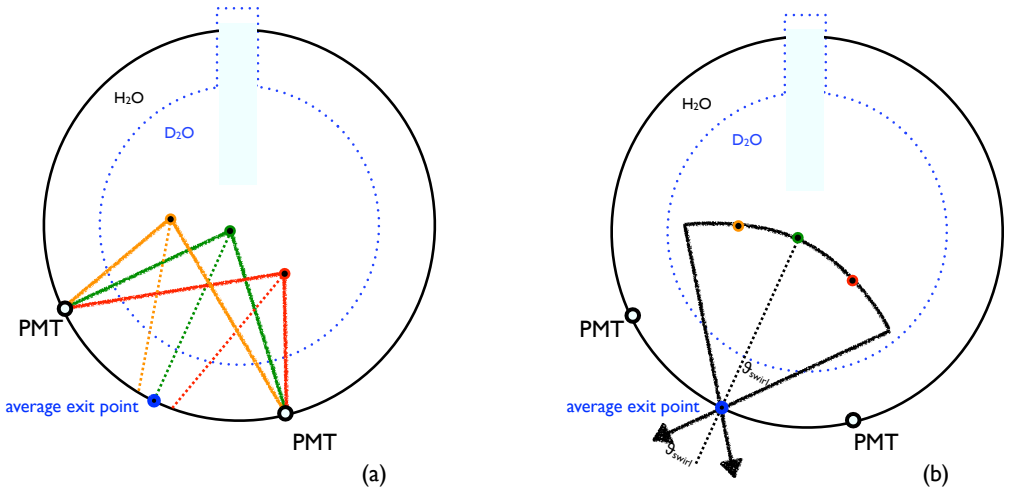

Figure 5.7: Swirl effect diagram. On plot (a) is shown various vertex position that lead to a similar PMT pattern on the PSUP. On plot (b) is shown an estimate of the maximal expected error (θ_{swirl}) on the reconstructed angle due to the uncertainty shown on plot (a).

[59] with direction in the positive x-axis. It was noticed that use of only the angular fitter was not enough to properly characterize events; timing information was also required. If no timing information was given, the fit results would be distributed throughout the detector in a "swirling" distribution[2].

As is seen in Figure 5.7, it is the opposite case that is relevant to this analysis. Instead of events generated at the origin with reconstruction "swirling" within the acrylic vessel, "swirling" events within the acrylic vessel are being reconstructed towards the origin of the detector. While the cases are different, some information can be extracted from this in the form of an upper limit on the contribution of the swirl effect.

If one takes the swirl to be an arc with respect to the (840.7, 0) point, then the maximum swirl allowed is $\tan^{-1}(400/600) = 33.7^o$. This swirling effect upper limit is useful in understanding the behavior of the reconstructed angle distribution detailed in section 5.5.

In the case of assumption (2), the ξ_{exp} distribution will vary with the position of the vertex since the amount of statistics contained within a specific opening angle varies with the position of the vertex. This does not affect the signal part of the ξ_{exp} distribution but

[2]The energies for nnbar signal are much higher than for events relevant to the path fitter which lead to the creation of the Angular Ring Vertex fitter.

it does affect the noise portion as will be seen in Section 5.5.1. Secondly, ξ_{exp} also has a dependence on the energy of the incoming particle, which affects the noise portion of the distribution because of the scattering of light by the acrylic vessel. In the case of energetic multiple ring events, such as nnbar signal events, the noise from other rings will also be added to the ring of interest.

The use of only one ξ_{exp} will be studied in more depths in section 5.5. It will be shown in that a single ξ_{exp} generated from electrons of energy of 400 MeV is the best compromise for ring detection, allowing a flexible reconstruction that allows for variation of both energy and vertex position.

5.4 Multiple Ring Fitter (MRF)

The Multiple Ring Fitter is the combination of algorithms which make up the final form of the fitter. It is a C++ class titled QMRF, written in CERN ROOT architecture as part of the framework QSNO, that can be called with a few simple functions to do the fit.

The combination of the Mid-Point Pair Transform and the Angular Ring Vertex Fitter is the backbone of the MRF, but they are not the only routines required to properly do the fit. Other routines include: routines to output fit information to either ROOT or text file format, routines to evaluated ξ_{obs} from a candidate vertex and routines to separate ring candidate fit results. In this section, the parameters of the MRF, as well as the subdivision of the detector made to detect multiple rings will be explained.

5.4.1 Combination of MPPT and Ring Angular Ring Vertex Fitter

After the MPPT has filled the Hough Space for an event, bins that exceed a certain threshold value $\zeta_{threshold}$ are passed to the Angular Ring Vertex Fitter. The bin positions and radius information are transformed into vertices in the direction of the center of the detector, with angle of the Čerenkov cone assumed to be 41.4^o. The ξ_{obs} distribution of

Parameter	Description	Properties
$(\cos\theta_c^i,\ \phi_c^j,\ \rho^k)$	Binned Hough Space	$(i,k) \in$ [1,132] $j \in$ [1,264]
ξ^i	Angular Estimator	$i \in$ [1,30]
$\chi^2_{likelihood}$	Acceptance Value	$0 \leq \chi^2_{likelihood} \leq 80$
ζ_{min}	Hough Bin Threshold	15
Ω_{max}	Maximal Opening Angle	60^o

Table 5.1: Multiple Ring Fitter Parameters. Values for $\zeta_{threshold}$ and $\chi^2_{likelihood}$ are obtained in section 5.5.

each of these vertices are then compared to the ξ_{exp} distribution and the resulting likelihood ratio $\chi^2_{likelihood}$ along with the parameters of the candidates are stored in an array $(\cos\theta_c, \phi_c, \rho, \chi^2_{likelihood})_i\Big|_{i=0}^{N_{candidate}}$.

5.4.2 Separation of Rings

The search for single ring within an event is made by looking for $(\cos\theta_c, \phi_c, \rho, \chi^2_{likelihood})_i$ with the minimal value of $\chi^2_{likelihood}$ for the event. To find a second ring is a little more tricky since one must find local minima of $\chi^2_{likelihood}$ which is far enough away from the center of the first ring so that the second ring can actually be considered a separate ring. In this section, a separation scheme is chosen in which local minima can be searched for in separated sections of the detector.

The approximation of a sphere from a series of simple surfaces can be described by two platonic solids: the dodecahedron composed of twelve pentagons and the icosahedron, composed of twenty triangles. The most common example of a dodecahedron geometry is the soccer ball. A more relevant example is the PSUP structure of the SNO detector which is built on a icosahedron geometry with each of the twenty surfaces further subdivided into smaller triangles.

The dodecahedron geometry divides the sphere into twelve distinct regions. The Cartesian coordinates of each of the pentagon sections projected on the PSUP are,

$$N(0, \pm 1, \pm\phi), N(\pm 1, \pm\phi, 0), N(\pm\phi, 0, \pm 1) \tag{5.14}$$

where $\phi = (1 + \sqrt{5})/2 \approx 1.618$ is the golden ratio and $N = R_{PSUP}/\sqrt{1 + \phi^2}$.

This projection give a total of 12 dodecahedron coordinates on the surface of the PSUP. These coordinates are rotated such that the most likely ring coordinate, i.e. the coordinate of the candidate with the lowest value of $\chi^2_{likelihood}$, is aligned to the center of the section of the dodecahedron with coordinate $N(0, +1, +\phi)$. This section contains the "best" (or most likely) ring of the event.

The distance between the other ring candidates and each of the dodecahedron coordinates is evaluated and the candidate is assigned to the closest dodecahedron section. All possible ring candidates, from the Hough Space $\mathfrak{M}''$, and the corresponding likelihood ratio from the ring vertex fitter are assigned to *only one* pentagon section by the proximity of the candidate coordinate ($\cos\theta_c$, ϕ_c,R_{PSUP}) to the pentagon center coordinates of equation 5.14.

Once all values are assigned, candidates that are below a negative likelihood threshold within a pentagon section are considered rings. The candidate within the pentagon shape with the lowest value of $\chi^2_{likelihood}$ is considered the ring for that particular section, which consists of the minimization of the negative likelihood ratio within that sub-space. A total of 12 sections leads to 12 possible rings. Furthermore, there is another symmetry to note.

Around the "best" section, section reserved for the most likely ring, five sections are connected. These five possible rings are considered "closest" multiple rings. These rings are sometime spill over of the likelihood space contained within the most likely ring section. Opposite the "best" ring is a section that is defined as the "opposite" ring section. Five sections are connected to this "opposite section" and these are called "farthest" sections.

And so the possible rings in an event can be characterize in the following way,

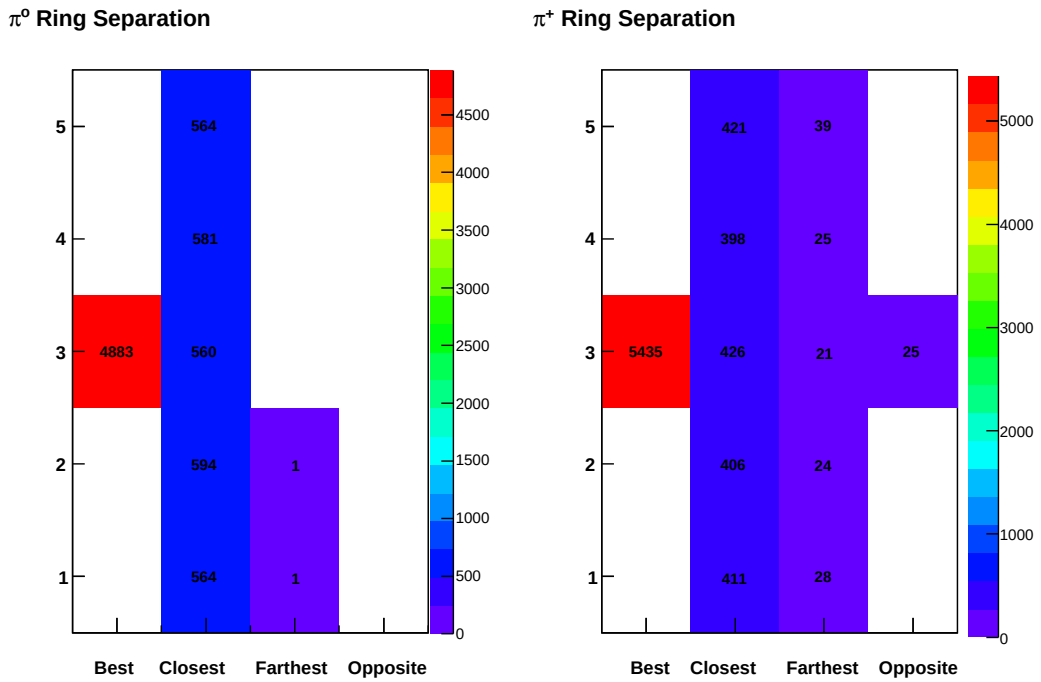

Figure 5.8: Examples of ring separation for charged and neutral Monte Carlo pions. The numbers within the bins represent the number of times a confirmed ring is detected within the section for the entire simulated data sets.

- 1 possible ring in "best" section (also known as Primary ring)
- 5 possible rings in "closest" section
- 5 possible rings in "farthest" section
- 1 possible ring in "opposite" section

shown in Figure 5.8 is an example of this for both charged and neutral Monte Carlo simulated pions (Monte Carlo data sets from section 5.5).

This characterization of rings will be useful in the evaluation of the systematics shifts in the fitter between the detector and the Monte Carlo simulation. The boundaries between the secondary rings are somewhat arbitrary and some boundary events will trigger as two distinct rings. The angle cosine between ring vertices cut that will be described in Section 6.2 takes into account this boundary issue.

5.5 Fitter Reconstruction of Single-Pronged Monte Carlo Events

While a nnbar signal is expected to consist of multiple pronged events, the study of single-pronged events is necessary to understand false multiple ring triggers. The studies presented in this section will cover single-pronged electron, muon and pion Monte Carlo generated events. This section will only cover these Monte Carlo simulated events within the acrylic vessel and will not cover other physical event classes (cosmic, upward going muons, atmospheric) or instrumental noise events which will be covered in the next chapter.

The generating energy for the Monte Carlo muons and pions was chosen by dividing the energy from a nnbar signal between the particles in a typical three-pronged event, i.e. of the order of 600 MeV per particle. By taking into account the extra light generation from electrons, the energy of the Monte Carlo electrons was chosen to be 400 MeV.

The acceptance of the multiple ring fitter across the different types of event depends on the parameters defined in the previous section. The quality of the reconstruction of a Čerenkov single-pronged event is related to the minimized negative log likelihood ratio $\chi^2_{likelihood}$ of equation 5.13. At values of $\chi^2_{likelihood} > 40$, the ring reconstruction may be good for rings in specific conditions while the reconstruction may bad in other conditions. A study of these conditions and the optimization of the $\chi^2_{likelihood}$ leading to good ring reconstruction will be explored in this section. The $\zeta_{threshold}$ parameter, which dictates the minimum number of pair of points in the annulus for the ring to be considered a candidate, also has an impact on the sensitivity of the ring fitter. The study of this sensitivity will be the focus of this chapter.

Two parameters are needed to understand the quality of ring reconstructions. The first parameter represents the position of the Čerenkov event within the acrylic vessel defined in equation 5.10. The second parameter is the angle between the fitted vertex direction and the actual Monte Carlo vertex direction.

A change of parameter is made from the spherical to the Cartesian coordinate (R_{PSUP}, $\cos\theta_c$, ϕ_c, ρ_c)→(x_c, y_c, z_c, ρ_c) with the constraint $x_c^2 + y_c^2 + z_c^2 = R_{PSUP}^2$. The ring candidate is mapped into a vertex with the constraint of equation 5.13. It is simpler to define the vertex along only one axis, following equation 5.9 and 5.10, such that reconstructed position $x'_{rec} = x'_{rec}(\rho)$,

$$x'_{rec} \equiv \mathrm{R}_{PSUP}\left(\cos(\rho/\mathrm{R}_{PSUP}) - \frac{\sin(\rho/\mathrm{R}_{PSUP})}{\tan\theta_c}\right) \tag{5.15}$$

is evaluated with respect to

$$\hat{u}'_{rec} \equiv (\hat{x}_c, \hat{y}_c, \hat{z}_c) \tag{5.16}$$

which is the direction axis that points to the center of the candidate ring. For smaller rings, the x'_{rec} value will be positive and for larger rings it will be negative along the u'_{rec} axis. This parameter follows the constraint imposed by equation 5.9 between the vertex position and direction.

The second parameter is the angle between $\hat{u}'_{rec}$ and the generating direction vertex of the Monte Carlo simulation $\hat{u}_{MC} \equiv (\hat{u}, \hat{v}, \hat{w})$. This reconstruction angle θ_{rec} is then,

$$\theta_{rec} \equiv \cos^{-1}(\hat{u}'_{rec} \cdot \hat{u}_{MC}). \tag{5.17}$$

Two types of events are studied: rings that come from an isotropic source at the origin of the detector and those from swirled directions (events generated uniformly and isotropically within the acrylic vessel that should not reconstruct toward the center of the detector).

An overall idea on the quality of reconstruction of the second type of events can be obtained if θ_{rec} is bounded by a swirling limit (an example is shown in Figure 5.14). As was seen in the previous section, the swirling effect can have an impact of up to 33.7^o on θ_{rec}.

In order to estimate the quality of the reconstructed rings, the mean and the RMS of the x'_{rec} and the θ_{rec} distributions are used and no fits are made. Since the distributions of these parameters may be formed from multiple underlying distributions, the RMS is used as a measure of the broadness of the distributions. In order to account for up to 11 secondary possible rings, the mean and RMS of the ring multiplicity distributions are also included.

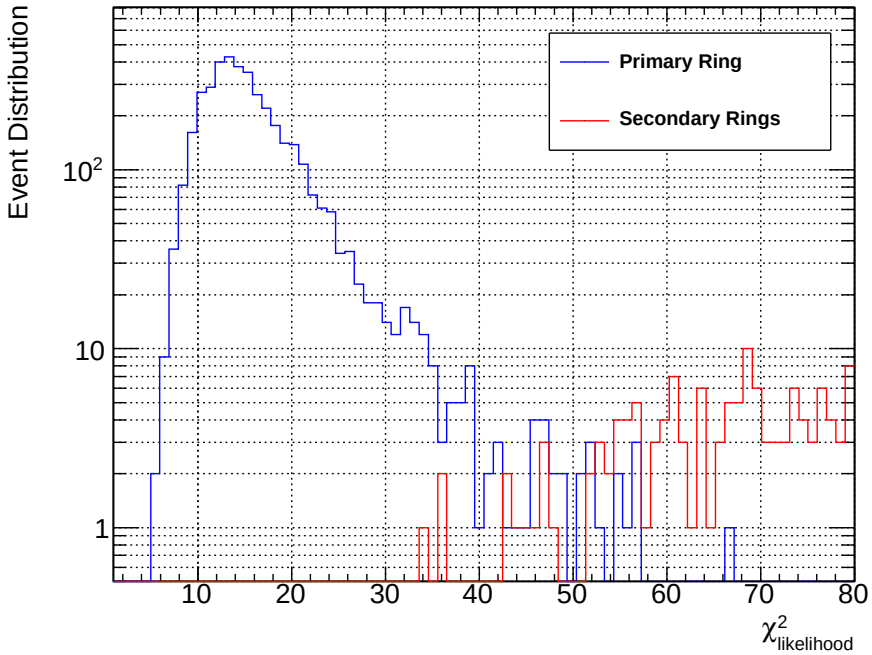

Figure 5.9: Multiple Ring Fitter $\chi^2_{likelihood}$ reconstruction of single electron events. The simulated Monte Carlo events were generated at the origin of the detector.

5.5.1 Electron Reconstruction

Electrons and positrons are two of the high energy particles expected from contained neutrino interactions[3]. The neutral pion is directly tied to the electron signature because of the decay channel $\pi^0 \rightarrow \gamma\gamma$ leading to e-like signatures[4]. Furthermore, the charged pion light signature is also tied to electron signature; in part because of the Single Charge Exchange (SCX) nuclear interaction that transforms a charged pion into a neutral one (as described in Chapter 3).

Five different Monte Carlo data sets were generated to study the properties of the multiple ring fitter on the reconstruction of electrons generated within the acrylic vessel.

The first simulated data set consists of events with kinetic energy of 400 MeV generated isotropically at the origin of the detector. The second and third simulated data sets consist of the same type of electron events but generated at (400,0,0) cm and (-400,0,0) cm, and

[3] see section 4.4

[4] γ's and electrons both have e-like signature

directed in the positive X-axis direction. The fourth data set consists of electrons of the same type of energy generated uniformly within the acrylic vessel. The final data set consists of electrons sampled from a Gaussian of mean 500 MeV and width 300 MeV generated at the center of the detector. The MRF results are shown in Table 5.2.

In order to obtain the expected estimator, the first data set, which contains events generated at the origin, was used for the e-like distribution ξ_{exp} (shown in Figure 5.5).

The final form of the ξ_{exp} distribution consist of the average of the ξ_{obs} from each events; the angular distribution is evaluated from the light pattern for each event using the Monte Carlo vertices of the first data set which has isotropic direction. ξ_{exp} is then used to fit events from the first data set using the negative log likelihood ratio from equation 5.13, the results are shown in Figure 5.9 and Table 5.2.

Once the ξ_{exp} has been validated on the first data set, the other data sets are used to verify the properties of ξ_{exp} in different conditions of electron energies and positions.

Energy

Figure 5.10 shows the reconstruction $\chi^2_{likelihood}$ as a function the electron Monte Carlo energy for data set 5 with $\zeta_{threshold} = 15$. The variation within the likelihood space as a function of the energy is due to the assumptions made in section 5.3. The MRF results of data set 5 for the primary ring reconstruction are consistent with the mono-energetic case of data set 1 (Table 5.2).

The distribution of events as a function of kinetic energy is not symmetric as it should be for a Gaussian distribution, this results since the fitter does not reconstruct well events with low PMT statistics. As is seen in Figure 5.10 no events below $\sim$ 140 MeV of energy are reconstructed for candidates with $\chi^2_{likelihood} < 80$.

For events containing multiple particles, spill-over noise from neighboring events will increase the possibility of finding rings with less than 140 MeV of energies.

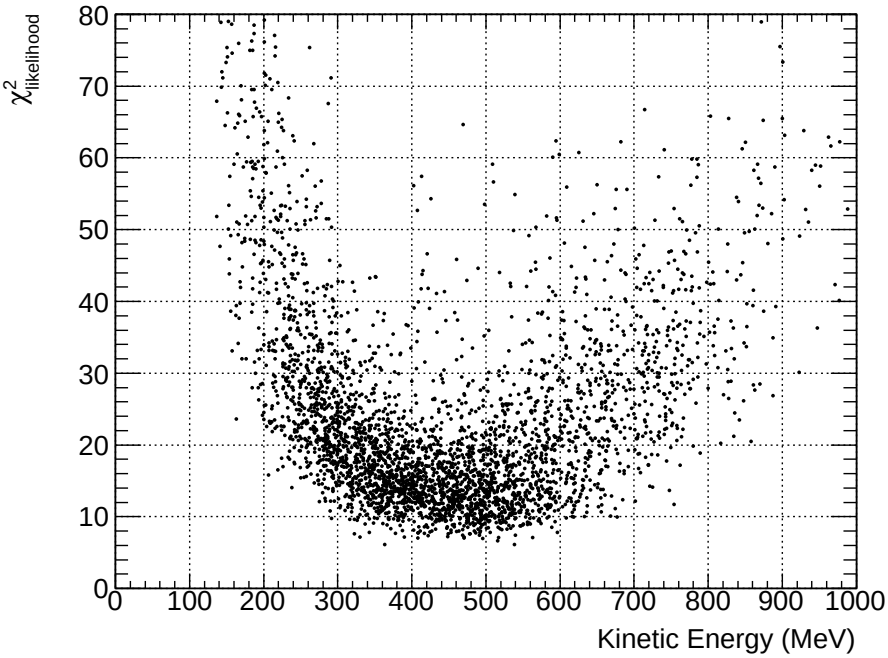

Figure 5.10: Primary ring reconstruction $\chi^2_{likelihood}$ as a function of event Monte Carlo kinetic energy of single electron events for $\zeta_{threshold}$=15. The simulated Monte Carlo events were generated at the origin of the detector.

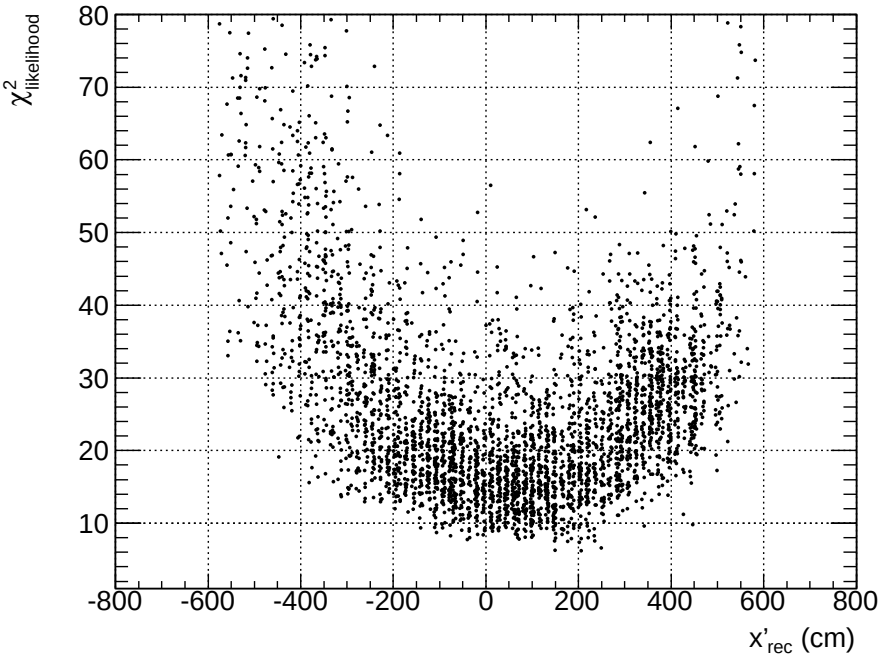

Figure 5.11: Primary ring reconstruction and $\chi^2_{likelihood}$ scatter plot with $\zeta_{threshold}$=15 for events generated isotropically within the detector volume with isotropic directions.

Swirl Effect

Figure 5.11 shows the correlation between the position of the reconstructed vertex and the reconstructed likelihood $\chi^2_{likelihood}$. Figure 5.14 shows the reconstruction of primary and secondary rings for isotropic events for a $\zeta_{threshold} = 15$. In the case of the primary rings, events with $\chi^2_{likelihood} < 80$ reconstruct below the swirling effect upper limit. In the case of the secondary one, the rings reconstruct toward the edge of the acrylic vessel at an average angle of 58.4^o (39^o away from primary ring θ_{rec}).

Choice of ζ Threshold

For low values of $\zeta_{threshold}$ the fitter contains an alarming rate of multiple rings. The likelihood space for rings that have been separated into primary and secondary rings are shown in Figure 5.9. Figure 5.12 shows the reconstruction distribution of both the vertex of the ring and the angle distribution between the rings fitted vertex and the Monte Carlo generated vertex.

In order to minimize false multiple ring identification within the reconstruction $\chi^2_{likelihood}$ space, a value of $\zeta_{threshold} = 15$ was chosen based on the results of Table 5.2. There is still contamination from the edge of the ring, especially for events with high energies from the fifth data set, but these will be treated with the analysis parameter cuts described in the next chapter.

Primary Ring Reconstruction

As can be seen in Table 5.2, a bias toward smaller rings ($x'_{rec} > 0$) is seen in both the first and forth data sets for the primary rings; this is due to the MPPT transform is sensitive to small ring (since equation 5.7 also diverges at $\rho = 0$) and the low statistics of PMTs for a cone opening angle of 60^o lead to smaller $\chi^2_{likelihood}$ values.

Due to the diffuse nature of the electron light signature, a certain spread on the reconstruction is also expected. A visual scan of the fit vertices using the software XSnoed also shows the reconstruction of the primary ring to be more than adequate with no obvious flaws (Figure G.6), however false ring identification is present for a small secondary ring. A

cut will be devised in the next chapter to remove these events.

The primary focus of the analysis is the optimization of ring detection. The precision of the reconstructed position is not as important due to the nuclear scattering properties of the charged pion which makes its tracking nearly impossible[5].

The case of rings originating from events generated at the center of the detector is not the most probable kind of events. Random events originating within the acrylic vessel are more likely to appear at the edge of the detector than at the center due to the greater volume at higher radius.

The advantages of the use of a single ξ_{exp} distribution for these types of events can be seen in Figures 5.10 and 5.11 where both variation in energy or position uncertainties can be taken into account within the $\chi^2_{likelihood}$ parameter.

Figure 5.14 shows the reconstruction of events that have been generated uniformly within the acrylic vessel volume. The estimated value of the impact on the swirl effect is shown by the blue dashed line. The behavior of θ_{rec} is similar to the behavior of Figure 5.12; however since for real events θ_{rec} is not known, the distinction between values of $\chi^2_{likelihood}$ that lead to good reconstruction and those that do not is blurred within the reconstruction space as seen in the bottom plot of Figure 5.14.

The presence of small secondary rings in single electron events points at a weakness of the Multiple Ring Fitter. The understanding of the behavior of these false rings within the $\chi^2_{likelihood}$ space is important.

[5] as seen in chapter 3

$\zeta_{threshold}$	$\epsilon_{primary}$	(x'_{rec}, x'_{rms}) (cm)	$(\theta_{rec}, \theta_{rms})$ (degree)	$\epsilon_{secondary}$	(x'_{rec}, x_{rms}) (cm)	$(\theta_{rec}, \theta_{rms})$ (degree)	Multiplicity
[(0,0,0),(isotropic)] data set 1, 3907 Entries [Energy=400 MeV]							
9	1.0000	(82.6,159.0)	(48.6,47.8)	0.9493	(342.7,192.0)	(31.8,17.1)	(5.57,1.24)
10	1.0000	(15.8,83.3)	(9.7,21.4)	0.9854	(432.1,95.4)	(36.2, 7.9)	(4.44,1.17)
11	1.0000	(4.1,43.9)	(4.8, 3.8)	0.9130	(436.9,73.2)	(36.1, 5.8)	(3.14,1.19)
12	1.0000	(4.0,40.5)	(4.7, 3.3)	0.6412	(434.6,76.6)	(35.4, 5.7)	(2.01,0.95)
13	1.0000	(4.4,39.3)	(4.6, 3.2)	0.3171	(428.7,81.3)	(34.8, 5.6)	(1.39,0.63)
14	1.0000	(4.8,37.7)	(4.5, 3.1)	0.1083	(426.4,86.3)	(34.3, 5.7)	(1.12,0.35)
15	0.9995	(5.6,38.9)	(4.4, 3.2)	0.0328	(406.5,109.2)	(32.6, 7.7)	(1.03,0.19)
16	0.9992	(6.2,37.5)	(4.2, 3.1)	0.0107	(399.6,122.8)	(32.6, 7.6)	(1.01,0.10)
17	0.9985	(7.2,37.5)	(4.1, 3.1)	0.0028	(358.2,180.0)	(25.3, 9.5)	(1.00,0.05)
[(400,0,0),(1,0,0)] data set 2, 3851 Entries [Energy=400 MeV]							
9	1.0000	(387.5,35.2)	(9.9,23.7)	0.2059	(425.0,96.6)	(25.3,18.4)	(1.74,1.03)
10	1.0000	(382.9,26.8)	(3.8, 2.4)	0.0631	(427.2,99.1)	(29.7, 7.6)	(1.28,0.55)
11	0.9997	(383.0,26.9)	(3.7, 2.4)	0.0267	(441.9,108.2)	(26.9, 9.8)	(1.14,0.40)
12	0.9997	(383.4,26.7)	(3.7, 2.2)	0.0099	(432.3,112.7)	(24.9,11.4)	(1.07,0.28)
13	0.9997	(384.4,26.9)	(3.6, 2.0)	0.0057	(437.1,106.3)	(23.3,12.7)	(1.04,0.20)
14	0.9995	(385.8,27.1)	(3.6, 1.8)	0.0026	(369.4,141.9)	(29.5,15.4)	(1.02,0.14)
15	0.9995	(387.8,27.6)	(3.5, 1.8)	0.0013	(299.6,150.9)	(30.8,19.6)	(1.01,0.09)
16	0.9984	(389.7,27.6)	(3.6, 1.9)	0.0005	(433.4, 7.1)	(10.5, 5.9)	(1.00,0.07)
17	0.9964	(392.0,27.2)	(3.7, 1.8)	0.0000	(0.0, 0.0)	(0.0, 0.0)	(1.00,0.04)
[(-400,0,0),(1,0,0)] data set 3, 3847 Entries [Energy=400 MeV]							
9	1.0000	(-395.0,132.6)	(9.8, 8.7)	0.9995	(257.4,165.1)	(52.8,16.6)	(5.95,0.98)
10	1.0000	(-402.6,101.3)	(9.1, 7.4)	0.9667	(254.4,169.1)	(50.2,14.4)	(3.98,1.33)
11	0.9997	(-405.5,74.1)	(8.2, 6.1)	0.6720	(249.8,185.5)	(49.4,13.9)	(2.14,1.05)
12	0.9984	(-404.6,55.9)	(7.4, 6.0)	0.2540	(233.1,212.8)	(48.5,14.6)	(1.33,0.59)
13	0.9966	(-402.0,48.4)	(6.5, 5.6)	0.0699	(195.1,237.2)	(46.0,15.6)	(1.08,0.29)
14	0.9930	(-400.5,36.3)	(5.4, 4.8)	0.0135	(119.1,284.2)	(43.9,18.6)	(1.02,0.14)
15	0.9818	(-398.3,35.9)	(4.5, 5.0)	0.0031	(-19.8,308.9)	(41.2,29.1)	(1.01,0.09)
16	0.9498	(-396.8,32.5)	(3.6, 4.3)	0.0005	(-183.1,176.2)	(50.5,46.8)	(1.00,0.05)
17	0.8960	(-395.0,31.5)	(3.0, 2.9)	0.0003	(56.6, 0.0)	(115.0, 0.0)	(1.00,0.05)
[(uniform),(isotropic)] data set 4, 3670 Entries [Energy=400 MeV]							
9	0.9975	(69.1,304.0)	(37.8,35.2)	0.8106	(344.9,169.6)	(46.6,22.8)	(4.23,1.84)
10	0.9973	(36.7,281.9)	(21.7,15.3)	0.7602	(395.2,140.6)	(51.2,19.1)	(3.07,1.49)
11	0.9967	(33.2,277.4)	(19.8, 9.4)	0.6643	(409.9,132.4)	(54.1,17.0)	(2.31,1.15)
12	0.9959	(31.5,276.2)	(19.6, 8.7)	0.5060	(417.7,127.5)	(56.3,15.7)	(1.77,0.87)
13	0.9946	(32.6,274.4)	(19.5, 8.4)	0.3131	(419.1,126.4)	(57.8,14.1)	(1.40,0.64)
14	0.9880	(35.3,271.6)	(19.4, 8.5)	0.1580	(419.9,128.7)	(58.5,13.4)	(1.19,0.45)
15	0.9695	(43.3,266.2)	(19.5, 8.8)	0.0654	(418.5,133.9)	(58.4,12.6)	(1.08,0.28)
16	0.9316	(50.9,256.4)	(19.6, 8.6)	0.0259	(403.8,159.7)	(58.4,12.9)	(1.03,0.18)
17	0.8749	(60.4,244.6)	(19.6, 8.7)	0.0112	(333.9,192.4)	(55.2,15.5)	(1.01,0.13)
[(0,0,0),(isotropic)] data set 5, 3853 Entries [Energy=(500±300)MeV]							
9	0.9696	(70.9,164.1)	(45.6,46.1)	0.7726	(326.8,207.5)	(32.6,19.9)	(4.92,2.55)
10	0.9613	(53.5,148.9)	(30.6,42.2)	0.7296	(373.7,187.7)	(33.4,16.4)	(4.07,2.23)
11	0.9533	(30.1,117.7)	(13.8,27.9)	0.6626	(431.4,138.7)	(35.8,11.1)	(3.40,2.03)
12	0.9439	(14.6,83.7)	(6.1,10.4)	0.5564	(461.9,94.3)	(37.1, 6.9)	(2.73,1.82)
13	0.9364	(10.6,69.6)	(5.0, 5.1)	0.4345	(464.7,86.5)	(37.0, 6.2)	(2.11,1.49)
14	0.9214	(9.4,61.8)	(4.7, 4.5)	0.2954	(457.5,92.9)	(36.8, 6.4)	(1.61,1.06)
15	0.9058	(8.4,52.9)	(4.4, 4.1)	0.1830	(448.2,97.8)	(36.3, 6.5)	(1.30,0.68)
16	0.8853	(7.8,46.5)	(4.2, 3.8)	0.0973	(442.0,106.5)	(35.5, 7.1)	(1.14,0.43)
17	0.8586	(8.1,43.3)	(4.0, 3.4)	0.0444	(430.8,120.9)	(34.8, 8.4)	(1.06,0.27)

Table 5.2: e^- vertex and multiplicity reconstruction for primary and secondary MRF ring triggers. The five Monte Carlo data sets are fitted with e-like ξ_{exp}.

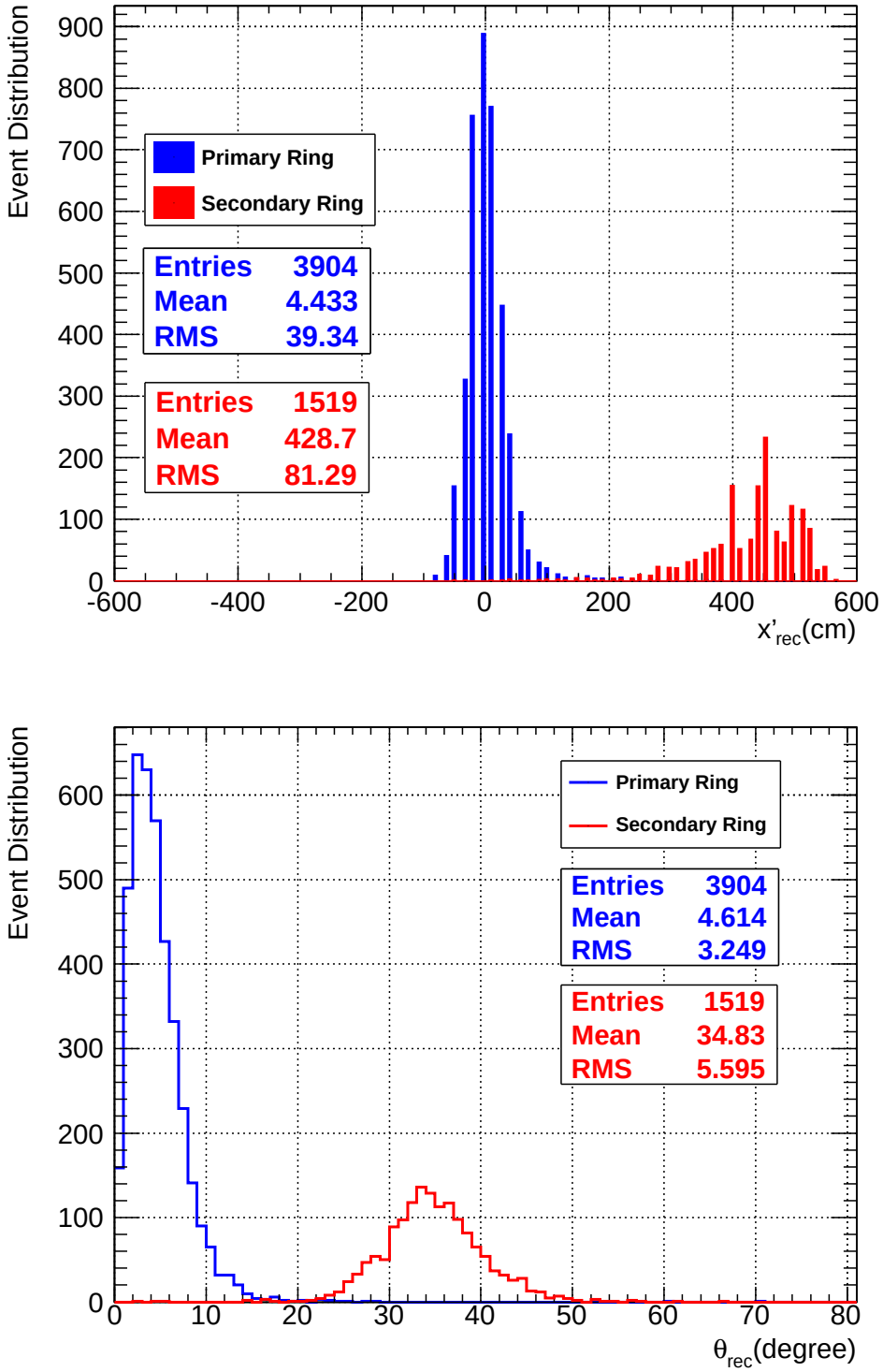

Figure 5.12: Multiple Ring Fitter x'_{rec} and θ_{rec} e^-reconstruction. The simulated Monte Carlo events generated at the origin of the detector with $\zeta_{threshold} = 13$ chosen for the ξ_{exp}.

Multiple Rings in Single Electron Monte Carlo Pathology

The pathology of false multiple rings can be seen in Figures 5.12, 5.13 and 5.14. Figure 5.12 shows the event distribution for the x'_{rec} and θ_{rec} parameters. Figures 5.13 and 5.14 show the correlation between the reconstructed position x'_{rec}, the reconstructed angle θ_{rec} - angle made between the reconstructed vertex and the Monte Carlo vertex - and $\chi^2_{likelihood}$; this is done for two cases where the electrons are generated at the center of the detector and where they are generated uniformly within the acrylic vessel volume.

The existence of the false multiple ring is a byproduct of the simplification described in section 5.3 in which only one ξ_{exp} estimator is used for all energies and for all vertex positions.

By keeping in mind that all rings are reconstructed with $\theta_{\check{c}} = 41.4^o$ by construct, small rings that are close to the acrylic vessel boundary, as is shown in Figure 5.13, with (4 m$< x'_{rec} <$ 6 m) and angle reconstruction values $\theta_{rec} \approx 35^o$, are located at that the edge of the primary Čerenkov ring. This can also be confirmed by the XSnoed reconstruction shown in Figure G.6.

In the case of events that are generated within the acrylic vessel, the minimization of these "edge of the ring" triggers can be achieved by setting a higher threshold for the ring candidate density $\zeta_{threshold}$ within the Hough space.

However, for more energetic events than the ones presented in Table 5.2, this "edge of the ring" pathology will have a more significant contribution to multiple false triggers. Energetic events that originate from outside the detector form a good sample for the study of this "edge of the ring" pathology and will be studied in the next chapter.

It will be shown that a cut on the reconstructed vertex position x'_{rec} is needed to eliminate these "edge of the ring" events.

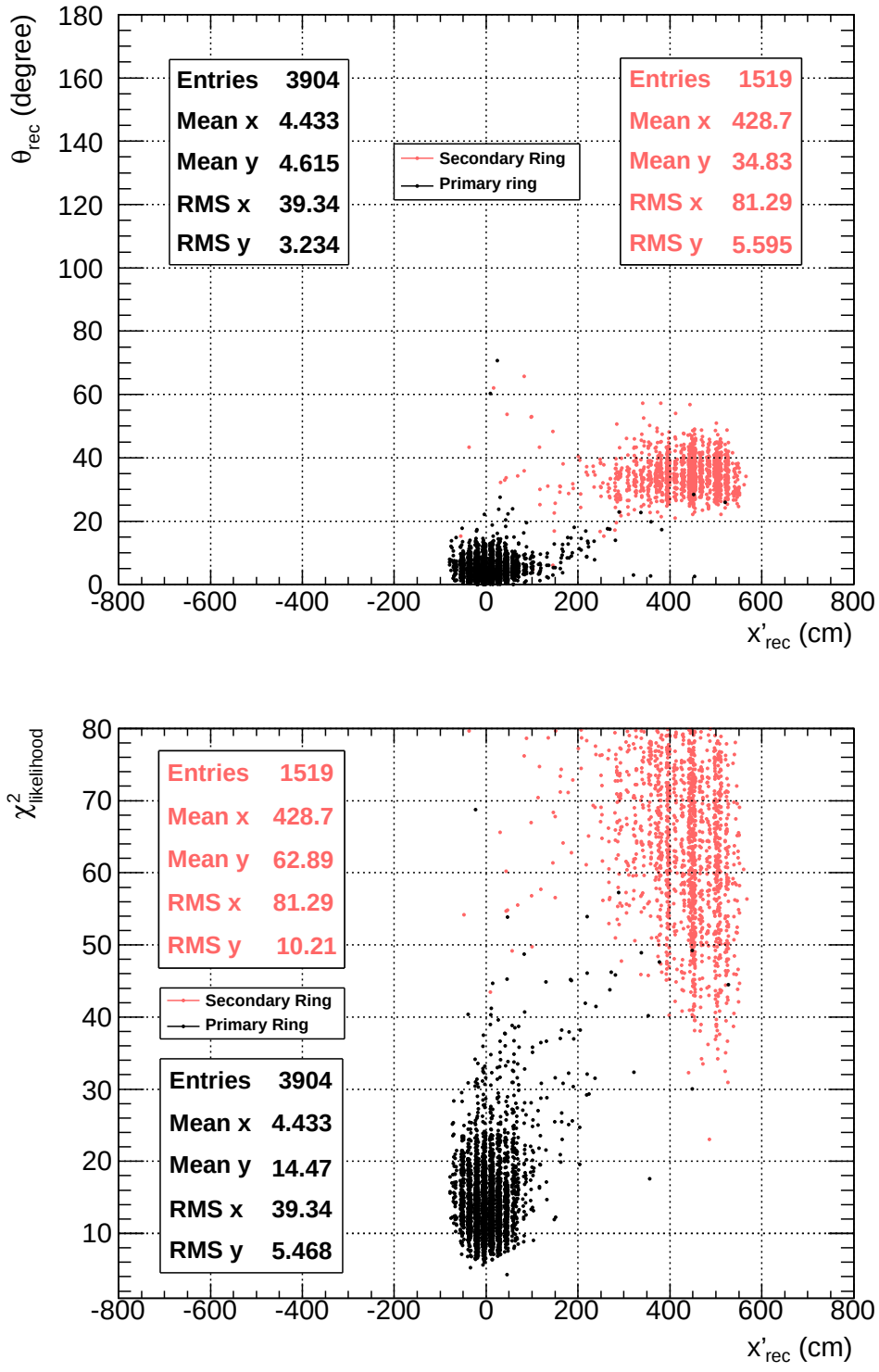

Figure 5.13: Multiple Ring Fitter e^- vertex reconstruction for primary and secondary rings. The simulated Monte Carlo events were simulated from the origin of the detector and a $\zeta_{threshold} = 13$ was chosen for the ξ_{exp}.

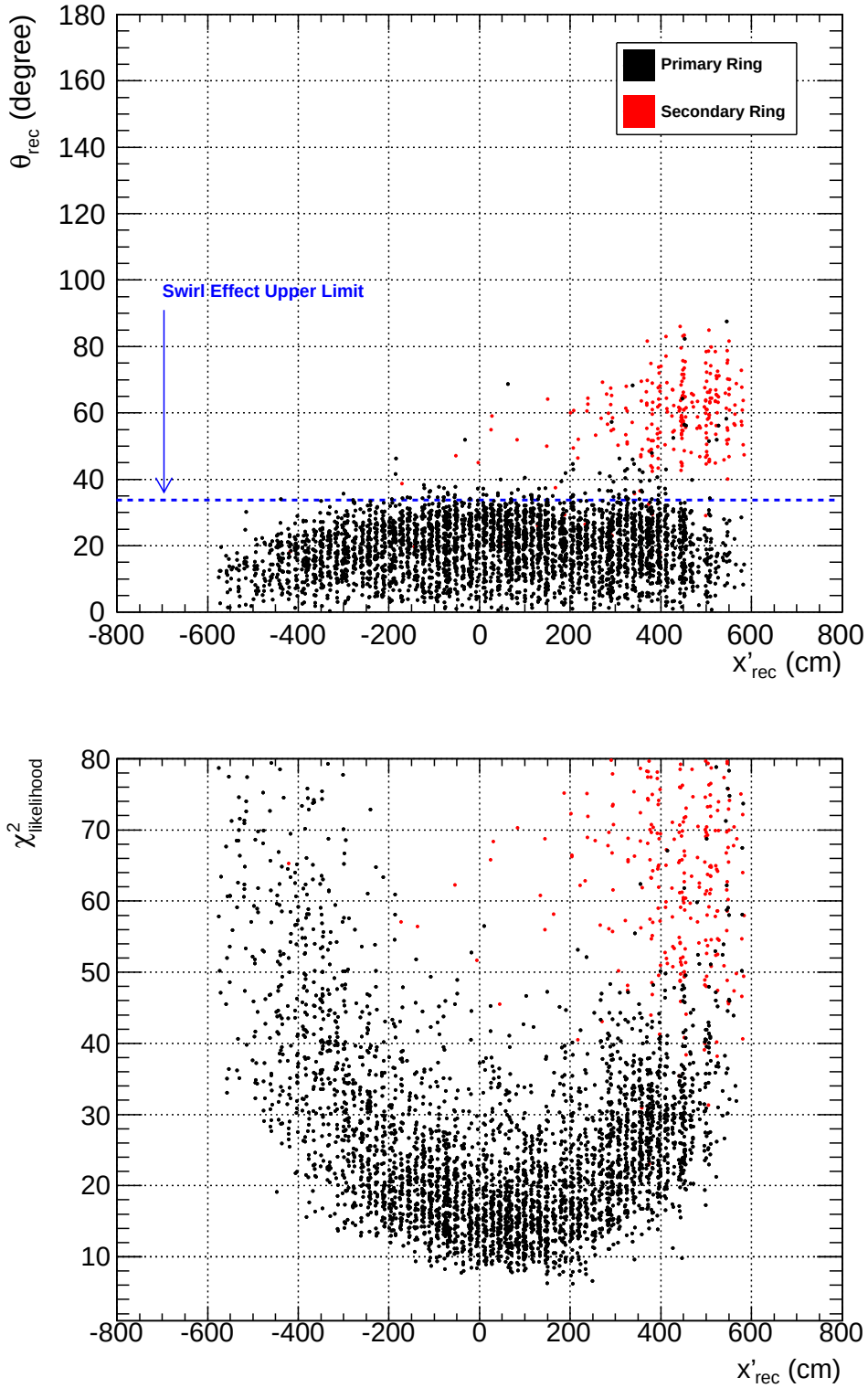

Figure 5.14: Multiple Ring Fitter e^- vertex reconstruction for primary and secondary rings. The simulated Monte Carlo events were generated isotropically within the acrylic vessel with $\zeta_{threshold} = 15$ chosen for the ξ_{exp}.

Conclusions

It is hard to choose a cut on x'_{rec}, $\chi^2_{likelihood}$ or $\zeta_{threshold}$ to eliminate false ring identification. The approach taken here was to choose $\zeta_{theshold} = 15$ to minimize the multiple ring mis-identification while not sacrificing too much detection efficiency for events generated within the acrylic vessel. From Table 5.2 one can see that the multiple ring appear in less than 10% of monoenergetic cases with $\zeta_{theshold} = 15$. While this study is for electrons, different types of particles can be generated within the detector. The following subsections are devoted to their specific studies.

5.5.2 Muon Reconstruction

The non-showering signature is the second type of light signature detectable by Water Čerenkov detectors as was seen in Chapter 3.2. The Čerenkov signature of a muon event of 600 MeV (non-showering) is different from the one for an electron event. This makes muons a good event class for the study of the non-showering signatures. The likelihood expectation distribution ξ_{exp} of an electron-type event can be applied to muon-like events and still results in a positive identification of a ring (while the inverse is not true[6]).

A total of 4839 Monte Carlo muon events were generated at the center of the detector with kinetic energy of 600 MeV. The events were fitted with both the e-like and μ-like ξ_{exp} (Figure 5.5) with the parameters of Table 5.1. One of the conclusions of the trial is the efficiency of the e-like ξ_{exp} is better than the μ-like ξ_{exp} for the same value of parameters; however this comes at the expense of the reconstruction resolution.

Reconstruction of events from the μ-like ξ_{exp} is very good as can be seen in Figure 5.15. The mean of the reconstructed angular distribution is less than 2^o from the Monte Carlo expectation and the position x'_{rec} is reconstructed with less than 11 cm from the Monte Carlo vertex position. On the other hand the e-like reconstruction for primary rings has a systematic shift for both the reconstruction of θ_{rec} and x'_{rec}.

[6]Results of the $\zeta_{threshold}$ analysis for μ^- are presented in Table D.1 of Appendix D

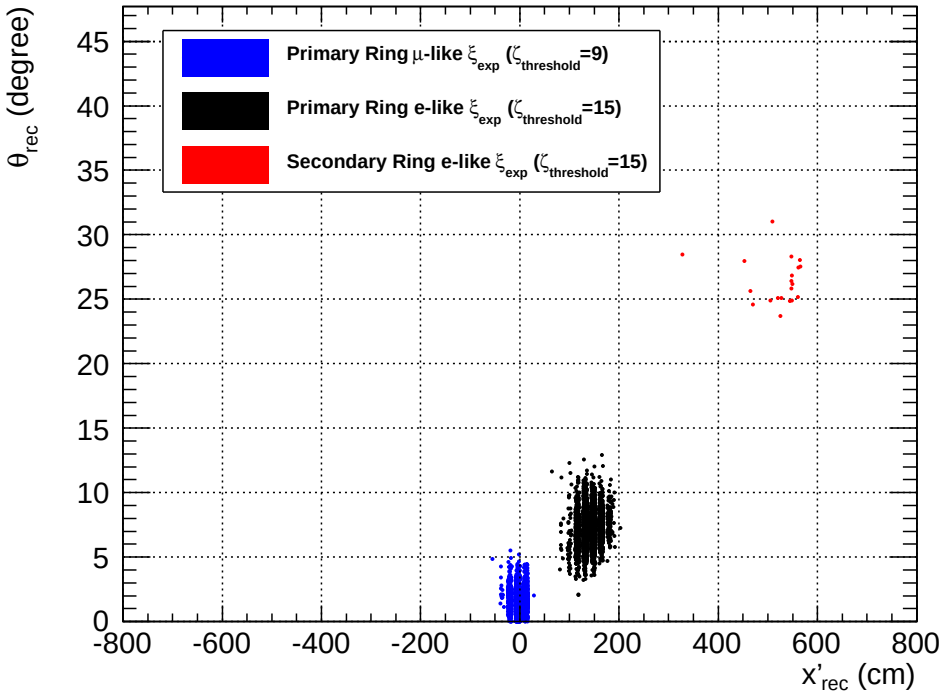

Figure 5.15: Multiple Ring Fitter μ^- Vertex Reconstruction using both the e-like and μ-like expectations. The simulated Monte Carlo events were simulated from the origin of the detector

This shift can be explained since the abrupt edge of the μ-like distribution (Figure 5.5) is averaged out to the noise composition of the showering e-like ξ_{exp} distribution; resulting in both a smaller detected ring radius ρ and a shift in the direction of the reconstructed vertex position x'_{rec} (as shown in Figure 5.15 and can be confirmed visually in Figure G.8).

The reconstruction using the μ-like expectation is also dependent on a lower amount of light, or noise, seen above the Čerenkov angle within ξ_{exp}. In the case of noise from multiple particle events, the reconstruction shown in Table D.1 is no longer valid and needs to be re-evaluated.

Conclusions

The reconstruction efficiencies of the e-like ξ_{exp} are better than the μ-like ξ_{exp} for the same value of parameters; this increase in detection efficiency comes at the expense of the reconstruction quality of the ring: rings are detected as being smaller and skewed from their

actual positions. However, in the case where two types of particle are present within an event, the e-like expectation can detect both type of events while the μ-like cannot as will be studied in the next section. It is then simpler to use only one ξ_{exp} for all events.

5.5.3 Neutral Pion Reconstruction

The neutral pion, described in section 3.3.1, is important for the Multiple Ring Fitter for two reasons. Firstly, it is a particle that will decay to at least two showering particles, nearly instantaneously, making it a good test for multiple ring detection. Secondly, it is one of the backgrounds for the nnbar signal.

Two cases are studied in this section: the case where the events are simulated at the origin of the detector and the case where the neutral pion are generated uniformly within the acrylic vessel[7].

A total of 4888 neutral pion Monte Carlo events of kinetic energy 440 MeV were generated at the center of the detector and a total of 3802 events of kinetic energy 440 MeV were generated isotropically within the detector. The signature of the outgoing gammas follow a e-like ξ_{exp} (fits with the μ-like ξ_{exp} failed for all events).

The neutral pion will decay into two gammas the majority of the time as was seen in Chapter 3. The analytical angle distribution between one of the outgoing gammas and the direction of travel has been calculated previously [19]. The lab frame is defined as $(E', \vec{P}')$ and the rest frame is defined as $(E, \vec{P})$. The second outgoing gamma has the opposite direction of the first one within the rest frame and is redundant in the calculation. The density has the following form,

$$\kappa(\theta') = \frac{\sin\theta'}{2\gamma^2(1-\beta\cos\theta')^2} \tag{5.18}$$

where β is the pion speed v/c and $\gamma = (1-\beta^2)^{-1/2}$. The energy of the outgoing gamma in

[7]Results of the $\zeta_{threshold}$ analysis for π^o are presented in Table D.2 of Appendix D

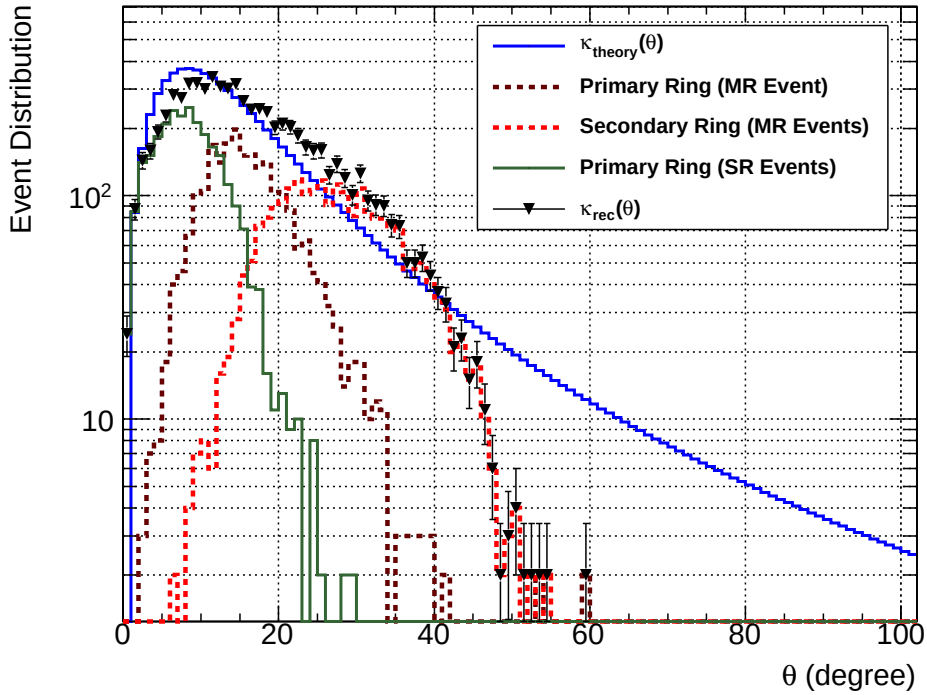

Figure 5.16: Multiple Ring Fitter π^0 angular distribution of detected rings. The simulated Monte Carlo events were simulated from the origin of the detector. The theoretical angular distribution κ from equation 5.18 is normalized to the number of entries of the primary and secondary MR (Multiple Ring found per event) plus twice the entries of the primary SR (Single Ring found per event). The factor of two comes because the secondary ring is not detected due to its low energy; for gammas ejected in the forward direction, the detection of the secondary ring is less likely because of the energy dependence of the MRF.

the lab frame is given by,

$$E'(\theta') = \frac{E}{\gamma(1 - \beta\cos\theta')} \tag{5.19}$$

where $E = m_{\pi^o}/2$ is the energy of the particle in the π^o rest frame [19].

A $\zeta_{threshold}$ value of 15 (at least 30 fired tubes within a Hough bin) leads to a second ring detection efficiency of 48.4%. This seems a low acceptance value but the density described by equation 5.18 leads to loss of events due to the energy dependance of the fitter.

As can be seen in Figure 5.16, no secondary rings are seen above a value of 50^o and some issues can be seen above the 40^o. For angles of 40^o and higher, secondary gammas will have energies less than 42 MeV; implying the primary gammas have energies greater than 543 MeV.

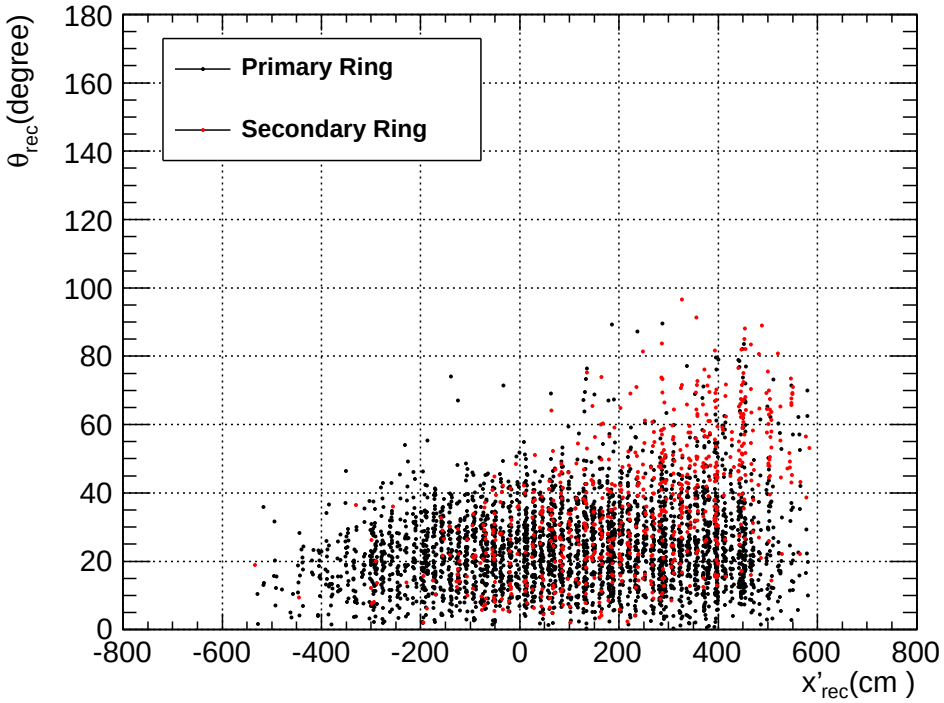

Figure 5.17: Multiple Ring Fitter π^0 primary and secondary vertex reconstruction for isotropic events.

As can be seen in Figure 5.10, the fitter is not sensitive to events with less than 100 MeV because of both the choice of ξ_{exp} and the limitation of the Mid-Point Pair Transform. However, noise from the primary rings lowers the energy threshold sensitivity for the detection of a second ring.

The probability that the secondary gamma will come out with an angle greater than 40^o (θ'_{min}) is,

$$P_{secondary}(\theta \geq \theta'_{min}) = \frac{\int_{\theta'_{min}}^{\pi} \kappa(\theta) d\theta}{\int_{\theta'_{median}}^{\pi} \kappa(\theta) d\theta} \tag{5.20}$$

where $\cos\theta'_{median} = \beta$ for the rest frame angle $\theta = \pi/2$ and κ is taken from 5.18. The solution of the above integral is given by,

$$\frac{1}{2\gamma^2}\int_{\theta_a}^{\theta_b} \frac{\sin\theta d\theta}{(1-\beta\cos\theta)^2} = \frac{1}{2\gamma^2}\int_{\cos\theta_b}^{\cos\theta_a} \frac{dx}{(1-\beta x)^2} = \frac{1}{2\gamma^2\beta}\frac{1}{(1-\beta x)}\Big|_{x=\cos\theta_b}^{\cos\theta_a} \tag{5.21}$$

leading to a a probability of the secondary gamma of $P_{secondary}(\theta \geq \theta'_{min}) = 0.188$. Assuming a perfect efficiency for the primary ring, the expected efficiency of finding a second ring

is capped at 81.2%.

If a strict approach is taken and no events below an energy of 100 MeV are expected due to the resolution of the fitter, then $P_{secondary}(\theta \geq \theta'_{min}) = 0.323$. For a choice of $\zeta_{threshold} = 15$, a multiple ring efficiency of 48.4% for events generated at the center of the detector and 27.5% for events generated evenly within the acrylic vessel, compared to 3.3% and 6.5% for the single electron case.

As stated previously, events with a low energy may not be picked up by the Multiple Ring Fitter due to the statistics requirements of the Mid-Point Pair Transform. For neutral pions that are produced along with other particles the energy detection threshold for the low energy gammas may be lowered due to light scattering.

5.5.4 Charged Pion Reconstruction

Along with the neutral pion, the charged pion is the main type of particle that emerges from an anti-neutron proton annihilation (Table 2.1). The behavior of the charged pion is explained in more detail in Chapter 3. It was shown in section 5.5.2 that the fitter for a e-like signature ξ_{exp} distribution was able to detect events with non-showering signatures. For charged pion detection, the e-like ξ_{exp} is actually more efficient than the μ-like ξ_{exp}.

A lower efficiency of pion detection is expected because of the low mean free path for nuclear interactions in D_2O in the order of 25 cm. Absorption within the nucleus ($\approx$10%) combined with the statistics requirement of the Mid-Point Pair Transform leads to a loss of detection efficiency.

The different scattering interactions (NCX, SCX, DCX and π creation) of Table 3.1 will create events that are "noisy"[8]. This increase in light noise is one of the reason why the e-like estimator is more efficient than the μ-like one[9]. The SCX interaction which create a neutral pion that will not be detected by the μ-like ξ_{exp} is another reason why the e-like

[8]Here noisy is not used to describe PMTs that have a high firing rate, it is used instead for events that have many tubes hit by scattered light.

[9]Tables of the $\zeta_{threshold}$ analysis for π^- are presented in Table D.3 of Appendix D

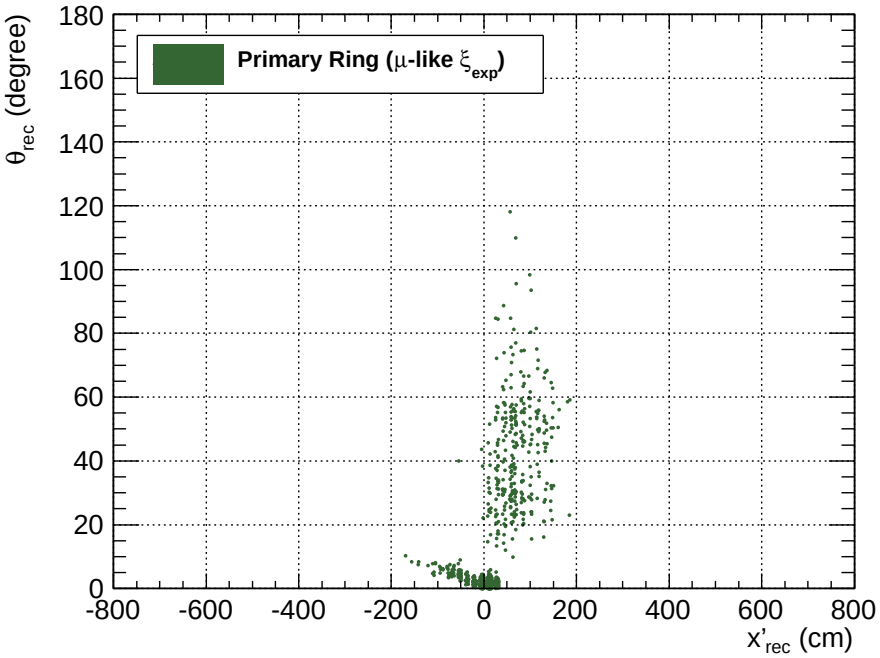

Figure 5.18: Multiple Ring Fitter π^- vertex reconstruction for primary rings with μ-like expectation. The simulated Monte Carlo events were generated at the origin with a $\zeta_{threshold} = 15$ was chosen for the ξ_{exp}.

expectation is more efficient.

The behavior of the Multiple Ring Fitter is shown in Figure 5.18 and 5.19. In the case of the primary ring for both the e-like and μ-like estimator, the reconstruction behavior is similar with the exception that the e-like estimator can detect events up to much larger scattered angle θ_{rec}.

However, above 3 m the "edge of the ring" pathology is also present in the e-like ξ_{exp} results. In the case of the secondary ring reconstruction for the e-like expectation, the distribution is consistent with the primary e-like distribution with a higher percentage of "edge of the ring" events.

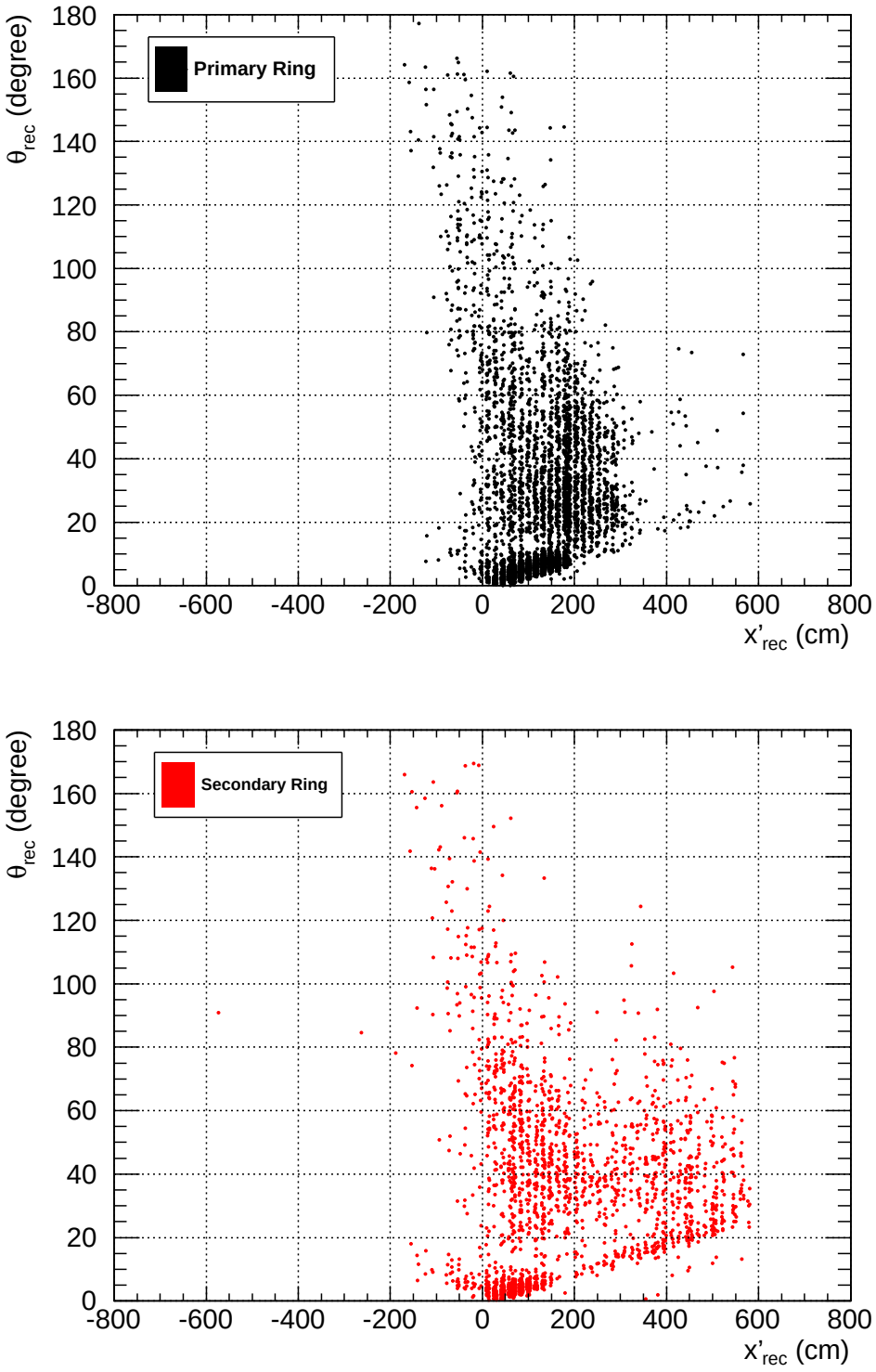

Figure 5.19: Multiple Ring Fitter π^- vertex reconstruction for primary and secondary rings with e-like expectation. The simulated Monte Carlo events were generated isotropically within the acrylic vessel with a $\zeta_{threshold} = 15$ was chosen for the ξ_{exp}.

Conclusions

In order to obtain the most rings possible in the case of a nnbar oscillation signal which is composed of charged and neutral pions, the *e*-like expectation value was chosen for the analysis. The erratic behavior of charged pions in the D_2O medium makes the mass reconstruction of the anti-neutron proton annihilation difficult.

5.6 MRF Conclusions

This chapter described the properties of the Multiple Ring Fitter. The properties described included: the fitter components, the fitter parameters, the reconstruction parameters and the fitter reconstruction of single-pronged Monte Carlo simulated events. The angular *e*-like estimator ξ_{exp} is chosen for both showering and non-showering type of events.

Results from the single-pronged studies all point to a contribution to the multiple ring efficiency of the "edge of the ring" false triggers of less than 10% for the energies of interest for events that have been generated within the acrylic vessel. Efficiencies for primary ring detection are greater than 96% for all type of particles with the exception of the charged pion.

The next chapter explores the tools and parameters that are implemented to understand the behavior between the different events scenarios within the detector (cosmic, atmospheric, nnbar oscillation, instrumental noise). Studies of the behavior of the Multiple Ring Fitter when applied to these types of events will also be presented.

Chapter 6

Analysis Parameters and Event Processing

An expert is a person who has made all the mistakes

that can be made in a very narrow field.

Niels Bohr

Parameters have been defined in Chapters 4 and 5 to understand the behavior of the nnbar signal and the atmospheric neutrino backgrounds. Two categories of parameters are defined: parameters that describe the individual ring properties within an event and parameters that characterize the global properties of the event. The first type of parameters are tied to the MRF routines - ring $\chi^2_{likelihood}$, (θ, ϕ, ρ) - while the second type of parameters - Nhits, photoelectrons - are obtained from SNO event processing.

The transformation of parameters describing individual ring properties to a single parameter describing the event global properties is the goal of this chapter. This single parameter evaluates the isotropy of an event and is useful in rejecting atmospheric neutrino backgrounds.

Information on the angular distribution between the vertex of the different fitted rings can also give information on the behavior of multiple rings in both the cosmic, atmospheric

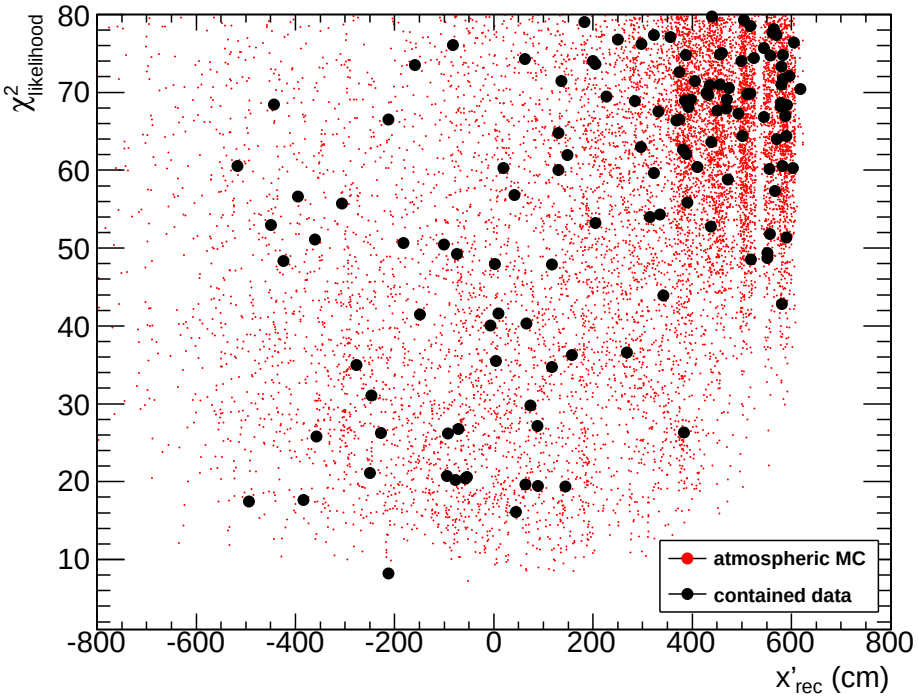

Figure 6.1: Vertex reconstruction x'_{rec} position of atmospheric events. Above a value of $x'_{rec} = 350$ cm (equivalent to a ring radius of $\rho = 370$ cm) there are an abundance of "edge of the ring" events.

backgrounds and nnbar signal and will be studied in this chapter.

The cuts presented in this section focuses on ring properties parameters that have been evaluated on events from data and in the Monte Carlo simulation for both the contained and through-going data sets[1].

6.1 Ring Vertex Studies of False Ring Identification

It was shown in the section 5.5.1 that there exists false ring identification from what have been called the "edge of the ring" effect. In this section the impact of this effect is studied in the context of typical physical events with both the Monte Carlo simulation and the open D_2O data sets.

The "edge of the ring" events have small ring radius and as such a cut on the ring size

[1] data sets defined in section 4.8.

is implemented in order to minimize this type of false ring identification.

Shown in Figure 6.1 are the atmospheric neutrino Monte Carlo (red dots on the scatter plot) and the contained data (black dots on the scatter plot): above a value of $x'_{rec} = 350$ the "edge of the ring" effect creates an abundance of events. A cut requiring $x'_{rec} < 350$ cm (or $\rho > 370$ cm) is implemented to remove false ring identification. x'_{rec} and ρ have been defined in the previous chapter.

For the rest of this chapter, through-going muon data sets are used to calibrate the fitter behavior on the data without creating a bias in the contained event data set.

6.2 Angular Distribution between Ring Vertex

The ring separation algorithm described in section 5.4.2 is efficient in separating the primary ring and secondary rings. However, due to the spread in the likelihood space for the fitted rings, redundant secondary ring identification is possible at the boundary of the different dodecahedron sections.

The angle made between two ring centers, defined as the angle between the center of two respective rings with respect to the center of the detector, defines the $\cos\theta_{ring}$ parameter. Shown in Figures 6.2 and 6.3 are the cosine distribution of pairs of rings for clipping muons; events with $\cos\theta_{ring}$ greater than 0.95 in Figure 6.2 show false ring identification due to the boundary between the secondary dodecahedron sections.

The case of $\cos\theta_{ring}$ for the angle made between the primary and secondary rings is a special case since the position of the primary ring center is at the middle of the dodecahedron section by construct: the secondary ring center cannot be located in the primary dodecahedron bin, a maximal cosine (minimal angle) value between the primary and secondary rings exist.

In the case of two secondary rings, the center of the secondary rings are not required to be at the center of the secondary dodecahedron section and may be at the border of two

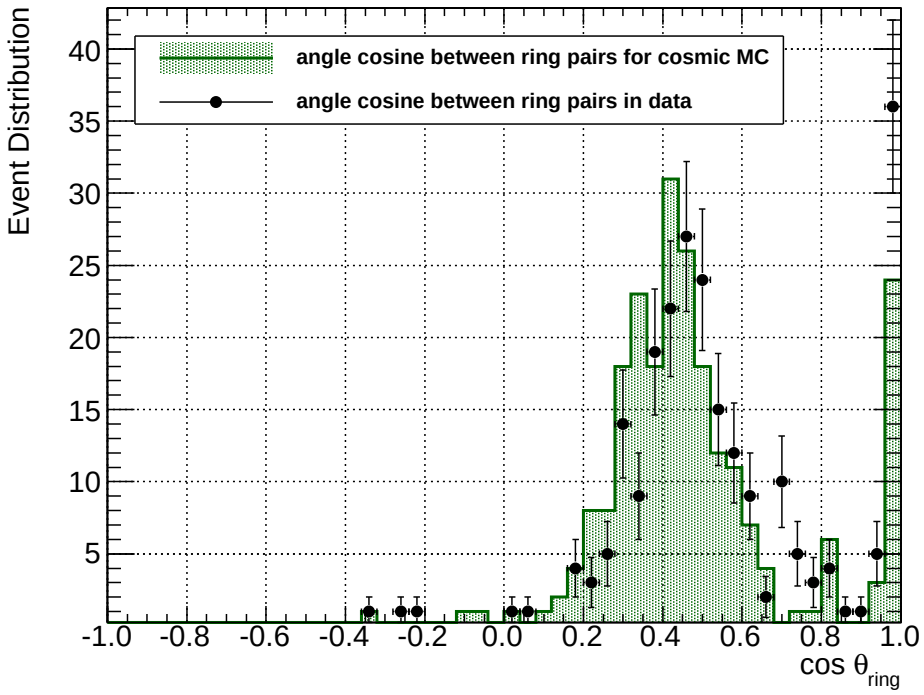

Figure 6.2: $\cos\theta_{ring}$ distribution of multi-ring cosmic events with no x'_{rec} cut applied. The Gaussian peak seen in both the data and the MC corresponds to clipping muons. A shift in the mean of the distribution of $(7 \pm 5)\%$ is observed.

dodecahedron sections.

Shown in Figure 6.3 are the $\cos\theta_{ring}$ for through-going muon events with no x'_{rec} cut applied. The primary-secondary distribution shows the cut-off at $\cos\theta_{ring} = 0.86$; this cut-off is not present in the secondary-secondary distribution.

In order to account for this, a minimal angle between the secondary rings value of $\cos\theta_{ring} < 0.86$ ($\theta_{ring} > 30.6^o$) is imposed in order for the secondary rings to be considered separate. If two rings are contained above this cutoff angle, the ring with the lowest value of $\chi^2_{likelihood}$ is chosen as the surviving ring.

The data and Monte Carlo are consistent with each other. A cut of $\cos\theta_{ring} = 0.86$ is implemented in the analysis in order to distinguish rings that are too close together.

Shown in Figure 6.4 is the $\cos\theta_{ring}$ distribution for ring pair from nnbar MC events. A cut of $\cos\theta_{ring} = 0.86$ removes a negligible number of secondary rings.

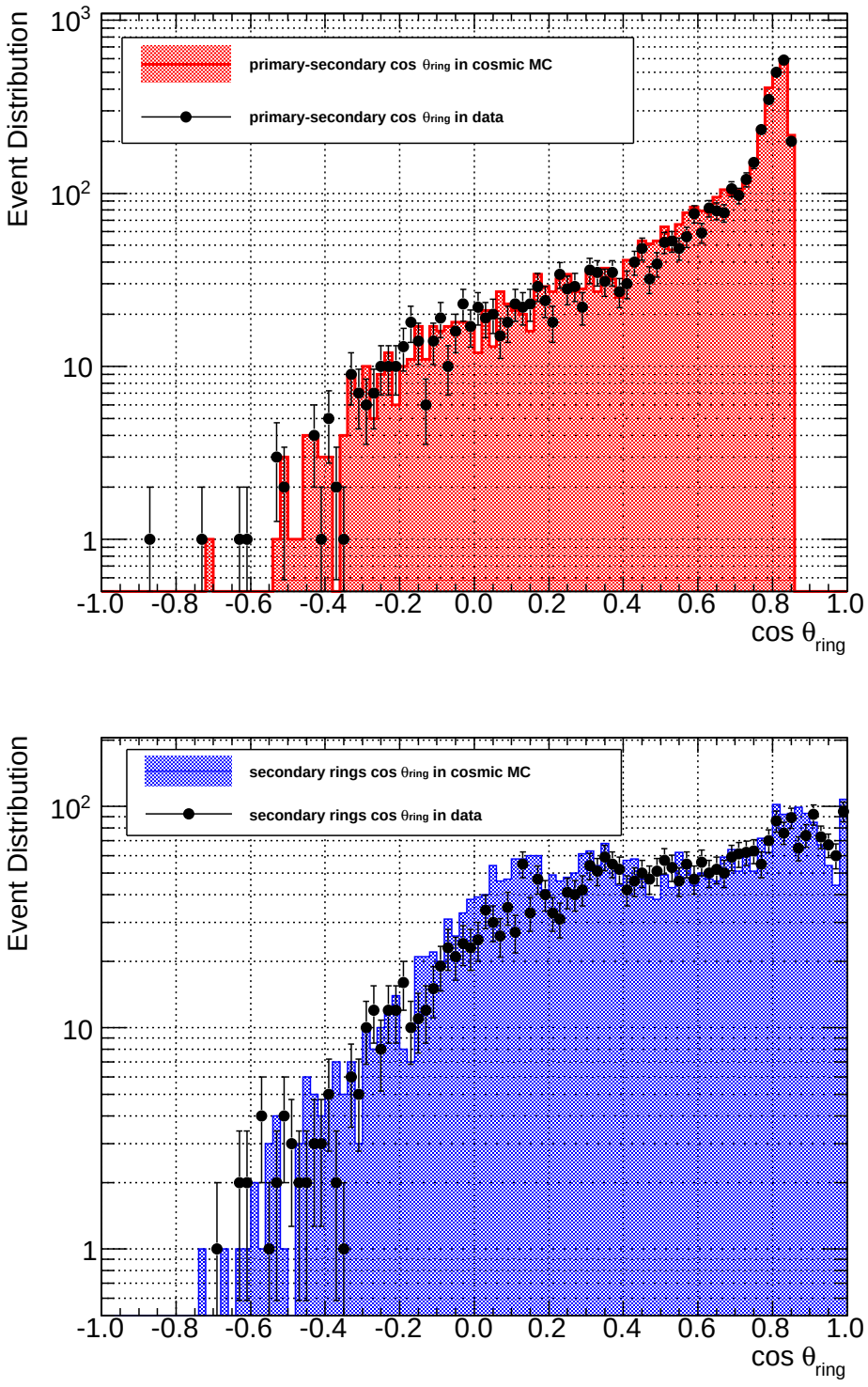

Figure 6.3: $\cos\theta_{ring}$ distribution for cosmic MC and data for both multiple ring pairs involving the primary and secondary ring-pair and multiple ring pairs involving only secondary ring pairs. No x'_{rec} cut was applied.

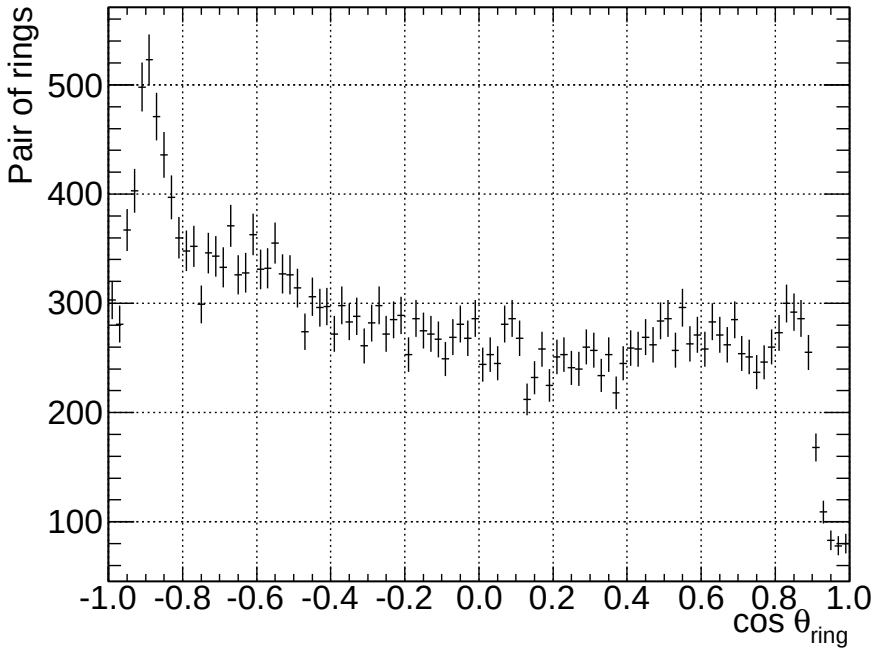

Figure 6.4: $\cos\theta_{ring}$ distribution of pairs of rings in the nnbar MC. A negligible number of rings are cut by removing one the rings out of the pair when $\cos\theta_{ring} > 0.86$.

6.3 Ring Cut Summary

Various instrumental background removal cuts used for the nnbar analysis have been described in section 4.8. Four cuts are explored on both the Monte Carlo and open data sets. These cuts are: the cut on the minimal angle between rings with the $\cos\theta_{ring}$ parameter, a cut on x'_{rec}, a cut is made to isolate single ring events and a cut is made to isolate multiple ring events.

The single and multiple ring detection efficiencies N_{single} and $N_{multiple}$ are important in the characterization of nnbar events. These parameters represent respectively events that contain only a primary ring and events that include at least one secondary ring. Because of the expected signature of nnbar events, events with 2 or more rings found after a $N_{multiple}$ cut constitute the sample in which the limit will be evaluated. These efficiencies will be detailed in the next chapter.

6.4 Isotropy P/E Parameter

The outgoing particles from a nnbar signal will be emitted isotropically within the detector compared to cosmic or atmospheric events. While multiple outgoing particles will occur with cosmic and atmospheric events, momentum conservation will make most of these events anisotropic. This is true for most particles with the exception of the pion. The nuclear inelastic scattering properties explored in Chapter 3 make the pion hard to track in the detector. Furthermore, the absence of particle identification - distinguishing between showering and non-showering particles - makes isotropy a difficult subject to handle correctly since one cannot evaluate the invariant mass of an event.

There are also additional complexity to the tracking of particles due to the energy threshold of the Čerenkov process[2] and the presence of the acrylic vessel which scatters light.

The parameter P/E was developed to understand the behavior of events in the SNO detector. The isotropy parameter $P/E \equiv |\vec{P}/E|$ is defined as,

$$\vec{P}/E = \sum_{i=1}^{N} \frac{\mathrm{PMT}^{i}_{ring}}{\mathrm{Nhits}} \cdot \hat{x}_c^{\,i} \tag{6.1}$$

where PMT^{i}_{ring} is the amount of PMT hit within an opening angle $\Omega = 60^o$ in the fitted ring i of the fitted ring vertex, N is the number of fitted rings within the event and $\hat{x}_c^{\,i}$ is the direction of the fitted ring vertex.

Through-going and Stopping Muon Events

The most probable type of physical events that will trigger the fitter are clipping muons (Section 4.5). These physical events may be used to calibrate the multiple ring fitter response.

Figure 6.5 shows the distribution of events as a function of the parameter P/E: the behavior between primary and secondary events in the Monte Carlo is consistent with the data for through-going events.

[2]The charge particle must be relativistic to emit Čerenkov light $\beta = c/n$

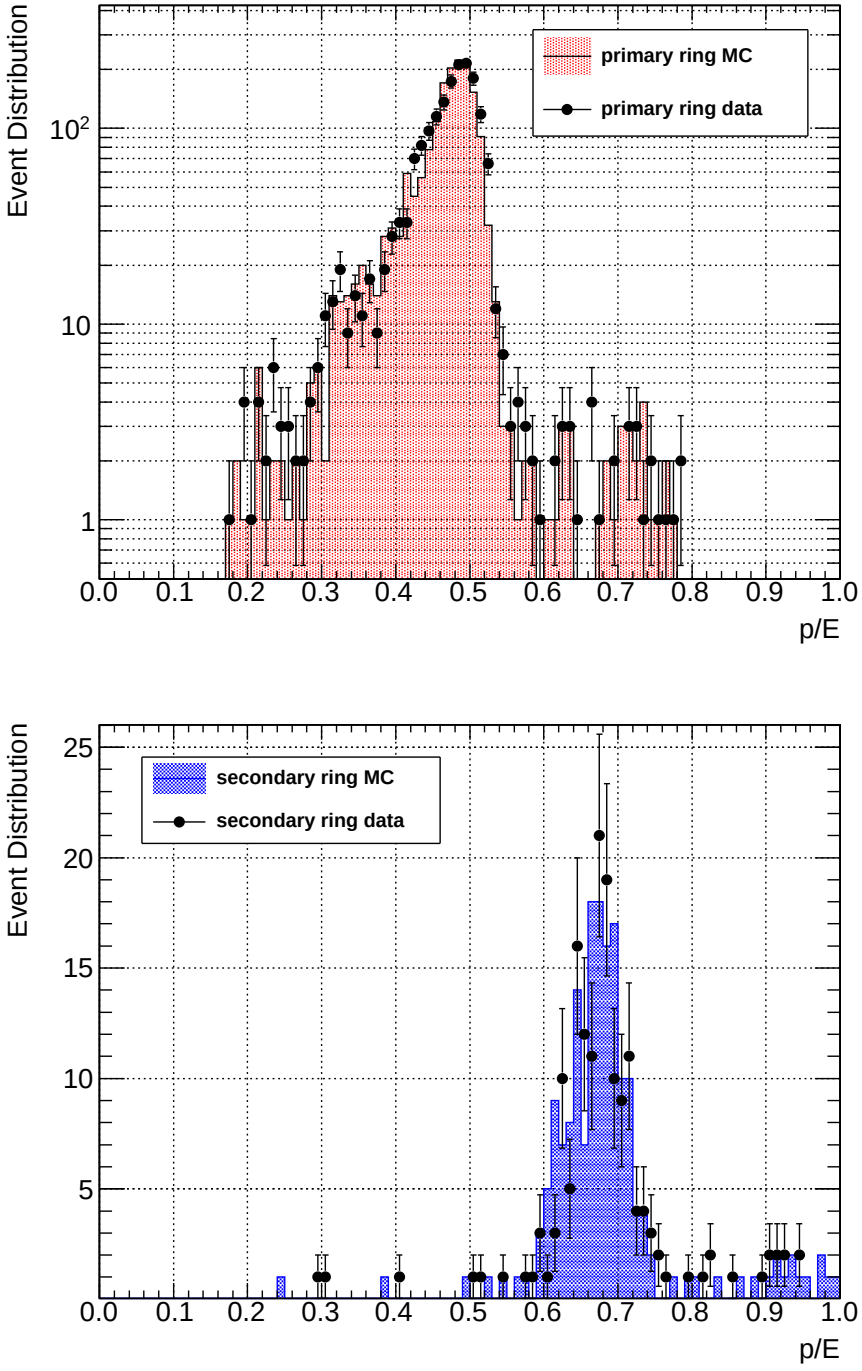

Figure 6.5: Fitter reconstruction between cosmic Monte Carlo and data. The isotropy factor P/E, defined in equation 6.1, shows that the primary and secondary events behavior is consistent between data and Monte Carlo.

Visual scanning of events with $P/E > 0.6$ shows a dominance of stopping muons (an example is shown in Figure G.2) and some multiple ring events. A visual scanning for $0.4 < P/E < 0.6$ shows a dominance of clipping muon events (an example is shown in Figure G.1).

6.5 Event Processing

Events are processed twice. In the first pass the MRF routine loads the PMT information of an event and records the resulting fit information ($\chi^2_{likelihood}$, $\cos\theta$, ϕ, ρ) into ROOT file format. The second pass loads the results from the first pass and applies the cuts defined in this chapter. These event acceptance criteria are,

- $\cos\theta_{ring} < 0.86$: If the cosine is above this threshold the ring with the poorer fit is removed from the analysis
- $x'_{rec} < 350$ cm (or $\rho > 370$ cm) : A cut on the size of the ring is made in order to remove the "edge of the ring" events

The P/E distribution is then evaluated and the events are separated in the single rings (N_{single}) and multiple rings ($N_{multiple}$) subsets. Events are recorded in a three-dimensional(Nhits, Photoelectron, P/E) histogram. These events will be further analyzed in the next chapter (Figure 7.6).

6.6 Summary

In this section the additional parameters and cuts needed to characterize the different classes of events were described: the additional parameters include N_{single} and $N_{multiple}$ which separate single and multiple-ring events, and the isotropy factor $\vec{P}/E$; the additional cuts include the minimal ring separating angle, and the cut on the position of the candidate ring within the detector volume.

In the next chapter, further treatments of the analysis are presented. The error analysis on the distributions and the cuts of the nnbar analysis will also be detailed. Finally, a limit to the nnbar signal will be given.

Chapter 7

Error Analysis and Signal Extraction

It is scientific only to say what is more likely and what less likely,

and not to be proving all the time the possible and impossible.

Richard Feynman

In this chapter, the systematic errors are evaluated and propagated through the analysis. These errors affect the final uncertainties on both the background estimation and signal detection efficiency. The systematic shift seen in parameter distributions and the implemented corrections are also detailed in this chapter. A study of the behavior of parameters between the three phases of SNO will also be detailed.

Once all errors have been propagated, the nnbar signal is extracted with the help of the profile likelihood technique [60]. This technique offers good coverage in the estimation of a rare signal against an expected background using a semi-frequentist approach; this technique is useful since it allows the inclusion of the systematic errors on both the rate of backgrounds and the efficiencies of the signal extraction in the evaluation of a signal limit.

7.1 Systematic Shifts

The four distributions that are relevant to this analysis are

- $\cos\theta_{ring}$ distribution
- MRF $\chi^2_{likelihood}$ distribution
- Nhits distribution
- Photoelectron distribution

Certain effects shift these distributions. A possible explanation to these distribution shifts could be the slight displacements between the actual PMT positions and those in the simulation. Another possible cause is the accuracy of the simulation code. Whatever the cause, a correction is mandatory since the Monte Carlo simulation does not describe the detector perfectly.

The systematic shift to the fitter and the associated error are presented in this section. The error on the MRF reconstruction of rings is evaluated with the through-going muon MC and real data sets instead of the contained event data sets in order to minimize any possible bias.

A linear shift on the MRF routine ring results - $\chi^2_{likelihodd}$ - is required to properly calibrate the fitter. A shift is applied in the following form,

$$Y^{MC}_{corrected} = \alpha\, Y^{MC} + \beta, \tag{7.1}$$

where Y^{MC} is the Monte Carlo MRF $\chi^2_{likelihood}$ reconstruction value, α is the slope of the correction and β is the offset of the correction. For each value of α and β the corrected Monte Carlo is fitted against the data: if the resulting $\Delta\chi^2_{likelihood}$ is less than a threshold value of 3.5[1] the fit result is recorded in Figure 7.1. As seen in Figure 7.1 a shift with

[1]This value correspond to the 68% C.L. for joint estimation of three parameters[47].

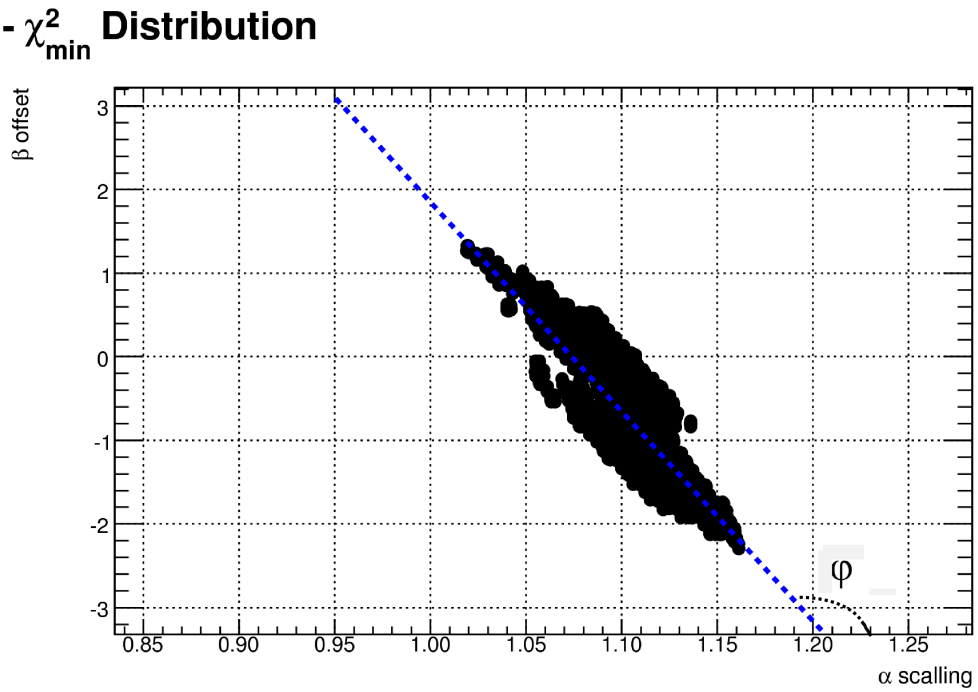

Figure 7.1: The calibration of the MRF routine evaluated between external (cosmic and upmu) MC events and external data. While the entries in the scatter plot are not smooth, a correlation of $\rho_{ij} = -0.89$ is seen between the two shift variable. The calibration yield a shift with $\alpha = 1.09 \pm 0.07$ and $\beta = -0.5 \pm 1.5$ at 68% C.L; it should be noted that $\alpha = 1.0$ and $\beta = 0.0$, which is equivalent to no correction to the fitter, is not included as a solution in the scatter plot. Two "blobs" can be seen in the figure, this is due to the fact that the calibration is made on both the tail of "edge of the ring" events and clipping muons; the overall uncertainty is taken.

$\alpha = 1.09 \pm 0.07$ and $\beta = -0.5 \pm 1.5$ is used to calibrate MRF. The correlation between the two parameters is evaluated from the relation [47],

$$\tan 2\phi = \frac{2\rho_{ij}\sigma_i\sigma_j}{\sigma_j^2 - \sigma_i^2} \tag{7.2}$$

where ρ_{ij} is the correlation coefficient and the angle ϕ is shown in Figure 7.1.

Since the two values are correlated, the total error from the calibration of the fitter is evaluated by propagating $(\alpha + \sigma_\alpha, \beta - \sigma_\beta)$ and $(\alpha - \sigma_\alpha, \beta + \sigma_\beta)$ in the second pass of the event processing routines (Section 6.5).

There are shifts to other distributions that are relevant to this analysis, such as the Nhits and the photoelectron distributions. However, they have been studied previously in the context of the atmospheric neutrino analysis. Further details of these shifts are given

in the next section.

In the case of the $\cos\theta_{ring}$ distribution, the angular response of the PMTs and their associated light concentrators may explain the shift seen in Figure 6.2. The uncertainty in the angular response of the PMT's above an angle of approximatively 40^o was an issue with the atmospheric neutrino analysis[44]: an increase of 6.7% to the PMT response at angles greater than 40^o was implemented. For events that originate within the acrylic vessel, fewer photons are affected by this increase in response than for a clipping muon[2].

This difference in the angular resolution of the PMT's has less impact in the nnbar analysis compared to the atmospheric muon analysis. The difference may explain why only the clipping muons are affected in the $\cos\theta_{ring}$ distribution. The shifted values will be processed in the second pass of event processing routines to evaluate the impact on the nnbar analysis.

7.2 Three-Phase Comparison

The overall detector run conditions changed throughout the different phases of the experiment. On the one hand, the number of photomultiplier tubes slowly decreased because of failures[3]. On the other hand in phase 3, the NCD phase, the introduction of ^{3}He proportional counters reduce the amount of light detected by the PMTs due to the shadowing by the counters. In this subsection, a study is made on the observed difference between phases and the effects on the nnbar oscillation analysis. In most cases the Monte Carlo characterizes the expected changes between phases well.

Shown in Figure 7.2 are the variations to the Nhits distribution for atmospheric and nnbar Monte Carlo events for the different phases. Shown in Figure 7.4 are the variations in the photoelectron distribution for all classes of events; the Monte Carlo models the variation between the phases accurately as can be seen by comparing the cumulative distributions for

[2]The maximal angle of a Čerenkov photon originating from the AV is $\sim 46^o$.

[3]Before the start of the NCD phase, an effort to diagnose failed PMTs was successful in resuscitating some of them, thereby increasing the operational PMTs at the start of that phase.

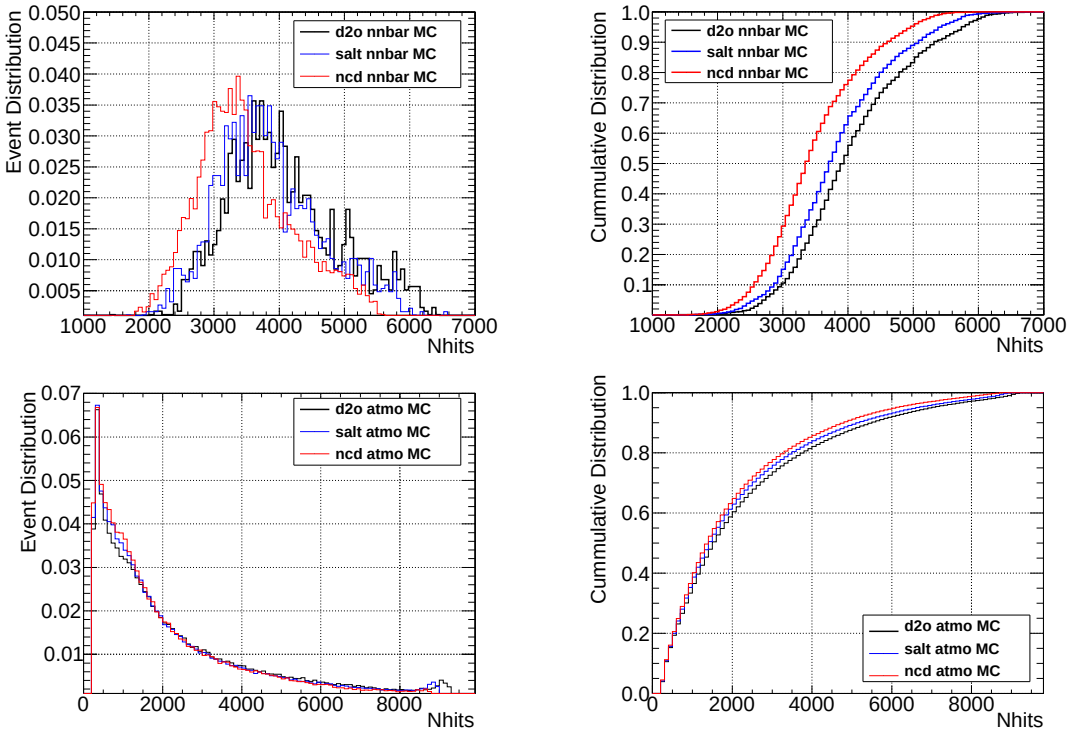

Figure 7.2: Phase comparison of the Nhits distribution for nnbar and atmospheric Monte Carlo events.The black curves show the results of the D_2O phase, the blue curves represent the salt phase and the red curves represent the result of the NCD phase. The shift between the distributions has been evaluated in the context of the atmospheric analysis. The MC overestimates the number of tubes hit in a an event, the corrections are D_2O:-125 tubes, SALT:-135 tubes, NCD:-35 tubes[44]

the different classes of events. Figure 7.3 shows the nnbar ring probability across the three phases; there is a loss of rings in the NCD phase compared to the D_2O and salt phase that may be due to the NCD array.

Table 7.1 shows the results of a Kolmogorov-Smirnov (KS) test of the P/E distribution for single ring events (with no energy cut applied) in various phases. While the KS probability in the NCD phase is lower than those of the other phases, this may be due to statistical fluctuation (such as the fluctuation shown in Figure 7.6 from the next section).

Shown in Figure 7.5 are the expected flux of background events within the energy window defined in Section 4.8. The error on the Monte Carlo include the propagated error on the fitter and the errors on the overall neutrino flux. The data are consistent with the Monte Carlo expectation.

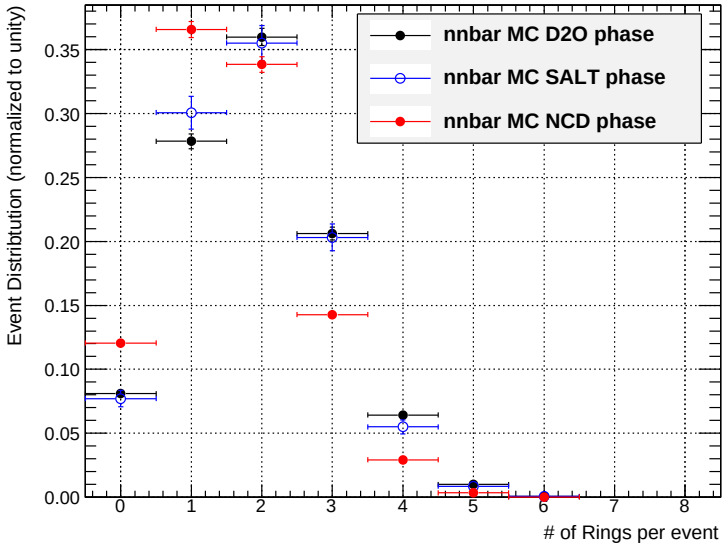

Figure 7.3: nnbar ring detection probability across all phases. The loss of detected rings - or the lower mean number of rings - of the NCD phase could be explained by the shadowing of light by the NCD array; as is seen in Figures 7.2 and 7.4 a lower amount of light is observed which may affect the sensitivity of the MRF.

	Atmo D2O	Atmo SALT	Atmo NCD
Data D2O	0.9163	0.8982	0.7418
Data SALT	0.7084	0.7197	0.6142
Data NCD	0.1241	0.1217	0.1568

Table 7.1: KS test of the atmospheric Monte Carlo and contained data P/E distributions for single ring events. The highest KS probabilities came from comparing the atmospheric MC and reduced open data sets from the same operational phase.

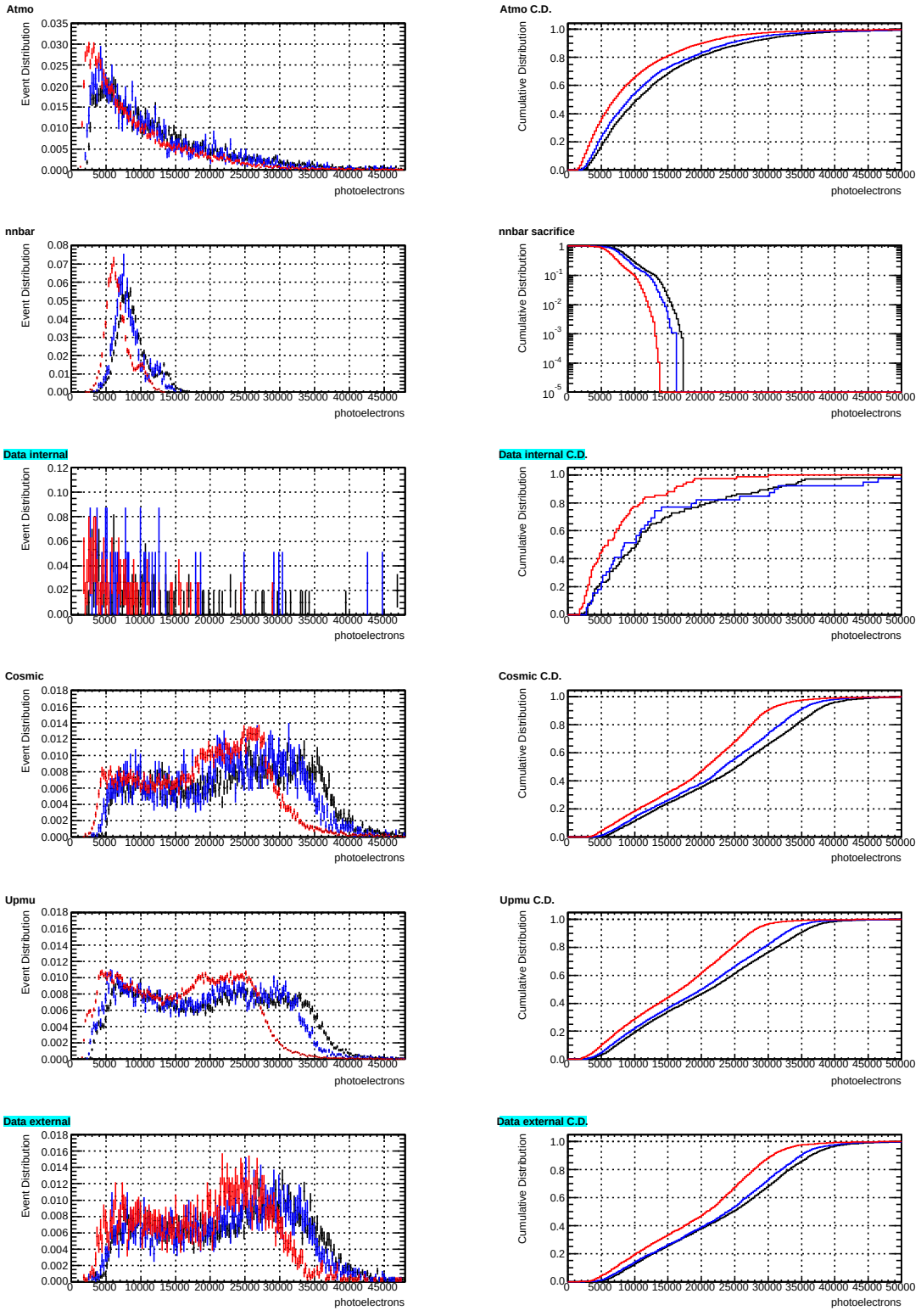

Figure 7.4: Three-phase comparison of the photoelectron distribution for both Monte Carlo and data. The black curves show the results of the D_2O phase, the blue curves represent the salt phase and the red curves represent the NCD phase. While some significant shifts are seen between phases, the Monte Carlo and data are consistent with one another for each phase. The shifts between the distributions have been evaluated in the context of the atmospheric analysis. The MC overestimates the number of tubes hit in a an event, the corrections are D_2O:-350 pe, SALT:-900 pe, NCD:-700 pe [44].

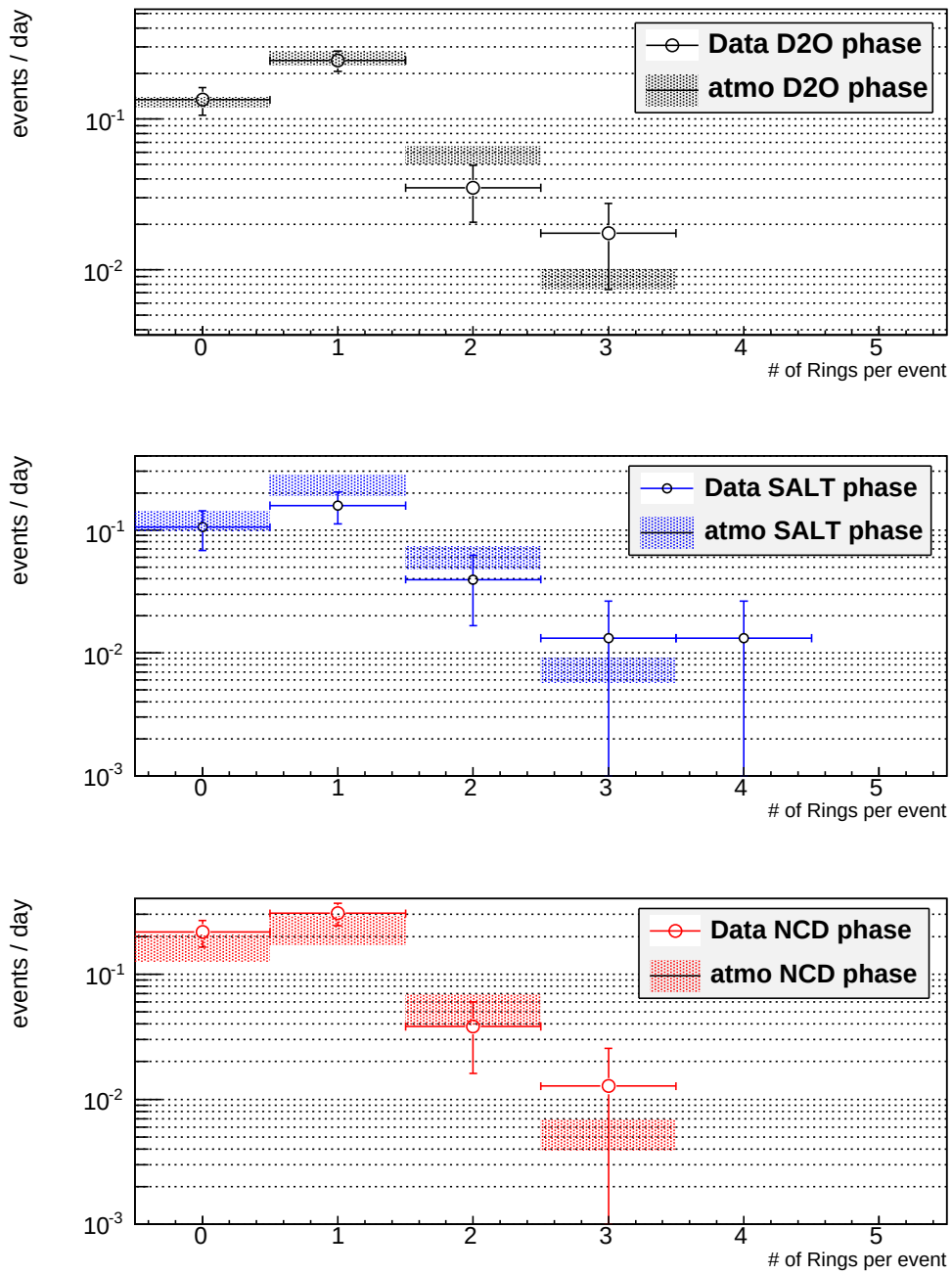

Figure 7.5: Ring distribution for the atmospheric neutrino flux. The box show the Monte Carlo expectation while the points show the measured flux within the detector. The systematic errors on the atmospheric Monte Carlo include only the error due to the performance of the fitter and the overall neutrino flux uncertainty.

7.3 Signal Extraction Across the Three Phases

The expected low nnbar signal statistics in the data and the low atmospheric neutrino background statistics leads to the following question: what is the probability that the events seen within a data set are consistent with a specific class of events? An answer to this problem is obtained by randomly sampling the parent distribution of the classes of events of interest - in this case the atmospheric neutrino and nnbar Monte Carlo distribution - with the statistics of the events seen within the data. For example, it is plausible that events seen in the data are localized in a specific region of the atmospheric distribution if the sampling is low enough (in the same sense that it is possible to obtain only 6's if one throws a die in a limited number of throws).

Shown in Figure 7.6 are the comparison of the mean of the data set measured in the detector compared to the simulated atmospheric data sets across all phases; the simulated data sets are sampled from the 3D probability density function of Nhits, photoelectron and P/E. Each point in those figures represents an individual atmospheric data set. The red point shows the mean of the data: the data points across all phases are consistent with statistical fluctuations of randomly sampling the atmospheric Monte Carlo distributions.

The combination of the three phases is made by combining the data set from each phase into a total data set after weighing each set with it's corresponding livetime. The livetime of the open data sets (from Table 4.1) are respectively $T_{D_2O} = 171.9$ days, $T_{salt} = 76.0$ days and $T_{ncd} = 78.5$ days leading to a total livetime of $T_{3phase} = 326.4$ days.

As can be seen in Figure 7.6, the events measured by the detector are consistent with the atmospheric expectation. Also shown is the expected mean of fake data sets if all events were originating from the nnbar parent distribution class. The conclusion from these figures is that the measured data set is consistent with the atmospheric expectation and is inconsistent with a data set that contains only nnbar events.

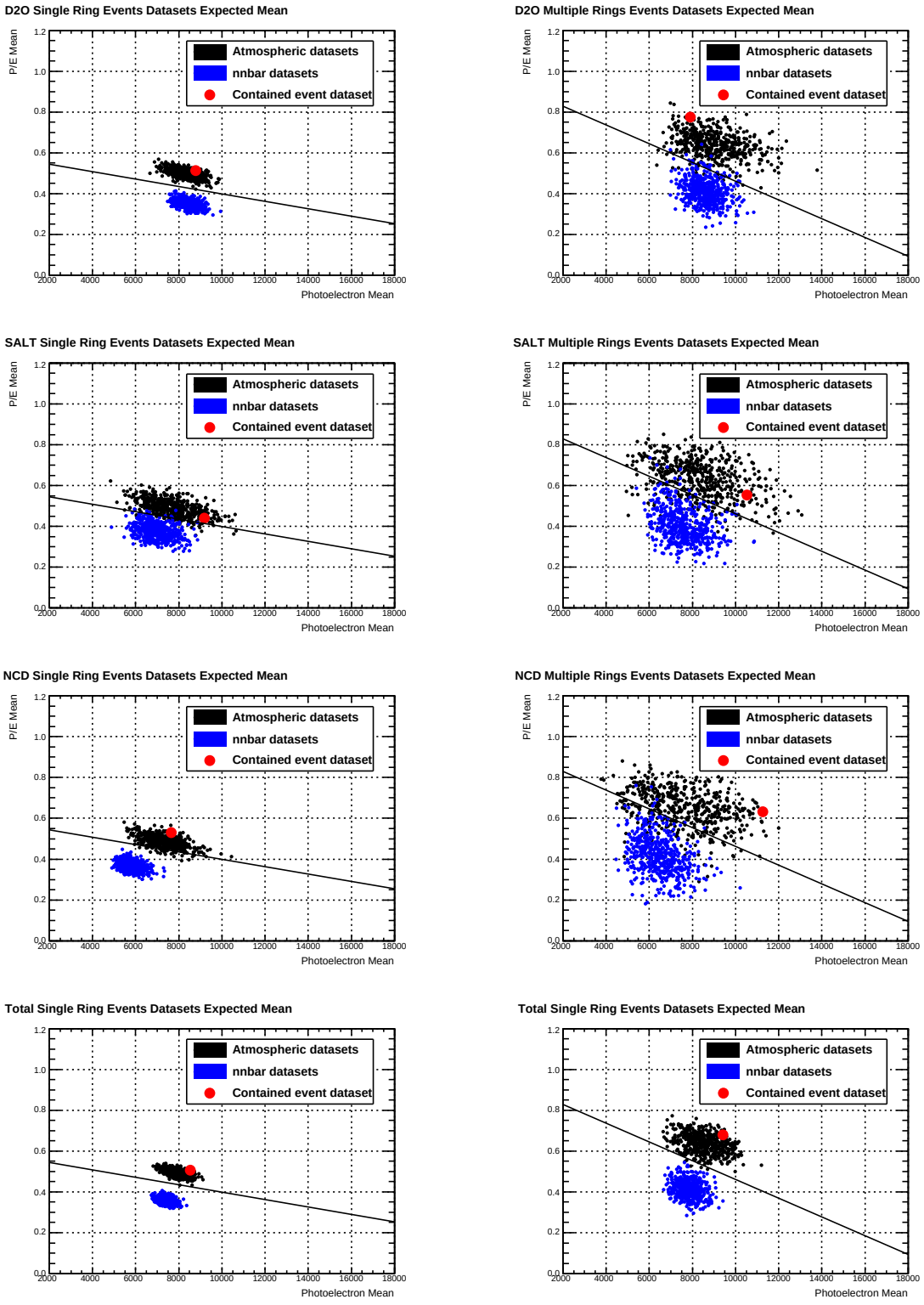

Figure 7.6: Three-phase combination of the P/E and photoelectron distributions for nnbar (blue dots) and atmospheric Monte Carlo events (black dots). The data is represented by the red dots; the data is consistent with the random sampling of the atmospheric distribution and is inconsistent with data that are sampled purely from the nnbar distribution.

7.3.1 Isotropy Cut

The trend of the mean of P/E and photoelecton distributions for the atmospheric and nnbar events in Figure 7.6 suggests that a cut may be constructed to further cut atmospheric events; this is shown with the black lines in Figure 7.6.

Events from both the nnbar and atmospheric distributions are expected to fall below the black line in Figure 7.6. However few nnbar events are cut below this line while a greater amount of atmospheric events are cut: 72.0% of multiple ring atmospheric events are rejected by the cut defined by the black line while only 21.9% of multiple ring nnbar events are cut.

Table 7.2 shows the nnbar acceptance efficiencies for the multiple ring cut, the isotropy cut and the total nnbar detection efficiency. Table 7.3 shows the rejection rate of the cuts for the various neutrino interactions, which are backgrounds to the nnbar signal.

As a consistency check, the analysis was evaluated with a lower ring detection threshold[4] of $\zeta_{thresh} = 13$. By lowering the ring detection threshold slightly, the MRF is more stable in finding multiple ring events for the different branching ratios.

[4]The ζ_{thresh} is defined along with other MRF parameters in Table 5.1

Final State	Channels	$\epsilon_{multiple}$	$\epsilon_{isotropy}$	ϵ_{tot}
		$\zeta_{thres} = 15$		
$2\pi^-\pi^+$	$\pi^-\rho^o(\rightarrow \pi^+\pi^-)$	0.543 ± 0.018	0.733 ± 0.021	0.398 ± 0.017
	$\pi^- f^o(\rightarrow \pi^+\pi^-)$	0.540 ± 0.018	0.746 ± 0.021	0.403 ± 0.017
	$\pi^- f_2'(\rightarrow \pi^+\pi^-)$	0.465 ± 0.018	0.749 ± 0.023	0.348 ± 0.017
weighted total (*)		0.537 ± 0.019	0.744 ± 0.025	**0.399 ± 0.017**
$2\pi^-\pi^+\pi^o$	$\pi^-\omega(\rightarrow \pi^+\pi^-\pi^o)$	0.620 ± 0.023	0.711 ± 0.028	0.441 ± 0.024
	$\pi^- X^o(\rightarrow \pi^+\pi^-\pi^o)$	0.638 ± 0.010	0.770 ± 0.011	0.491 ± 0.011
	$\pi^- X'^o(\rightarrow \pi^+\pi^-\pi^o)$	0.574 ± 0.018	0.741 ± 0.021	0.426 ± 0.018
	$\pi^- A_2^o(\rightarrow \pi^\pm\rho^\pm)$	0.602 ± 0.017	0.767 ± 0.019	0.462 ± 0.018
	$\pi^o A_2^-(\rightarrow \pi^-\rho^o)$	0.525 ± 0.011	0.752 ± 0.013	0.395 ± 0.011
	$\rho^-\rho^o$	0.605 ± 0.012	0.787 ± 0.013	0.476 ± 0.012
weighted total (*)		0.603 ± 0.025	0.768 ± 0.032	**0.464 ± 0.020**
$3\pi^+2\pi^+$ (*)		0.378 ± 0.028	0.864 ± 0.055	**0.327 ± 0.024**
		$\zeta_{thres} = 13$		
$2\pi^-\pi^+$	$\pi^-\rho^o(\rightarrow \pi^+\pi^-)$	0.740 ± 0.016	0.631 ± 0.020	0.467 ± 0.018
	$\pi^- f^o(\rightarrow \pi^+\pi^-)$	0.742 ± 0.016	0.705 ± 0.019	0.524 ± 0.018
	$\pi^- f_2'(\rightarrow \pi^+\pi^-)$	0.685 ± 0.017	0.609 ± 0.021	0.417 ± 0.018
weighted total (*)		0.739 ± 0.019	0.686 ± 0.044	**0.507 ± 0.033**
$2\pi^-\pi^+\pi^o$	$\pi^-\omega(\rightarrow \pi^+\pi^-\pi^o)$	0.786 ± 0.020	0.617 ± 0.026	0.485 ± 0.024
	$\pi^- X^o(\rightarrow \pi^+\pi^-\pi^o)$	0.788 ± 0.009	0.721 ± 0.011	0.568 ± 0.011
	$\pi^- X'^o(\rightarrow \pi^+\pi^-\pi^o)$	0.718 ± 0.016	0.631 ± 0.021	0.452 ± 0.018
	$\pi^- A_2^o(\rightarrow \pi^\pm\rho^\pm)$	0.756 ± 0.015	0.707 ± 0.018	0.534 ± 0.018
	$\pi^o A_2^-(\rightarrow \pi^-\rho^o)$	0.652 ± 0.010	0.707 ± 0.012	0.461 ± 0.011
	$\rho^-\rho^o$	0.777 ± 0.010	0.720 ± 0.012	0.559 ± 0.012
weighted total (*)		0.760 ± 0.031	0.704 ± 0.029	**0.535 ± 0.023**
$3\pi^+2\pi^+$ (*)		0.626 ± 0.041	0.806 ± 0.051	**0.505 ± 0.034**

Table 7.2: The nnbar multiple ring detection efficiency of the different decay channels. The weighted average for $\zeta_{tresh} = 15$ is $\epsilon_{nnbar} = 0.432 \pm 0.041$ and $\epsilon_{nnbar} = 0.526 \pm 0.047$ for $\zeta_{tresh} = 13$. The channels are taken from Table 2.1 and the data selection criteria are taken from Table 4.3. (*) Shows the weighted average which also include the weight error in the evaluation of the total error.

interaction	$\eta_{multiple}$	$\eta_{isotropy}$	η_{tot}
$\zeta_{thres} = 15$			
ν_{cc}	0.849 ± 0.004	0.784 ± 0.012	0.967 ± 0.002
ν_{nc}	0.704 ± 0.016	0.580 ± 0.032	0.876 ± 0.012
ν_{π}	0.762 ± 0.005	0.720 ± 0.012	0.933 ± 0.003
$\nu_{\pi\pi}$	0.692 ± 0.011	0.641 ± 0.020	0.889 ± 0.007
ν_{other}	0.714 ± 0.112	0.500 ± 0.189	0.857 ± 0.095
$\bar{\nu}_{cc}$	0.877 ± 0.006	0.842 ± 0.017	0.981 ± 0.002
$\bar{\nu}_{nc}$	0.847 ± 0.014	0.596 ± 0.049	0.938 ± 0.010
$\bar{\nu}_{\pi}$	0.790 ± 0.008	0.817 ± 0.017	0.962 ± 0.004
$\bar{\nu}_{\pi\pi}$	0.416 ± 0.028	0.730 ± 0.033	0.842 ± 0.021
$\bar{\nu}_{other}$	0.000 ± 0.160	1.000 ± 0.236	1.000 ± 0.124
$\zeta_{thres} = 13$			
ν_{cc}	0.726 ± 0.007	0.755 ± 0.013	0.933 ± 0.004
ν_{nc}	0.583 ± 0.022	0.498 ± 0.034	0.790 ± 0.018
ν_{π}	0.645 ± 0.008	0.677 ± 0.013	0.885 ± 0.005
$\nu_{\pi\pi}$	0.588 ± 0.015	0.616 ± 0.023	0.842 ± 0.011
ν_{other}	0.636 ± 0.130	0.750 ± 0.178	0.909 ± 0.096
$\bar{\nu}_{cc}$	0.779 ± 0.009	0.796 ± 0.019	0.955 ± 0.005
$\bar{\nu}_{nc}$	0.565 ± 0.036	0.482 ± 0.054	0.775 ± 0.030
$\bar{\nu}_{\pi}$	0.690 ± 0.013	0.775 ± 0.020	0.930 ± 0.007
$\bar{\nu}_{\pi\pi}$	0.619 ± 0.025	0.620 ± 0.041	0.856 ± 0.019
$\bar{\nu}_{other}$	1.000 ± 0.163	1.000 ± 0.289	1.000 ± 0.163

Table 7.3: The atmospheric rejection efficiency (η_{atmo}) of the different neutrino interactions. The average atmospheric event rejection efficiency is $\eta_{isotropy} = (72.0 \pm 4.7)\%$ for $\zeta_{thresh} = 15$ and is $\eta_{isotropy} = (67.5 \pm 4.4)\%$ for $\zeta_{thresh} = 13$. The weight of the channels are taken from Table D.5 and the data selection criteria are taken from Table 4.3.

atmo flux (Φ)	uncertainty
$\phi_{normalisation}$ (SNO)	7.4%
Δm^2_{minos} (2.43 ± 0.13)	<0.01%
$\sin^2 2\theta_{SK}$ (1.000 ± 0.032)	0.7%
Total	7.4%

Table 7.4: Systematic error of the atmospheric neutrino oscillation.

7.4 Error Propagation and Systematic Errors

The overview of the systematic error in the extraction of the contained events is the subject of this section. There are two parameters that are of interest for the nnbar analysis, they are the rate of background events and the detection efficiency of nnbar events. The rate of background is given by,

$$b = b_{atmo} + b_{inst} = \Phi\sigma\epsilon_{windows}(1 - \eta_{atmo}) + \Gamma_{inst}\epsilon_{multiple}\epsilon_{isotropy} \tag{7.3}$$

where Φ is the total flux of atmospheric neutrinos, σ is the neutrino cross section, $\epsilon_{windows}$ is the energy window defined in Section 4.8, η_{atmo} is the rejection efficiency of neutrino events in the energy window used for the nnbar analysis and Γ_{inst} is the rate of instrumental background events. This rate is evaluated with a bifurcated analysis in Appendix B with $\Gamma_{inst} = 1.2 \pm 0.6$ events for $T_{3phase} = 326.4$ days of the three-phase analysis for $\zeta_{thresh} = 15$; the total amount of instrumental background is $b_{inst} = 0.024 \pm 0.022$ and $b_{inst} = 0.048 \pm 0.034$ for $\zeta_{thresh} = 13$ (equation B.5).

The errors in Table 7.4 are those from the application of the neutrino oscillation from equation 4.3; the neutrino oscillation is applied to the non-oscillated atmospheric neutrino Monte Carlo by weighing the rate of events with equation 4.3.

The systematic effects that dictate the uncertainties of atmospheric rate seen in the energy window are shown in Table 7.5. These effects are due to either a shift of the energy distributions - the Nhits and photoelectron distributions - or effects due uncertainties in the neutrino cross section. The Δ-resonance has an additional 20% uncertainty that has

($\Phi\sigma$)	D_2O	Salt	NCD
Nhits	1.5%	1.8%	1.7%
photoelectrons	0.3%	0.2%	0.2%
$\bar{\nu}/\nu$ ratio (5% error)	1.4%	1.5%	1.5%
Δ Resonance (20%)	8.0%	8.4%	8.5%
Total	8.3%	8.7%	8.8%

Table 7.5: Systematic error of the rate of atmospheric events seen in the nnbar energy window.

Uncertainty	ϵ^{nnbar}_{d2o}	η^{atmo}_{d2o}	ϵ^{nnbar}_{salt}	η^{atmo}_{salt}	ϵ^{nnbar}_{ncd}	η^{atmo}_{ncd}
Nhits	0.1%	0.2%	0.1%	0.3%	0.1%	0.3%
photoelectrons	<0.01%	0.3	<0.01%	<0.01%	<0.01%	0.1
χ^2_{ring}	6.5%	16.7%	5.6%	14.4%	8.3%	15.4%
$\cos\theta_{ring}$	1.4%	8.4%	1.6%	8.1%	2.2%	9.2%
$\bar{\nu}/\nu$ ratio (5% error)	n/a	1.4%	n/a	1.5%	n/a	1.5%
Δ Resonance (20%)	n/a	10.6%	n/a	11.5%	n/a	10.9%
isotropy cut	n/a	6.5%	n/a	6.5%	n/a	6.5%
annihilation BR	9.4%	n/a	9.4%	n/a	9.4%	n/a
Total	11.5%	22.5%	11.1%	21.2%	12.7%	22.0%

Table 7.6: Systematic errors of nnbar and atmospheric efficiency across all phases. By combining the results across the three phases leads to a systematic error of 11.7% on the nnbar detection efficiency for both the open and close data sets. The systematic uncertainty for the background rate of atmospheric neutrinos is 22.1% for the total data sets and 21.8% for the open data set.

been evaluated from studies for the muon analysis [8]. This uncertainty is important in the context of the nnbar analysis and is evaluated by manually changing the rate of Δ-resonance by $\pm$20% in the atmospheric Monte Carlo.

The uncertainty on the ratio of antineutrinos to neutrinos is evaluated at 5%: this value was chosen based on the Super-Kamiokande results [61] which hold true for neutrino energy below 10 GeV[5].

Shown in Table 7.6 are the effects that influence the amount of multiple rings events that fall within our energy window. The fitter calibration ($\chi^2_{ring} \equiv \chi^2_{likelihood}$(corrected)) which was defined at the beginning of this chapter and the ring counting effect such as the

[5]The error linearly increases with log E_n up to 10% ($\bar{\nu}_e/\nu_e$) and 25% ($\bar{\nu}_e/\nu_e$) at 100 GeV [61]

Final Result	D_2O	Salt	NCD	Three-phase
	(events/day)	(events/day)	(events/day)	(expected/seen)
b_{atmo} ($\zeta_{thresh} = 15$)	0.0540	0.0521	0.0465	(16.9±4.1)/18
b_{atmo} ($\zeta_{thresh} = 13$)	0.0912	0.0959	0.0867	(29.8±7.5)/32
b_{inst} ($\zeta_{thresh} = 15$)	-	-	-	(0.060±0.038)/18
b_{inst} ($\zeta_{thresh} = 13$)	-	-	-	(0.084±0.055)/32
b ($\zeta_{thresh} = 15$)	-	-	-	(17.0±4.1)/18
b ($\zeta_{thresh} = 13$)	-	-	-	(29.9±7.5)/32
	$\epsilon_{d2o}/\epsilon_{d2o}$	$\epsilon_{salt}/\epsilon_{d2o}$	$\epsilon_{ncd}/\epsilon_{d2o}$	ϵ_{phase} (open/total)
ϵ_{nnbar} ($\zeta_{thresh} = 15$)	1.000	0.9670	0.7936	0.9427/0.9207
ϵ_{nnbar} ($\zeta_{thresh} = 13$)	1.000	1.0137	0.9255	0.9854/0.9818

Table 7.7: Expected rate of background events and detection efficiency of the three phases. The rates are converted to an expectation of event rate using the livetime of the open data sets as weights. The nnbar detection efficiency is weighted by both the open data set livetime and total livetime found in Table 4.1. Results shown in this table do not include the isotropy cut detailed in the previous section.

Final Result	$\epsilon^{nnbar}_{3phase}$	b^{atmo}_{3phase}	b^{inst}_{3phase}	b_{3phase}
$\zeta_{thresh} = 15$	0.407±0.048	4.73 ± 1.04	0.024±0.022	4.75 ± 1.04
$\zeta_{thresh} = 13$	0.518±0.061	9.68 ± 2.13	0.048±0.034	9.73 ± 2.13

Table 7.8: Summary of expected rate of atmospheric and instrumental background after all cuts.

$\cos\theta_{ring}$ shift have a significant effect on both the background rate and signal detection efficiency.

Shown in Table 7.7 are the summary of the two parameters of interest of this analysis with no isotropy cut. The number of events seen in the data is also consistent with the background expectation prior to the isotropy cut: 18 events are seen and 17.0±4.1 are expected for $\zeta_{thresh} = 15$ and 32 events are seen and 29.9±7.5 are expected for $\zeta_{thresh} = 13$.

By applying the isotropy cut, one obtains the following expectation for b: 4.75±1.04 events are expected and 2 events are seen for $\zeta_{thresh} = 15$; while 9.73±2.13 events are expected and 4 events are seen for $\zeta_{thresh} = 13$. The value of the data point is 2.6σ lower the expectation in the $\zeta_{thresh} = 15$ case and 2.7σ for $\zeta_{thresh} = 13$; this shows that the behavior of the fitter is sound as one changes the acceptance threshold of the ring counting

algorithm. Section G.4 gives a visual display of the event of interest.

As is shown in Figure 7.6, this $2.6/2.7\sigma$ effect is consistent with statistical variations of random sampling of the atmospheric distribution of multiple ring events.

7.5 Signal Extraction

The choice of which technique to use in the estimation of the number of nnbar events within the detector livetime can follow two competing methods: the frequentist and the Bayesian prescriptions. At the core, the two techniques differ in philosophy and the choice of one technique over another may lead to different final answers. In this section the technique chosen for the limit extraction is explored and justified.

7.5.1 Frequentist vs. Bayesian Approach

Frequentist Limits

The frequentist approach applies to experiments that are repeatable. As the experiment is repeated and new data are collected the real value will be *covered* with a certain probability known as the confidence level (CL). In high energy physics not many experiment are repeatable due to monetary constraints. The philosophy behind this approach is very attractive since it is an objective measurement of the frequency of occurrence (if one can construct identical experiments).

Bayesian

The philosophy behind the Bayesian approach consists of the inclusion of the prior knowledge of the observer in the estimation of the probability. This is a measure of the degree of belief. The Bayes theorem is given by:

$$P(\theta_i|\mathbf{X}^0) = P(\mathbf{X}^0|\theta_i) \cdot P(\theta_i)/P(\mathbf{X}^0) \tag{7.4}$$

where $P(\theta_i|\mathbf{X}^0)$ is the probability of the hypothesis θ_i if $\mathbf{X}^0$ is observed and is known as the posterior distribution.

The Bayesian approach may include the experimenter's knowledge in the evaluation of the probability for an unrepeatable event. This prior knowledge is reflected in the prior factor $P(\mathbf{X}^o|\theta_i)$. In certain cases, the inclusion of the prior knowledge might be contested.

Nuisance Parameter

Nuisance parameters are parameters that have no physical relevance to the result that is being sought. These parameters do impact the final result and a technique to properly account for them needs to be established. For example, the rate of background events and the detection efficiency of the nnbar events are two example of nuisance parameters. In the next section a technique to account for the nuisance parameters and their associated error is detailed.

7.5.2 The Profile Likelihood Method

The Profile Likelihood Method [60] introduces a way to include the systematic errors in the evaluation of the signal limit. The systematic errors are introduced as *nuisance parameters* as defined in the previous section. First, it is assumed that the errors on the background rate and efficiency are Gaussian such that the likelihood function is given by

$$L(\mu, b, \epsilon|x, b_o, \epsilon_o) = \frac{(\epsilon\mu + b)^x}{x!} e^{-(\epsilon\mu+b)} \cdot \frac{1}{\sigma_b\sqrt{2\pi}} e^{-\frac{(b_o-b)^2}{2\sigma_b^2}} \cdot \frac{1}{\sigma_\epsilon\sqrt{2\pi}} e^{-\frac{(\epsilon_o-\epsilon)^2}{2\sigma_\epsilon^2}} \tag{7.5}$$

The profile likelihood method uses the suppremum of the likelihood function to create a likelihood ratio quantity λ such that

$$\lambda(\mu|x, b_o, \epsilon_o) = \frac{\sup(L(\mu, \hat{b}(\mu), \hat{\epsilon}(\mu)|x, b_o, \epsilon_o))}{\sup(L(\hat{\mu}, \hat{b}, \hat{\epsilon}|x, b_o, \epsilon_o))} \tag{7.6}$$

where μ is the signal, b_o and ϵ_o are the measured value of background rate and efficiency and $\hat{b}$, $\hat{\epsilon}$ or $\hat{\mu}$ are the corresponding values that maximize the Likelihood function. The value of the negative of the logarithm of the previous expression is given by:

$$-2\log\lambda(\mu|x, b_o, \epsilon_o) = -2\log L(\mu, \hat{\epsilon}(\mu), \hat{b}(\mu)|x, b_o, \epsilon_o) + 2\log L(\hat{\mu}, \hat{\epsilon}, \hat{b}|x, b_o, \epsilon_o) \tag{7.7}$$

Here $-2\log\lambda$ converges to a χ^2 distribution of one degree of freedom; this $2\log\lambda$ quantity is defined as the profile likelihood. The maximum of the numerator in equation 7.5 is given by solving [60]

$$\begin{aligned}\frac{\partial}{\partial\epsilon}\log L(\mu,b,\epsilon|x,b_o,\epsilon_o) &= \left(\frac{x}{\epsilon\mu+b}-1\right)\mu+\frac{(\epsilon_o-\epsilon)}{\sigma_\epsilon^2}=0\\ \frac{\partial}{\partial b}\log L(\mu,b,\epsilon|x,b_o,\epsilon_o) &= \frac{x}{\epsilon\mu+b}-1+\frac{(b_o-b)}{\sigma_b^2}=0\end{aligned} \tag{7.8}$$

The terms $\hat{b}(\mu)$ and $\hat{\epsilon}(\mu)$ for the $-2\log L(\mu,\hat{\epsilon}(\mu),\hat{b}(\mu)|x,b_o,\epsilon_o)$ term are solved analytically. The evaluation of $\hat{\mu},\hat{\epsilon},\hat{b}$ from $-2\log L(\hat{\mu},\hat{\epsilon},\hat{b}|x,b_o,\epsilon_o)$ is done by solving the equations above with the added constraint

$$\frac{\partial}{\partial\mu}\log L(\mu,b,\epsilon|x,b_o,\epsilon_o) = \left(\frac{x}{\epsilon\mu+b}-1\right)\epsilon=0. \tag{7.9}$$

This is solved with $\hat{\mu}=\frac{x-b}{\epsilon}$ which leads to $\hat{b}=b_o$ and $\hat{\epsilon}=\epsilon_o$.

The difference between the bounded and unbounded evaluation of the upper limit is related to the evaluation of $\hat{\mu}$: on the one hand $\hat{\mu}$ is allowed to be negative and on the other it is artificially set to zero.

Figure 7.7 shows the example of the bounded versus the unbounded method. For the example given in this thesis, $\hat{\mu}=-6.71$; the efficiency is folded in the profile likelihood. However in order to follow to the convention of equation 7.11 defined in Section 7.6 a *relative* efficiency may also be defined such that

$$L(\mu',b,\epsilon'|x,b_o,\epsilon_o)=\frac{(\epsilon'\mu'+b)^x}{x!}e^{-(\epsilon'\mu'+b)}\cdot\frac{1}{\sigma_b\sqrt{2\pi}}e^{-\frac{(b_o-b)^2}{2\sigma_b^2}}\cdot\frac{1}{\epsilon_o\sigma_{\epsilon_o}\sqrt{2\pi}}e^{-\frac{(1-\epsilon')^2}{2\sigma_{\epsilon_o}^2}} \tag{7.10}$$

where $\epsilon'\equiv\epsilon/\epsilon_o$, $\mu'\equiv\epsilon_o\mu$ and $\sigma_{\epsilon_o}\equiv\sigma_\epsilon/\epsilon_o$.

With this convention, $\hat{\mu}'=-2.75$, then $-2\log L(\hat{\mu}',\hat{\epsilon}',\hat{b}|x,b_o,\epsilon_o)$=1.95. Both convention are equivalent and lead to the same final result for the τ_{nnbar} limit.

Figure 7.8 shows a hypothetical situation where a nnbar signal is measured. In this scenario the bounded and unbounded method give the same results since $\hat{\mu}>0$.

The experimental results seen in this thesis brings up the following question: how should a limit be cited to the community when fewer events are seen than are expected ($\hat{\mu}<0$)?

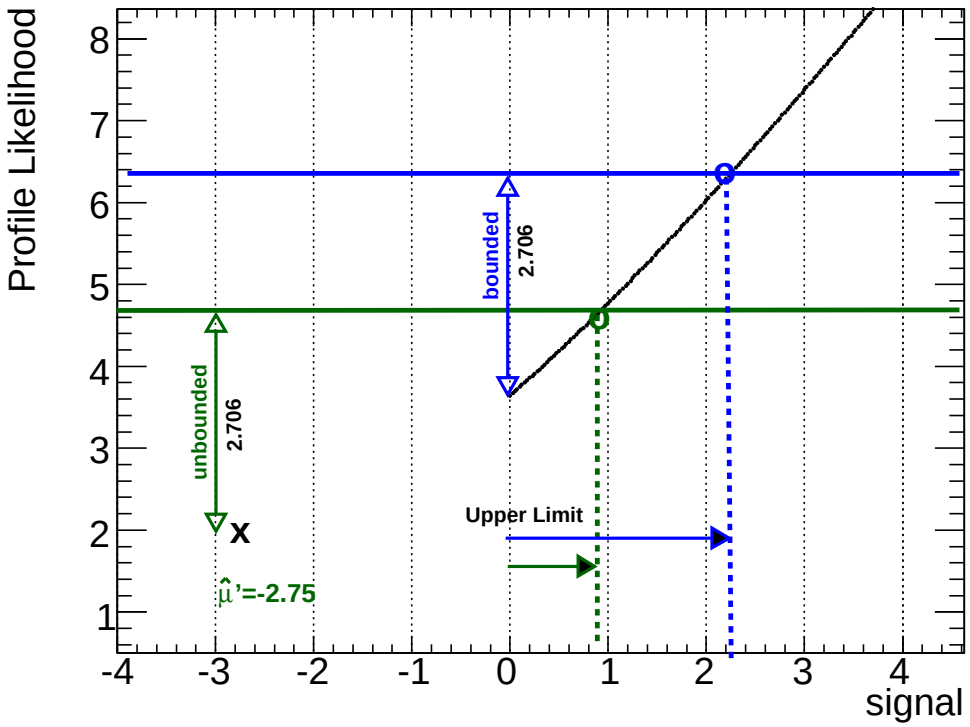

Figure 7.7: Example of the *bounded* vs *unbounded* upper limit of the $-2\log L(\mu', \hat{b}, \hat{\epsilon}'|x, b_o, \epsilon_o)$ for the case where $x = 2$ and $b_o = 4.75 \pm 1.04$. The 90% confidence interval is determined by taking $-2\log\lambda$ as a χ^2 variable with one degree of freedom; this implies an increase of $-2\Delta\log\lambda$ of 2.706 for 90% CL. The $-2\Delta\log\lambda$ is taken either at $\mu = 0$ for the *bounded* evaluation of the limit or at $\hat{\mu}' = -2.75$ for the *unbounded* evaluation of the limit. Both the systematic errors on the efficiency and atmospheric neutrino rate are included in the profile likelihood.

As is seen in Figure 7.7, the upper limit will vary greatly depending on the choice of the technique when $\hat{\mu} < 0$. It is suggested to also quote the experimental sensitivity: this sensitivity is defined as the mean upper limit for a set of experiments with the observed background and efficiency but no rare signal [62].

The upper limit evaluated on the Monte Carlo sampled data sets of Figure 7.6 will be the subject of the next section. This is also useful in the evaluation of coverage.

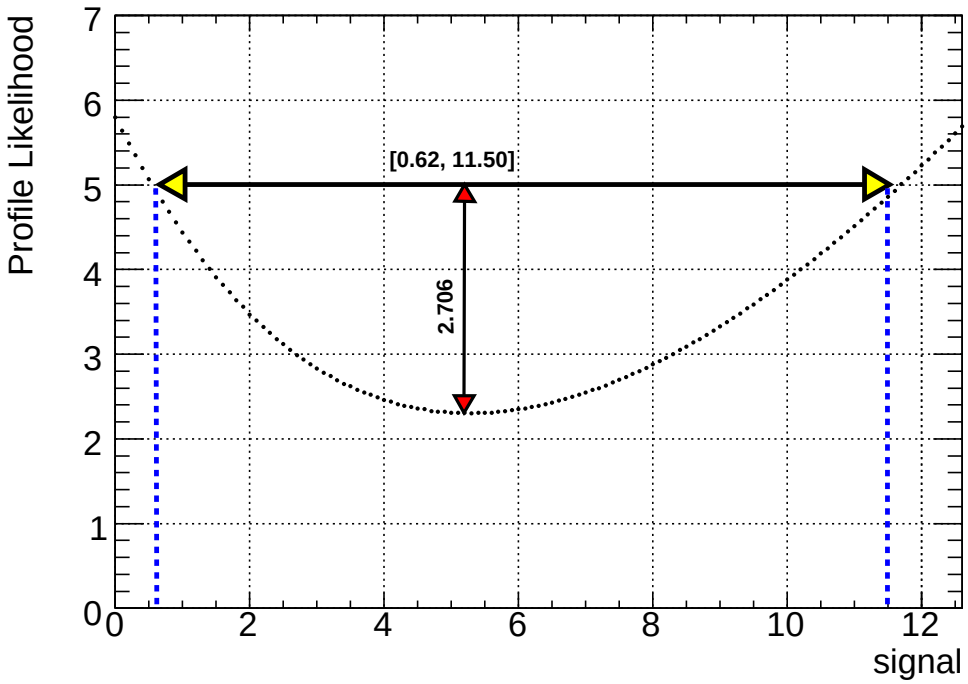

Figure 7.8: The $-2\log\lambda$ curve for a hypothetical scenario where a nnbar signal is measured. This is the case where $x = 10$ and $b_o = 4.75 \pm 1.04$. The efficiency ϵ_{nnbar} was set to unity in order to compare with previous experiments as shown in Table 7.9. The interval is evaluated at [0.62, 11.50] at 90% confidence interval by taking the $-2\log\lambda$ as a χ^2 variable with one degree of freedom; this implies an increase of $-2\log\lambda$ of 2.706 for 90% CL. Both the systematic errors on the efficiency and atmospheric neutrino rate are included in the profile likelihood.

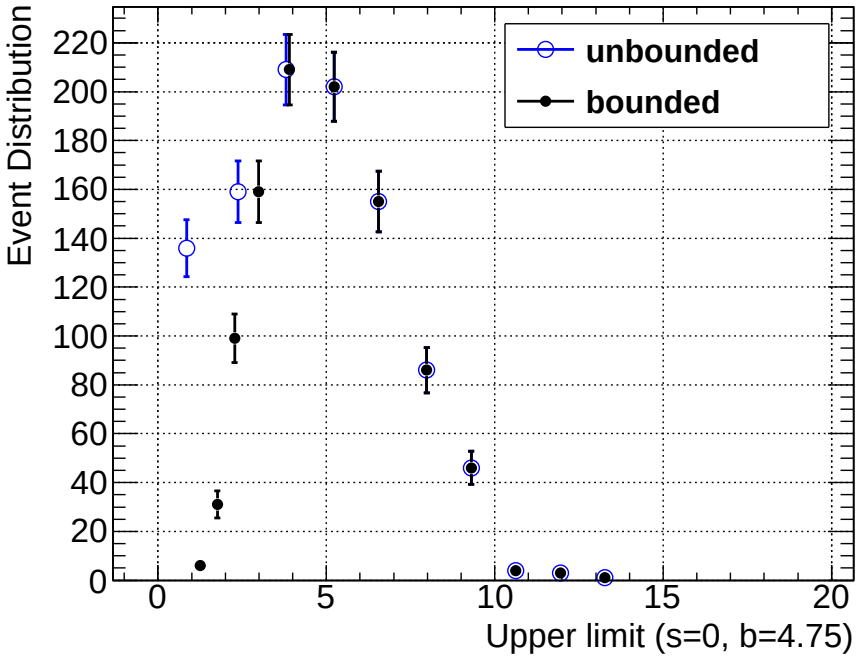

Figure 7.9: Upperlimit on Monte Carlo atmospheric samples using the profile likelihood method. The bound and unbounded upper limit were evaluated at the 90% C.L. on the data sets presented in Figure 7.6. No negative upper limit value were returned for the unbounded estimation.

7.5.3 Coverage

In the frequentist or semi-frequentist type of approach the important concept is what is called coverage: how accurate is the degree of belief, or confidence level, that the true value is contained in the quoted result. Coverage is not guaranteed in the profile likelihood method [60] and a verification is necessary.

The unbounded technique offers better coverage and is set by default within the TRolke 2.0 routines [62]. However, it is the norm to evaluate an upper limit on a process using the bounded region[6].

The coverage in this analysis is verified by Monte Carlo simulations. Shown in Figure 7.9 are the upper limits evaluated in both the bounded and unbounded regions using the fake data sets shown in Figure 7.6. As stated previously, for $\hat{\mu} > 0$ the upper limit is the same

[6]The evaluation of the profile likelihood with bound or unbounded limits is enabled through a flag within the TRolke routines.

Exp.	Neutron source	Exposure 10^{32} n-yr	ϵ (%)	Cand.	BG	signal rate	Limit (T) 10^{32} years	T_R 10^{23} s^{-1}	τ_{nnbar} 10^8 sec
Super-K I	^{16}O	245.4	10.4	20	21.3	8.1	1.77*	1.0	2.36*
Soudan-II	^{56}Fe	21.9	18.0	5	4.5	5.5	0.72	1.4	1.3
ILL	Reactor Beam	-	52	0	-	< 2.3	-	-	0.86

Table 7.9: Current upper limits for the nnbar signal of other experiments. The Super-Kamiokande experiment used a Bayesian technique which incorporated the systematic errors. The Soudan-II and ILL experiment used a Poisson limit in the evaluation of the upper limit. The * symbol shows quantities which include systematic errors.

for the two techniques. For the case where fewer events are seen than expected ($\hat{\mu} < 0$) the two techniques diverge. While the general shape of the unbounded distribution seems to follow more of a Gaussian shape compared to the bounded distribution, no negative values are actually measured.

While the result of this analysis will be summarized with the values bounded in the physical region, the bounded and unbounded limits as well as the experiments sensitivity are given below.

7.6 Neutron Anti-Neutron Lifetime

The value of the limit is dependent on the choice of the signal extraction method and it is important to understand the limitation of all techniques. Shown in Table 7.9 are the previous lower limits on τ_{nnbar}; all limits are evaluated at 90% CL. The free oscillation lifetime τ_{nnbar} is evaluated as

$$\tau_{nnbar} > \sqrt{T_{nucl} \cdot \left(\frac{3.16 \times 10^7 \text{ sec/years}}{T_R} \right)} \tag{7.11}$$

where $T_{nucl} = \frac{\text{exposure} \cdot \epsilon_{nnbar}}{\text{upper limit}}$ and the exposure is 5.4×10^{31} neutron-year for $T_{3phase} = 326.4$ days of the open three-phase analysis (see Section 7.3) and T_R is defined in Section 2.7.

The Super-Kamiokande published limit use a Bayesian type of approach which is different than the one from SNO. The decay rate is evaluated by integrating out the nuisance

parameters such that

$$P(\Gamma|n) = A \iiint \frac{e^{-(\Gamma\lambda\epsilon+b)}(\Gamma\lambda\epsilon+b)^n}{n!} P(\Gamma)P(\lambda)P(\epsilon)P(b)d\lambda d\epsilon db \tag{7.12}$$

with n is the number of candidate events, Γ is the decay rate, λ is the detector exposure, ϵ is the detection efficiency and b is the background [35].

In order to compare the results, the Super-Kamiokande limit is re-evaluated using the profile likelihood technique detailed in this thesis. The Super-Kamiokande limit evaluated with the profile likelihood technique at $\tau_{nnbar} > 2.44 \times 10^8$ sec (bounded) and $\tau_{nnbar} > 2.45 \times 10^8$ sec (unbounded) at 90% CL.

The SNO results for the open data set are shown in Table 7.10. The lower limit for the free oscillation lifetime in deuteron is $\tau_{nnbar} > 1.11 \times 10^8 sec$ (bounded) for $\zeta_{thresh} = 15$ and $\tau_{nnbar} > 1.18 \times 10^8 sec$ (bounded) for $\zeta_{thresh} = 13$. The values in the unbounded case are $\tau_{nnbar} > 1.77 \times 10^8$ sec (unbounded) for $\zeta_{thresh} = 15$ and $\tau_{nnbar} > 1.96 \times 10^8$ sec (unbounded) for $\zeta_{thresh} = 13$.

The difference between the bounded and unbounded values come from the statistical fluctuation of the sample of events which leads to fewer events seen than are expected. As can be seen in Figure 7.6 the combined data measurement is at the outer edge of the atmospheric distribution which creates the situation seen in Figure 7.9.

The lower ζ_{thresh} seems more robust in both the detection efficiency of the various annihilation channels as seen in Table 7.2; it also more robust between phases as seen in Table 7.7.

Exp.	Neutron source	Exposure 10^{32} n-yr	ϵ (%)	Cand.	BG	signal rate (B/UB)	Exp. Sensitivity (B/UB)	T_{nucl} 10^{31} yr	T_R 10^{23} s^{-1}	τ_{nnbar} 10^8 s (B/UB)
Super-K I	^{16}O	245.4	10.4	20	21.3	(13.5/13.4)*	(15.8/15.4)	(18.8/19.0)	1.0	(2.44/2.45)*
SNO ($\zeta_{tresh} = 15$)	D	0.54	40.7	2	4.75	(2.24/0.88)*	(5.17/4.90)*	(0.96/2.45)	0.248	(1.11/1.77)*
SNO ($\zeta_{tresh} = 13$)	D	0.54	51.8	4	9.73	(2.56/0.92)*	(7.41/7.06)*	(1.09/3.01)	0.248	(1.18/1.96)*
SNO($\zeta_{tresh} = 15$)	D_2O	2.68	40.7†	2	4.75	(2.24/0.88)†*	(5.17/4.90)*	(4.90/12.3)	0.85	(1.35/2.14)†*
SNO($\zeta_{tresh} = 13$)	D_2O	2.68	51.8†	4	9.73	(2.57/0.92)†*	(7.41/7.06)†*	(5.42/15.1)	0.85	(1.42/2.37)†*

Table 7.10: Limit extraction for the SNO and the Super-Kamiokande experiment using the Profile Likelihood method. The * symbol shows quantities which include systematic errors contribution. The † symbol refers to the hypothesis that the nnbar detection efficiency is the same in the case of ^{16}O than the deuteron case. The B column shows the evaluation of the limit with physical bound and UB represent the unbounded evaluation of the limit.

7.7 Summary

In this chapter the techniques used in the extraction of the nnbar signal were described. The three-phase expectation was evaluated from the weighted expectation of each individual phase. The technique used to obtain a limit follows a semi-frequentist prescription that allow the inclusion of the systematic errors on both the flux of background events and the error of the detection efficiency.

The different techniques for limit evaluation of rare signal could lead to different results. The technique used in this thesis to evaluate the limit is different from the Super Kamiokande experiment. The lower limit for the Super-Kamiokande experiment is re-evaluated by the author to a value of 2.44×10^8 sec (bounded) with the profile likelihood; this value is consistent with the value 2.36×10^8 sec (bounded) using a purely Bayesian technique which was used by Super-Kamiokande [35].

The lower limit for the SNO experiment was evaluated at two different thresholds of the ζ_{thresh} parameter. The limits were shown to be consistent with each other, however $\zeta_{thresh} = 13$ is more robust for both the different annihilation branching ratio and the phase transition.

The lifetime for the combined three-phase detector livetime of 326.4 days of the open data of SNO is evaluated at $\tau_{nnbar} > 1.18 \times 10^8$ sec (bounded) and $\tau_{nnbar} > 1.96 \times 10^8$ sec (unbounded) at 90% CL. In the next chapter, the path to opening the box will be detailed.

Chapter 8

Conclusions

Tomber a été inventé pour se relever. Malheur à ceux qui ne tombent jamais.

Félix Leclerc

In this thesis, results on the search for the nnbar oscillation across the three phases of SNO were presented. A lower limit on the three-phase open data set of SNO giving a oscillation lifetime for a bound neutron in deuteron of $T_{nucl} > 1.09 \times 10^{31}$ sec (bounded) and $T_{nucl} > 3.01 \times 10^{31}$ sec (unbounded) at 90% CL for 326.4 days of detector livetime. The nnbar free oscillated lifetime is estimated at $\tau_{nnbar} > 1.18 \times 10^{8}$ sec (bounded) and $\tau_{nnbar} > 1.96 \times 10^{8}$ sec (unbounded) at 90% CL for the open data set with 326.4 days of livetime using the model developed by Dover and Gal [30]. This result includes the systematic error on both the signal detection efficiency which have been calculated from Monte Carlo simulation and the systematic error on the rate of expected atmospheric neutrino backgrounds.

Due to the publication requirements of the SNO collaboration, the analysis was conducted only on a portion of the available data in order to avoid bias prior to the collaboration review. The result obtained on this portion of the data is equivalent with the result found in the Soudan-II experiment [37]. The detector livetime for this analysis is $T_{3phase} = 326.4$ days. The full analysis will contain $T_{3phase}^{FULL} = 1,242$ days. In the case of τ_{nnbar} however, the full analysis will improve as approximately the square root of this quantity such that

$\sqrt{T_{3phase}^{FULL}/T_{3phase}} = 1.951$.

Results from the Super-Kamiokande experiment on the nnbar search were presented at the B-L workshop at the Lawrence Berkeley National Laboratory [35]; these results offer higher limits than the results found in this thesis, however, the expected improvement to the publication results if the measurement follow the same statistical conditions as the blinded study from the SNO experiment is $\tau_{nnbar} > 2.30 \times 10^8$ sec (bounded) which are comparable with the limit from the Super-Kamiokande experiment of $\tau_{nnbar} > 2.36 \times 10^8$ sec (bounded) at 90% C.L.[35]. The unbounded limit would lead to a limit of $\tau_{nnbar} > 3.82 \times 10^8$ sec at 90% CL if the measurement follow the same statistical conditions as this blinded study.

The experimental sensitivity for the SNO experiment has been defined in Section 7.5.3 as the average upper limit. The experimental sensitivity is $\tau_{nnbar} = (0.69/0.71) \times 10^8$ sec for respectively the (bounded/unbounded) limit in the blinded phase leading to an expected sensitivity of $\tau_{nnbar} = (1.35/1.38) \times 10^8$ sec for the full analysis.

This is lower than the possible reach discussed in Section 2.7 because of the detection efficiency which was assumed 100% is in reality 51.8% and the signal rate which was assumed as a Poisson limit of 2.3 events is about three time lower than the mean upper limit evaluated from Monte Carlo; this leads to a nuclear lifetime that is six time smaller than the total possible reach and a limit on τ_{nnbar} which is 40% of the total reach. This result includes the systematic errors within the evaluation of the upper limit.

8.1 Discussion of Results

The results found in this thesis were evaluated on the deuteron only. This is the first result of this target. As discussed in Section 2.7, an improvement in limits of 21% is expected by the inclusion of ^{16}O. Because of the propagation nature of pions, SNO is not sensitive in the evaluation of the individual decays channels and as such the different decays chosen in the case of the deuterons exhibit more or less the same behavior to each other as was seen

in Table 7.2.

The surrounding nucleons within ^{16}O add an extra complexity in the measurement of both proton decay or nnbar signal. A Monte Carlo study of the effect of these surrounding nucleons would need to be made in order to understand the full impact. However, as was studied in Chapter 3, charged pions interact heavily within the D_2O medium and their outgoing behavior will be similar to the one seen in the deuteron once they have exited ^{16}O; no major difference in the signal is expected.

8.2 Path to the Box Opening

The results presented in this thesis were done on a part of the total available data. An internal committee will need to review the analysis in order to open the blind data box for a full analysis of the SNO data. While the rate of the atmospheric events will remain constant throughout the phases, the combined three-phases detection efficiency and background expectation will be different because of the time weight of each phase is different. The detection efficiency for the three-phase analysis is 51.6%.

Prior to the isotropy cut, 134 ± 25 events of atmospheric neutrino backgrounds are expected for the full analysis; after the isotropy cut $b_{atmo} = 37.2 \pm 8.1$ events are expected. The instrumental background contribution will be around $b_{instr} = 0.183 \pm 0.130$ events; the instrumental contribution will be re-evaluated using the bifurcated analysis detailed in Section B.

3/4 remaining ($b_{tot} = 27.5 \pm 5.9$)		**Whole data** ($b_{tot} = 37.2 \pm 8.1$)	
count	excess	signal	total count
67	$6.7\sigma_b$	3σ	71
80	$8.8\sigma_b$	4σ	84
93	$11.0\sigma_b$	5σ	97

Table 8.1: Discovery potential in the non-open data set.

Bibliography

[1] Stephen Gasiorowicz. *Quantum Physics, Second Edition.* John Wiley & Sons, Inc, (1996).

[2] C Giunti and C.W Kim. *Fundamentals of Neutrino Physics and Astrophysics.* Oxford Press, (2007).

[3] A. D. Sakharov. Violation of CP invariance, C asymmetry, and baryon asymmetry of the universe. *JETP Lett*, 5:24–27, 1967.

[4] Y. Fukuda et al (Super Kamiokande Collaboration). Evidence for oscillation of atmospheric neutrinos. *Phys. Rev. Lett.*, 81(8):1562–1567, Aug 1998.

[5] J.N. Bahcall *et al. Solar Neutrinos, The First Thirty Years.* Westview Press, (202).

[6] B. Aharmim *et al.* (SNO Collaboration). Low-energy-threshold analysis of the phase I and phase II data sets of the sudbury neutrino observatory. *Phys. Rev. C*, 81(5):055504, May 2010.

[7] B. Aharmim *et al* (SNO Collaboration). Independent measurement of the total active B^8 solar neutrino flux using an array of ^3He proportional counters at the sudbury neutrino observatory. *Phys. Rev. Lett.*, 101(11):111301, Sep 2008.

[8] SNO Collaboration. *Measurement of the cosmic ray and neutrino-induced muon flux at the Sudbury neutrino observatory.* Phys. Rev. D 80, 012001, (2009).

[9] David Casper. The nuance neutrino physics simulation, and the future. *Nucl. Phys. Proc. Suppl.*, 112, 161, (2002).

[10] The SNO Collaboration. The sudbury neutrino observatory. *Nucl.Instrum.Meth*, A449:172–207, 2000.

[11] ZEBRA. CERN Program Library Long Writeup Q100/101, CERN, Geneva, Switzerland.

[12] CERN. http://geant4.cern.ch/.

[13] CERN. http://root.cern.ch/.

[14] A. Fasso *et al.* FLUKA: present status and future developments. *Proc. IV Int. Conf. on Calorimetry in High Energy Physics,La Biodola (Italy), Ed. A. Menzione and A. Scribano, World Scientific, p. 493-502*, 21-26 September 1993.

[15] T. A. Gabriel, J. E. Brau, and B. L. Bishop. The physics of compensating calorimetry and the new calor89 code system. *IEEE Trans. Nucl. Sci.*, 36, 14, 1989.

[16] R.W. Nelson *et al.* The egs4 code system. *Technical Report 265*, SLAC, 1985.

[17] Neil K. McCauly. *Producing a Background Free Data Set for Measurement of the Charge Current Flux and Day-Night Asymmetry at the Sudbury Neutrino Observatory, PhD Thesis.* The Queen's College, Oxford, (2001).

[18] Hendrick Labranche. *Time Series Analysis For The Cf Source in Sudbury Neutrino Observatory, MSc Thesis.* University of Guelph, (2003).

[19] Marc Bergevin. *Multiple Ring Fitter for the search for Baryon Number Violation in the Sudbury Neutrino Observatory, MSc Thesis.* University of Guelph, 2005.

[20] R.N. Mohapatra. Neutron anti-neutron oscillation: theory and phenomenology. *Journal of Physics G: Nuclear and Particle Physics*, 36:104006(18pp), 2009.

[21] K. Biswal, L. Maharana, and S. P. Misra. Proton decay in SU(5) in a field-theoretic quark model. *Phys. Rev. D*, 25(1):266–269, Jan 1982.

[22] Super-Kamiokande Collaboration. Search for proton decay via $p \to e+\pi$ and $p \to \mu+\pi$ in a large water cherenkov detector. *Phys. Rev. Lett.*, 102(14):141801, Apr 2009.

[23] Paul Langacker. Grand unified theories and proton decay. *Physics Reports*, 72(4):185 – 385, 1981.

[24] Bhaskar Dutta, Yukihiro Mimura, and R. N. Mohapatra. Suppressing proton decay in the minimal SO(10) model. *Phys. Rev. Lett.*, 94(9):091804, Mar 2005.

[25] H. S. Goh, R. N. Mohapatra, S. Nasri, and Siew-Phang Ng. Proton decay in a minimal SUSY SO(10) model for neutrino mixings. *Physics Letters B*, 587(1-2):105 – 116, 2004.

[26] Yu. Kamyshkov. Neutron-antineutron oscillation. *Nuclear Physics B - Proceedings Supplements*, 52(1-2):263 – 268, 1997.

[27] M. Baldo-Ceolin *et al.* A new experimental limit on neutron-antineutron oscillations. *Zeitschrift fr Physik C Particles and Fields*, 63:409–416, 1994. 10.1007/BF01580321.

[28] Yuri Kamyshkov. Private Comunication.

[29] Yuri Kamyshkov. Neutron Antineutron Oscillations. Large Detectors for Proton Decay, Supernovae and Atmospheric Neutrinos and Low Energy Neutrinos from High Intensity Beams Workshop at CERN, 16-18 January 2002.

[30] C. B. Dover, A. Gal, and J. M. Richard. Neutron-antineutron oscillations in nuclei. *Phys. Rev. D*, 27:1090, 1983.

[31] Kenneth S. Krane. *Introductory Nuclear Physics*. Wiley, 1988.

[32] Bernie Nickel. Private Comunication.

[33] E. Friedman and A. Gal. Realistic calculations of nuclear disappearance lifetimes induced by $n\bar{n}$ oscillations. *Phys. Rev. D*, 78(1):016002, Jul 2008.

[34] Carl B. Dover and J. M. Richard. Elastic, charge exchange, and inelastic $p\bar{p}$ cross sections in the optical model. *Phys. Rev. C*, 21(4):1466–1471, Apr 1980.

[35] Kenneth S. Ganezer. The Search for $n\bar{n}$ Oscillations at Super-Kamiokande I. Search for Baryon and Lepton Number Violations International Workshop Proceedings, Sept 2007, Lawrence Berkeley National Lab, http://inpa.lbl.gov/blnv2/proceedings.html.

[36] T Bressani and A Filippi. Antineutron physics. *Physics Reports*, 383:213–217, 2003.

[37] J. Chung *et al.* Search for neutron-antineutron oscillations using multiprong events in soudan 2. *Phys. Rev. D*, 66(3):032004, Aug 2002.

[38] B. Y. Oh, P. S. Eastman, Z. Ming Ma, D. L. Parker, G. A. Smith, and R. J. Sprafka. A formation study of interactions between 1.09 and 3.45 GeV/c (ii). strange particles. *Nuclear Physics B*, 51:57 – 76, 1973.

[39] R. Bridges *et al.* Difference spectra: Dominance of two-body cascades in antiproton-neutron annihilation at rest. *Phys. Rev. Lett.*, Vol 56, number 3:pp 215–18, (January, 1986).

[40] C.E. Okada S. Biller, J.A. Formaggio. Nucleon Decay Prospects in the Sudbury Neutrino Observatory. *internal document*, November 15, 2002.

[41] D.A. Fustin. Motivation for a neutron antineutron oscillation search in the sudbury neutrino observatory. August 2003.

[42] Marc Bergevin. n-nbar oscillation in SNO. Search for Baryon and Lepton Number Violations International Workshop Proceedings, Sept 2007, Lawrence Berkeley National Lab, http://inpa.lbl.gov/blnv2/proceedings.html.

[43] W.R. Leo. *Techniques for Nuclear and Particle Physics Experiments.* Springer-Verlag, (1994).

[44] The Muon and Atmospheric Neutrino Working Group. *μ-nidoc version 4, Unified Document for the Muon and Atmospheric Neutrino Analysis.* SNO str Documents, June 5, 2008.

[45] N. V. Groom, D. E. Mokhov and S. I. Striganov. Muon stopping power and range tables 10 MeV-100 TeV. *Atomic Data and Nuclear Data Tables*, 78, 183356, 2001.

[46] A.D. Marino and C. A. Currat. Muon Range in SNOMAN: A First Look. *internal document*, September 8, 2004.

[47] S. Eildeman *et al. Physical Review B, Review of Particle Physics, vol. 592, Issues 1-4.* Elsevier, (2004).

[48] Hugo W. Bertini. Intranuclear-cascade calculation of the secondary nucleon spectra from nucleon-nucleus interactions in the energy range 340 to 2900 MeV and comparisons with experiment. *Phys. Rev.*, 188(4):1711–1730, Dec 1969.

[49] T. Ullrich and Z. Xu. Treatment of errors in efficiency calculations. *arxiv/physics/0701199v1.*

[50] Christopher Conrad Maximillian Kyba. *Measurement of The Atmospheric Neutrino Induced Muon Flux at the Sudbury Neutrino Observatory, PhD Thesis.* University of Pennsylvania, (2006).

[51] Thomas John Sonley. *A Measurement of the Atmospheric Neutrino Flux and Oscillation Parameters at the Sudbury Neutrino Observatory, PhD Thesis.* MIT, 2009.

[52] T.K. Gaisser. *Cosmic Rays and Particle Physics.* Cambridge, (1990).

[53] Y. Ashie *et al.* (Super-Kamiokande). Evidence for an oscillatory signature in atmospheric neutrino oscillations. *Phys. Rev. Lett.*, 93(10):101801, Sep 2004.

[54] J. Favier, R. Kossakowski, and J. P. Vialle. Three-dimensional simulation of the atmospheric neutrinos. *Phys. Rev. D*, 68(9):093006, Nov 2003.

[55] Richard Van de Water. *Data Cleaning: The Q/NHIT Cut.* SNO internal document, University of Pennsylvania, April 20, 2000.

[56] R. O. Duda and P. E. Hart. Use of the hough transformation to detect lines and curves in pictures. *Comm. ACM*, Vol. 15:pp 11–15, (January, 1972).

[57] T. J. Radcliff. Pattern recognition for event-type identification in the sno detector sno-str-94-019. *SNO Internal Document*, june 22,1994.

[58] Tyron Tsui. *Through-Going Muons at the Sudbury Neutrino Observatory, PhD Thesis.* University of British Columbia, 2009.

[59] Josh Klein and Mark Neubauer. *Using Time and Angle Information in Reconstruction and the SNOMAN Fitter.* SNO-STR-2000-022, University of Pennsylvania, March 22, 2001.

[60] A Rolke, W, A.M. Lopez, and J Conrad. Limits and confidence intervals in the presence of nuisance parameters. *Nuclear Instruments and Methods in Physics Research Section A: Accelerators, Spectrometers, Detectors and Associated Equipment*, 551:493–503, 2005.

[61] Y Ashie *et al.* (Super-Kamiokande). Measurement of atmospheric neutrino oscillation parameters by super-kamiokande i. *Phys. Rev. D*, 71(11):112005, Jun 2005.

[62] W. Rolke A. Lopez J. Lundberg, J. Conrad. Limits, discovery and cut optimization for a poisson process with uncertainty in background and signal efficiency: Trolke 2.0. *Computer Physics Communications*, 181(3):683 – 686, 2010.

[63] G. D. Barr, T. K. Gaisser, P. Lipari, S. Robbins, and T. Stanev. Three-dimensional calculation of atmospheric neutrinos. *Phys. Rev. D*, 70(2):023006, Jul 2004.

Appendix A

Survival and Transition Probabilities

An important concept of particle physics is the transition between two quantum states. The probability that after a time t the state of the particle has not changed to another state is called "survival" probability while the probability that the state has changed is called "transition" probability.

A.1 Antineutron Transition Probability

As was described in section 2.3, the temporal Schroedinger equation is given by (with $\hbar = 1$),

$$i\frac{\partial}{\partial t}\begin{pmatrix} n \\ \bar{n} \end{pmatrix} = \begin{pmatrix} E_n & \delta m \\ \delta m & E_{\bar{n}} \end{pmatrix}\begin{pmatrix} n \\ \bar{n} \end{pmatrix} \equiv A\begin{pmatrix} n \\ \bar{n} \end{pmatrix}, \tag{A.1}$$

which corresponds to a linear differential equation in matrix form. The eigenvalue of A are $\lambda_{\pm} = \frac{1}{2}(E_n + E_{\bar{n}}) \pm \frac{1}{2}\sqrt{\Delta^2 E + 4\delta m^2}$ with $\Delta E \equiv E_n - E_{\bar{n}}$.

The A matrix from equation A.1 can be written in the SU(2) vectorial base[1] such that,

$$A = \frac{1}{2}\left(2\delta m \cdot \sigma_x + \Delta E \cdot \sigma_z\right) + \frac{1}{2}\left(E_n + E_{\bar{n}}\right) \cdot I \tag{A.2}$$

[1]The author would like to thank Bernie Nickel for pointing out the SU(2) property which leads to this elegant solution.

where I is the 2x2 identity matrix and σ_x and σ_z are the Pauli matrices. The e^{-iAt} expression can be expanded such that $e^{-iAt} = 1 + (-iAt) + \frac{1}{2!}(-iAt)^2 + \frac{1}{3!}(-iAt)^3 + ...$ the behavior of A^n needs to be understood in order to further reduce this expansion.

The $\frac{1}{2}(E_n + E_{\bar{n}}) \cdot I$ term will vanish as a phase: since $I\sigma_i = \sigma_i I$ when the absolute value is taken and the exponential can be expressed as $e^{-\frac{it}{2}(E_n+E_{\bar{n}})\cdot I} e^{-\frac{i}{2}(2\delta m\cdot\sigma_x+\Delta E\cdot\sigma_z)t}$; the interesting behavior is therefore confined to the σ_x and σ_z terms. Since $\sigma_x\sigma_z = -\sigma_z\sigma_x$ and $\sigma_i^2 = I$ for $i = x, y, z$, then,

$$\begin{aligned}(2\delta m \cdot \sigma_x + \Delta E \cdot \sigma_z)^n &= \gamma^n \cdot I & \text{; for even n} \\ (2\delta m \cdot \sigma_x + \Delta E \cdot \sigma_z)^n &= \gamma^n \cdot \left(\frac{2\delta m \cdot \sigma_x + \Delta E \cdot \sigma_z}{\gamma}\right) & \text{; for odd n}\end{aligned} \tag{A.3}$$

where $\gamma \equiv \sqrt{\Delta E^2 + 4\delta m^2}$. The expansion can then be reduced to,

$$e^{-\frac{i}{2}(2\delta m\cdot\sigma_x+\Delta E\cdot\sigma_z)t} = \cos\frac{\gamma t}{2}\cdot I - i\sin\frac{\gamma t}{2}\cdot\left(\frac{2\delta m\cdot\sigma_x + \Delta E\cdot\sigma_z}{\gamma}\right) \tag{A.4}$$

The probability of an neutron oscillating to a antineutron is given by $|<\bar{n}|e^{iAt}|n>|^2$ such that,

$$\begin{aligned}P_{\bar{n}}(t) &= \left|(0\ \ 1)\begin{pmatrix}\cos\frac{\gamma t}{2} + i\frac{\Delta E}{\gamma}\sin\frac{\gamma t}{2} & -i\frac{2\delta m}{\gamma}\sin\frac{\gamma t}{2} \\ -i\frac{2\delta m}{\gamma}\sin\frac{\gamma t}{2} & \cos\frac{\gamma t}{2} - i\frac{\Delta E}{\gamma}\sin\frac{\gamma t}{2}\end{pmatrix}\begin{pmatrix}1\\0\end{pmatrix}\right|^2 \\ P_{\bar{n}}(t) &= \frac{4\delta m^2}{\gamma^2}\sin^2(\frac{\gamma}{2}t).\end{aligned} \tag{A.5}$$

The final form of the transition probability is therefore:

$$P_{\bar{n}}(t) = \frac{4\delta m^2}{\Delta E^2 + 4\delta m^2}\sin^2\left(\frac{\sqrt{\Delta E^2 + 4\delta m^2}}{2}t\right) \tag{A.6}$$

Appendix B

Instrumental Background Estimate

The bifurcated analysis was used to estimate the amount of instrumental backgrounds events in the context of the SNO cosmic-ray and atmospheric neutrino flux analysis analysis [58]. It is used in this analysis to estimate the number of expected instrumental backgrounds that fall in the energy window defined in Table 4.2.

B.1 Bifurcated Analysis

The bifurcated analysis is a technique used to estimate the amount of instrumental contamination; this technique uses at least two orthogonal instrumental cuts. In the context of the nnbar analysis three instrumental removal cuts are isolated from the cuts defined in Table 4.2. These cuts are

- Cut 1 : Muon Burst Cut
- Cut 2 : Q/NHIT and Pmt_hit/NHIT Cuts

The other cuts from Table 4.2 are applied to the data, but are not otherwise used in the bifurcated analysis. The bifurcated analysis parameters are defined in Table B.1. In the limit where there is no signal sacrifice[1] ($\epsilon_1 = \epsilon_2 = 1$) then the signal and contamination

[1] In the context of this analysis, it will be shown in Appendix C that no signal loss is expected due to the muon burst cut. It was also shown in Chapter 4 that no loss is expected from the Pmt_hit/NHIT cut. For

	cut 2 Pass	cut 2 Fail
cut 1 Pass	a	d
cut 1 Fail	b	c

Table B.1: Bifurcated analysis parameter definition. Here a, b, c and d are the events that either pass/fail the two cuts. The convention is taken from [58]

follow the following relations,

$$\begin{aligned} a &= \nu + \lambda_1\lambda_2\beta \\ b &= (1-\lambda_1)\lambda_2\beta \\ c &= (1-\lambda_1)(1-\lambda_2)\beta \\ d &= (1-\lambda_2)\lambda_1\beta \end{aligned} \tag{B.1}$$

where ν is the signal and β is the total instrumental events, λ_i is the leakage fraction of the i cut [58]. In this limit than the leakage, signal and total instrumental events is given by,

$$\begin{aligned} \lambda_1 &= \frac{d}{c+d} \\ \lambda_2 &= \frac{b}{c+b} \\ \beta &= \frac{(c+d)(b+c)}{c} \\ \nu &= a - \lambda_1\lambda_2\beta = a - \frac{bd}{c} \end{aligned} \tag{B.2}$$

The instrumental contamination is given by $a - \nu = \lambda_1\lambda_2\beta = \frac{bd}{c}$. The values of the bifurcated analysis parameters for the different phases of SNO are shown in Table B.2. For the combined three-phase scenario, the leakage and signal estimate is given by,

$$\begin{aligned} \lambda_1 &= 0.066 \pm 0.026 \\ \lambda_2 &= 0.167 \pm 0.037 \\ \beta &= 109.2 \pm 19.7 \\ \nu &= 142.8 \pm 12.0 \\ \lambda_1\lambda_2\beta &= \frac{bd}{c} = 1.2 \pm 0.6 \quad \text{(contamination)} \end{aligned} \tag{B.3}$$

a more detailed treatment of the bifurcated analysis, the reader is encouraged to read [58]

B.2 MRF Behavior and Background Estimation

The $\epsilon_{multiple}$ and $\epsilon_{isotropy}$ cuts described in Section 7.4 are studied here for instrumental events. The total expected rate of instrumental events is given by

$$b_{inst} = \lambda_1 \lambda_2 \beta \epsilon_{multiple} \epsilon_{isotropy} \tag{B.4}$$

such that,

$$\begin{aligned} b_{inst} &= 0.024 \pm 0.022 \quad (\zeta_{thresh} = 15) \\ b_{inst} &= 0.048 \pm 0.034 \quad (\zeta_{thresh} = 13) \end{aligned} \tag{B.5}$$

for $T_{3phase} = 326.4$ days of the blinded analysis.

D_2O	cut 2 Pass	cut 2 Fail
cut 1 Pass	74	6
cut 1 Fail	11	36
Salt	cut 2 Pass	cut 2 Fail
cut 1 Pass	25	0
cut 1 Fail	3	13
NCD	cut 2 Pass	cut 2 Fail
cut 1 Pass	45	0
cut 1 Fail	3	36
Total	cut 2 Pass	cut 2 Fail
cut 1 Pass	144	6
cut 1 Fail	17	85

Table B.2: Bifurcated analysis parameter values for all blinded phases. In the case of the D_2O phase, two bursts with more than 120 events in each burst are seen at the very beginning of the D_2O phase. These events were taken out due to a possible bias in the estimation of instrumental noise for the remainder of the the three phases of SNO.

	$\epsilon_{multiple}$	$\epsilon_{isotropy}$	ϵ_{total}
$\zeta_{thresh} = 15$	0.05±0.02	0.40±0.17	0.02±0.02
$\zeta_{thresh} = 13$	0.07±0.03	0.57±0.16	0.04±0.02
$\zeta^{\dagger}_{thresh} = 15$	0.31±0.03	0.95±0.03	0.29±0.03
$\zeta^{\dagger}_{thresh} = 13$	0.37±0.03	0.97±0.02	0.36±0.03

Table B.3: Instrumental multiple ring detection efficiency and the isotropy cut efficiency for the 108 events instrumental events from Table B.2. †Run 10141 and 10177 contained intense burst of 245 successive events that fell within the energy window described in Table 4.2; these events are similar to each other and the inclusion of them would create a bias in the estimation of the detector condition for the rest of the detector livetime.

Appendix C

Muon Burst Cut Characterization

Flags used in data to tag either retrigger or muon burst events[1] are not present in the Monte Carlo simulations. A study is made to understand the possible sacrifice of either atmospheric or nnbar events these cut may have. It will be shown in this section that no significant sacrifice is seen.

The study of both these cuts and the study of instrumental noises can be made through a Time Series Analysis (TSA) [18]. While the Muon burst cut has been studied in the context of a previous publication [8], a cross-check on the sacrifice of this cut is made for nnbar events.

The Time Series Analysis offers a unique view in identifying the first and last event in a burst and all the events in between.

C.1 Time Series analysis (TSA)

The time difference between the event and the previous event and the time difference between the event and the next event is recorded in a two dimensional matrix ($\Delta T_{previous}$, ΔT_{next}). This classification of events separates events into four main categories:

The long and short concept is arbitrary and a proper boundary needs to be defined: a

[1]The DAMN masks were not filled in muon, atmospheric neutrino or nnbar simulations

Long-Short ΔT	Long-Long ΔT
Short-Short ΔT	Short-Long ΔT

boundary of 10 seconds is used for the classification of the different type of events,

- Long $\equiv \Delta$T $>$ 10 sec
- Short $\equiv \Delta$T $<$ 10 sec

A Long-Long entry represent events that have no other previous or following events in the 10 sec time window. A Long-Short entry represent the first event in the series of burst. A Short-Long entry represent the last entry in the burst. A Short-Short entry represent the events in between the first and last event in the burst.

The plot shown in Figure C.1 shows respectively: the Nhits distribution for events within the different time windows, the two-dimensional TSA time array showing the behavior of all possible events within the detector and the burst distribution of events. No cuts have been applied with the exception of a cut on events with Nhits $<$ 1000.

The lower limit shown on the plot allows events of 10 nanosecond of time difference while the upper bound is larger than the lifetime of all phases (the largest of which being the salt phase with a lifetime of 4.315 x 10^7 sec) before the two cuts. After the two cuts, no events are seen in the LS, SS and SL sections.

Retrigger

The retrigger cut is a flag placed on any event that has occurred within 5 μs of a previous event; this translates to a value of -5.3 on the log scale of Figure C.1. Most events be it cosmic, atmospheric neutrino or nnbar will have retrigger events after the prompt event; as can be seen in Figures C.2 and C.3, there are clusters of events below a Log(ΔT$_{after}$) value of -5.3.

Muon Burst Cut

The muon burst cut is a flag on events when four events with greater than 250 Nhits

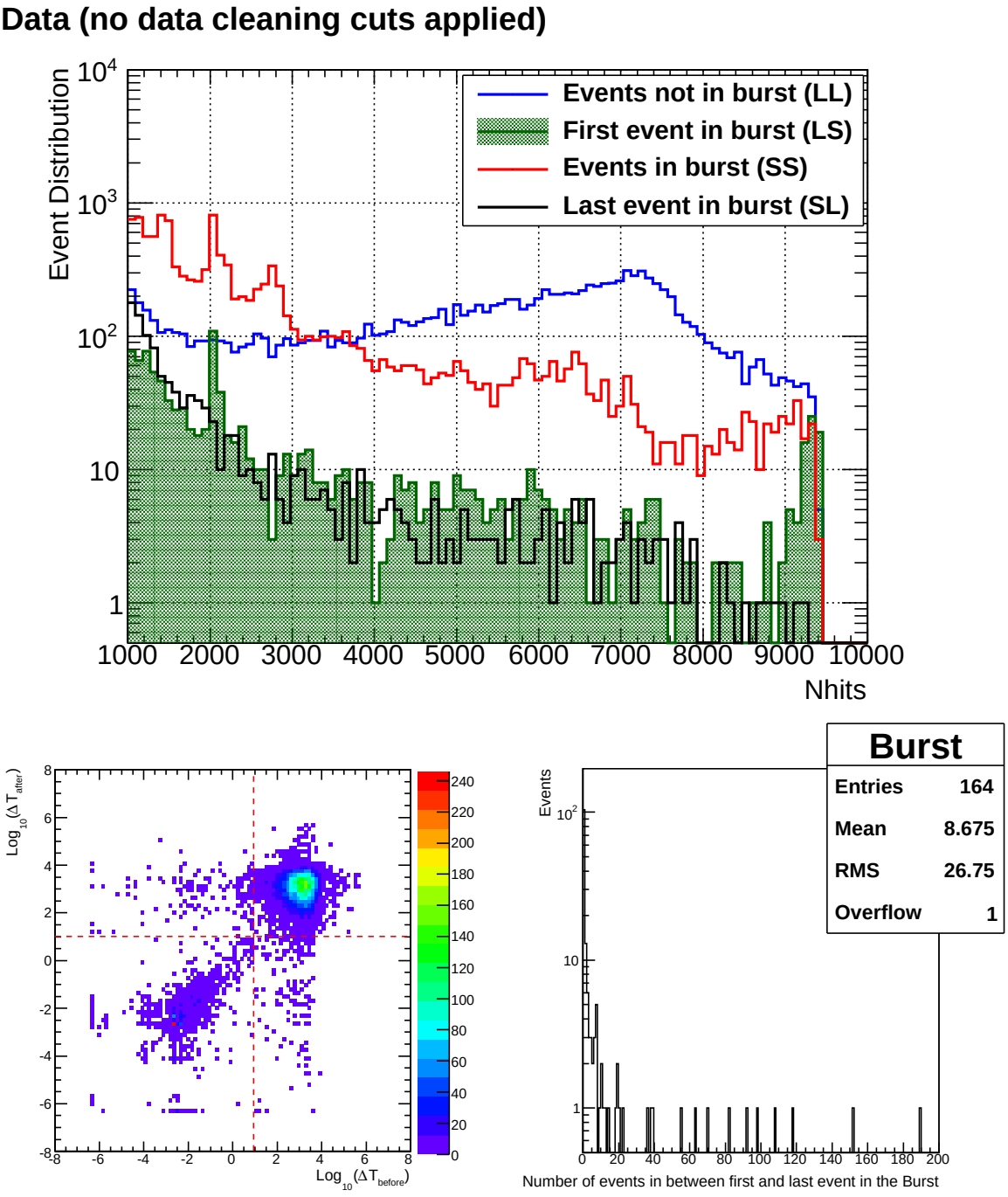

Figure C.1: The TSA distribution for data in the D_2O phase. The upper right section shows the LL section where no events are seen before or after a time window of 10 sec. The upper left section shows event that have a following event in a 10 sec window, but with no previous event in a 10 sec window. The lower right and left section show events that follow a primary or even a secondary event; in the case of the lower right section events represent the last event of a burst. Also shown are the Nhits distribution for the various TSA regions and the number of events within each bursts.

occur within two second of each another not including retrigger events. On Figure C.1 is represented the TSA distribution and the multiplicity of instrumental burst.

Atmospheric and Neutron antineutron Sacrifice

The information that will survive a retrigger cut are located in the LL and LS distributions of Figures C.2 and C.3. Information in the SS and SL distributions of Figures C.2 and C.3 are in majorities below the retrigger limit of -5.3.

In the case of the nnbar events a very small fraction of signal is below Nhits < 2000 (less than 0.36%). While some spillover from the 5 μs cut is present ($\approx 10\%$), no events are be rejected by the Muon burst cut by applying a retrigger cut on ΔT_{after} as can be seen in Figure C.4. In the case of the atmospheric events, less than 0.01 retrigger events are expected with values of Nhits > 2000; this justifies the use of the Monte Carlo simulation with the absence of the retrigger cut. There are events with high multiplicity of retrigger events that are due to very energetic neutrino interactions that will not be considered for the analysis. No atmospheric events are expected to be cut in the energy window of interest of this analysis.

Once the retrigger cut as been applied, 0.04% of nnbar events would contain 3 events within a time window of 2 seconds, but no 4 events in a burst as shown in Figure C.4. For atmospheric events, less than 9.29×10^{-6} of events will have 3 events within a burst and no 4 events are present as shown in Figure C.5.

No significant sacrifice for atmospheric neutrino events or nnbar events is measured.

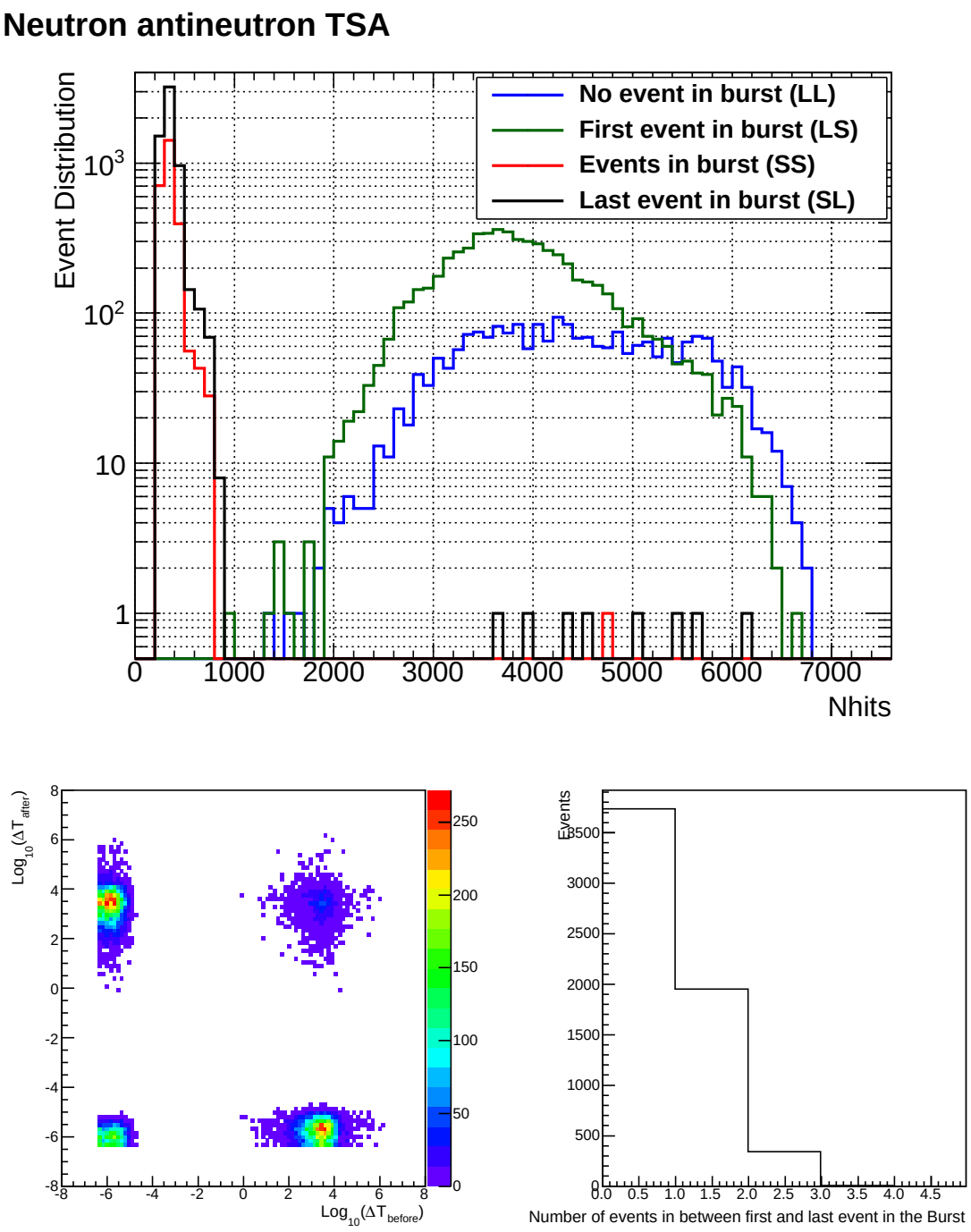

Figure C.2: The TSA distribution for nnbar Monte Carlo in the D_2O phase. The upper right section shows the LL section where no events are seen before or after a time window of 10 sec. The upper left section shows event that have a following event in a 10 sec window, but with no previous event in a 10 sec window. The lower right and left section show events that follow a primary or even a secondary event; in the case of the lower right section events represent the last event of a burst. Also shown are the Nhits distribution for the various TSA regions and the number of events within each bursts.

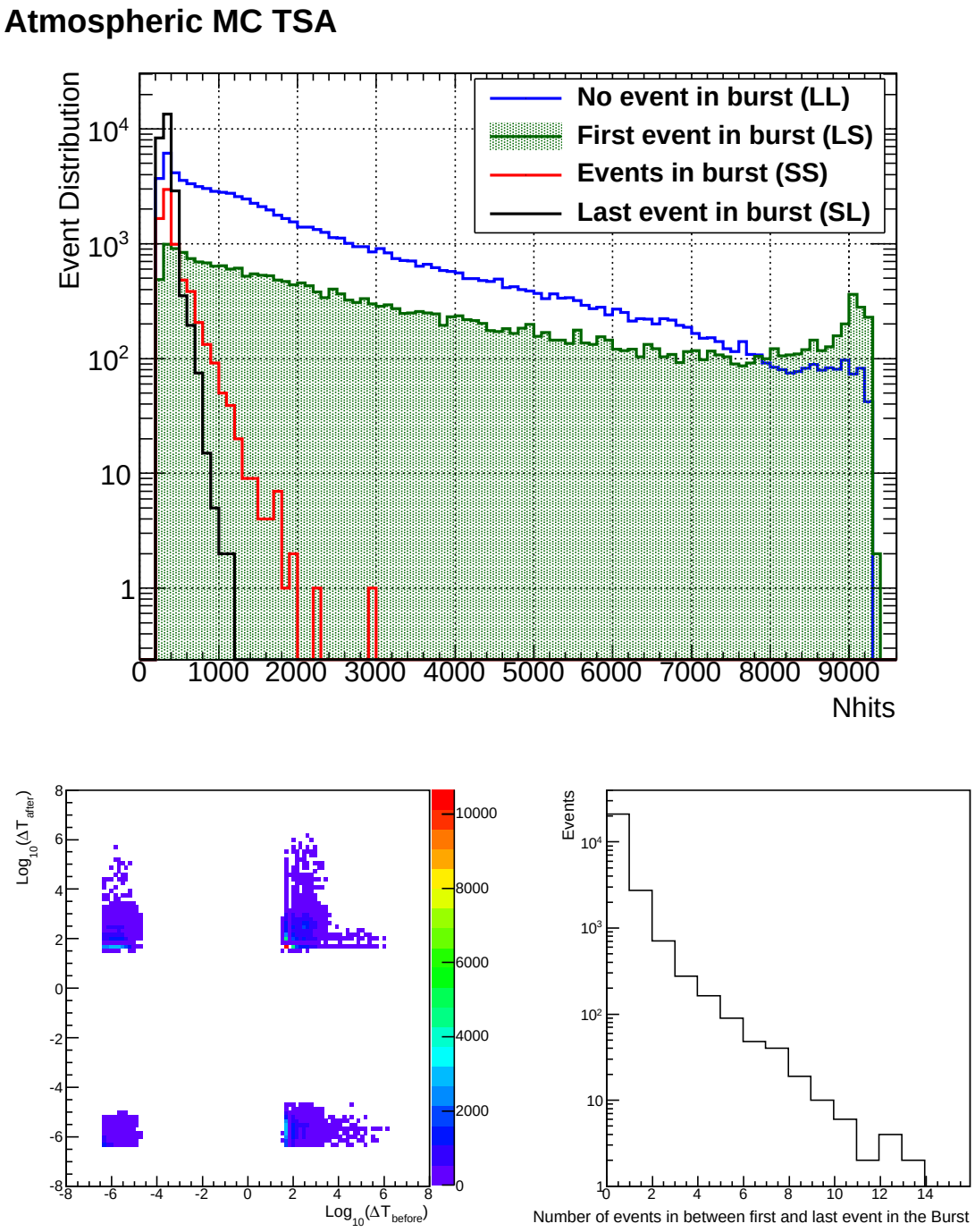

Figure C.3: The TSA distribution for atmospheric Monte Carlo in the D_2O phase. The upper right section shows the LL section where no events are seen before or after a time window of 10 sec. The upper left section shows event that have a following event in a 10 sec window, but with no previous event in a 10 sec window. The lower right and left section show events that follow a primary or even a secondary event; in the case of the lower right section events represent the last event of a burst. Also shown are the Nhits distribution for the various TSA regions and the number of events within each bursts.

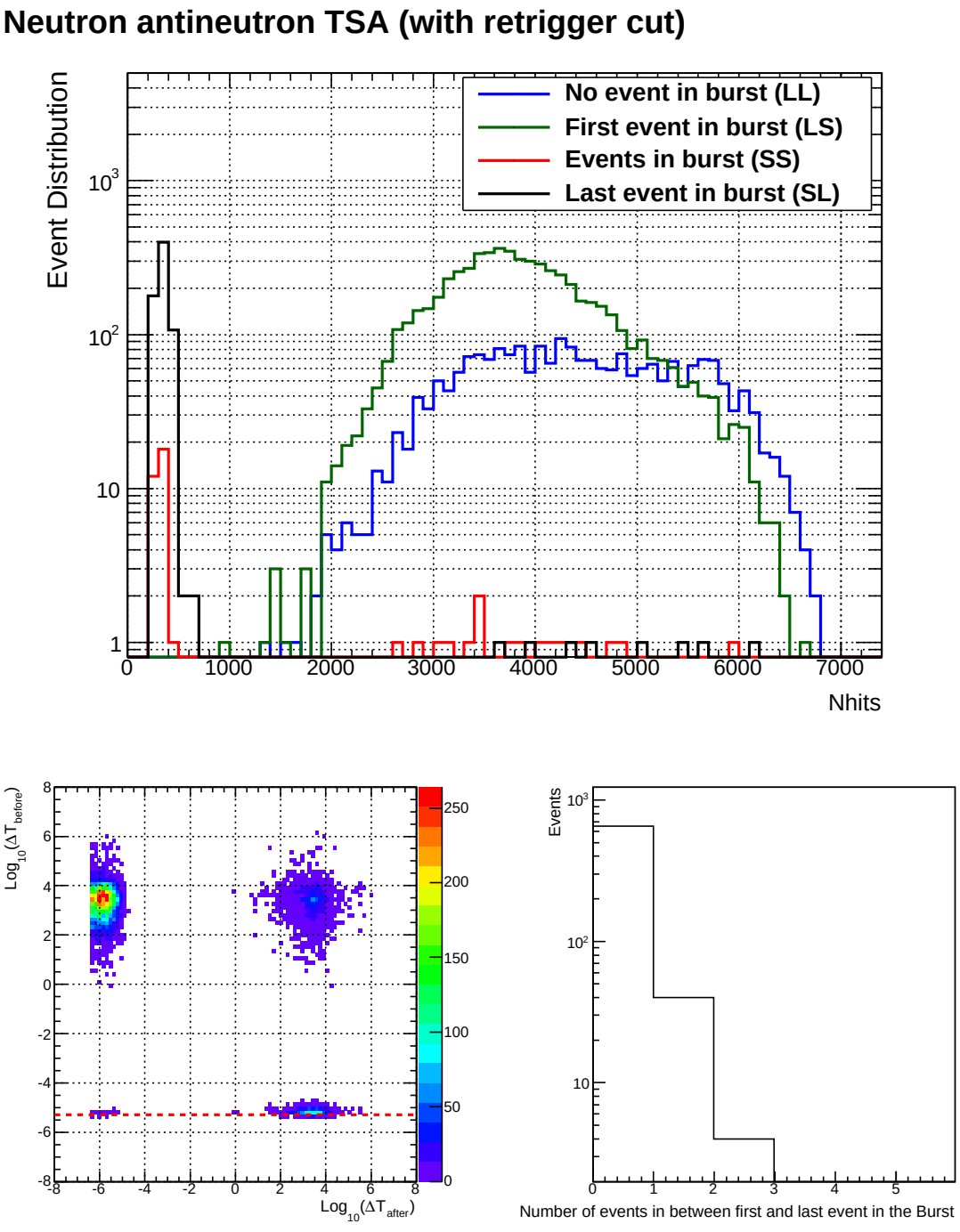

Figure C.4: The TSA distribution for nnbar Monte Carlo in the D_2O phase with the retrigger cut applied. There are no bursts with 4 events or more after the application of the retrigger cut; the muon burst cut will not remove nnbar events. The upper right section shows the LL section where no events are seen before or after a time window of 10 sec. The upper left section shows event that have a following event in a 10 sec window, but with no previous event in a 10 sec window. The lower right and left section show events that follow a primary or even a secondary event; in the case of the lower right section events represent the last event of a burst. Also shown are the Nhits distribution for the various TSA regions and the number of events within each bursts.

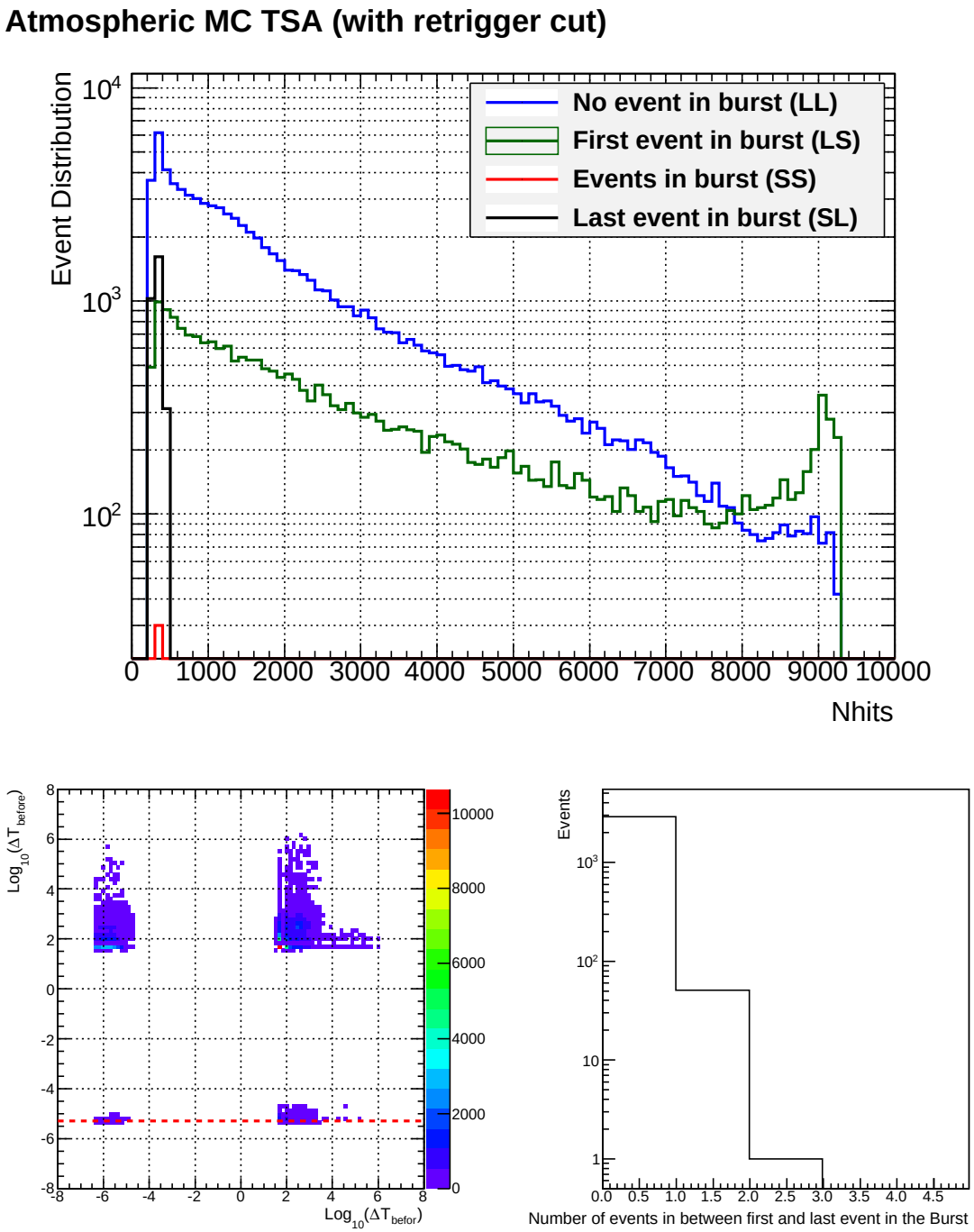

Figure C.5: The TSA distribution for atmospheric Monte Carlo in the D_2O phase with the retrigger cut applied. There are no bursts with 4 events or more after the application of the retrigger cut; the muon burst cut will not remove atmospheric neutrino events. The upper right section shows the LL section where no events are seen before or after a time window of 10 sec. The upper left section shows event that have a following event in a 10 sec window, but with no previous event in a 10 sec window. The lower right and left section show events that follow a primary or even a secondary event; in the case of the lower right section events represent the last event of a burst. Also shown are the Nhits distribution for the various TSA regions and the number of events within each bursts.

Appendix D

Miscellaneous Tables

$\zeta_{threshold}$	$\epsilon_{primary}$	(x'_{rec}, x'_{rms}) (cm)	$(\theta_{rec}, \theta_{rms})$ (degree)	$\epsilon_{secondary}$	(x_{rec}, x_{rms}) (cm)	$(\theta_{rec}, \theta_{rms})$ (degree)	Multiplicity
[(0,0,0),(isotropic)] Muon Dataset, 4839 Entries fitted with e-Like ξ_{exp}							
9	1.0000	(215.8,123.4)	(46.9,46.3)	0.8540	(347.3,170.5)	(21.9,15.8)	(3.40,1.36)
10	1.0000	(141.6,32.7)	(9.3,11.8)	0.6673	(467.6,85.2)	(27.4, 5.4)	(1.93,0.83)
11	1.0000	(139.9,19.9)	(7.7, 2.5)	0.3536	(478.9,62.4)	(27.8, 3.7)	(1.41,0.60)
12	1.0000	(140.5,18.5)	(7.6, 1.4)	0.1439	(484.1,61.7)	(27.3, 3.6)	(1.16,0.40)
13	1.0000	(141.1,18.5)	(7.5, 1.4)	0.0511	(482.4,73.7)	(26.8, 4.0)	(1.06,0.24)
14	1.0000	(141.4,15.0)	(7.4, 1.2)	0.0159	(491.9,74.5)	(26.7, 3.8)	(1.02,0.14)
15	1.0000	(142.1,14.3)	(7.3, 1.2)	0.0048	(521.8,56.1)	(26.5, 1.9)	(1.01,0.08)
16	1.0000	(143.0,14.9)	(7.2, 1.2)	0.0019	(548.3,14.9)	(25.9, 1.6)	(1.00,0.06)
17	1.0000	(143.9,17.4)	(7.1, 1.3)	0.0012	(489.9,120.8)	(23.9, 5.5)	(1.00,0.05)
[(0,0,0),(isotropic)] Muon Dataset, 4839 Entries fitted with μ-Like ξ_{exp}							
9	0.8389	(-1.8, 8.1)	(1.5, 0.8)	0.0002	(0.0, 0.0)	(0.0, 0.0)	(1.00,0.00)
10	0.7921	(0.5, 8.4)	(1.5, 0.8)	0.0002	(0.0, 0.0)	(0.0, 0.0)	(1.00,0.00)
11	0.7217	(2.8, 8.4)	(1.5, 0.7)	0.0002	(0.0, 0.0)	(0.0, 0.0)	(1.00,0.00)
12	0.6263	(5.0, 8.2)	(1.4, 0.7)	0.0002	(0.0, 0.0)	(0.0, 0.0)	(1.00,0.00)
13	0.5106	(6.9, 7.6)	(1.4, 0.7)	0.0002	(0.0, 0.0)	(0.0, 0.0)	(1.00,0.00)
14	0.3770	(8.2, 6.9)	(1.4, 0.7)	0.0002	(0.0, 0.0)	(0.0, 0.0)	(1.00,0.00)
15	0.2669	(9.2, 6.2)	(1.4, 0.7)	0.0000	(0.0, 0.0)	(0.0, 0.0)	(1.00,0.00)
16	0.1727	(10.1, 5.4)	(1.4, 0.7)	0.0000	(0.0, 0.0)	(0.0, 0.0)	(1.00,0.00)
17	0.1025	(10.3, 5.1)	(1.4, 0.7)	0.0000	(0.0, 0.0)	(0.0, 0.0)	(1.00,0.00)

Table D.1: μ^- vertex and multiplicity reconstruction for primary and secondary MRF ring triggers. The Monte Carlo dataset is fitted with both e-like and μ-like ξ_{exp}.

$\zeta_{threshold}$	$\epsilon_{primary}$	(x'_{rec}, x'_{rms}) (cm)	$(\theta_{rec}, \theta_{rms})$ (degree)	$\epsilon_{secondary}$	(x_{rec}, x_{rms}) (cm)	$(\theta_{rec}, \theta_{rms})$ (degree)	Multiplicity
[(0,0,0),(isotropic)] Neutral Pion Dataset, 4888 Entries							
9	0.9998	(159.5,180.4)	(63.6,43.8)	0.9499	(294.1,197.4)	(34.1,17.6)	(5.92,1.33)
10	0.9998	(72.6,129.0)	(20.8,25.3)	0.9910	(370.8,160.2)	(37.2,10.3)	(4.69,0.99)
11	0.9998	(50.6,94.1)	(13.6, 9.3)	0.9887	(364.4,161.8)	(36.4, 8.5)	(3.86,0.95)
12	0.9998	(47.2,85.6)	(13.1, 7.9)	0.9384	(327.0,176.1)	(34.6, 8.6)	(3.00,0.92)
13	0.9998	(43.7,76.7)	(12.7, 7.4)	0.7932	(270.6,186.9)	(32.5, 8.7)	(2.30,0.88)
14	0.9996	(40.9,68.5)	(12.4, 6.9)	0.6240	(204.3,181.8)	(30.2, 8.5)	(1.85,0.78)
15	0.9996	(40.1,63.0)	(12.2, 6.6)	0.4840	(148.9,160.2)	(27.7, 8.2)	(1.59,0.67)
16	0.9988	(40.6,61.1)	(12.0, 6.4)	0.3685	(110.7,130.5)	(25.6, 7.6)	(1.41,0.57)
17	0.9957	(41.8,60.8)	(11.8, 6.1)	0.2590	(87.4,103.1)	(24.1, 6.8)	(1.28,0.48)
[(isotropic),(isotropic)] Neutral Pion Dataset, 3802 Entries							
9	0.9970	(109.3,285.4)	(38.6,32.1)	0.9054	(292.5,200.5)	(47.3,23.1)	(4.39,1.65)
10	0.9965	(85.9,267.7)	(25.6,15.8)	0.8870	(310.9,204.1)	(48.5,20.8)	(3.40,1.28)
11	0.9957	(79.8,264.8)	(24.6,13.9)	0.8358	(307.4,211.2)	(48.4,20.4)	(2.73,1.03)
12	0.9940	(81.3,263.3)	(24.7,13.8)	0.7187	(296.2,215.4)	(47.7,20.4)	(2.20,0.92)
13	0.9859	(83.1,260.8)	(24.6,13.5)	0.5626	(280.9,218.3)	(46.0,20.6)	(1.81,0.80)
14	0.9721	(90.9,256.8)	(24.8,13.4)	0.4114	(256.0,218.8)	(43.1,20.1)	(1.54,0.69)
15	0.9396	(99.8,249.4)	(24.6,13.0)	0.2751	(239.0,207.0)	(40.3,20.1)	(1.34,0.56)
16	0.8783	(113.9,239.4)	(24.5,12.8)	0.1715	(231.5,192.6)	(37.1,18.9)	(1.21,0.44)
17	0.7762	(129.4,227.5)	(24.3,12.7)	0.0886	(216.1,182.7)	(33.8,18.1)	(1.12,0.34)

Table D.2: π^0 vertex and multiplicity reconstruction for primary and secondary MRF ring triggers. The Monte Carlo datasets for events and the origin and those generated isotropically within the AV are fitted with e-like ξ_{exp}.

$\zeta_{threshold}$	$\epsilon_{primary}$	(x'_{rec}, x'_{rms}) (cm)	$(\theta_{rec}, \theta_{rms})$ (degree)	$\epsilon_{secondary}$	(x_{rec}, x_{rms}) (cm)	$(\theta_{rec}, \theta_{rms})$ (degree)	Multiplicity
[(0,0,0),(isotropic)] Charged Pion Dataset, 9770 Entries **e-Like** ξ_{exp}							
9	0.8125	(176.9,135.7)	(40.0,37.2)	0.5410	(224.8,216.2)	(42.2,35.0)	(2.81,2.06)
10	0.7676	(154.4,119.8)	(33.9,34.6)	0.4291	(235.2,214.7)	(42.0,33.5)	(2.32,1.67)
11	0.7262	(141.5,105.9)	(30.4,32.3)	0.3469	(242.4,210.5)	(40.0,31.7)	(2.01,1.37)
12	0.6820	(133.8,94.3)	(28.5,30.8)	0.2811	(236.0,203.3)	(38.7,30.8)	(1.80,1.19)
13	0.6401	(132.3,88.0)	(27.3,29.8)	0.2325	(217.6,193.2)	(36.9,30.1)	(1.64,1.01)
14	0.5974	(131.0,81.8)	(26.1,28.9)	0.1953	(196.6,182.0)	(35.6,30.2)	(1.52,0.86)
15	0.5566	(129.4,77.3)	(24.9,28.1)	0.1599	(170.6,164.5)	(34.2,30.2)	(1.41,0.72)
16	0.5156	(128.5,73.3)	(23.3,26.8)	0.1258	(149.3,144.0)	(32.4,29.4)	(1.32,0.62)
17	0.4755	(126.5,68.0)	(21.7,25.3)	0.0950	(138.0,131.8)	(31.0,28.5)	(1.24,0.52)
[(0,0,0),(isotropic)] Charged Pion Dataset, 9770 Entries μ-**Like** ξ_{exp}							
9	0.1956	(15.9,34.9)	(8.5,16.9)	0.0001	(0.0, 0.0)	(0.0, 0.0)	(1.00,0.00)
10	0.1688	(18.5,31.0)	(8.0,16.0)	0.0001	(0.0, 0.0)	(0.0, 0.0)	(1.00,0.00)
11	0.1422	(19.8,26.7)	(6.9,14.4)	0.0001	(0.0, 0.0)	(0.0, 0.0)	(1.00,0.00)
12	0.1169	(20.1,22.4)	(5.8,12.7)	0.0001	(0.0, 0.0)	(0.0, 0.0)	(1.00,0.00)
13	0.0884	(21.5,21.6)	(5.3,11.9)	0.0000	(0.0, 0.0)	(0.0, 0.0)	(1.00,0.00)
14	0.0628	(21.7,15.6)	(4.5,10.8)	0.0000	(0.0, 0.0)	(0.0, 0.0)	(1.00,0.00)
15	0.0433	(22.0,13.4)	(3.8, 9.5)	0.0000	(0.0, 0.0)	(0.0, 0.0)	(1.00,0.00)
16	0.0261	(22.3,12.4)	(3.4, 8.9)	0.0000	(0.0, 0.0)	(0.0, 0.0)	(1.00,0.00)
17	0.0155	(23.2,11.1)	(3.0, 7.2)	0.0000	(0.0, 0.0)	(0.0, 0.0)	(1.00,0.00)

Table D.3: π^+ vertex and multiplicity reconstruction for primary and secondary MRF ring triggers. The Monte Carlo dataset is fitted with both e-like and μ-like ξ_{exp}.

Interaction Type	Channels	Γ_i/Γ (%) ($\nu_l/\bar{\nu}_l$) (3481/1353)	Total (%) ($\nu_l/\bar{\nu}_l$) (3481/1353)
Charged Current			**34.56/35.62**
CC Quasi-Elastic Interaction	$\nu_l N \to Nl$	19.48/24.83	
CC Deep Inelastic Interaction	$\nu_l N \to Nl$	15.08/9.16	
CC Cabibbo-suppressed Scattering	$\nu_l N \to Nl$	0.00/1.63	34.56/35.62
Neutral Current			**5.66/7.24**
NC Quasi-Elastic Interaction	$\nu_l N \to N^* l \to Nl$	0.06/0.00	
NC Deep Inelastic Interaction	$\nu_l N \to N^* l \to Nl\pi$	5.60/7.24	5.66/7.24
Single Pion Creation			**43.52/ 44.71**
CC Single Pion Creation	$\nu_l N \to N^* l \to Nl\pi$	36.83/33.11	
NC Single Pion Creation	$\nu_l N \to N^* \nu_l \to N\nu_l\pi$	2.93/3.99	
CC Diffractive/Coherent π Production		3.13/5.91	
NC Diffractive/Coherent π Production		0.63/1.70	43.52/ 44.71
Multiple Pion Creation			**16.16/12.34**
CC η Creation	$N^* \to N\eta$	1.72/0.81	
NC η Creation	$N^* \to N\eta$	0.57/0.30	2.29/1.11
CC ρ Creation	$N^* \to N\rho$	2.64/1.55	
NC ρ Creation	$N^* \to N\rho$	0.49/0.59	3.13/2.14
CC $\Delta + \pi$ Creation	$N^* \to N\Delta(1232)\pi$	7.12/4.88	
NC $\Delta + \pi$ Creation	$N^* \to N\Delta(1232)\pi$	1.29/2.07	8.31/6.95
CC Σ + K Creation	$N^* \to N\Sigma\mathrm{K}$	0.11/0.00	
NC Σ + K Creation	$N^* \to N\Sigma\mathrm{K}$	0.03/0.00	0.14/0.00
CC Λ + K Creation	$N^* \to N\Lambda\mathrm{K}$	0.52/0.22	
NC Λ + K Creation	$N^* \to N\Lambda\mathrm{K}$	0.00/0.15	0.52/0.37
CC Multiple Pion Creation	$\nu_l N \to N^* l \to Nl\pi\pi$	0.00/0.00	
NC Multiple Pion Creation	$\nu_l N \to N^* \nu_l \to N\nu_l\pi\pi$	1.67/1.77	1.67/1.77
Other process			**0.09/0.07**
Photonuclear Production	$\nu_l N \to Nl\gamma$	0.09/0.07	0.09/0.07
elastic scattering (electron)	$\nu_e e \to \nu_e e$	0.00/0.00	0.00/0.00
inverse muon decay		0.00/0.00	0.00/0.00

Table D.4: Atmospheric neutrino interactions prior to the isotropy cut integrated over all phases. This table shows the various possible background pion sources due to neutrino interactions for the SNO detector. Here N $\in [n, p]$.

Interaction Type	Γ_i/Γ (%) $(\nu_l/\bar{\nu}_l)$ (955/253)
Charged Current	**(25.9±1.4)/(27.3±2.8)**
Neutral Current	**(10.5±1.0)/(15.8±2.3)**
Single Pion Creation	**(42.3±1.6)/(38.3±3.0)**
Multiple Pion Creation	**(21.2±1.3)/(18.6±2.4)**
Other process	**(0.2±0.2)/(0.0±0.4)**

Table D.5: Atmospheric neutrino interactions after isotropy cut. This table shows the various possible background pion sources due to neutrino interactions for the SNO detector. Here N $\in [n, p]$.

Appendix E

Neutrino Antineutrino Flux Discussion

The neutrino and antineutrino ratio shown in Table 3.2 - with the ratio $\frac{\nu}{\bar{\nu}} = 2.79$ ($\frac{\nu_\mu}{\bar{\nu}_\mu} = 2.51$, $\frac{\nu_e}{\bar{\nu}_e} = 3.04$) - seems to be in disagreement with the proposition of Section 4.4 that $\frac{\nu_\mu}{\bar{\nu}_\mu} \simeq 1$, $\frac{\nu_e}{\bar{\nu}_e} \simeq \frac{\phi_{\mu^+}}{\phi_{\mu^-}}$ and $\frac{\nu_\mu + \bar{\nu_\mu}}{\nu_e + \bar{\nu_e}} \simeq 2$.

The resolution to this discrepancy comes in two parts: the proposition applies only to the flux without taking into account the neutrino and anti-neutrino cross-sections; at higher energies the neutrino-antineutrino ratio increases [63], this as an impact to the ratio since the nnbar analysis samples atmospheric neutrinos in a specific energy window.

In the Bartol publication [63], the cross-section difference between the neutrino and antineutrino is estimated as $\frac{1}{2}\bar{\nu}$ will contribute to the e-like and μ-like neutrino events[1] and these show good agreement to the Super-Kamiokande data.

Shown in Figures E.1 and E.2 are the 3D estimates of the neutrino ratios as a function of energy and zenith angle. At higher energies there are less antineutrino interactions than neutrino interactions. For the energy window of interest of the nnbar search, this explain the difference of neutrino to antineutrino seen in Table 3.2.

[1] Figure E.1 shows to expected neutrino events as $\nu + \frac{1}{2}\bar{\nu}$.

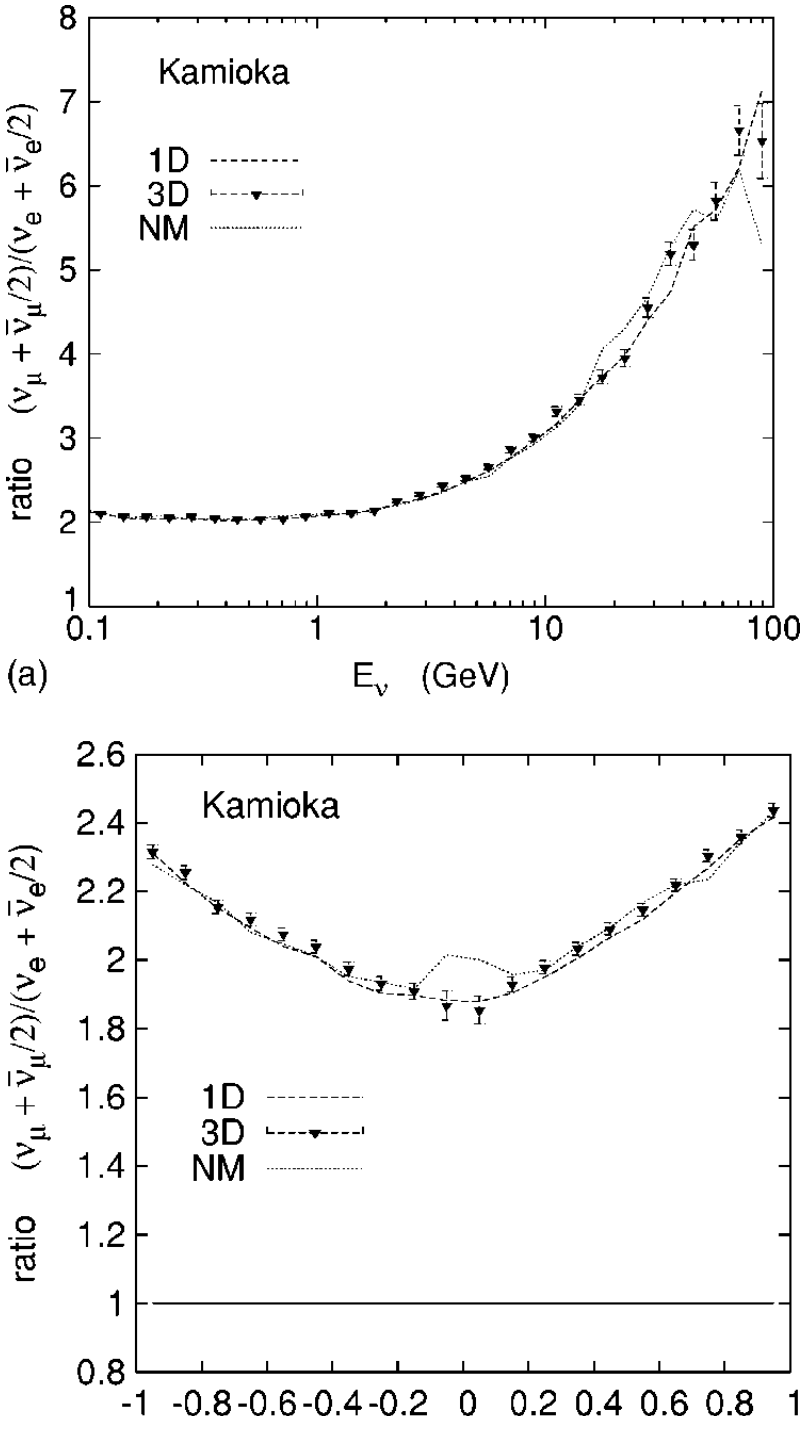

Figure E.1: Super-K atmospheric $(\nu_\mu + \bar{\nu}_\mu/2)/(\nu_e + \bar{\nu}_e/2)$ ratio. The factor of 1/2 is there to approximate the anti-neutrino cross-section difference.

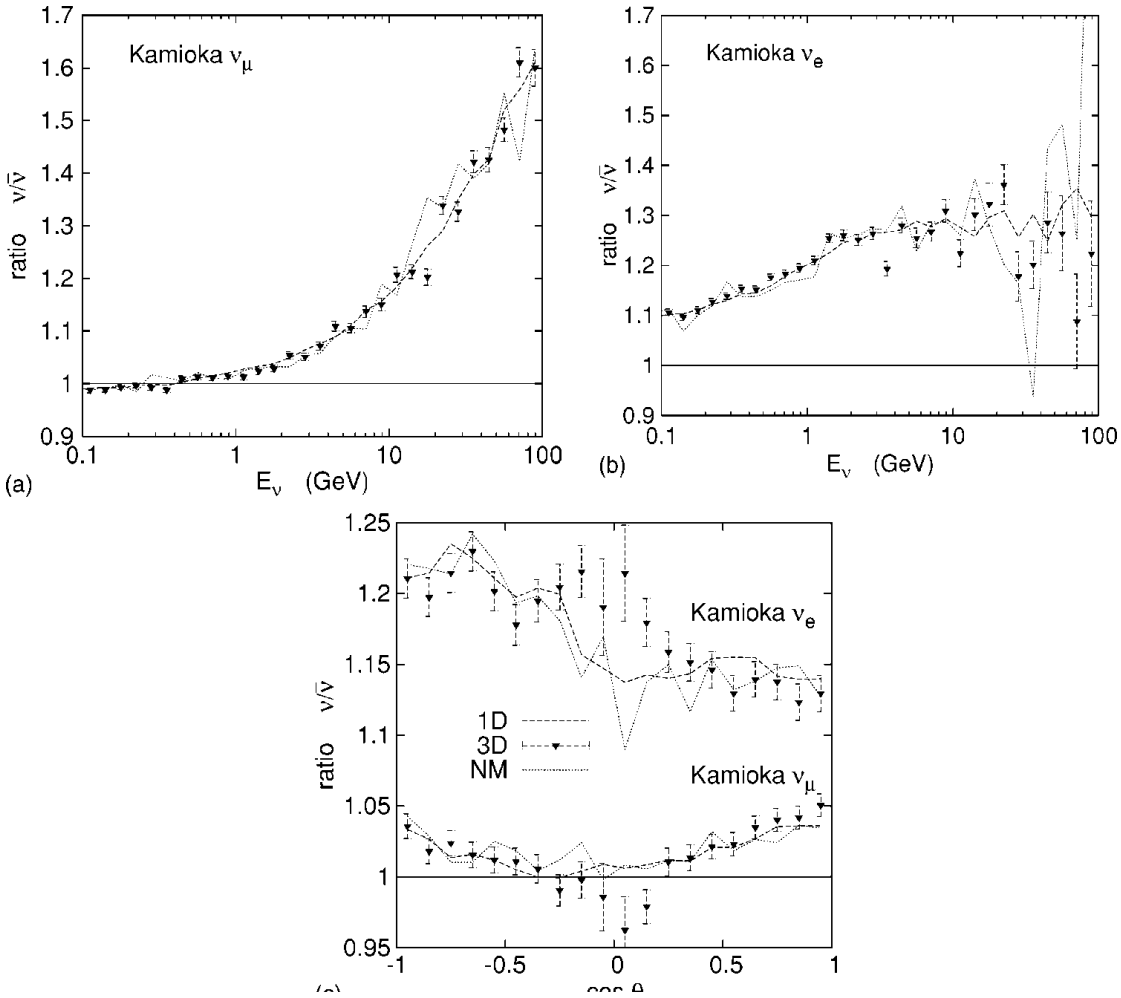

Figure E.2: Super-K atmospheric $\nu/\bar{\nu}$ ratio. At higher energy more neutrino events than antineutrino events will be observed in the detector.

Appendix F

Run List Addendum

Run list used for atmospheric neutrino analysis [8] may be found in [44][50]. A problem was found in some of the atmospheric Monte Carlo files in the NCD phase.

F.1 Atmospheric Monte Carlo NCD problem files

A small fraction of files have different entries between the ntuple and root files in the NCD phase. These file are taken out of the atmospheric run list and the detector livetime is adjusted accordingly. The total lifetime correction for the atmospheric Monte Carlo is:

Number of runs	: 46
Total length	: 992022.37 seconds
Total length(50MHz)	: 992010.64 seconds
Raw length	: 11.4817 days
Raw length(50MHz)	: 11.4816 days

leading to a shorter lifetime by 2.9%. These files are:

[050388 050434 050457 050464 050683 050703 051358 051445 051454 051560 051724 051744 051760 052287 052310 052314 052339 052624 054705 054773 055524 055616 055655 057376 057483 058290 058310 060192 060937 061184 061196 061207 061753 061755 061782 061785 061788 061889 062296 063132 063210 063829 063830 065586 065889 066386]

Appendix G

Event Visualization

The pathologies events are shown with XSnoed visualization software for both events that have been generated by Monte Carlo and the SNO data from the open data set.

G.1 Cosmic and Upward going muons

The most probable physical class of events are cosmic muons. Clipping muons are more probable than muons that pass in the middle of the detector due to the circular surface area. These clipping muons mimic electron events in the MRF and are used to calibrate the MRF routines.

Shown in Figure G.2 is the example of a stopping muon. These events are particularly prone to the "edge of the ring" ring mis-identification.

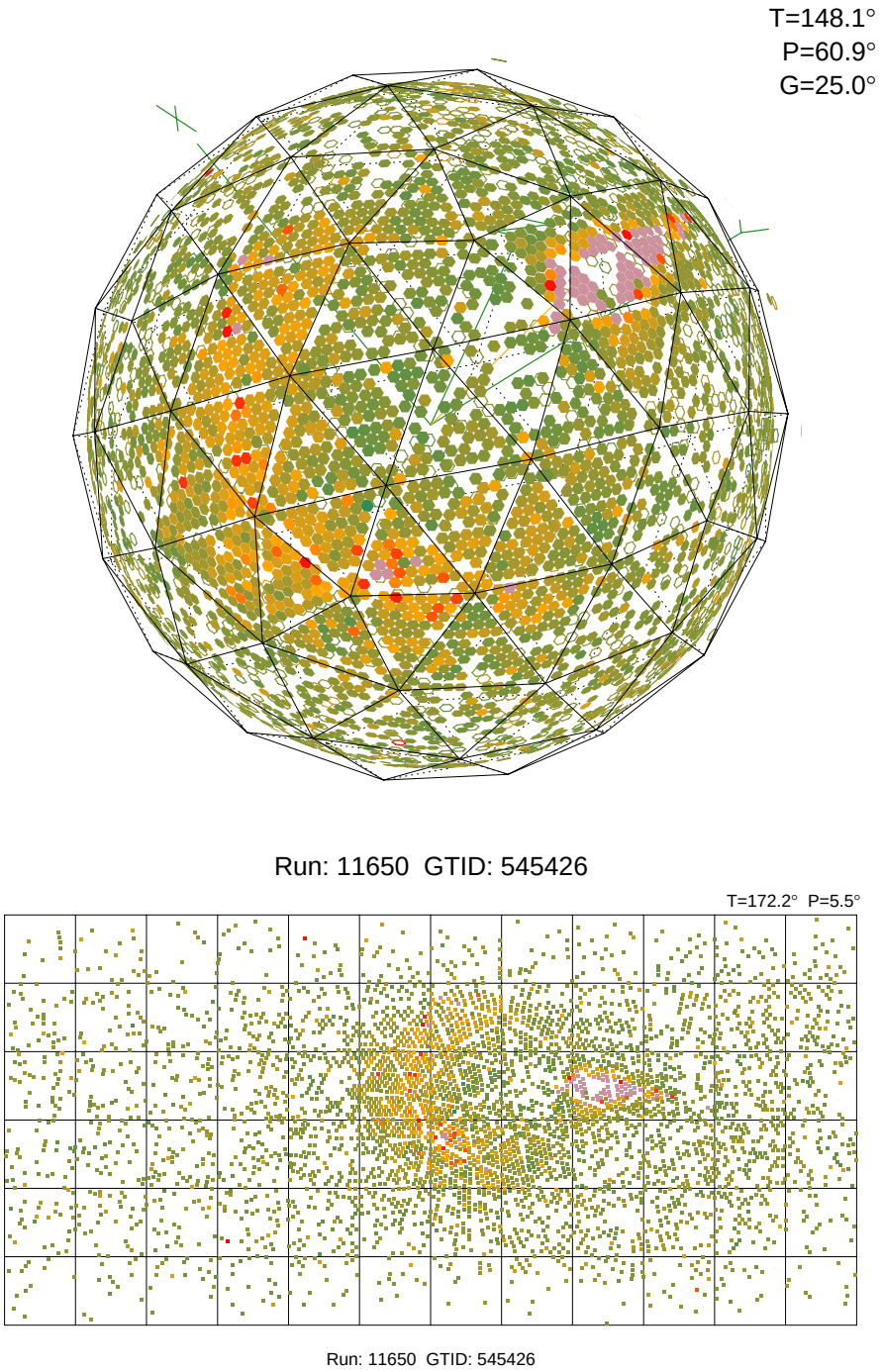

Figure G.1: XSnoed display of a clipping muon within the SNO data with P/E value of 0.436.

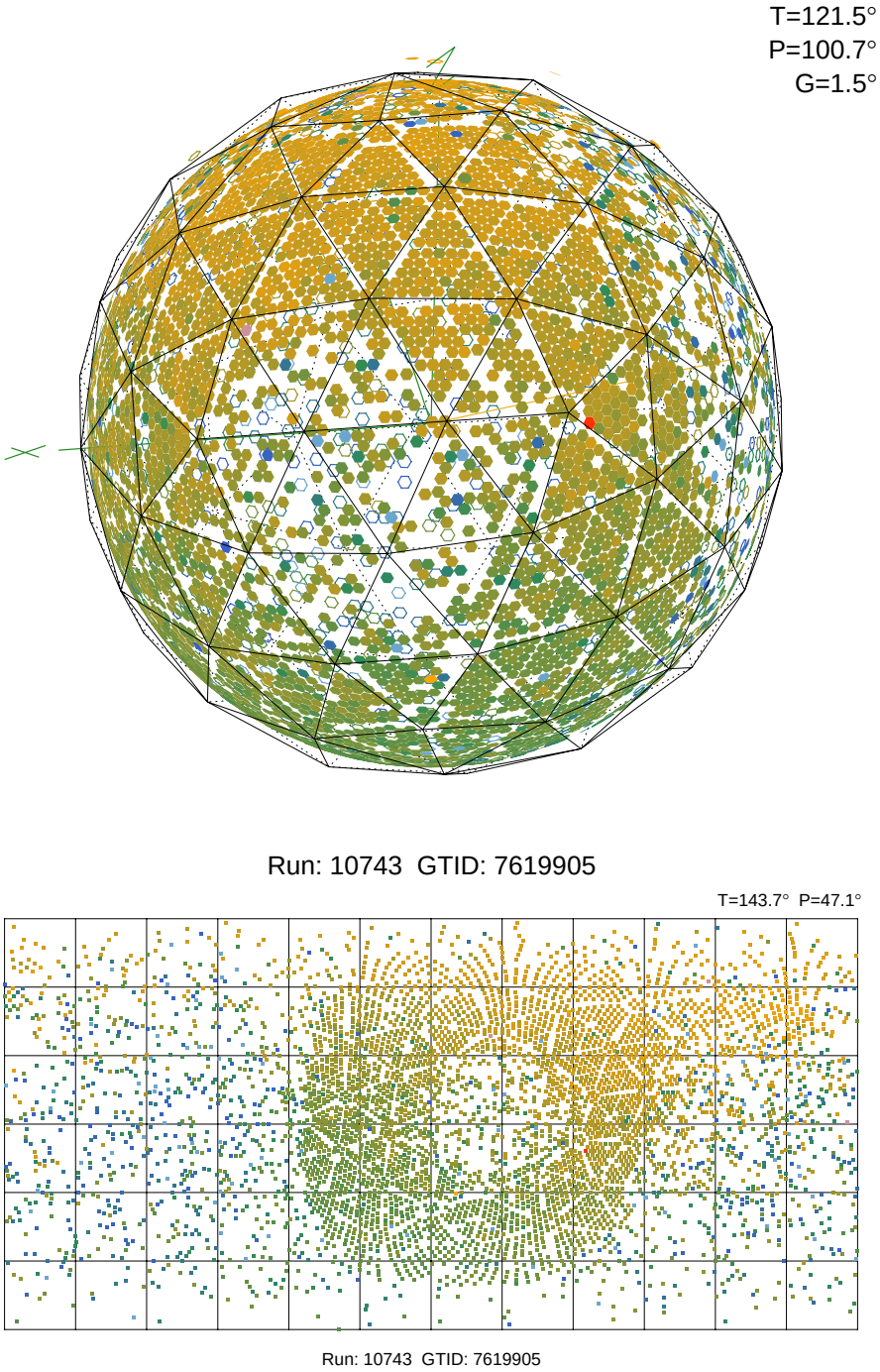

Figure G.2: XSnoed display of a stopping Muon within the SNO data with P/E value of 0.634.

G.2 Instrumental Noise

Shown in this section are two of the main instrumental noise sources.

- Flashers usually have lower energy than the neutron anti-neutron signal window, however there is a tail of high energy flashers that have a tube count higher than 1000 Nhits.

- Electronic pickup events will usually appear in intense bursts. Two example are presented, one with only the pickup event and the other having a burst of light in addition to the pickup event. The Pmt_hit/NHIT was created to remove the second type of events.

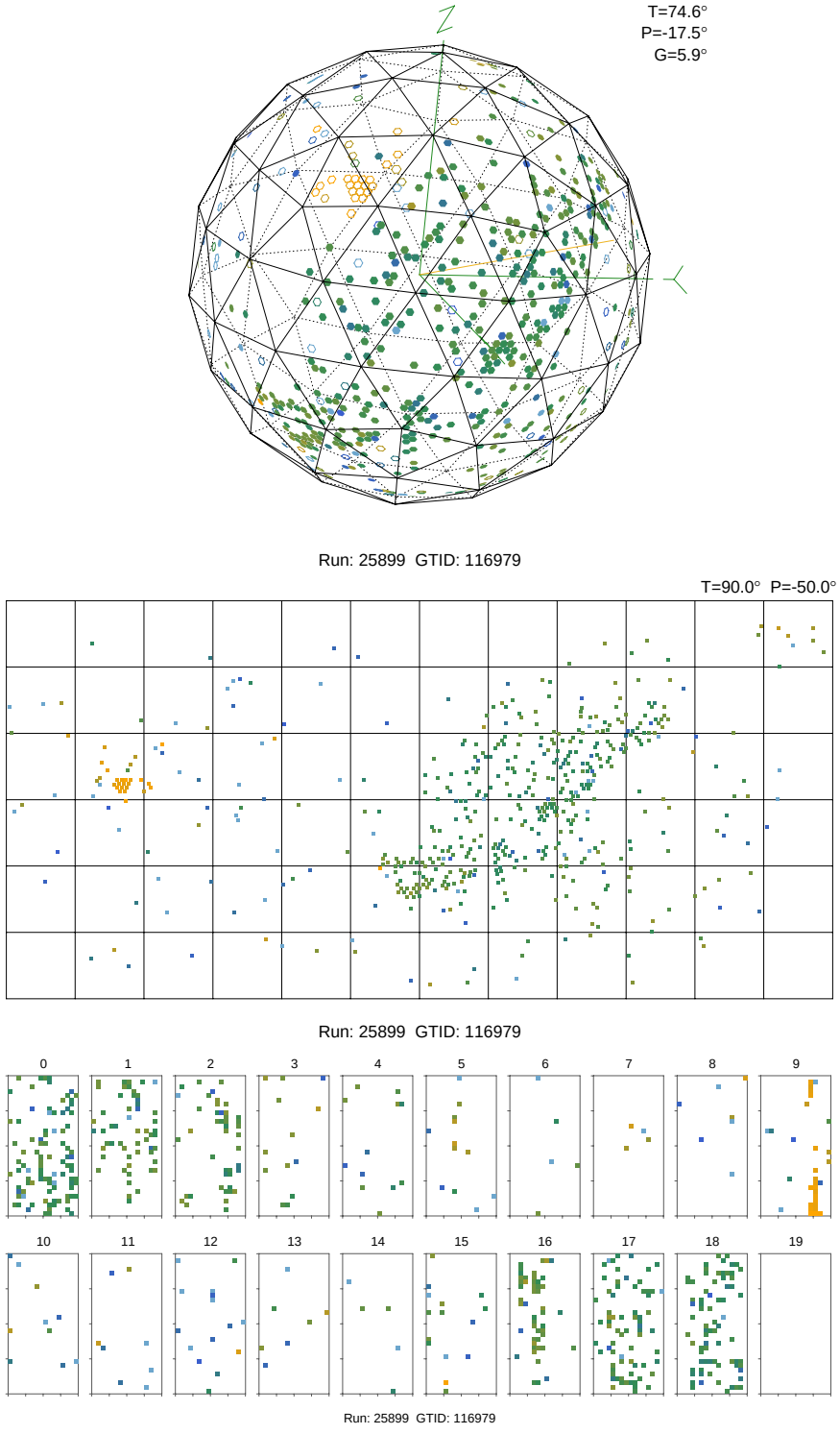

Figure G.3: XSnoed display of a flasher event. The event shown was taken from a collection of pickup events included the qsno package for pathology identification purposes

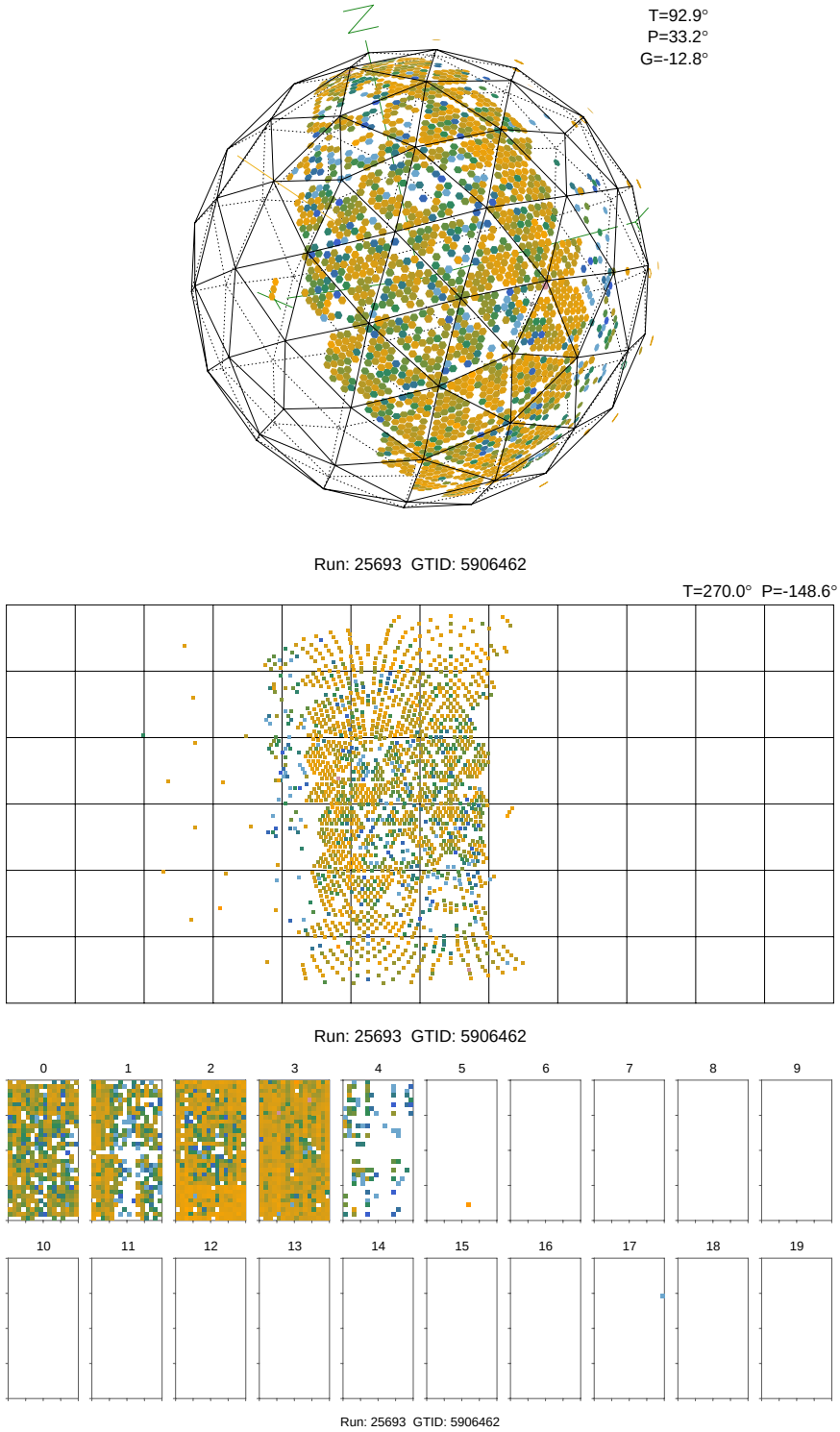

Figure G.4: XSnoed display of an electronic pickup event. The event shown was taken from a collection of pickup events included the qsno package for pathology identification purposes.

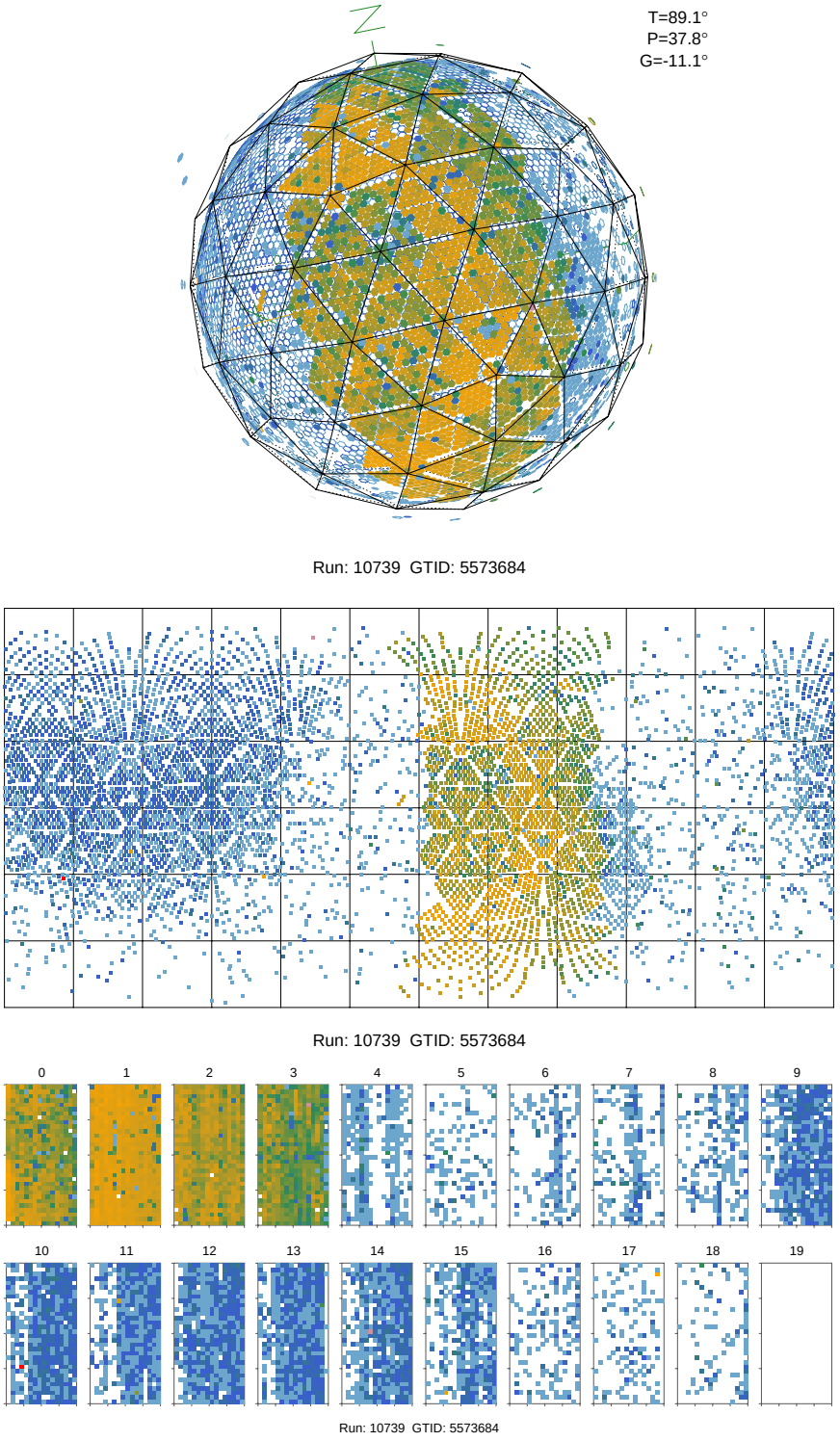

Figure G.5: XSnoed display of electronic pickup event with a additional burst of light.

G.3 Single Monte Carlo Events

In this section, a visual display of some the single Monte Carlo events used in the evaluation of the MRF reconstruction algorithm and the associated reconstruction (shown by the green and red circles). Shown in this section are:

- Single Electron Event with e-like reconstruction
- Single π^0 Event with e-like reconstruction
- Single Muon Event with e-like (red circle) and μ-like (green circle) reconstruction

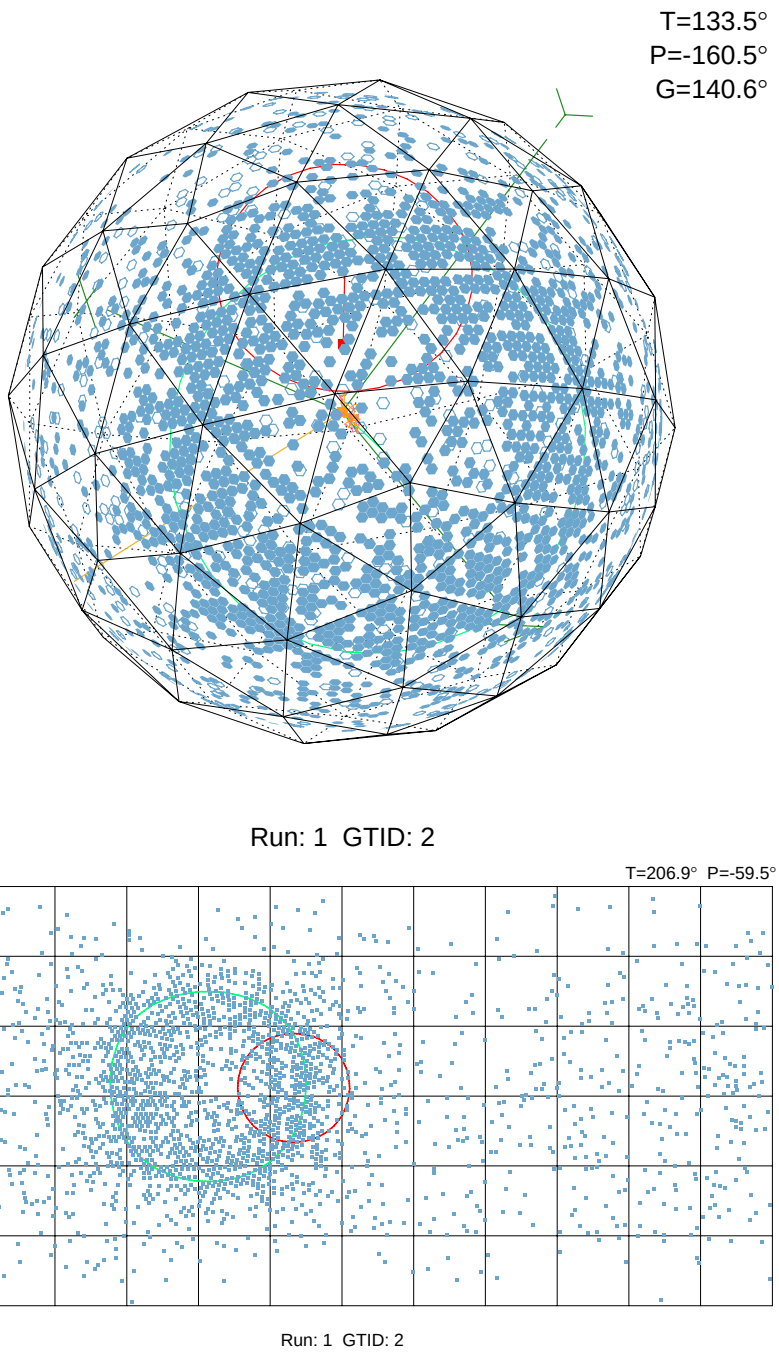

Figure G.6: XSnoed display of the multiple-ring pathology for MC generated e^-. The small red ring is the product of a flaw in the MRF routines: there are multiple mid-points for small rings and the Angular Fitter is not able to reject them efficiently due to the low statistics in the opening angle of the cone when the vertex is too close to the acrylic vessel.

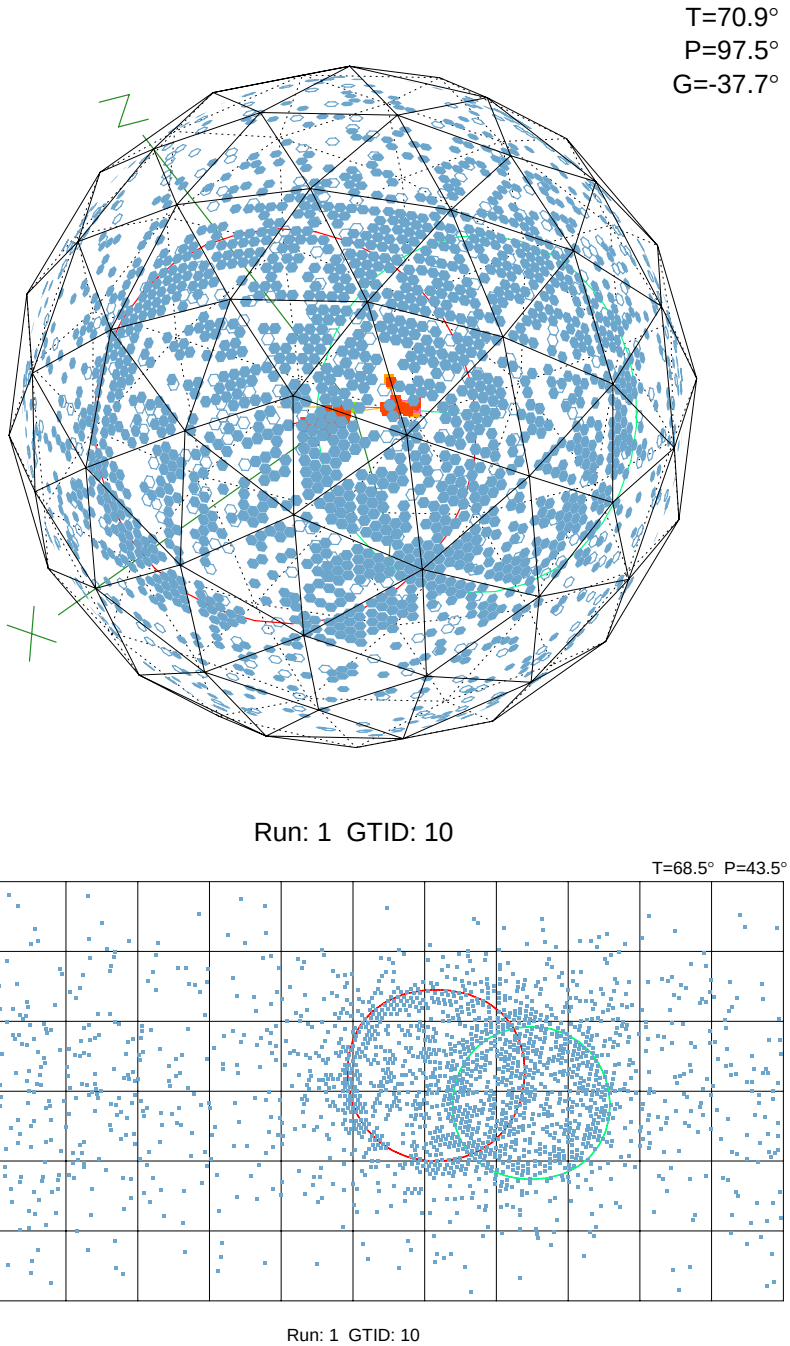

Figure G.7: XSnoed display of the multiple-ring for MC generated π^o. The fit using a e-like expectation reconstruct well the two rings of the π^o.

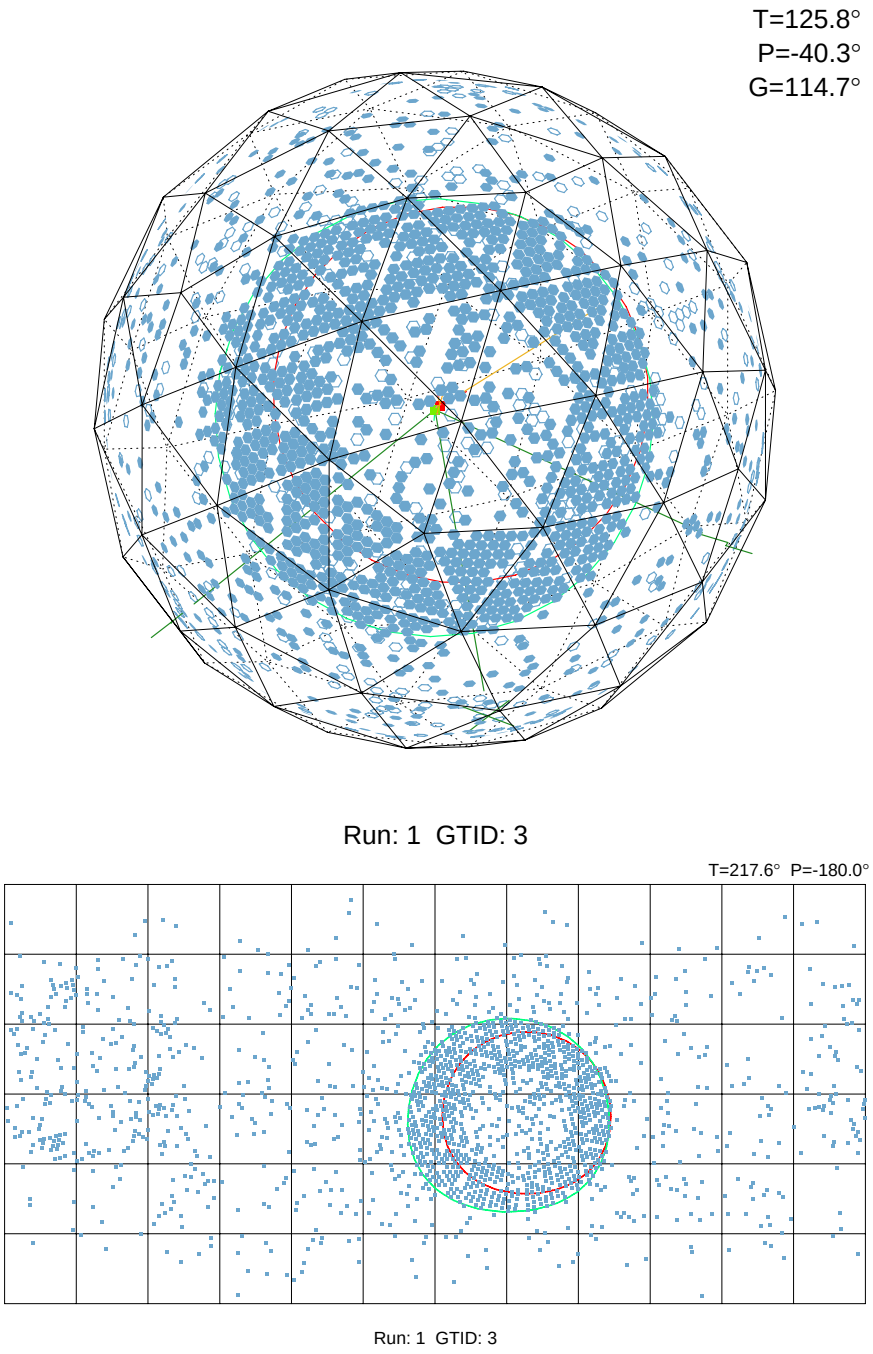

Figure G.8: Fitter reconstruction with e-like (red circle) and μ-like (green circle) expectation for Monte Carlo generated muons. The μ-like fit (green circle) reconstructs very well the ring. The e-like fit finds a ring that is off-center and smaller than the actual ring, this is always the case as can be confirmed in the fit results shown in Figure 5.15. The e-like expectation finds rings in a greater number of events than the μ-like expectation.

G.4 Candidate Events

Shown in this section are the events found in the data that survive all cuts. The events that pass these cuts are:

```
15:
salt:(run, gtid,NRings)=(21562 569604 3)  (owl,butts)=(0, 0) P/E=0.4109
d2o: (run, gtid,NRings)=(11824 5375247 2) (owl,butts)=(2, 0) P/E=0.4553
---
13:
salt:(run, gtid,NRings)=(21562 569604 3)  (owl,butts)=(0, 0) P/E=0.4109
d2o: (run, gtid,NRings)=(10177 295534 2)  (owl,butts)=(0, 0) P/E=0.4551
d2o: (run, gtid,NRings)=(10886 2374662 2) (owl,butts)=(0, 0) P/E=0.4731
d2o: (run, gtid,NRings)=(12168 34526 2)   (owl,butts)=(0, 0) P/E=0.0982
```

distribution

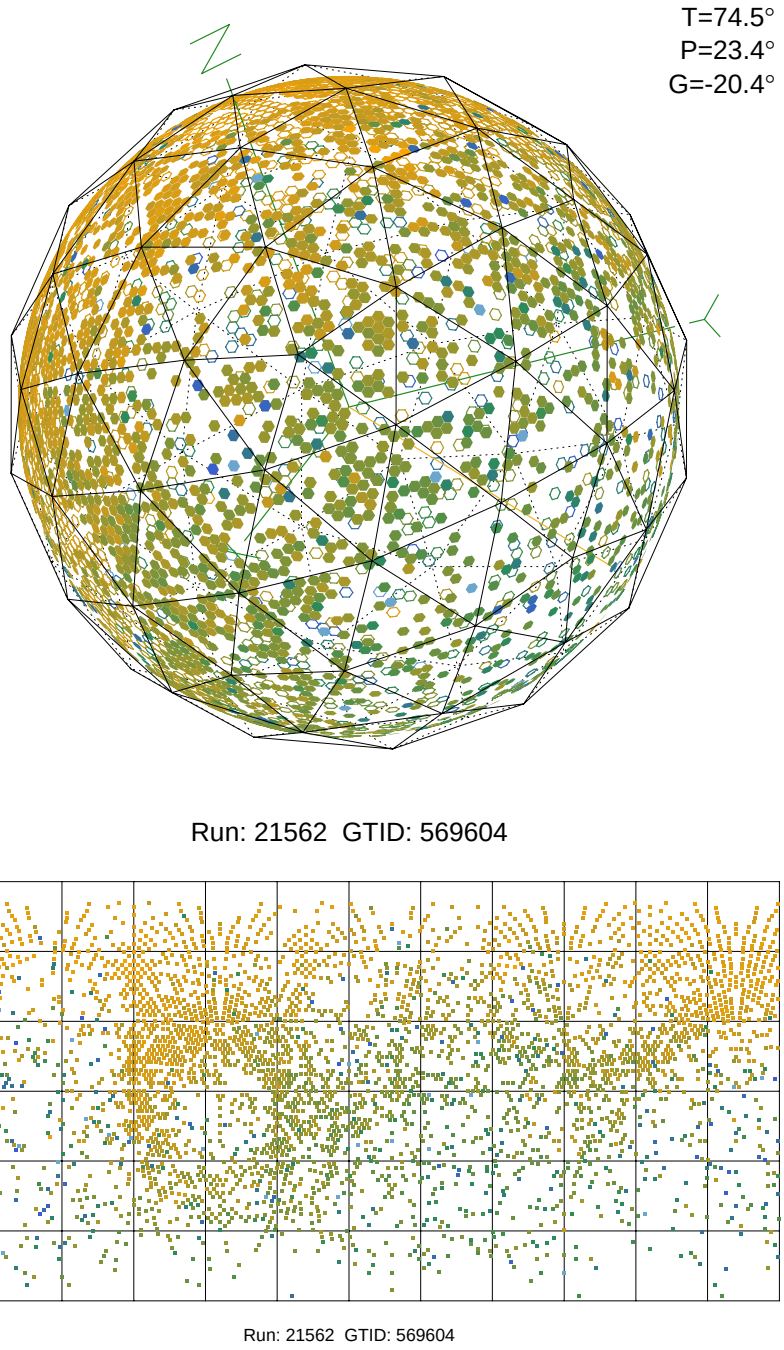

Figure G.9: XSnoed display of nnbar candidate number 1 found in the salt phase. This event pass all the cut for both $\zeta_{thresh} = 13$ and $\zeta_{thresh} = 15$.

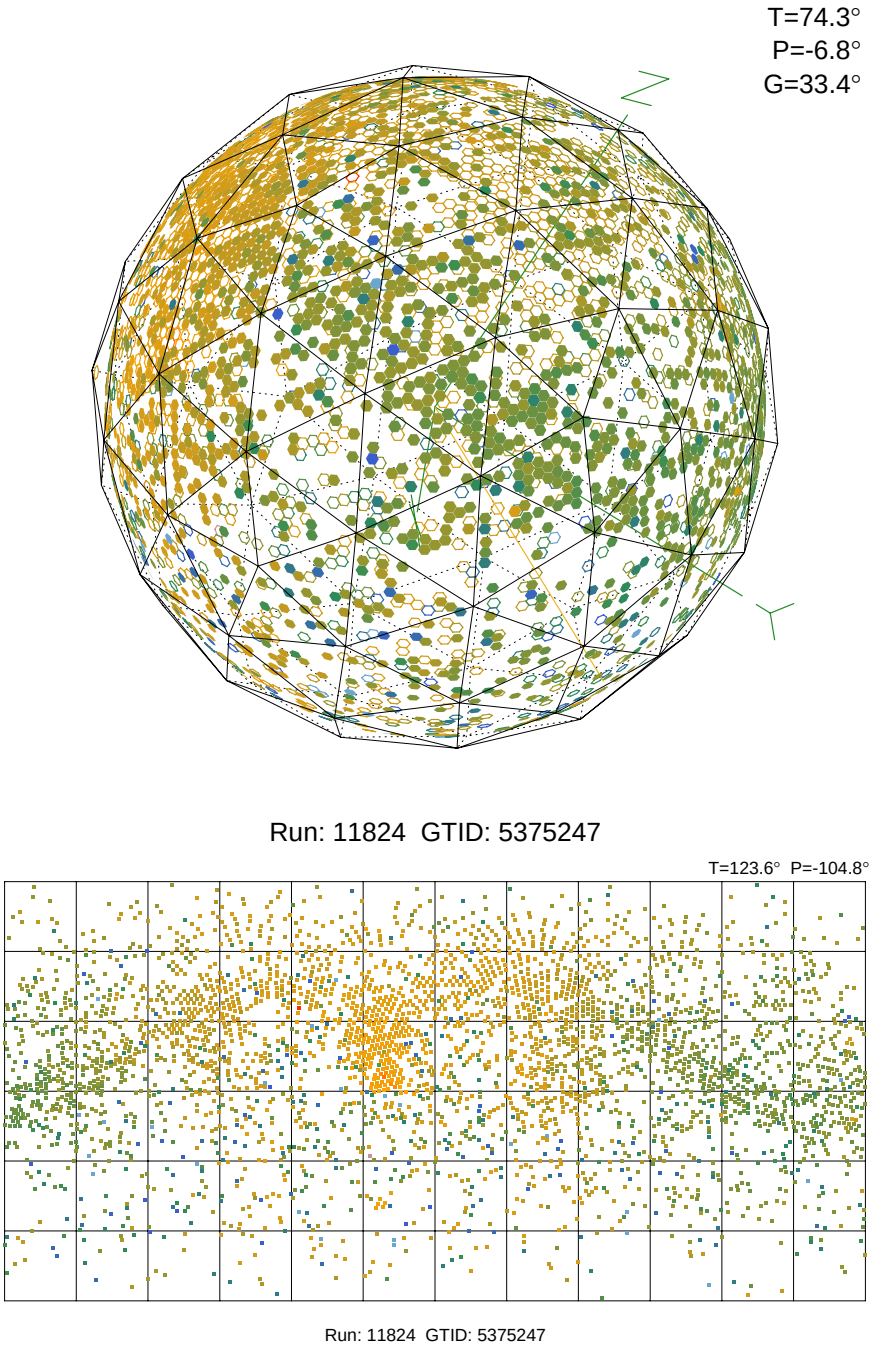

Figure G.10: XSnoed display of nnbar candidate number 2 found in the d2o phase. This event pass all the cuts for $\zeta_{thresh} = 15$ but failed for $\zeta_{thresh} = 13$.

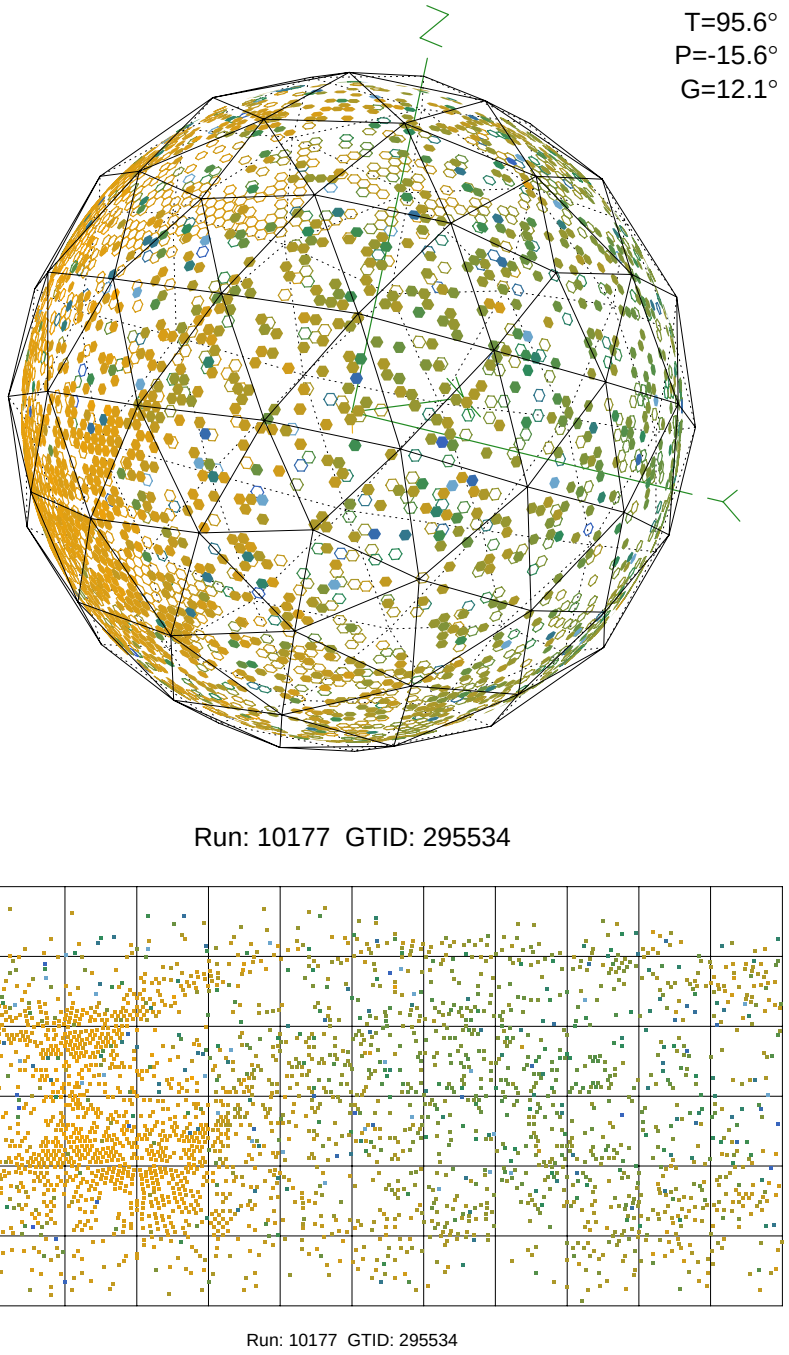

Figure G.11: XSnoed display of nnbar candidate number 3 found in the d2o phase. This event pass all the cuts for $\zeta_{thresh} = 13$, but failed for $\zeta_{thresh} = 15$

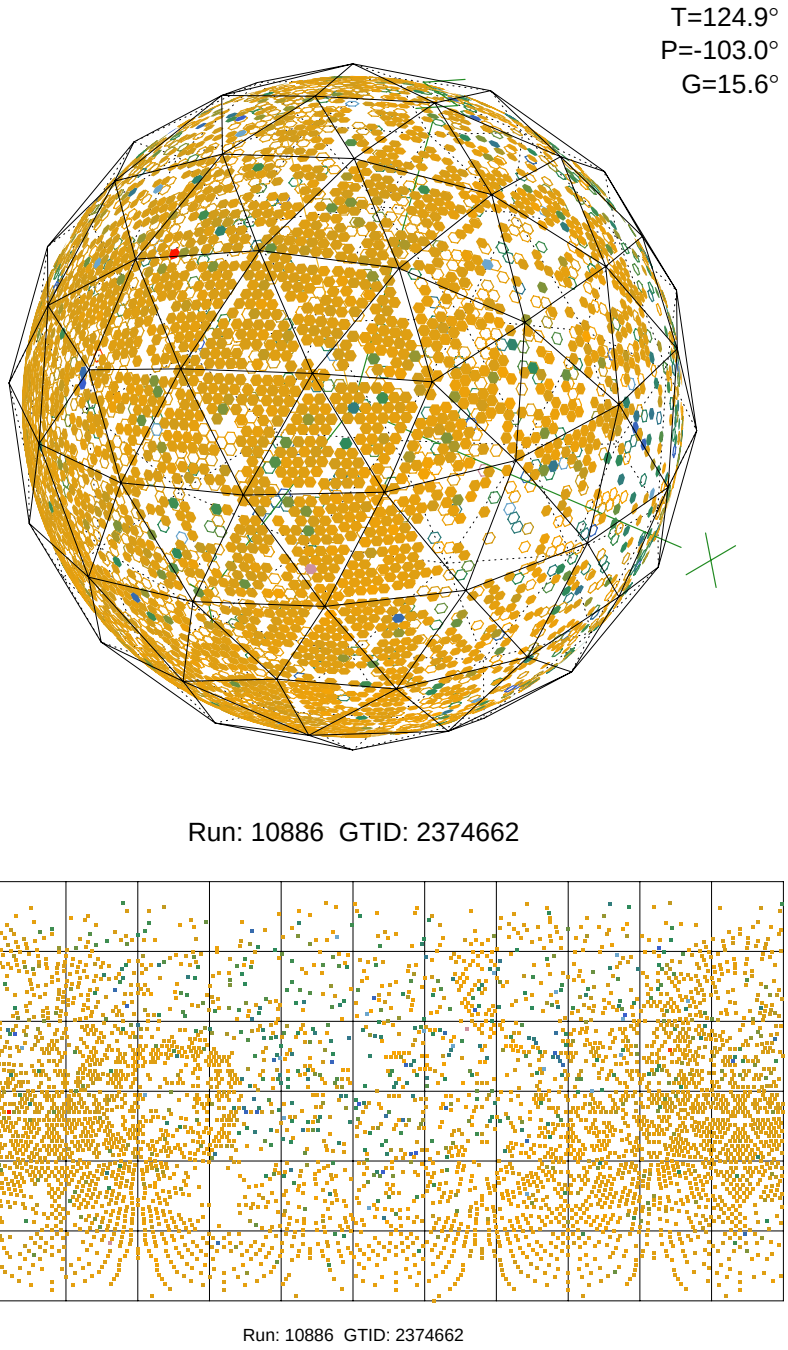

Figure G.12: XSnoed display of nnbar candidate number 4 found in the d2o phase. This event pass all the cuts for $\zeta_{thresh} = 13$, but failed for $\zeta_{thresh} = 15$

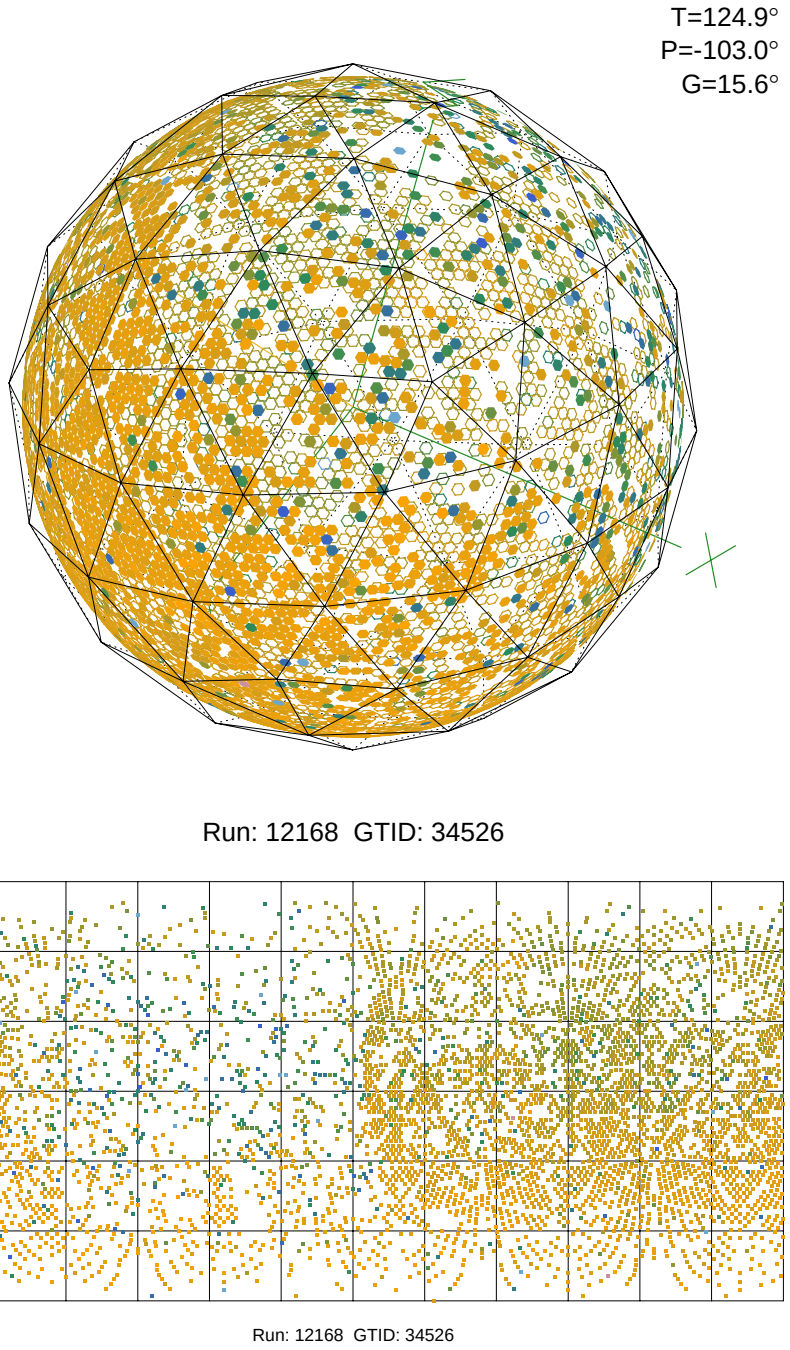

Figure G.13: XSnoed display of nnbar candidate number 5 found in the d2o phase. This event pass all the cut for $\zeta_{thresh} = 13$, but failed for $\zeta_{thresh} = 15$